The Effects of Salt Precipitation During CO₂ Injection into Deep Saline Aquifer and Remediation Techniques

Donatus Ephraim Edem (@00539941)

Supervisor(s):

Dr Amir Nourian

Dr Meisam Babaie

School of Science, Engineering, and Environment (SEE)

University of Salford

Manchester, UK

May 2023

Table of Contents

List of Tables

List of Figures

List of Abbreviations

CO_2	Carbon dioxide
CCS	Carbon dioxide capture and storage
CT	Computed Topography
GHG	Greenhouse gases
IPCC	Intergovernmental panel on climate change
IEA	International energy agency
PPM	Part per million
ppg	Ib/gallon
EGR	Enhanced Gas Recovery
EOR	Enhanced Oil Recovery
Mt	Mega tonnes
$MgCl_2$	Magnesium Chloride
NaCl	Sodium Chloride
KCl	Potassium Chloride
$CaCl_2$	Calcium Chloride

List of Nomenclatures

A	Cross-Sectional Area of the sample. (cm^2)
Q	Flow Rate $= \Delta V / \Delta T$ (cm^3 / sec)
ΔV	Volume of the gas flowed in time ΔT measured at atm. pressure (cm^3)
ΔT	the time period over which flow is measured (s)
K	Permeability of the sample (millidarcies, mD)
L	Length of the sample. (cm)
Pa	Absolute Atmospheric Pressure Initially in Sample chamber
P_1	Upstream Pressure (atmospheres)
P_2	Downstream Pressure (atmospheres)
Po	Outlet Fluid Pressure (atmospheres absolute, atma)
Pi	Inlet Fluid Pressure (atmospheres absolute, atma)
Δp	Differential Pressure (psig)
V	Flow Volume (millilitres)
Vp	Pore volume of the core sample (cm^3)
Vb	Bulk volume of the core sample (cm^3)
Vc	Sample Chamber Volume (cm^3)
Vg	Grain Volume (cm^3)
Vr	Reference Chamber Volume (cm^3)
Vv	Valve Displacement Volume (cm^3)
μ	Dynamic Viscosity of the fluid (centipoise, cP)

Acknowledgements

Declaration

I, Donatus Ephraim Edem, declare that this work is my original work, and has not been submitted elsewhere for any award. Any section, part or phrasing that has been used or copied from other literature or documents copied has been clearly referenced at the point of use as well as in the reference section of the work.

………………………..   ……………………….

Signature (Donatus Edem)   Date

………………………..   ………………………..

Approved by Dr Amir Nourian (Supervisor)   Date

Abstract

The by-products of combustion from the utilisation of fossil fuels for energy generation are a source of greenhouse gas emissions, mainly Carbon dioxide (CO_2). This has been attributed to climate change because of global warming. Carbon capture and storage (CCS) technology has the potential to reduce anthropogenic greenhouse gas emissions by capturing CO_2 from emissions sources and stored in underground formations such as depleted oil and gas reservoirs or deep saline formations. Deep saline aquifers for disposal of greenhouse gases are attracting much attention as a result of their large storage capacity. The problem encountered during CO_2 trapping in the saline aquifer is the vaporisation of water along with the dissolution of CO_2. This vaporisation cause salt precipitation which eventually reduces porosity and impairs the permeability of the reservoir thereby impeding the storage capacity and efficiency of the technology. Salt precipitation during CO_2 storage in deep saline aquifers can have severe consequences during carbon capture and storage operations in terms of CO_2 injectivity.

This work investigates and assesses, experimentally, the effects of the presence of salt precipitation on the CO_2 injectivity, the factors that influence them on selected core samples by core flooding experiments, and remediation of salt precipitation during CO_2 injection. The investigation also covered the determination of optimum range of deep saline aquifers for CO_2 storage, and the effects of different brine-saturated sandstones during CO_2 sequestration in deep saline aquifers. In this investigation, three (3) different sandstone core samples (Bentheimer, Salt Wash North, and Grey Berea) with different petrophysical properties were used for the study. This is carried out in three different phases for a good presentation.

- Phase I of this study involved brine preparation and measurement of brine properties such as brine salinity, viscosity, and density. The brine solutions were prepared from different salts ($NaCl$, $CaCl_2$, KCl, $MgCl_2$), which represent the salt composition of a typical deep saline aquifer. The core samples were saturated with different brine salinities (5, 10, 15, 20, 25, wt.% Salt) and testing was conducted using the three selected core samples.
- Phase II entailed the cleaning and characterisation of the core samples by experimental core analyses to determine the petrophysical properties: porosity and permeability. Helium Porosimetry and saturation methods were used for porosity determination. Core flooding was used to determine the permeability of the core samples. The core flooding process was conducted at a simulated reservoir pressure of 1500 psig, the temperature of 45 °C, with injection rates of 3.0 ml/min respectively. Interfacial tension (IFT) measurements between the CO_2 and various brine salinities as used in the core flooding were also conducted in this phase. Remediation scenarios of opening the pore spaces of the core samples were carried out using the same core flooding rig and the precipitated core samples were flooded with remediation fluids (low salinity brine and seawater) under the same reservoir conditions. The petrophysical properties (Porosity, Permeability) of the core samples were measured before core flooding, after core flooding and remediation test respectively.
- In phase III of the study, SEM Image analyses were conducted on the core samples before core flooding, after core flooding, and remediation test respectively. This was achieved by using the FEI Quanta FEG 250 FEG high-resolution Scanning Electron Microscope (SEM) interfaced to EDAX Energy Dispersive X-ray Analysis (EDX).

Results from Bentheimer, Salt Wash North, and Grey Berea core samples indicated a reduction in porosity, permeability impairment, as well as salt precipitation. It was also found that, at 10 to 20 wt.% brine concentrations in both monovalent and divalent brine, a substantial volume of CO_2 is sequestered, which indicates the optimum concentration ranges for storage purposes. The salting-out effect was greater in divalent salt, $MgCl_2$ and $CaCl_2$ as compared to monovalent salt (NaCl and KCl). Porosity decreased by 0.5% to 7% while permeability was decreased by up to 50% in all the tested scenarios. CO_2 solubility was evaluated in a pressure decay test, which in turn affects injectivity. Hence, the magnitude of CO_2 injectivity impairment depends on both the concentration and type of salt species. The findings from this study are directly relevant to CO_2 sequestration in deep saline aquifers as well as screening criteria for carbon storage with enhanced gas and oil recovery processes. Injection of remediation fluids during remediation tests effectively opened the pore spaces and pore throats of the core samples and thereby increasing the core sample's porosity in the range of 14.0% to 28.5% and 2.2% to 12.9% after using low salinity brine and seawater remediation fluids respectively. Permeability also increases in the range of 40.6% to 68.4% and 7.4% to 17.2% after using low salinity brine and seawater remediation fluids respectively. These findings provide remediation strategies useful in dissolving precipitated salt as well as decreasing the salinity of the near-well brine which causes precipitation.

The SEM images of the core samples after the flooding showed that salt precipitation not only plugged the pore spaces of the core matrix but also showed significant precipitation around the rock grains thereby showing an aggregation of the salts. This clearly proved that the reduction in the capacity of the rock is associated with salt precipitation in the pore spaces as well as the pore throats. Thus, insight gained in this study could be useful in designing a better mitigation technique, CO_2 injectivity scenarios, as well as an operating condition for CO_2 sequestration in deep saline aquifers.

Chapter 1: Introduction

1.1. Overview

Since the beginning of the industrial revolution in 1750 and with the increase in the use of fossil fuels and the development of deforestation globally, the emission of greenhouse gases has increased significantly [1]. As a result, the CO_2 concentration in the atmosphere has increased tremendously from 280 to 392.6 parts per million (ppm) in 2012. In 2017, the CO_2 global emissions from fossil fuels and industry were once again rise by 2%, to a record 37 billion tonnes. The resurgence tightens the time constraint on the world's efforts to keep the global warming from exceeding 2 ℃. This is a gap that scientist increasingly believe is important to ward off climate change's most catastrophic effects [2]. According to a report from the 'Intergovernmental Panel on Climate Change (IPCC)' in 2014, carbon dioxide sourced from fossil fuels and industrial processes, was responsible for 65% of all global Greenhouse Gas (GHG) emissions. The burning of coal, natural gas and oil for electricity and heat is the largest single source of global greenhouse emissions, accounting for 25% of global greenhouse emissions compared to other economic sectors [3]. According to recent data from the National Oceanic and Atmospheric Administration and the Scripps Institution of Oceanography, the concentration of CO_2 in the global atmosphere reached 419.28 ppm in February 2022 [4]. The rising concentration of CO_2 in the atmosphere has undoubtedly contributed to the worsening of the global climate problem. Carbon dioxide capture and storage (CCS) in geological media is a technology that is recognised significantly as a viable option for reducing the atmospheric emission of anthropogenic CO_2. CCS is a process consisting of the separation of CO_2 from industrial and energy-related sources, location, and long-term isolation from the atmosphere. This has already been demonstrated around the world on a large scale few projects [5]. However, this technology is cost-intensive and rapidly undergoing improvement for cost-effectiveness as well as efficiency [6]. The major factors that required pre-assessment for CO_2 storage in a particular geological formation are:

i. High capacity to store a large amount of CO_2, and
ii. High injectivity to enable injection at desired rates and containment efficiency [7].

In order to achieve a successful injection of large amount of CO_2 into a geological reservoir, a proper well injectivity is required. The injection of dry supercritical CO_2 into saline aquifer and subsequent vaporisation of the brine leads to precipitation of the salt. This precipitation induced

by brine vaporisation is a distinct problem during CO_2 injection and can lead to injectivity impairment around injection wells in saline aquifer [7, 8]. This can further result in the reduction of the porosity and permeability of the reservoir by significantly affecting wellbore injectivity [9, 10]. However, well injectivity may be controlled by a lot of numerous factors such as formation thickness, relative permeability, formation permeability as well as the porosity reduction emanating from the various salts and other minerals present in the formation [11].

Deep saline aquifers (or formations) are known to contain water with high salt concentrations and most likely have the largest storage capacity among the geological media under consideration. Deep saline formations have been recommended as promising storing sites because of their abundance and theoretically large volume [12]. However, compared with oil and gas reservoirs, deep saline aquifers are less well known and have received less attention in terms of their properties because of the lack of economic interest in the past. Thus, characterisation of deep saline aquifers on a regional scale becomes an important objective in recent studies for suitable sites and for the purpose of CO_2 storage. From an industrial opinion, the main concerns of CO_2 sequestration in aquifers are associated with the characterisation of suitable aquifer, accessible storage volume, attendance of cap rock of low permeability, and injection flow rate of CO_2 during the injection [13]. Core flooding experiments were used to determine the extent of reduction in porosity caused by salt precipitation which can considerably reduce the reservoir permeability. The process of salt precipitation seems to be rather simple, but the insight is complex and is a long-standing issue in the petroleum and gas industry. Several laboratory investigations have been carried out to determine salt precipitation and analyse its influence on the fluid flow [9, 14-17]. Core flooding experiments were used to determine the interactions between CO_2-brine-rock core and the extent of reduction in porosity caused by salt precipitation which can significantly reduce the reservoir permeability.

Furthermore, global greenhouse gas emissions are still far below what is required to maintain a liveable climate, and support for the most vulnerable countries affected by climate change is woefully inadequate. However, COP26/27 produced new "building blocks" to advance Paris Agreement implementation through actions that can put the world on a more sustainable, low-carbon path forward. Countries reaffirmed the Paris Agreement goal of keeping global average temperature rise well below 2°C above pre-industrial levels and pursuing efforts to keep it below 1.5°C. They went on to say that "human activities have caused around 1.1 °C of warming to date, that impacts are already being felt in every region, and that carbon budgets consistent with meeting the Paris Agreement temperature goal are now small and rapidly depleting." They

recognized that the effects of climate change will be much less severe if temperatures rise by 1.5°C rather than 2°C. Thus, Carbon Capture and storage is envisaged as a potential solution for COP 26/27 to maintain a balance of adaptation and mitigation.

Global action to combat climate change is critical to the UK's long-term prosperity. Net zero targets now cover the vast majority of global GDP. As the world decarbonizes, UK action can benefit businesses and households throughout the country. The United Kingdom has been at the forefront of global climate action, leading the way by decarbonizing its economy faster than any other G7 country. In 2019, the United Kingdom became the world's first major economy to set a legally binding goal of reducing greenhouse gas emissions to zero by 2050. By 2050, the transition to net zero will mean changes in the way businesses operate and people live in England, Scotland, Wales, and Northern Ireland, which will be unique to each person based on their individual circumstances. Some of these changes are known, but there are areas of significant uncertainty over a 30-year transition, with major system-wide decisions on the UK's future energy mix and the role of negative emission technologies in achieving net zero to be made over the next decade (Net Zero Review Analysis exploring the key issues, 2022). Thus, CCS technology however can play a vital role in abating the menaces of these greenhouse gases especially CO_2 to the barest minimum.

Saline aquifers, depleted oil and gas reservoirs, and coal seams are currently the most common types of reservoirs suitable for CO_2 sequestration. Apart from saline aquifers, the above storage methods have limited CO_2 storage capacity, the appropriate technology is still in its early stages, and CO_2 separation and reinjection processes must be added. Suitable storage sites for CO_2 sequestration in brine layers are widely distributed, with the benefits of stable storage, high feasibility, high reservoir porosity and permeability, and large storage capacity. As a result, carbon storage in saline aquifers is regarded as the most feasible and promising method. The capacity of different reservoirs in North America to sequester CO_2 is shown in Table 1.1. It is clear that saline aquifers in North America play the most important role in large-scale CO_2 sequestration. In China, saline aquifers have a much higher CO_2 sequestration potential than depleted oil and gas reservoirs and coal seams.

The capacity of saline aquifers in different regions of China to sequester CO_2 is shown in Table 2.2. The Ordos Basin, Sichuan Basin, Songliao Basin, Qaidam Basin, Tarim Basin, Bohai Bay, and the Pearl River Mouth have high CO_2 sequestration potential [18].

Table 1.1: CO₂ sequestration potential of different reservoirs in North America [19]

Reservoir Types	Estimated Storage Capacity (Gt)	Reservoir Integrity
Depleted oil and gas reservoir	186 – 232	High
Coal steam	54 – 113	Medium
Saline aquifers	2379 – 21633	Highest
TOTAL	**2618 – 21978**	

Table 1.2: CO₂ Sequestration capacity of saline aquifers in various basins in China [20]

Name of the Basin	Estimated Storage Capacity (Gt)
Pearl River Mouth	308.00
Tarim	247.26
East China Sea	201.25
Bohai Bay	189.42
Sichuan	133.44
Ordos	128.78
Qaidam	126.28
Zhujiangkou	124.37
Zhunggar	88.75
Erlian	69.52
Songliao	65.05
Western Taiwan	59.46
Qiangtang	51.62
Beibu Gulf	48.56

1.2. Problem Statement

Global warming, as it indicates by the name, is the rise in the average temperature of the earth's atmosphere and it is one of the prolonged ecological problems facing by the current humanity. This temperature rise caused by the increase in the level of greenhouse gases, mainly carbon dioxide, and it is detrimental to the environment as a whole and mankind in general. Therefore, the current need is to control the CO_2 emission to the barest minimum with new technologies. CCS technique is one of the methods for isolating or removing emitted CO_2 into the atmosphere by industries and other human activities. CCS is the process of capturing waste carbon dioxide from large point sources, such as fossil fuel power plants, transporting it to a storage site by pipeline or ship, and injecting it where it will not enter the atmosphere, normally an underground geological formation. In this method, the large amount of CO_2 from fossil fuel

used in power generation and other industries is capturing to prevent them to be release into the atmosphere [1]. In order to achieve the most effective way of storing CO_2 in many geological reservoirs, a thorough understanding of the mechanics involved during the storage process is required.

However, water vaporisation is one of the main problems encountered during CO_2 trapping in saline aquifer along with the dissolution of CO_2. This vaporisation cause salt precipitation which eventually reduces porosity and impairs the permeability of the reservoir. This impairment can lead to reduction in CO_2 injectivity which depends on the degree of reduction of the formation permeability with salt saturation [21]. This major challenge has not only limited the CO_2 storage operations but has also made the process simple and efficient to predict the amount of salt precipitation over space and time. Although the process of salt formation seems rather simple, but the insight is complex and is a long-standing issue in the oil and gas industry [22].

Therefore, there is a need for further research and study to specify how salt precipitation affects CO_2 storage as well as the mitigation techniques to minimise salt precipitation during storage in deep saline aquifer. Muller et.al [14] studied the formation dry-out and precipitation with focus on CO_2 sequestration. They reported 60% reduction in absolute permeability after the experiment and this was attributed to salt precipitation with the confirmation of Scanning Electron Microscopy (SEM) micrographs. Several other researchers conducted extensive research on the sensitivity of some parameters to ascertain observations regarding salt precipitation but they did not give a proper formulation of the components to use in preventing or mitigating salt precipitation [7, 10, 16, 23-25]. Investigating proper formulation or mitigation strategies will help reservoir engineers to plan an appropriate CO_2 sequestration process without any interruption attributed by salt precipitation.

1.3. Aims and Objectives

In this study, a comprehensive approach has been used to study, understand, and assess the factors as well as mechanisms that affect salt precipitation in carbon dioxide capture and storage. This entails carrying out of a core flooding experiment with different sandstone core samples and using different salt types and concentration of brine solutions. The main aims of this study are:

- to investigate the effect of salt precipitation during CO_2 injection into deep saline aquifer for sequestration, and

- possible remediation strategies to abate salt precipitation.

To achieve the above aims, the main objectives are:

- Characterisation of the core samples which involves cleaning and measurements of the petrophysical properties.
- Investigate and assess experimentally, the effects of the presence of salt precipitation on the CO_2 injectivity on selected core samples by core flooding experiments.
- Investigate the concentration, pressure decay rate, solubility, and the interaction of the CO_2 in the porous media at different concentrations with different types of salt (NaCl, KCl, $CaCl_2$ and $MgCl_2$).
- Analysis of the core samples before and after each experiment by means of Scanning Electron Microscopy (SEM) micrographs and Energy Dispersive X-Ray (EDX) mapping to ascertain the extents of the rock morphology variation and changes because of precipitation.
- Adopt effective remediation strategies through injection of variation of different brine salinities to improve permeability as well as injectivity.

1.4. Contribution to Research

a) One of the contributing factors to this research was the determination of the optimal concentration range for CO_2 sequestration in deep saline aquifers, and it was useful to determine the amount of CO_2 stored in each brine concentration with respect to the salt type.

b) A pressure decay rate was useful in evaluating the degree of solubility of CO_2 in different brine solutions in porous media. Thus, the solubility of CO_2 with respect to the the salt type as well as the concentration of the brine was investigated.

c) The successful remediation approach of combating precipitated salt in the pore matrix of the core sample during CO_2 sequestration is of immense contribution to this work.

1.5. Structure of the Thesis

This thesis is structured into five different chapters and each chapter presents the details as stated therein. The summary of each chapter is presented as follows:

- *Chapter 1 – Introduction:* This chapter introduces the concept of salt precipitation during storage of CO_2 in deep saline aquifer. The problem statements with respect to the thesis are stated as well as the thesis aims and objectives

- *Chapter 2 – Literature Review:* This chapter presents the survey of literature related to the thesis topic. It provides the insight into geological storage of CO2 and how dry-out or vaporization occurs thereby leading to salt precipitation. It also covers the characteristics and mechanism of salt precipitation.

- *Chapter 3 – Experimental Setup and Methodology:* This chapter demonstrates the experimental setup, methodology and materials required to carry out the experiments. This section also described the apparatus and enumerates the working principles of each of them. It also highlighted the procedure and safety precaution with respect to the use of the equipment.

- *Chapter 4 – Results and Discussions:* The results obtained from using the methods described in chapter 3 are presented in this section and are discussed accordingly.

- *Chapter 5 – Conclusion and Future Work Recommendations:* This chapter concludes the outcome of the experimental work and highlighted the necessary recommendations for future work.

Chapter 2: Literature Review

2.1. Overview

This chapter discusses carbon dioxide capture and storage (CCS) in deep saline aquifers. It focuses on the fundamentals of CCS and the specific research conducted experimentally and numerically on brine aquifers. It also provides a synopsis of the salt precipitation characteristics and during CO_2 geological storage. In addition, relevant literature is evaluated to establish the conceptual foundation for this investigation.

2.2. Concept of Carbon Dioxide Capture and Storage (CCS)

Carbon dioxide (CO_2) capture and storage (CCS) is a process that involves separating CO_2 from industrial and energy-related sources, transporting it to a storage location, and isolating it from the atmosphere for an extended period of time. This report considers CCS as one of several mitigation options for stabilizing atmospheric greenhouse gas concentrations. Other mitigation options include increasing energy efficiency, switching to less carbon-intensive fuels, nuclear power, renewable energy sources, improving biological sinks, and reducing non-CO_2 greenhouse gas emissions. CCS has the potential to lower overall mitigation costs while increasing flexibility in reducing greenhouse gas emissions. The widespread application of CCS would be dependent on technical maturity, costs, overall potential, technology diffusion and transfer to developing countries and their capacity to apply the technology, regulatory aspects, environmental issues, and public perception. In other words, Carbon dioxide capture and storage (CCS) is known as one of the options for reducing atmospheric emission of CO_2 obtained from anthropogenic activities. CO_2 is emitted mostly from the burning of fossil fuels from large combustion units for electric power generation as well as in smaller distributed sources such as automobiles engines, furnaces used in commercial and residential buildings [26]. CO_2 discharge into the environment is also emanated from burning of bushes after clearing the land as well as effluents from industrial and resource extraction processes such as petroleum refining and petrochemicals. CCS technology is applied to large point sources of CO_2 such as large industrial processes or electric power plants. These sources could eventually provide decarbonized fuel (hydrogen) to industrial and transportation sectors thereby reducing emission of CO_2 in those sources. Studies demonstrate that the power and industrial areas jointly contribute to the present worldwide CO_2 releases accounting for about 60% of entire CO_2 releases [27].

CCS technology involves primarily the collection and concentration of CO_2 produced in industrial and energy related sources, transport it to the storage site and subsequently store it underground away from the atmosphere for a very long period. Application of CCS to biomass energy sources could lead to the net evacuation of CO_2 from the atmosphere by capturing and storing CO_2 taken up by the biomass, provided the biomass is not harvested at an unsustainable rate [28].

2.3. Characteristics of Carbon Capture and Storage (CCS)

CO_2 capture can be applied to large point sources. The CO_2 would then be compressed and transported to geological formations, the ocean, mineral carbonates, or industrial processes for storage. Table 2.1 shows that large point sources of CO_2 include large fossil fuel or biomass energy facilities, major CO_2-emitting industries, natural gas production, synthetic fuel plants, and fossil fuel-based hydrogen production plants.

Table 2.1: Profile by process or industrial activity of worldwide large stationary CO_2 sources with emissions of more than 0.1 million tonnes of CO_2 (Mt CO_2) per year

Process	Number of Sources	Emissions (Mt CO_2 per Year)
Fossil Fuels		
Power	4942	10539
Cement Production	1175	932
Refineries	638	798
Iron and Steel Industry	269	646
Petrochemical Industry	470	379
Oil and Gas Processing	N/A	50
Other Sources	90	33
Biomass		
Bioethanol and Bioenergy	303	91
TOTAL	**7889**	**13466**

Geological storage (in geological formations such as oil and gas fields, unmineable coal beds, and deep saline formations), ocean storage (direct release into the ocean water column or onto the deep seafloor), and industrial CO_2 fixation into inorganic carbonates are potential technical storage methods.

Figure 2.1 illustrates the major components of the CCS process which include capture, transport, and storage components. All these components are present in industrial operations

today, although mostly not for the purpose of CO_2 storage. The capture step involves the separation of CO_2 from other gaseous products. For power plants that is involving fuel burning processes, separation technologies can be used to capture CO_2 after combustion. Transport step involves the carrying of the captured CO_2 to storage site located at a distance from the CO_2 source. The captured CO_2 gas is usually compressed to a high density at the capture facility to aid both transport and storage. More so, potential storage methods include injection into underground geological formations, injection into deep ocean or saline aquifer, or industrial fixation in inorganic carbonates. Some industrial processes store small amounts of captured CO_2 in manufactured products and sale some for institution to use for research purpose.
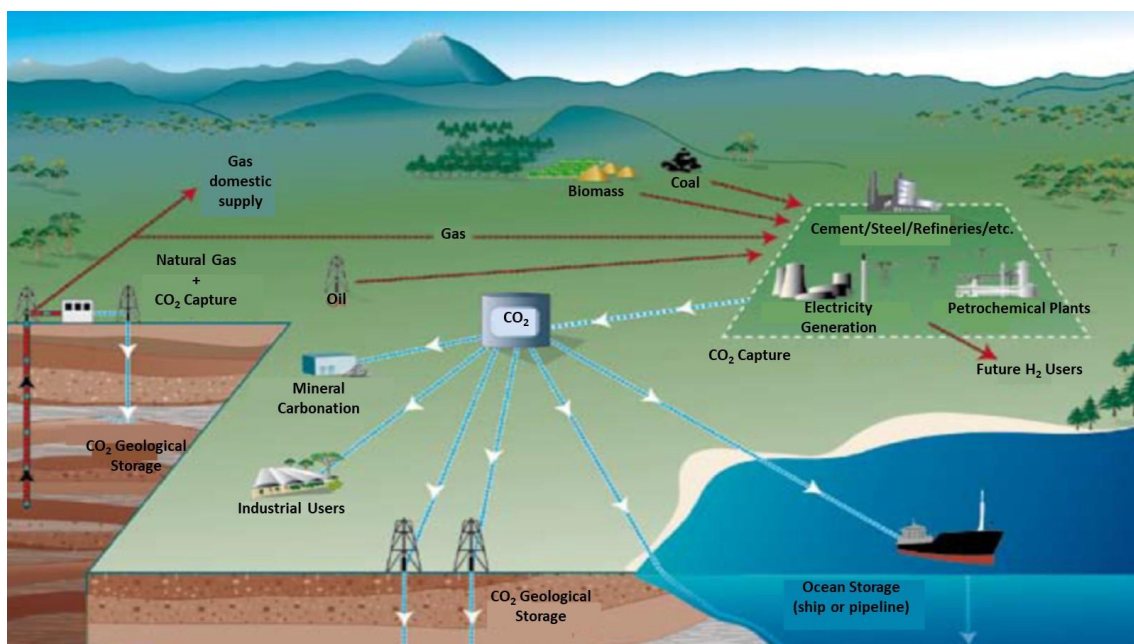
Figure 2.1: Schematic diagram of possible CCS systems [1]

The net reduction in emissions to the atmosphere achieved through CCS is determined by the fraction of CO_2 captured, the increased CO_2 production caused by a loss in overall efficiency of power plants or industrial processes due to the additional energy required for capture, transport, and storage, any leakage from transport, and the fraction of CO_2 retained in storage over time. Currently available technology captures approximately 85-95% of the CO_2 processed in a capture plant. A power plant equipped with a CCS system (with access to geological or ocean storage) would require roughly 10-40% more energy than an equivalent output plant without CCS, the majority of which would be for capture and compression. In terms of secure storage, a power plant with CCS could reduce CO_2 emissions to the atmosphere

by approximately 80-90% when compared to a plant without CCS. (Figure 2.2). To the extent that leakage from a storage reservoir is possible, the percent maintained is defined as the proportion of the total quantity of injected CO_2 that is held during a specific time period. CCS systems using mineral carbonate storage would need 60-180% more energy than a reactor of equal output without CCS [26].
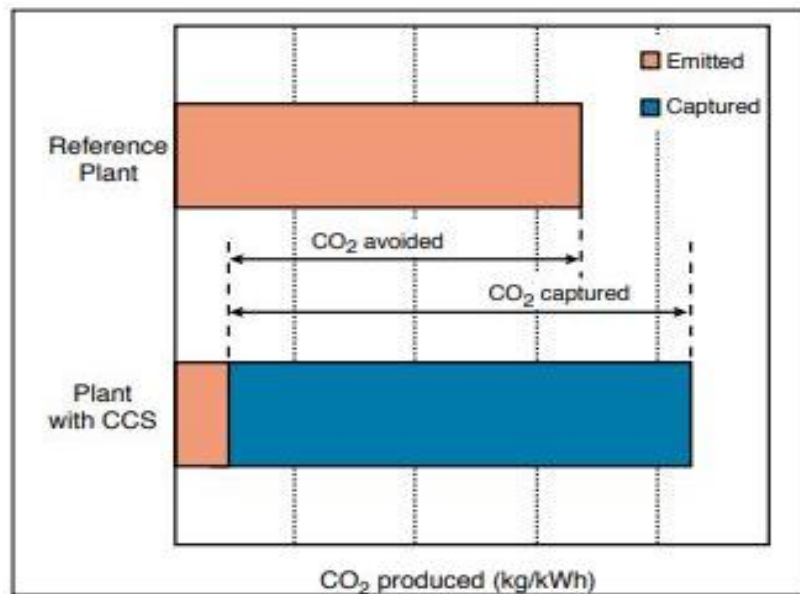
Figure 2.2: CO₂ capture and storage from power plants

2.4. CO₂ Geological Storage and Principles

There are some formations which are porous and contain fluid in them, either water or oil and gas. To meet energy requirement humans have explored and extracted oil and gas from the reservoirs deep within the earth surface. These depleted fields and other saline aquifers can also be used to store CO_2 into them, and by doing this helps to reduce the amount of CO_2 into the atmosphere [11].

In CCS process the first step is to capture the CO_2 from the fixed industrial emission sources, compression, and transportation of CO_2, and then injecting into the underground reservoir formation for permanent storage as shown in Figures 2.1 and 2.3. For progression in CCS project, the essential thing is the selection of suitable site and the reservoir characterisation [13].
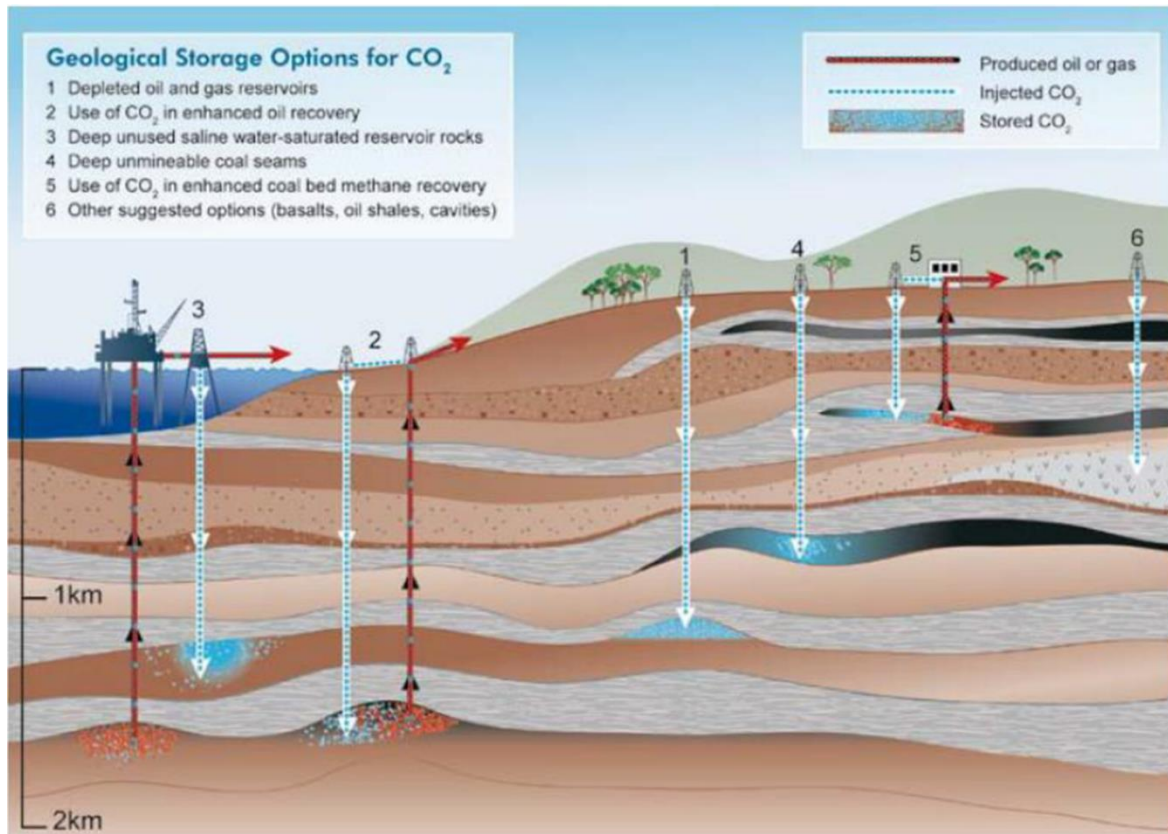
Figure 2.3: Different geological CO2 storage in a variety of formations [1]

The storage of CO_2 into geologic formations includes the following options:

- Storing of CO_2 in the depleted petroleum fields.
- Deep saline aquifers.
- Injecting CO_2 for enhanced gas recovery.
- Enhanced coal bed methane recovery.
- Injecting CO_2 for enhanced oil recovery.
- For coal seams which are unmineable.

CO_2 can be stored using several methods and one method that is gaining popularity is the use of CO_2 to enhance the recovery of oil (EOR). The method utilizes the properties of CO_2 that enables it to dissolve within the oil, which has the effect of decreasing the viscosity of the oil and therefore increasing the flow. When CO_2 is injecting as a gas, it can also increase the pressure within the formation to push the desired natural gases though the reservoir, thus enhancing the gas recovery (EGR) [27]. These methods are popular due to their potential to enhance the reservoir's profitability. However, EOR and EGR do not provide the storage capacity needed to make a significant impact to reduce global emissions. Thus, the use of

depleted oil and gas reservoirs are another option. The benefit of this option is the fact that the reservoir characteristics are well known and documented. With this understanding, engineers would be able to calculate the conditions needed to fully utilise the reservoir. Although this is an incredible advantage that engineers can utilise, depleted oil and gas reservoirs are not as voluminous as saline aquifers which are more suitable for substantial long-term CO_2 storage. Saline aquifers, as previously mentioned, provide far greater capacities than depleted reservoirs. They often contain high salinity water that is unsuitable for human consumption. For this reason, they are unprofitable for oil and gas corporations, and they are therefore hard for engineers to fully characterise to enable the full and effective utilisation of them. However, due to their cavernous volume, they are ideal for massive CO_2 storage and shall be discussed further in the next section.

2.5. CCS capacities, challenges, and cost for the different storage methods

2.5.1. Carbon capture and storage capacities

For successful geological storage, site assessment, selection, and performance prediction are critical. Before deciding on a location, the geological setting must be assessed to determine whether the overlying cap rock will provide an effective seal, whether there is a sufficiently voluminous and permeable storage formation, and whether any abandoned or active wells will jeopardize the seal's integrity. Techniques established for oil and gas reservoir development, natural gas storage sites, and liquid waste disposal sites are applicable for defining geological CO_2 storage locations. Seismic imaging, pumping tests for testing storage formations and seals, and cement integrity logs are a few examples. Computer programs that simulate subsurface CO_2 circulation are utilized to aid in site characterisation and selection. Initially, these programs were designed for applications such as oil and gas reservoir engineering and groundwater resource assessments. Although they incorporate many of the physical, chemical, and geomechanical processes required to anticipate both short-term and long-term CO_2 storage performance, more experience is required to develop confidence in their ability to predict long-term CO_2 storage performance when modified for CO_2 storage. Furthermore, the availability of adequate site characterization data is crucial for model dependability. Table 2.2 summarizes the estimations of technological potential for several geological storage alternatives. The estimates and degrees of confidence are based on a review of the literature, which includes both regional bottom-up estimates and global top-down estimations. There is no probabilistic technique to evaluate capacity estimations in the literature, which would be necessary to properly measure degrees of uncertainty.

Table 2.2: Estimated storage capacities for major geologic storage reservoirs [2]

Sequestration option	Worldwide capacity (Gt of CO_2)
Deep coal seems	140
Depleted natural gas reservoirs	700
Depleted oil reservoirs	120
Saline aquifers	100 – 10,000

Sites and capacities where CO_2 storage has been completed, is now underway, or is planned, ranging from tiny experimental projects to large-scale commercial applications are shown below in Table 2.3.

Table 2.3: Sites where CO2 storage has been done, is currently in progress or is planned, varying from small pilots to large-scale commercial applications

Project name	Country	Injection Start (year)	Approximate average daily injection rate (t CO_2 per day)	Total (planned) storage (t CO_2)	Storage Reservoir type
Weyburn	Canada	2000	3000 – 5000	20,000,000	EOR
In Salah	Algeria	2004	3000 – 4000	17,000,000	Gas field
Sleipner	Norway	1996	3000	20,000,000	Saline formation
K12B	Netherlands	2004	100 (planned 1000 for after 2006)	8,000,000	Enhanced gas recovery
Frio	U.S.A	2004	177	1600	Saline formation
Fenn Big Valley	Canada	1998	50	200	ECBM
Qinshui Basin	China	2003	30	150	ECBM
Yubari	Japan	2004	10	200	ECBM
Recopol	Poland	2003	1	10	ECBM
Gorgon Planned)	Australia	~2009	10000	unknown	Saline formation
Snohvit Planned)	Norway	2006	2000	unknown	Saline formation

2.5.2. Carbon capture and storage challenges

CCS clearly faces a wide range of challenges on all fronts, including policy and regulatory issues, financial and economic issues, climate and environment, quality of life and health, social and income inequalities, and global agreement on a fair and sound mitigation strategy. On the technical side, the diversity of technologies, processes, and materials along the CCS and CCU chains creates additional obstacles, knowledge gaps, and problems that need basic study and understanding, as well as engineering solutions, to overcome. In random order, some of the more prominent issues are collected and outlined below [26]:

1. To broaden the technology options for CCS, advances in functional materials with superior properties ranging from more efficient and cost-effective separation of oxygen from air and CO_2 from flue gas streams to novel liquid and solid sorbents with higher CO_2 uptake capacity with less environmental impact are required.

2. A fundamental knowledge of CO_2-sorbent interactions, as well as control of surface binding mechanisms that determine preferential CO_2 absorption from flue gases, will accelerate progress toward the development of new materials with superior sorption capabilities.

3. Theoretical simulations will increase basic knowledge of atomic-scale binding mechanisms while also speeding up material screening and selection procedures.

4. Similarly, the use of modern materials processing tools and techniques to tune, change, and alter material characteristics through nano structuring and microstructure control would aid in the improvement of desirable attributes required for CO_2 removal from gaseous streams.

5. Developing non-aqueous solvents with increased CO_2 affinity will aid in increasing absorption capacity.

6. The development of scalable, stable, and ecologically benign CO_2 capture solvents, sorbents, and procedures will help reduce the threshold for social and political hurdles to large-scale worldwide CCS adoption.

7. Both pre-combustion and post-combustion capture incur significant energy penalty.

8. Direct air capture (DAC) requires the most energy and is undoubtedly the most expensive, but it still deserves consideration since it removes CO_2 from the atmosphere regardless of the origin, nature, or geography of the emission source. Advances in materials and solvents for post-combustion capture will also considerably help DAC.

9. Improving the efficiency of individual phases in the combustion-power-generation-CCS process chain will lower emissions as well as the financial, technical, and energy load of CO_2 collection.

10. Integrating renewable energy sources and fuel cells into the power generation-CCS process chain will also assist to reduce CCS's energy penalty.

11. Creating scalable CCS processes, materials, and technologies will benefit from economies of scale and assist in cost reduction.

12. A better knowledge of the geochemistry of CO_2-soil interactions will allow for more precise evaluation of long-term storage locations.

13. Developing earth abundant catalysts and understanding the basic principles of CO_2 reduction on catalytic surfaces to higher hydrocarbons and fuels would allow for the usage and recycling of this precious carbon source to produce useful goods.

14. The scale of CCS is huge, with quantities required in the tens of gigatonnes. This is on a far larger scale than any industrial capacity ever developed previously. To tackle the extraordinary complexity of the challenge, this undertaking will necessitate a distinct engineering strategy.

15. CCS is a costly proposition, and the present cost is typically far greater than most cap-and-trade pricing or carbon taxes. Even with legislation, this mismatch encourages enterprises to choose the lowest-cost option for polluting and emitting, while failing to offer the essential motivation for industries, governments, and the private sector to invest in creating technical alternatives. This gap needs to be closed.

16. While pricing carbon emissions is an effective deterrent, establishing a fair, equitable, and consistent price that is acceptable to global citizens and governments is a difficult and politically problematic challenge with many pitfalls.

17. Climate change is undoubtedly an existential threat, and inactivity is the costliest possible option.

2.5.3. Costs of carbon capture and storage system

The stringency of future needs for greenhouse gas emission reduction, as well as the predicted prices of CCS systems, will decide the future deployment of CCS technologies in comparison to alternative greenhouse gas mitigation solutions. There has been minimal experience with combining CO_2 collecting, transport, and storage in a fully integrated CCS system. The literature reveals a rather wide range of CCS component costs. The variation is primarily due to the variability of site-specific factors, particularly the design, operating, and financing

characteristics of the power plants or industrial facilities that use CCS; the type and cost of fuel used; the required distances, terrains, and quantities involved in CO_2 transport; and the type and characteristics of CO_2 storage. Furthermore, there is still some ambiguity about the performance and cost of existing and future CCS technology components and integrated systems. The literature, on the other hand, represents a commonly held notion that the cost of building and managing CO_2 capture systems would decrease over time as a result of learning-by-doing (through technology implementation) and ongoing research and development. Historical data also implies that the costs of first-of-a-kind capture plants may surpass current estimates before falling. The cost of capture (including compression) is the most expensive component of most CCS systems. Electricity and fuel costs vary greatly between countries, and these considerations significantly impact the economic sustainability of CCS alternatives.

The costs of CO_2 collecting, transport, and storage are summarized in Table 2.4. The costs of the separate components cannot simply be summed to calculate the costs of the whole CCS system in US$/$CO_2$ avoided. All numbers are representative of the cost for large-scale, new installations, with natural gas prices assumed to be 2.8-4.4 US$ GJ-1 and coal prices 1-1.5 US$ GJ-1. Monitoring expenses are also included.

Table 2.4: Cost ranges in 2002 for the components of a CCS system as applied to a given type of power plant or industrial sources

CCS system components	Cost range	Remarks
Capture from a coal- or gas-fired power plant	15-17 US$/tCO$_2$ net captured	Net costs of captured CO$_2$, compared to the same plant without capture.
Capture from hydrogen and ammonia production or gas processing	5-55 US$/tCO$_2$ net captured	Applies to high-purity sources requiring simple drying and compression.
Capture from other industrial sources	25-115 US$/tCO$_2$ net captured	Range reflects use of a number of different technologies and fuels.
Transportation	1-8 US$/tCO$_2$ Transported	Per 250 km pipeline or shipping for mass flow rates of 5 (high end) to 40 (low end) Mt CO$_2$ per year.
Geological storage [a]	0.5-8 US$/tCO$_2$ net injected	Excluding potential revenues from EOR or ECBM.
Geological storage: monitoring and verification	0.1-0.3 US$/tCO$_2$ Injected	This covers pre-injection, injection, and post-injection monitoring, and depends on the regulatory requirements.
Ocean storage	5-30 US$/tCO$_2$ net injected	Including offshore transportation of 100-500 km, excluding monitoring and verification.
Mineral carbonation	50-100 US$/tCO$_2$ net mineralized	Range for the best case studied. Includes additional energy use for carbonation

[a] Over the long term, there may be additional costs for remediation and liabilities

The component costs are summed in Table 2.5 to demonstrate the overall costs of CCS and energy generation for three power systems with pipeline transport and two geological storage alternatives.

The cost of CCS for plants with geological storage and no EOR credit varies from 0.02-0.05 US$/kWh for PC plants to 0.01-0.03 US$/kWh for NGCC plants. CCS costs range from 0.01-0.03 US$/kWh for IGCC facilities (using pre-combustion capture) compared to a comparable unit without CCS.

When utilizing EOR with CO_2 storage, the cost of CCS can be decreased by around 0.01-0.02 US$/kWh for all energy systems since the EOR earnings partially offset the CCS expenditures. The greatest cost savings are realized for coal-fired power stations, which collect the most CO_2. In a few circumstances, the low end of the CCS cost range might be negative, indicating that the projected credit for EOR over the life of the plant is larger than the system's lowest reported CO_2 capture cost. This may also be true in a few cases of low-cost capture from industrial operations.

In addition to fossil-fuel-based energy conversion processes, CO_2 might be absorbed in biomass-fueled power plants or fossil-fuel plants that use biomass. Biomass plants are on a modest scale (less than 100 MWe), and as a result, the costs of production with and without CCS are rather expensive when compared to fossil alternatives. Full CCS prices for biomass might be as high as 110 US dollars per tonne of CO_2 saved. Using CCS in biomass-fueled or cofired conversion plants might result in reduced or negative13 CO_2 emissions, potentially lowering the costs of this alternative, depending on the market value of CO_2 emission reductions. CO_2 might also be absorbed in biomass-fueled H2 plants. The cost is claimed to be 22-25 US$/tCO2 (80-92 US$/tC) saved in a facility producing 1 million Nm3 day-1 of H_2, corresponding to a 2.7 US$ GJ-1 increase in H_2 product pricing. Significantly bigger biomass facilities might possibly benefit from economies of scale, lowering CCS system costs to levels comparable to coal plants. However, because there has been little experience with large-scale biomass facilities to far, their feasibility has yet to be established, and costs and potential are difficult to assess.

Table 2.5: Range of total costs for CO2 capture, transport and geological storage based on current technology for new power plants using bituminous coal or natural gas

Power plant performance and cost parameters [a]	Pulverized coal power plant	Natural gas combined cycle power plant	Integrated coal gasification combined cycle power plant
Reference plant without CCS			
Cost of electricity (US$/kWh)	0.043-0.052	0.031-0.050	0.041-0.061
Power plant with capture			
Increased fuel requirement (%)	24-40	11-22	14-25
CO_2 captured (kg/kWh)	0.82-0.97	0.36-0.41	0.67-0.94
CO_2 avoided (kg/kWh)	0.62-0.70	0.30-0.32	0.59-0.73
% CO_2 avoided	81.88	83-88	81-91
Power plant with capture and geological storage [b]			
Cost of electricity (US$/kWh)	0.063-0.099	0.043-0.077	0.055-0.091
Cost of CCS (US$/kWh)	0.019-0.047	0.012-0.029	0.010-0.032
% increase in cost of electricity	43-91	37-85	21-78
Marginal cost (US$/t$CO_2$ avoided)	30-71	38-91	14-53
(US$/tC avoided)	110-260	140-330	51-200
Power plant with capture and enhanced oil recovery [c]			
Cost of electricity (US$/kWh)	0.049-0.081	0.037-0.070	0.040-0.075
Cost of CCS (US$/kWh)	0.005-0.029	0.006-0.022	(-0.005)-0.019
% increase in cost of electricity	12-57	19-63	(-10)-46
Marginal cost (US$/t$CO_2$ avoided)	9-44	19-68	(-7)-31
(US$/tC avoided)	31-160	71-250	(-25)-120

[a] All changes are relative to a similar (reference) plant without CCS. See Table TS.3 for details of assumptions underlying reported cost ranges.

[b] Capture costs based on ranges from Table TS.3; transport costs range from 0-5 US$/t$CO_2$; geological storage cost ranges from 0.6-8.3 US$/t$CO_2$.

[c] Same capture and transport costs as above: Net storage costs for EOR range from -10 to -16 US$/t$CO_2$ (based on pre-2003 oil prices of 15-20 US$ per barrel).

The cost of CCS for non-power uses has not been researched as thoroughly. It is because these sources differ greatly in terms of CO_2 concentration and gas stream pressure, the cost studies available reveal a wide range. The lowest prices were discovered for technologies that segregate CO_2 as part of the manufacturing process, such as hydrogen generation. Based on the same cost estimates as in table 2.5, the total CCS cost, including transport and storage, boosts the cost of hydrogen generation by 0.4 to 4.4 US$ GJ-1 for geological storage and -2.0 to 2.8 US$ GJ-1 for EOR.

2.6. Saline Aquifers for CO_2 Storage

Saline aquifers are permeable geological formations (sedimentary rocks) that contain very salty water and are considered as a viable option for disposing of CO_2 emissions because of their large potential capacity for CO_2 storage [27]. Saline aquifers possess the ability to contain CO_2 for hundreds of years and are quite different from oil and gas reservoirs in that there is often not a well-defined structural trap. Instead, containment of CO_2 will depend on the existence of a confining layer, or a cap rock, that extends laterally along the top of the formation.

Aquifers primarily used for the storage of anthropogenic carbon dioxide have a good porosity and permeability to allow carbon dioxide to be injected into pores occupied by the fluids [29]. Slightly saline water has a salinity of 1,000 ppm to 3,000 ppm of salt, while moderately saline water has a salinity of 3,000 ppm to 10,000 ppm of salt. Highly saline water, such as sea water, has a salinity of 10,000 ppm to 35,000 ppm of salt and is therefore unfit for drinking. These formations are present in every continent and in most coastal areas and because of this abundancy, the potential capacity of saline aquifers is higher than depleted oil and gas reservoirs to store carbon dioxide. According to Shogenov et al. [30], a reservoir for CO_2 storage can be divided into four categories based on capability of CO_2 geological storage:

- *'Very appropriate'* which has a high porosity in the range of 9–20% and the permeability of greater than 300 mD.
- *'Appropriate'* which has a porosity of (>18% and 9-18%) and the permeability range of 100 to 300 mD.
- *'Cautionary'* which contains rocks, and it has a porosity of 7–23% and the permeability of 10–100 mD.
- *'Not Appropriate'* which composed of rocks with a permeability of lower than 10 mD.

More so, these reservoirs have cap rock that helps to prevent carbon dioxide leakage. As a result of high aquifer temperature and pressure, carbon dioxide is injected into the reservoir in a supercritical state which increases storage capacity. Within a reservoir, CO_2 typically remains in a supercritical state with a critical temperature of 31.06 °C and a critical pressure of 7.39 MPa.

2.7. Existence and observation of salt precipitation during carbon capture and storage

Salt precipitation consist predominantly of halite, and it is one of the outstanding issues affecting injection of CO_2 into saline aquifer. Several fields and laboratory experiences have been reported the presence of salt participation during production/injection from gas reservoirs and during storage of natural gas in some oil fields [31]. Based on industry field experience, Kleinitz et al. [31] reported on plugging of pores by halite scaling to an extent that the salt could not be remediated by using fresh water. More so, Baumann et al. [32] identified and reported a one metre interval of salt accumulation in the Ketzin reservoir (350 °C, 7.5 MPa and 220 g/l NaCl) by employing radiometric pulsed neutron-gamma (PNG) logging technique. Thus, the source of extra pressure builds up in the Ketzin CO_2 storage projects was partly due to the salt precipitation. Grude et al. [33] through an analysing the fall-off pressure data, detected a low permeability zone in the Tubåen formation at the Snøhvit Field (95 °C, 28 MPa and 14 wt.% NaCl) surrounding the well at the early stage of CO_2 injection. Thus, this was attributed to salt precipitation in the reservoir.

Further laboratory experiments or numerical simulation also reported evidence for salt precipitation. In a laboratory study on formation dry-out and precipitation with focus and emphasis on CO_2 sequestration by Muller et al. [14] a core flooding test was conducted on a dry Berea core sample with permeability of 100 mD and porosity of about 20% saturated with a 25% NaCl solution. The study reported 60% reduction in the absolute permeability after the experiment with the help of Scanning Electron Microscopy (SEM) micrographs. This reduction in permeability was attributed to salt precipitation in the system. Ott et al. [23] studied using Micro Computed Tomography (µCT), to map the profile of precipitated salt during injection of dry supercritical CO_2 along a brine saturated Berea sandstone core sample. They reported that the local pore space was occupied by salt, thereby causing as high as 20% to 75% reduction in absolute permeability. This result is similar to previous study conducted by Ott et al. [23] in which a large accumulation of salt was observed near the injection inlet.

Further study to show the evidence of salt precipitation during supercritical core flooding experiment was conducted by Bacci et al. [16]. They observed and reported absolute

permeability reduction of about 86%. Oh et al. [24] observed salt precipitation in the inlet Berea fractured core by employing X-ray scanning but the measurement on permeability reduction was not performed.

Additionally, the previous experiment conducted by Ott et al. [34] on core flooding using Berea core sample was repeated by using higher injection flow rate. They reported a homogenous distribution of salt which was due to a significant reduction of solid saturation measured as 4.5%. They also reported that, due to the presence of micro-porous subsystem, the effective permeability impairment was observed owing to reduction in the CO_2 pathways cross-section. Investigation on the mechanisms of brine evaporation and salt precipitation was carried out by Peysson et al. [10] on the low permeability Moliere (with 0.01 mD) and a high permeability Vosges (with 100 mD) sandstone formations. They used an X-ray CT imaging to quantify the spatial distribution of phases. They observed that a homogeneous distribution was found for the low permeability, while the high permeability showed a local salt accumulation.

However, Kim et al. [25] and Miri et al. [7] on a micro scale experimental plant have reported salt precipitation as crystal in two different forms through laboratory on a chip experiment. These include large crystals which grow in the liquid phase away from the CO_2 interface and near-interface aggregated polycrystalline structures which is supported by a flow of high saline brine along thin films driven by capillary forces along the pore channels. Jeddizahed et al. [35] investigated the influence of the injection rate and brine salinity on injectivity reduction due to evaporation and salt precipitation also observed salt precipitation. They pointed out that a high rate in the early stage of injection induces rapid salt precipitation and the level of salt precipitation increases with salinity.

Benashor et al. [28] on the study of the effect of halite on sandstone permeability reported precipitated salt around the core sample and that there was a reduction in the core sample permeability and injectivity. A recent study by Yusof et al. [15] used core flooding tests on Berea sandstones saturated with varied brine salinities to explore the combined influence of salt precipitation and fines migration on CO_2 injectivity impairment. The experimental results revealed that brine salinity has a greater impact on permeability reduction than particles and CO_2 injection flow rates [15].

Thus, Experimental results for salt precipitation triggered by CO2 injection are summarized below in table 2.6.

Table 2.6: Salt precipitation in typical CO2 flooding experiments

Researcher	Water composition	Porosity and permeability	Temperature and pressure	Analysis technics	Variation in porosity and permeability after salt precipitation
Muller et al. [14]	25 wt% NaCl	$\phi = 0.2$ $k = 100$ mD	35 °C 6.3 MPa	SEM, ESEM	60 % reduction in permeability
Wang et al. [2009]	25 wt% NaCl	$\phi = 0.18$ $k = 79$ mD	50 °C 8.2 MPa	SEM, ESEM	50 % reduction in CO_2 permeability
Wang et al. [2010]	25 wt% NaCl	$\phi = 0.17$ $k = 143$ mD	50 °C 8.2 MPa	Permeability measurement MRI imaging	50 % reduction in CO_2 relative permeability – MRI confirm salt precipitation near the core inlet
Bacci et al. [16]	26.4 wt% NaCl	$\phi = 0.23$ $k = 7.78$ mD	45 °C 8 MPa	ICP-AES	3 % reduction in porosity, 75 % reduction in permeability
Oh et al. [24]	15 wt% NaCl	$\phi = 0.2$ $k = 170$ mD	45 °C 10 MPa	X-ray, SEM	Local salt precipitation near injector
Ott et al. [34]	34 wt% NaCl	$\phi = 0.2$ $k = 170$ mD	110 °C 11 MPa	μCT	Reduction in CO_2 permeability
Peysson et al. [10]	3.5 wt% (55 % KCl, 45 % KI)	$\phi = 0.218$ $k = 74$ mD	80 °C change in pressure	X-ray	Local salt precipitation near injector, and 70 % reduction in CO_2 permeability
Peysson et al. [10]	Brin in Paris Basin [a]	$\phi = 0.214$ $k \approx 0.01$ mD	90 °C 120 °C change in pressure	X-ray	Local salt precipitation near injector, and 50 % reduction in permeability
Tang et al. [36]	20 wt% NaCl	$\phi = 0.3$ $k = 200$ mD	100 °C 1 MPa	SEM	14.6 % reduction in porosity and 83.3 % reduction in permeability
Ott et al. [9]	20 wt% NaCl	$\phi = 0.3$ $k = 200$ mD	50 °C 10 MPa	X-ray, SEM	Uniform salt precipitation, and CO_2 permeability increases
Shaibu [37]	7.5 – 15 wt% NaCl	$\phi = 0.17 – 0.19$ $k = 90 – 105$	50 °C 10 MPa	-	10 – 35% reduction in permeability
Edem et al. [38-40]	5 – 25% NaCl	$\phi = 0.19 – 0.2$ $k = 200 – 315$	45 °C 6.9 MPa	SEM	0.75 – 6 % reduction in porosity, 10 – 70 % reduction in permeability
Ott et al. [2021]	6 – 28 wt% NaCl	$\phi = 0.13 – 0.19$ $k = 30 – 300$	110 °C 11 MPa	SEM	Permeability decreases by 1 – 3 orders of magnitude
Yusof et al. [15]	6 – 10 wt% NaCl	$\phi = 0.2$ $k = 185$ mD	60 °C 12.4 MPa	ANOVA	Permeability reduction up to threefold
Cui et al. [41]	7 – 16 wt% NaCl	$\phi = 0.2$ $k = 170$ mD	110 °C 11 MPa	μCT	Reduction in CO_2 permeability

[a] The salinity of brine in Paris Basin is 160 g/L, and its composition includes 4.12 g/L KCl, 5.23 g/L $MgCl_2.6H_2O$, 22.00 g/L $CaCl_2.2H_2O$, and 139.33 g/L NaCl

2.8. Characteristics and mechanism of salt precipitation

Physical and Chemical processes control dry out in the near-wellbore and salt precipitation in either depleted oil/gas reservoir or deep saline aquifers. However, the effect of chemical processes to the formation dry-out is minimal as compared to physical processes. Physical process gives rise to the establishment of majority of existing numerical codes, which are capable to simulate the process of drying-out and salting-out. The main purposes of these tools are to predict the progression of the dry-out zone and the average porosity reduction (macroscopic distribution of the precipitant) and to estimate the extent of formation damage.

Many works and studies have been done by several researchers on the physical mechanisms associated with salt precipitation on macro scale [11, 42-45]. Pruess et al. [42] stated that the counterflow of CO_2 and brine can greatly increase the aqueous phase salinity and can promote substantial salt precipitation, even in formations with low dissolved solids. The report also demonstrated that salt precipitation occurs only in the dry-out region around the injection well, but not in the two-phase zone beyond the dry-out region. Kim et al. [11] on their study on Salt precipitation for high permeability rocks at low injection rates observed that Localized salt acts like a barrier hampering pressure dissipation.

Liu et al. [44] derived a relationship for permeability change caused by salt precipitation near a CO_2 injection well. This connection takes into account the fact that salt precipitation only occurs in the pore space filled by brine during the precipitation process, and it is based on well-established relative-permeability relationships for two-phase flow in porous media. Andre et al. [43] observed a good agreement between experiments and simulations. It was noticed that the higher the brine salinity, the greater the salt deposit and the location of salt deposits depends strongly on the injection rate.

Meng et al. [45] show that the region of high pressure is substantially larger than the extent of the CO2 plume in numerical simulations. Salt precipitation owing to gas phase evaporation occurs only in a narrow zone of the single gas phase. Thus, evaporation of the gas phase causes precipitation near the well, and capillary pressure causes brine backflow, resulting in an impervious zone near the well's bottom part. Peysson et.al [10] reported that the salt precipitation process and the amount of salt deposited are related to various parameters such as the salinity of the initial brine; there is a large salt deposit when the brine concentration is high, and a sufficiently high gas injection rate can overcome the capillary forces to limit the precipitation of salts close to the injection well.

Injection of CO_2 into saline aquifers may cause formation dry-out and precipitation of salt near the injection well, which may in turn reduce formation permeability, porosity and injectivity

[42]. The extent of salt precipitation and the continuation of dry-out constitute to be the outcome of several physical mechanisms which perform on distinct length scale and time. These physical mechanisms influencing salt precipitation and dry-out process include the following [22]:

i. A two-phase displacement of brine away from the injection well by viscous pressure gradients imposed through injected CO_2

ii. Dissolution (evaporation) of brine into flowing CO_2 stream

iii. Capillary-driven backflow of aqueous phase toward the injection point due to capillary pressure gradients

iv. Molecular diffusion of dissolved salt in the aqueous phase

v. Gravity override of injected CO_2, and

vi. Salt self-enhancing.

These mechanisms are illustrated schematically in Figure 2.4.
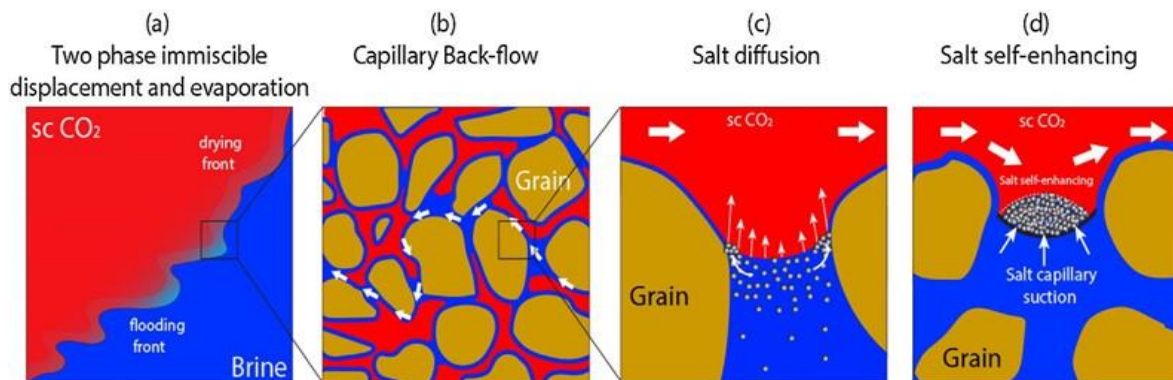
Figure 2.4: Schematic illustration of different physical mechanism contributing to the process of salt precipitation [22]

When a large quantity of dry supercritical CO_2 is injected into a saline aquifer, a two-phase flow zone is forming, which are an aqueous phase and a CO_2-rich phase respectively (as shown in Figure 2.4a). This two-phase zone is leading with a shock front (flooding front) which moves with a velocity determined primarily by the injection peculiarities. This phenomenon is referred to as a two-phase displacement process in which the main drainage undischarged by the viscous displacement pushes brine out of the injection well [9, 10, 42]. Furthermore, as the flooding front advances into the aquifer, a zone is left behind whereby residual brine is trapped in various layouts such as thin wetting films enclosing the grain surfaces and liquid bridges or pools of

brine in the pores [7]. Instantly, this drained region is however exposed to continuous flow of dry supercritical CO_2 with low water vapour pressure initiating an evaporation regime. Under a continuous flow, a sufficiently amount of water will evaporate into the CO_2 stream resulting to dry-out.

Moreover, as the evaporation of water continues, the relative permeability of CO_2 increases and thereby allowing further evaporation [10]. Finally, as shown in Figure 2.4a, a dry-out front is form and moves with a velocity much smaller than the flooding front velocity [25]. Thus, the two-phase displacement and evaporation (dissolution) give rise to the removal of water from the near well area. Hence, there is no convective flow during dry-out, but there is only little evaporation during two-phase displacement [9, 10, 23, 46].

Mass interchange occurs in the dry-out zone thereby producing saturation gradient covering the drying front which is far greater than the saturation gradient generated in that of a pure viscous displacement [10]. The arising out capillary pressure gradient (shown in Figure 2.4b) in due course prevail over the injection pressure gradient and control the direction of water towards the evaporation front thereby giving rise to more evaporation [9, 10, 42]. Furthermore, as shown in Figure 2.4c, because of evaporation of water into CO_2 stream, the concentration of salt presence in the confined brine increases and thereby leading to salt diffusion outside of the drying front [42]. This solute diffusion and capillary backflow basically determined the relative distance between the flooding front and the dry-out front. Due to continuous evaporation, salt will precipitate out of solution when the salt concentration reaches its solubility limit [22]. The precipitate (salt) has a remarkable affinity towards brine and can also successfully absorb water from long distances to the evaporation front resulting to additional precipitation [7, 22]. The phenomenon of this salt diffusion mechanism thereabouts is the same as that of capillary pressure gradient but quite different from their mode of origination. Thus, capillary flow due to salt self-enhancing process is sturdy and gives sufficiently firmness to water films by intensifying precipitation of salt (see Figure 2.4d).

Injection of dry supercritical CO_2 into saline aquifers give rise to several flow regions based on the interaction between the foregoing mechanisms. Without losing generality, as illustrates in Figure 2.5, these Regions can be divided into three zones [47, 48].
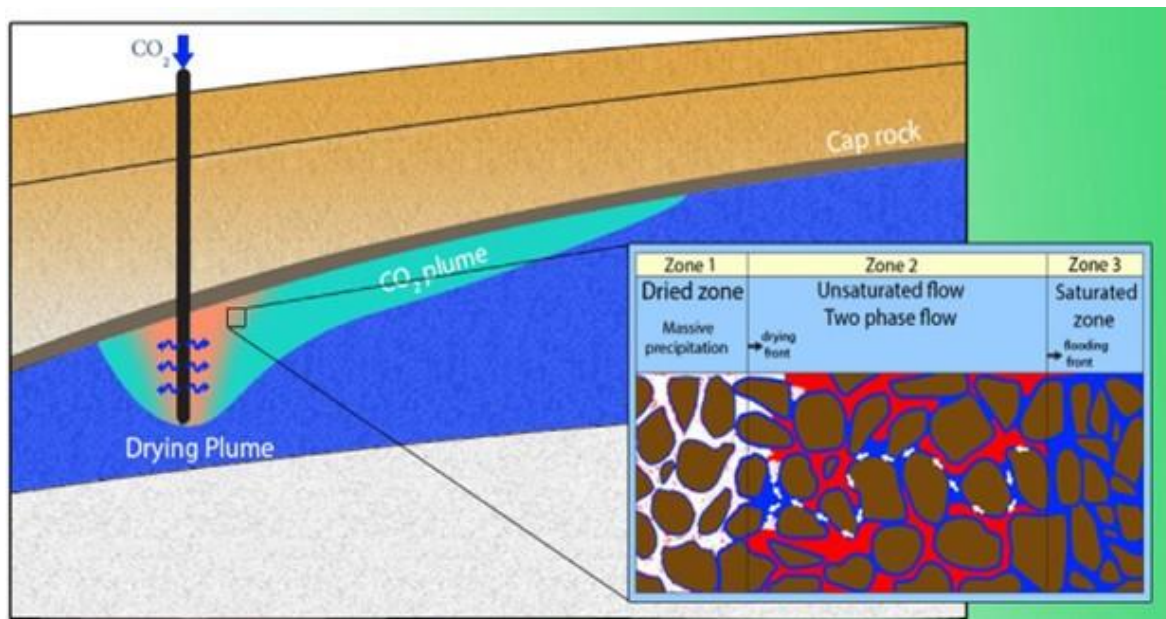
Figure 2.5: Schematic of CO$_2$ injection in a saline aquifer and possible configuration of phases in the near-well region [22]

Region-1 is the dried zone which is made up of massive precipitation and separated from the saturated brine phase which is Region-3. More so, Region-2 (unsaturated flow/two phase flow zone) is very outstanding and is characterized with an extended mixing zone where both aqueous phase and CO$_2$ are in contact. When the system is under evaporation only (without CO$_2$ injection) and no salt precipitation, all these regions will develop. Region-2 is made up of disconnected liquid clusters which partially screen this region from the evaporating medium. This cluster develop in the front of the continuum liquid region to decelerate mass transfer into the gas phase [48]. The precipitated salt in the Region-1 formed from the evaporation-precipitation process create effectual firmness to liquid clusters connecting them to the evaporation front. Thus, the liquid clusters behave like a conduit by transporting the liquid from the saturated zone to the dried (dry-out) zone thereby increasing the amount of salt precipitation in the dried zone (Region-1) [7].

2.9. Parameters affecting salt precipitation

2.9.1. Salinity

One of the most influential parameters controlling the extent of salt precipitation in aquifer is salinity. Ji et al. [49] and Miri et al. [50] observed that increasing in brine concentration leads to a slight decrease of water solubility in the CO$_2$ phase. This is widely accepted because high rate of salinity will be tantamount to higher amounts of salt precipitation [22, 51]. Therefore,

increasing salinity leads to more-free CO_2 in the gaseous phase, reduces the dissolution of CO_2 in the brine significantly and causing the velocity of the leading shock to increase. Doubling the salinity causes roughly 8% increase in the velocity of CO_2 advancement into the aquifer [51]. The behavioural pattern in which increase in salinity resulted to increases in the solid salt saturation may not be linear. However, solid salt saturation also varies with the aqueous phase density and the gaseous phase saturation at the trailing shock. Hence, salt precipitation is primarily controlled by the salinity and that changes in aqueous phase density and trailing shock saturation are negligible [51]. Higher salinity resulted to higher amount of salt precipitation and eventually leads to higher reduction of porosity as well as impairment of permeability. It is worth to known in this context that the range for occurrence or risky salinities have not been known but it widely depends on the injection rate [11, 36, 43, 51]. Figure 2.5 shows the effect of salinity on the mutual solubility of CO_2 and water at 75 °C (or 348.15 K) and different pressures [49, 50].
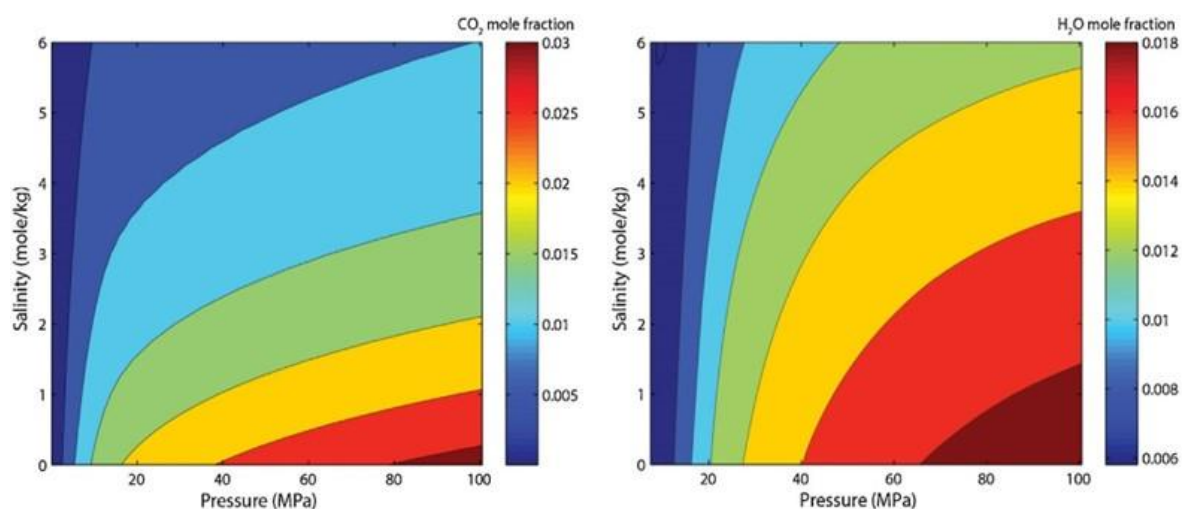
Figure 2.6: Effect of salinity on the mutual solubility of CO_2 and water at 75 °C and different pressure [49]

As shown in Figure 2.6, increasing brine salinity causes a slight decrease in water solubility in the CO_2 phase (a decrease in evaporation rate). However, there is a significant decrease in CO_2 dissolution in the brine. It is widely accepted in the literature that higher salinity causes more salt precipitation and, as a result, higher porosity reduction. Despite popular belief, severe salt precipitation can occur in aquifers with intermediate salinity. To the best of our knowledge, the risky salinity boundaries have not yet been defined. There are, however, indications that it is

dependent on the injection rate. Reservoirs with low to intermediate permeabilities are most vulnerable at low injection rates, regardless of formation water salinity [49].

Moreover, Pruess et al. [42] showed through a series of experiments that by reducing salinity by a factor of 2, the solid saturation reduces by over a factor of 2.23. Thus, irrespective of the initial brine salinity, salt precipitation could impair CO_2 injectivity [22].

It has been reported that by Eiken et al. [52] that there is no sign of well clogging or injectivity impairment in Utsira formation in Sleipner field located in North Sea which has a low level of salinity and permeability (3.5 wt.% salinity). More so, salt precipitation was reported in the Ketzin storage site with high salinity of 25% and intermediate permeability of about 100 mD [33]. This was as a result of pressure build-up during injection of CO_2 with a lower injection rate of approximately 100 tonne/day. The injection of low concentration of salinity water can reduce the rate of salt precipitation, but the type of reservoir involved, and the time of injection is different [53]. Thus, the level of salt precipitation increases with salinity within a permeability reduction range of 21 to 60% and decreases with the injection rate within a permeability reduction range of 43 to 62%. Hence, salinity and injection rate both affect the relative permeability of CO_2 [35].

Any change in salinity of the aquifer significantly affect the equilibrium between the water vapour and liquid water. According to Raoult's law [54], as the salinity of the brine increases, the equilibrium vapour pressure, which is the pressure exerted by vapour escaping from the liquid or solid, decreases and it eventually resulted to a reduction in evaporation. Thus, vapour production decreases with salinity and it can be deduced that, by increasing salinity, the reduction in evaporation overcomes the increase in the remaining water saturation effect on evaporation [35]. Moreover, it is pertinent to state that an increase in brine salinity increases the Total Dissolved Solid (TDS) which in turn increase salt precipitation. Increase in TDS and the interaction of the reduction in evaporation (as the salinity of the brine increases) determines which one has the more significant effect on salt precipitation [35].

Yusof et al. [15] recently completed a study on the influence of brine-rock factors on rock physical changes during CO_2 sequestration in saline aquifer. According to the findings, brine salinity is the most important component, followed by reactive pore surface area and length of exposure. Field emission scanning electron microscope images taken before and after experiments revealed changes in potassium chloride (KCl), sodium chloride (NaCl), and calcium chloride ($CaCl_2$) brines, resulting in dramatic changes in pore spaces due to mineral dissolution, deposited salts, and fines migration.

2.9.2. Injection flow rate

The well injectivity is one of the technical and economic issue concerning CO_2 geological project since a huge amount of CO_2 must be stored for a long period of time. However, a high storing capacity is not the only criteria that is to be considered as a suitable storage site and other criterion includes high injectivity and safe containment [27, 28]. The well injectivity measures the ability of a single injection well to accept CO_2 into a formation without reactivating existing faults or creating new fractures. To avoid the reactivating of the reservoir, the injection pressure must not exceed 90% of fracturing pressure by considering all other regulatory factors such as maximum pressure [55].

Injection flow rate of CO_2 into saline aquifer is one of the most parameters affecting precipitation process. In saline aquifer, the higher injection rate increases the CO_2 displacement efficiency and enlarge the CO_2 storage capacity, but when the injection rate reaches a certain value, the CO_2 storage capacity remains constant [56]. Other factors that affect the injectivity during CO_2 storage include planned rate of CO_2 captured, number of wells and well design such as vertical, horizontal, and multilateral well. Some researchers pointed out that, high injection rate will induce high pressure gradient thereby suppressing the capillary backflow towards the evaporation surface [11, 22, 37, 42, 43, 54]. When the capillary flow is reduced, there is a tendency and a possibility of reduction of the extent of salt accumulation.

Zeidouni et al. [21] utilised an analytical model for the vaporisation-precipitation process and showed that the combined effect of vaporisation rate and aqueous phase mobility are used to determine the rate of salt precipitation. Increase in injection flow rate leads to an increase in injection pressure which will slow down the plume mobility owing to increased viscosity of the supercritical CO_2 phase. Further evaporation at higher injection pressures will eventually leads to increase in the amount of salt precipitation. More so, results obtained from Zeidouni et al. [21] showed that, decrease in capillary back flow is less significant as compared to an increase in evaporation rate which contradict previous findings. Many attempts have been made to define a relationship between the injection rate and the critical velocity above which the massive salt accumulation corresponding to the capillary drying regime can be avoided [22]. However, the majority of these studies lack a theoretical basis, and their findings depend on rock properties of the tests and the thermodynamic conditions [9, 22, 37, 43, 54].

Absolute permeability of core samples may be reduced as a result of salt precipitation during injection of CO_2 and at the same time evaporation of trapped water may provide more space for CO_2 and thereby increasing the relative permeability. To assess the injectivity loss properly, it is pertinent to take cognizance of measuring the effect of these mechanisms [9, 57]. The two

set of experimental data obtained from measuring the effective permeability and alteration relationship between porosity and permeability are not consistent [22]. Wang et al. [58] obtained their experimental data on salt precipitation and injectivity impairment during supercritical CO_2 injection in brine saturated Berea sandstone cores. They used Magnetic Resonance Images (MRI) to envisage halite precipitation at the rear of the dry gas front and reported a drastic reduction in CO_2 relative permeability by almost a half.

On the other hand, Ott et al. [23] conducted a core flooding experiment by injecting dry supercritical CO_2 on brine saturated Berea sandstone with two different injection flowrates (2.2 ml/min and 4.4 ml/min) and absolute permeability of 500 mD [9]. As explained by a capillary backflow pressure, local salt accumulation was observed at low injection rate. Conversely, precipitation pattern was homogenous for the case of high injection rate and both flow rates experienced improvement in effective permeability. The effective CO_2 permeability during the dry-out process increased by a factor of 5 despite reduction in the absolute permeability and indicating little or no change in injectivity. Ott et al. [9] in their verification by using micro-CT scanning reported that, precipitation of salt only occurs in the volume earlier occupied by the trapped brine and thereby leaving the cross-sectional area to strain through the part ways open to CO_2 flow.

In addition, Jeddizahed et al. [35] conducted their study to investigate the effects of the injection rate and brine salinity on salt precipitation due to evaporation. They reported that salt precipitation and permeability loss increase with salinity and reduction in the injection rate. Also, increase in injection rate leads to CO_2 relative permeability increases while increasing salinity will lead to a decrease in CO_2 relative permeability.

More so, Shaibu et al. [37] uses a Berea sandstone rock sample reconstructed with a bundle-of-tubes. This bundle-of-tubes model was developed to investigate basic mechanisms of salt precipitation and to quantify injectivity loss induced by precipitated salt during CO_2 injection into saline formations. It was reported that, salt precipitation occurs in the dry-out zone where most of the irreducible water in the trapped brine have evaporated leaving a high saturation of salt in that region. Also, adverse effect on injectivity occurs when increasing brine salinity and high flowrates induce high salt precipitation which causes a significant pressure build-up.

2.9.3. Temperature

Temperature is a key parameter regarding chemical equilibrium of minerals, reaction kinetics and solubility of CO_2 in the brine [16]. A detailed description of the effect of temperature on salt precipitation in deep saline aquifer suggested a pressure dependency [51]. At higher pressure, the rate of salt precipitation is observed to be increasing with increase in temperature. Conversely, at lower pressures there is an initial decline in the salt precipitation as the temperature increases. Ji et al. [49] and Miri et al. [50] during their investigation of salt precipitation suggested that the vertical migration of CO_2 plumes primarily depends on the density difference between the injected CO_2, the host brine, and the vertical permeability (see Figure 2.7).
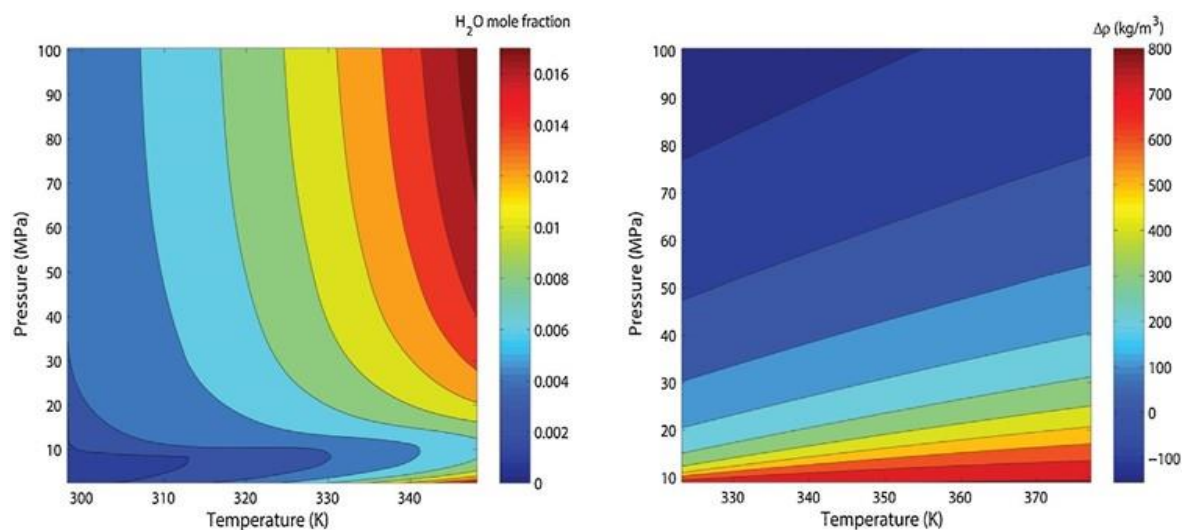
Figure 2.7: Solubility of water in CO2 Phase (Left) and density difference between CO2 and brine (right) for different pressures and temperature [49, 50]

Increasing in temperature causes a noticeable increase of water solubility in CO_2 phase and water quickly reaches its saturation limit resulting to salt precipitation. Moreover, higher, or elevated CO_2 temperature decreases the CO_2 density by enhancing the gravity override which at the same time proceeds to localised salt precipitation and the dry out-front [11]. Thus, the effect of temperature on salt precipitation is lesser than other parameters.

Changes in temperature due to non-isothermal processes may have a notable effect on the precipitation and dissolution mechanisms. Appreciable temperature gradient can occur near the wellbore when CO_2 is injected at a temperature remarkably different from that of the reservoir or because of non-isothermal processes [59]. Past study revealed that the temperature around

the wellbore can drop by more than 20 °C through Joule-Thomson cooling effect [60]. However, little attention has been given to the influence of temperature on this mechanism.

2.9.4. Capillary pressure

Capillary pressure serves as both an opposing or driving force for fluid transport and is a significant property for research and industrial purposes. It serves to increase the rate of evaporation by supplying fresh brine to the drying front [22]. Numerical simulations performed to evaluate the effect of capillary pressure have shown different results. However, Hurter et al. [61] make known that, capillarity is a significant process to the salt formation and that no precipitation will occur if one disregard it in simulation. In contrast, Pruess and Muller [42] pointed out that, by activating the capillary pressure option during simulation simply alters the precipitation patterns and less or limited effect on the rate of precipitation. A study by Miri et al. [7] showed that salt aggregates forming in the gas phase also have significant capillarity owing to their micro-porous structure and therefore strongly imbibe brine over long distances to the evaporation front.

Pressure drop becomes highest in the case of high salinity and lowest when salinity is zero. The degree of accumulation of the precipitated salt depends on salinity. The precipitated salt acts as a barrier that hampers the propagation of CO_2 and adds an extra pressure drop component which results in the high overall pressure drop [37].

2.9.5. Phase mobility

According to Miri et al. [22], the shape and endpoint of the aqueous phase relative permeability curves are critical parameters controlling the balance between viscous and capillary forces. Increasing in velocity of the flooding front as a result of increase in brine mobility leads to less gaseous phase encroachment. Thus, the resulting increase in the local gas saturation reduces the brine saturation at dry-out front and therefore decreasing the rate of salt precipitation. The brine relative permeability can be increased by decreasing the residual water saturation. Giorgis et al. [54] conducted a study on salt formation under different CO_2 injection rates to distinguish between the aqueous phase relative permeability and the local gas saturation. They reported that solid saturation decreases above a critical injection rate due to limiting capillary back flow irrespective of the initial brine saturation.

2.10. Salt precipitation simulation

The distribution of salt precipitation during CO_2 injection into saline aquifers has been predicted using numerical simulation models. In 2007, Giorgis et al. [54] used TMGAS to investigate salt precipitation during CO_2 injection into depleted gas reservoirs, and they discovered a local accumulation of salt precipitation near the injection well when the water saturation exceeds the irreducible water saturation. Hurter et al. [61] used reservoir numerical simulation software to study the European CO_2SINK geological storage project, and they predicted that a lot of salt precipitation would occur at the bottom of injection Wells when the salinity of the saline aquifer is high.

Following that, Kim [11], Wang and Liu [62], Guyant [46], and Norouzi [63] investigated the process of CO_2 injection into saline aquifers using TOUGH2 or GEM and discovered a local accumulation of precipitated salt near the wellbore. After accounting for capillary in his analytic equations, Norouzi [64] discovered an increase in salt precipitation near the wellbore. By developing an analytical model, Zeidouni [21] assumed that the precipitated salt would be distributed uniformly in the reservoir. In general, due to formation water backflow, a local accumulation of precipitated salt near the injection wellbore can occur, and the salt precipitation amount reaches a maximum at a specific injection rate, but some simulations still show that salt precipitates uniformly.

The obvious differences in the distribution of salt precipitation can be attributed to several factors. One is that simulation models did not account for the kinetics of salt precipitation, and another is that simulation models did not account for precipitated salt migration and retention. Dashtian et al. [65] attempted to analyse the distribution of precipitated salt in detail using a model based on the pore-network equation, but the simulation model does not account for forced convection at the gas-liquid interface, so precipitated salt migration and retention are not considered as well as a clear explanation for under CO_2-water seepage. Furthermore, current numerical simulations typically use a thermodynamic equilibrium equation to simulate formation water evaporation, which does not account for the evaporation process of formation water [66-68]. However, Bacci [16], Li [69], and Jeddizahed [35] discovered that the rate of salt precipitation during CO_2 flooding experiments was affected by the evaporation rate of formation water.

Ott et al. [9] and Roels et al. [57] observed that the distribution of precipitated salt in the experiment differed from that in the numerical simulation when comparing experimental and simulation results when the evaporation process of formation water was not considered. To accurately predict the salt precipitation distribution and its influence on the reservoir's physical

properties, the simulation model should include the water evaporation and salt precipitation migration processes. Otherwise, it is easy to overestimate reservoir impairment caused by salt precipitation, which can have an impact on saline aquifer selection and the CO_2 injection scheme. Table 2.7 summarised the salt precipitation findings obtained from simulation results.

Table 2.7: Summary of the research outcomes using rigorous simulation studies for the salt precipitation induced by CO2 injection

Reference	Injection condition	Reservoir properties	Sensitivity parameter	Remarks
Giorgis et al. [54]	Salinity = 9wt% T = 45 °C P = 60 bar Q = 1 Kg/s	K = 400 md Φ = 0.32% H = 10 m	Injection rate Initial brine Saturation	− Extended V & P model − Precipitation extent depends on K-Φ relationship − Amount of precipitation increases with increase in initial brine saturation − For Q > Qcr, increasing rate, decreased amount of precipitation − For very low injection rate, amount of precipitation in independent of brine saturation
Hurter et al. [61]	Salinity = 25wt% T =35 °C P =75 bar Q = 1 Kg/s	K = 200 md Φ = 20% H = 30 m	Salinity Water content	− Dry-out zone progresses 10 m in 2 years − Experiments are needed for K-Φ relations − Higher salt concentration at edge of plume − Dry CO_2 injection improved injectivity − Low salinity brine suggests little precipitation
Hurter et al. [61]	Salinity = 25wt% T = 35 °C P =75 bar Q = 1 Kg/s	K = 200 md Φ = 20% H = 30 m	Injection rate Capillary pressure Relative permeability	− For zero capillary pressure precipitation did not occur − Increase in injection rate decrease the solid saturation − Relative permeability control the spatial distribution of precipitant
Zeidouni et al. [21, 51]	Salinity = 15, 25wt% T =35, 45 °C P =75, 120 bar Q = 1, 100 Kg/s	K = 200 md Φ = 0.32% H = 100 and 30 m	Salinity Pressure Temperature Relative permeability	− Kozeny-Carman model is used − Capillary and gravity were ignored − Homogenous precipitation is obtained − Amount of precipitation is minor, 3% − Salt precipitation increases with pressure and salinity − Temperature has minimal effect − Increase in brine relative permeability reduces amount of precipitation

Pruess and Müller [42]	T = 50 ºC P = 120 bar Q = 5 Kg/s	K = 33 md Φ = 0.33% H = 100 m	Injection rate Capillarity Mechanism	– Precipitation occurs few meter from the well – Constant and homogenous salt distribution independent of injection rate – Gravity in combination with capillary-driven flow leads to heterogeneous precipitation – 20% salt saturation observed for heterogeneous precipitation
Kim et al. [11]	T = 40 ºC P = 96 - 100.6 bar Q = 1-30 Kg/s	K = 10-150 md Φ = 0.33% H = 100 m	Injection rate Temperature Salinity	– Salt precipitation for high permeability rocks at low injection rates – localized salt acts like a barrier hampering pressure dissipation – Suggested using negative skin zone
André et al. [43]	T = 80 ºC P =50 bar Q = 1 Kg/s	K = 5-500 md H = 100 m	Injection rate Salinity	– Good agreement between experiments and simulations – The higher the brine salinity, the greater the salt deposit – Location of salt deposits depends strongly on the injection rate
Guyant et al. [46]	P = 300-350 bar T = 70-80 ºC Q = 0.1-1 mt/year	K = 5-500 md Φ = 0.15-0.2% H = 230 m	Injection rate Permeability Perforation	– High permeability reservoir under low injection rate has the most permeability reduction
Cui et al. [41]	110 ºC 11 MPa	k = 170 mD Φ = 0.20	Injection rate Permeability Perforation	– Reduction in CO_2 permeability

2.11. CO_2-brine-rock interactions and solubility during sequestration

The interaction among CO_2, brine, and formation rock minerals plays an important role during CO_2 sequestration in deep saline aquifers. Firstly, carbon dioxide dissolves in formation water (brine) followed by attainment of equilibrium between the formation of dissolved CO_2 and carbonic acid (H_2CO_3) which finally dissociates into HCO_3^- and CO_3^{2-} respectively. It is of immense important to note that about 1% of the dissolved CO_2 exits as carbonic acid H_2CO_3 [70].

$$CO_2(gas) \rightarrow CO_2(aq)$$
$$CO_2(aq) + H_2O\ (l) \rightleftharpoons H_2CO_3(aq) \rightleftharpoons H^+ + HCO_3^- \rightleftharpoons 2H^+ + CO_3^{2-}$$

(2.1)
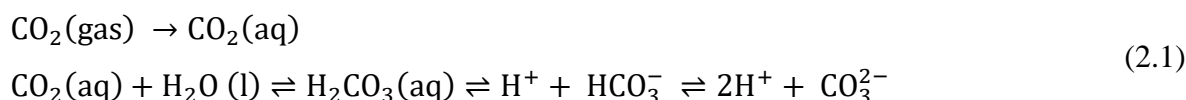
As shown in Equation 2.1, the carbonate anion CO_3^{2-} interacts with cations such as Ca^{2+} and Mg^{2+} to precipitate carbonate minerals and the type of reactions that occurred depend on the mineral composition of the formation rock. However, these reactions are affected by temperature, pressure, multiphase flow of CO_2 and water as well as rock and brine compositions. Other factors such as injection scenarios can affect the interactions between the circulating fluid and the rock as well as permeability impairment after CO_2 injection, thereby leading to dissolution fluctuation [71].

Furthermore, Hurter et al. [61] and Yang et al. [72] predict that the solubility of CO_2 and brine affects the injection process and flow properties in three ways: First, the dissolution of CO_2 in brine apparently increases its density; dissolution of CO_2 in brine leads to the reaction with water, forming an acid and finally, H_2O dissolves into CO_2 increasing the salinity of brine. The level of solubility of CO_2 in brine however depends primarily on pressure, temperature, total salinity, and brine composition. Other factors include density difference between CO_2 and brine, as well as CO_2 saturations. Thus, in general, CO_2 solubility increases with increasing pressure and decreases with increasing temperature and brine salinity [73].

However, some reactions may lead to mineral dissolution and thereby promoting the formation of migration pathways while others may be beneficial to CO_2 storage. Thus, it is imperative to understand the magnitude and direction of such reactions in order to ensure the host formation sequestering CO_2 is safely over a long period of time [74-78].

Furthermore, it is imperative to understand the role of salts including the predominant salt that are found in the formations suitable for CO_2 capture and storage. Different kinds of salts are present in brines found in storage locations, but the most prevalent salts are NaCl, KCl, $MgCl_2$

an $CaCl_2$ [79]. Understanding CO_2-H_2O-Salt system is of enormous importance to predict safe storage capacity. According to Tong et al. [73], solubility trapping of CO_2 in saline aquifers accounts for 90% of the estimated total storage capacity and thus, the solubility of CO_2 in brine (salt-water) can be used in estimation of the total amount of CO_2 stored. Therefore, extensive study of the phase equilibria of CO_2 in aqueous systems and ions such as Na^+, K^+, Mg^{2+}, Ca^{2+}, Cl^- etc, in wide formation temperature as well as pressure ranges is important. Innumerable systems, as shown below, have been studied at different pressures and temperatures.

- CO_2-brine [74]
- CO_2-H_2O [74, 80-83]
- CO_2-H_2O-NaCl [67, 75, 84]
- CO_2-H_2O-KCl [85]

The output summary of these studies is stated below:

- The solubility of CO_2 in water and the salt solutions increases with the increase of the pressure and decreases with the increase of the temperature.
- The Solubility of CO_2 in the low-pressure range is more sensitive to pressure.
- Solubility depends on the salt concentration of each component. Thus, solubility decreases with increasing salt concentration.
- Salting-out effect of NaCl and $CaCl_2$ is larger than that of KCl.
- Salting-out effect is greater in $MgCl_2$ than in NaCl or KCl that have a similar effect.

Experimental data are available on the extent of CO_2 solubility in NaCl solution (brine) and pure water at the conditions necessary for CO_2 capture and storage but extensive data at higher brine concentration would be of advantage. Also, solubility of CO_2 with respect to $CaCl_2$ brine has been studied for temperature and pressure range of 298 to 424 K and 0 to 40 MPa respectively, and 1 to 6 mol/kg of CO_2 solubility in KCl and $MgCl_2$ brines have been studied at salinity up to 4 mol/kg, however, temperature data below 33 °C pressure and above 1300 psi (approx. 9 MPa) are needed. Thus, extensive studies have been carried out in the study of CO_2 solubility with individual/mixed salt solutions, but no study has been reported with respect to pressure decay test during core flooding. This can be useful in predicting the rate of solubility of CO_2 in a porous media with respect to the type of salt in the brine solution.

In this study, we investigate the concentration, pressure decay rate, solubility, and the interaction of the CO_2 in the porous media at different concentrations with different types of salt (NaCl, KCl, $CaCl_2$ and $MgCl_2$) at a simulated reservoir pressure of 1500 psig, temperature of 45 °C at a constant injection rate of 3 ml/min.

2.12. CO_2 Solubility in Brine and Interfacial Tension (IFT)

The relationships between solubility of CO2 in brine and the interfacial tension will be discussed in this section. The criteria will be addressed and explained individually first, and then their relationship will be demonstrated.

2.12.1. Interfacial tension measurement between CO_2 and Brine

The interface between the CO_2 and brine, when they are in contact with each other, is a thin layer. This is due to an imbalance in the interfacial interaction forces displayed by the two fluids in contact. Interfacial tension is the quantitative index of the interfacial contact force that exists at the interface. It is defined as the force exerted per unit length at the interface of the fluids in contact. The unit of measurement is dyne/cm or mN/m [86].

The pendant drop method is the most used method of IFT measurements in harsh working situations. This is based on the concept of creating a droplet of a fluid (typically denser phase) in a lighter phase when the phases are in equilibrium. The droplet profile can be used to assess interfacial tension between phases. Figure 2.8 depicts an example in which the dimensions of the droplets represented are employed in a mathematical calculation to calculate the IFT based on the density difference between the phases under consideration.
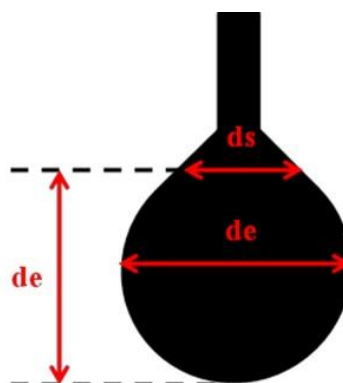
Figure 2.8: Dimensions of droplet used for IFT measurement

The theory for computing the IFT is presented in Equation 2.2.

$$\gamma = \frac{\Delta\rho \times g \times d_e^2}{H} \tag{2.2}$$

Where "γ" is the interfacial tension (mN/m), "g" is acceleration due to gravity in (cm/s^2), "$\Delta\rho$" is the density difference (g/cm^3) between the two phases (liquid and gas), "d_e" is the diameter of the droplet at the equator (cm), and "H" is the droplet shape factor which can be calculated from Equation 2.3, where "d_s" is the diameter of the droplet (in cm) from the tip of the droplet to the equivalent length of "d_e".

$$H \propto \left(\frac{d_s}{d_e}\right) \tag{2.3}$$

The IFT can be measured by using the droplet image shown in Figure 2.8.

The rising bubble method in comparison to the pendant drop method is better for measuring the gas liquid IFT since the sole variation being the injection configuration of the lighter phase [87]. In the pendant drop method, the denser phase is injected from the top of the measuring cell, whereas in the rising bubble method, the lighter phase is injected from the bottom, where the gas bubble is encouraged by the buoyancy within the denser phase to develop. In this work, the importance of IFT measurement between CO_2 and brine is to associate the parameter with CO_2 solubility in brine which was experimentally identified by using the rising bubble method.

2.12.2. The Interaction of CO_2 Solubility and Interfacial Tension in Brine

There is an abundance of literature data for CO_2 solubility that shows the behaviour of CO_2 at subcritical and supercritical states in the presence of brines at various temperatures and pressures [88-98]. These studies were conducted utilising both experimental and numerical modelling methods.

The ability of a gas to dissolve in brine/oil to produce an aqueous and homogenous solution is referred to as solubility. This CO_2 feature is desirable in miscible flooding for EOR/EGR applications, and CO_2 gas storage in deep saline aquifers. For its capacity to dissolve and reduce volume, it is perfect for CO_2 sequestration in water formation during CCS operations. As a result, analysing CO_2 solubility during sequestration is important in order to determine the

reservoir's storage capacity (in deep saline aquifer) as well as the effect of this solubility in various brine formulations.

However, there is a substantial link between IFT and the solubility of two phases (CO_2 and the brine) [89, 99]. Several studies have demonstrated a relationship between IFT and CO_2 solubility, which can be utilised to analyse the gas's dissolution in an external phase [100-103]. Bennion et al. [99] utilised extensive data from the literature to develop a correlation between the solubility of CO_2 in various brines as well as the IFT between them as shown in Figure 2.9.
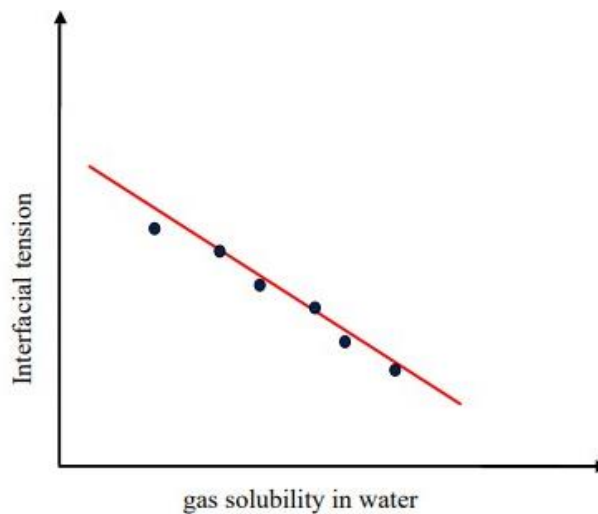
Figure 2.9: Relationship between IFT and Gas solubility in water

According to the literatures reviewed by Bennion et al. [99] solubility increases with decreasing brine salinity, increasing temperature, and decreasing brine pressure.

This continues to illustrate that solubility is heavily reliant on all of these key variables, and IFT data taken from the literature also showed the similar dependency of the IFT on these same variables of temperature, pressure, and salinity. They discovered a relationship between the variables at temperatures ranging from 41 to 120 °C, pressures ranging from 2 to 27 MPa, and freshwater brine salinity (about 350,000 ppm of total dissolved solid (TDS)). This shows in Equation 2.4.

$$\gamma = -0.0004S^4 + 0.0241S^3 - 0.3836S^2 - 0.7305S + 73.264 \tag{2.4}$$

Where "γ" is the IFT (mN/m) and "S" is the CO_2 solubility in aqueous phase (m^3 CO_2 per m^3 aqueous solution).

Thus, an experimental technique to measuring CO_2 solubility in brine can be achieved through its association with interfacial tension measurements (IFT), which will be used in this study. This is due to mass transfer between the gas and brine phases.

2.13. Key issues during CO_2 sequestration and remediation technique to abate salt precipitation in a porous media

The best-known option in the carbon capture, utilisation, and storage community for salt remediation during CO_2 storage is the treatment with fresh water [22]. This procedure can be employed as a pre-flushing prior to CO_2 injection or after clogging to dissolved precipitated salt, lowering the salinity of near-well brine. It is important to note that technical issues involving the design of water injections into deep saline aquifers to mitigate the impacts of salt precipitation necessitate extensive experimental examination, and this method is feasible as demonstrated by various numerical simulations [14, 61].

Hurter et al. [61] compared the results of simulations of CO_2 injection into salty aquifers for two years to another example in which fresh water was injected for one month. The results of the fresh water pre-flushing demonstrated less salt precipitation as well as a significant reduction in pressure build-up near to the injection well.

Muller et al. [14] on the other hand, conducted an injection impairment analysis for the CO_2SINK Project and proposed simple reservoir engineering modifications to counteract significant halite precipitation near the injection point. A fresh water pre-flush for 16.2 hours before CO_2 injection was found to reduce salt deposition and pore obstruction near the borehole. Pre-saturating CO_2 with water before to injection was also advised to reduce brine evaporation and salt precipitation during CO_2 sequestration.

Another numerical simulation study by Pruess et al. [42] examined utilising a brief pre-flush with fresh water to push precipitable solids away from the injection well as a method of delaying the commencement of precipitation. According to their models, the largest effects of precipitation on injectivity are often confined to a few metres surrounding the injection well, and that a brief pre-flush of a few hours can produce long-term benefits in terms of sequestration.

Bacci et al. [59] in a series of experimental and numerical studies on the understanding of the halite scaling process, showed that utilising fresh water as the initial solvent can lead to an improvement in the permeability of the sample. Furthermore, because of the constant changes in the rock pore size distribution, there is a considerable danger of injectivity losses in the later stages.

Moreover, salt precipitation was considered as a plausible source of reduced near wellbore injectivity during the injection of 1.6 Mt of CO_2 in the Tubaen formation at the Snohvit field. To reduce salt precipitation and increase injectivity, a weekly injection of a 90:10 mixture of methyl ethyl glycol (MEG) and water was used [8, 33]. Thus, injection of MEG resolved low injectivity, and fall-off pressure study revealed that weekly injection of MEG eliminated undesirable blocking. Hosseini et al. [104] conducted an experimental examination on the control of salt precipitation using a wetted wall column and inhibitor injection. To investigate the performance of inhibition and NaCl creation, a pilot-scaled dynamic loop was created. Inhibitors of polyethylene glycol (PEG) and sodium dodecyl sulphate (SDS) were examined, and both compounds were found to be effective in lowering the amount of salt precipitated [104]. They also reported that SDS is more efficient than PEG and that the optimum SDS concentration in solution to suppress halite production is 400 ppm.

Another method for addressing the issue of low CO_2 injectivity is to use highly permeable materials as fill between the borehole and the aquifer along the perforation interval. Thus, in the disciplines of Petroleum Geosciences and Groundwater Technology, this method has been established beyond reasonable question [22]. Kim et al. [11] utilised numerical simulations to explore the feasibility of this strategy for preventing salt precipitation and near-well pressure build-up. Variations in the porosity and permeability of the skin zone were used to collect pressure build-up data and saturation profiles. Their findings demonstrated that injectivity is most susceptible to permeability, and so employing highly permeable material fillings can significantly reduce injectivity impairment caused by salt precipitation.

Another study by Sokama-Neuyam et al. [105] was conducted to investigate CO_2 alternating low salinity water injection as a potential mitigating approach to lessen the influence of salt precipitation on CO_2 injectivity. Following salt precipitation, a slug of diluent (Low salinity water brine, LSW) was injected at 0.05 ml/min into a core in an attempt to dissolve the precipitated salt and temporarily improve CO_2 injectivity. Their findings revealed that increasing the mass fraction of salt in the diluent from 8.44% to roughly 2.11% enhanced CO_2 injectivity from 8.66% to 31.62%. Sokama-Neuyam et al. [105] studies also suggested that fresh water might not be a good alternative for wellbore pre-flush in sandstone because, below a certain threshold brine salinity, the diluent can react negatively, causing effects such as fines mobilisation and clay swelling.

However, no precise description of when the remediation fluid is to be introduced into the reservoir to remove some of the precipitated salt in the core sample was provided in the preceding study. Core flooding experiments using Scanning Electron Microscopy (SEM) and

Energy Dispersive X-Ray imaging (EDX) were employed in this study to evaluate the fundamental strategy in dissolving accumulated salt and enhancing CO_2 injectivity during CO_2 sequestration in deep saline aquifers.

The process of salt precipitation, migration, and retention near the wellbore during CO2 injection into saline aquifers is depicted in Figure 2.10. Based on the in-depth analysis of salt precipitation presented above, it is possible to conclude that salt crystallization, migration, and accumulation at pore throats are the primary mechanisms of formation blockage. To accurately predict the distribution and amount of salt precipitation, we must first clarify the main controlling factors of salt crystallization and reveal the precipitated salt dynamic migration, and then develop a comprehensive numerical model that takes into account all of these processes.
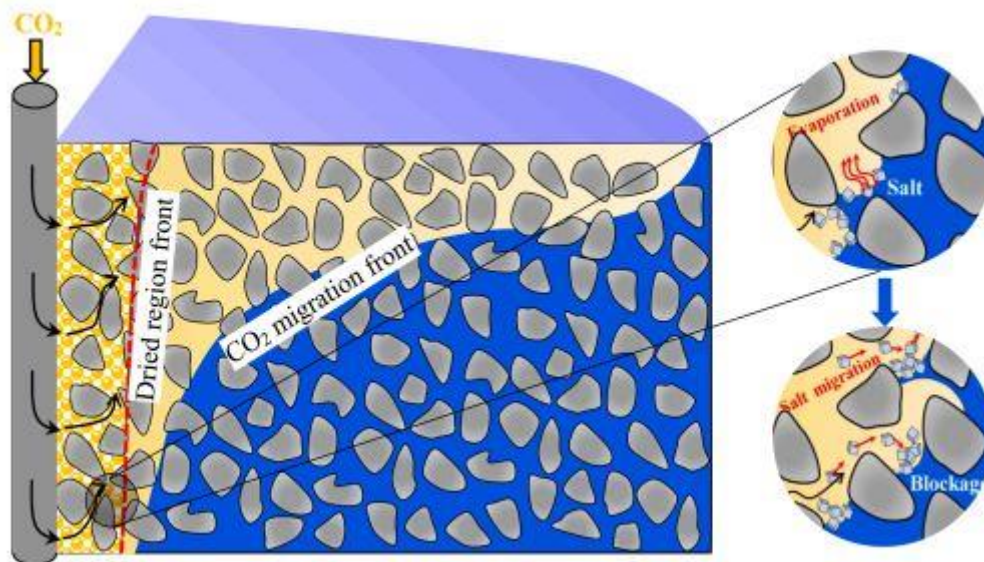
Figure 2.10: The process of precipitation, migration, and retention of salt near the wellbore during CO2 injection into saline aquifers

2.13.1. Salt crystallization kinetics

Key problem description

The hydraulic conductivity of pore water (water pool, water film, and water domes) during CO_2 injection into saline aquifers can influence the location of salt crystallization. As a result, the crystallization of salt can affect the flow of nearby pore water at the pore scale. The dissolved salt constantly precipitates out of the water after it exceeds its solubility limit due to the interaction between pore water mobility and salt crystallization. The foundation for revealing the mechanism of salt crystallization kinetics in pores is how to capture and quantify

salt crystallization and then clarify the main salt crystallization influencing factors. As a result, elucidating the salt crystallization kinetics is the first key scientific problem for revealing the mechanism of reservoir impairment caused by salt precipitation.

Method for remediating this critical issue

The ability to reproduce salt crystallization at the pore scale is important for revealing the physical mechanism of salt crystallization during CO_2 injection into saline aquifers. To capture the crystallization process of dissolved salt and quantify the salt precipitation rate, a novel lab-on-chip experiment under high temperature and pressure must be developed.

The high-temperature and high-pressure lab-on-chip structure shown in Figure 2.11 can be designed. The device must withstand a maximum pressure of 25 MPa and a maximum temperature of 100 °C.
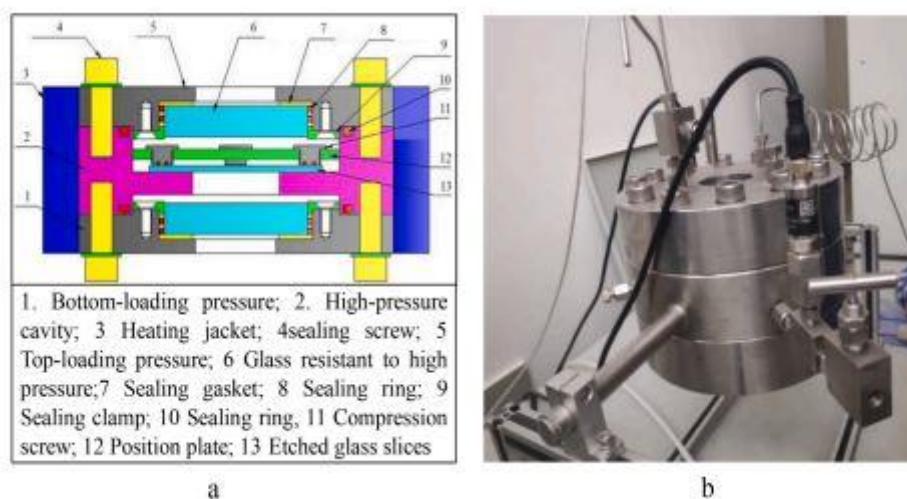
Figure 2.11: Structure diagram of a high-temperature and high-pressure lab-on-chip. (a) A high-pressure lab-on-chip structure diagram. (b) A real high-pressure lab-on-chip

The pore structures of various saline aquifers can be simulated using various etched glass slices. Following that, by combining it with high-precision electron microscopy, the evolution of the pore water and salt precipitation process can be captured [106]. This device can provide experimental support that is both practical and operational in revealing the salt crystallization kinetics in the pore structure.

A novel quantitative analysis of water film hydraulic connectivity can be developed after high-precision electron microscopy captures pore water evolution and salt crystallization.

A novel quantitative analysis of water film hydraulic connectivity can be developed after high-precision electron microscopy captures pore water evolution and salt crystallization. As shown in Figure 2.12, the characteristics of pore water distribution in pores are extracted first by binarization and nonlinear filtering of high-order grey images. The image processing is then repeated to identify and label the added black tracers in the water. Finally, a command (such as Plugins Tracking Manual Tracking by ImageJ) can be set up to track the black tracers and quantify the hydraulic connectivity of the water film. This method can help reveal the salt crystallization kinetics in the pore structure by providing operational and technical support.

a   b
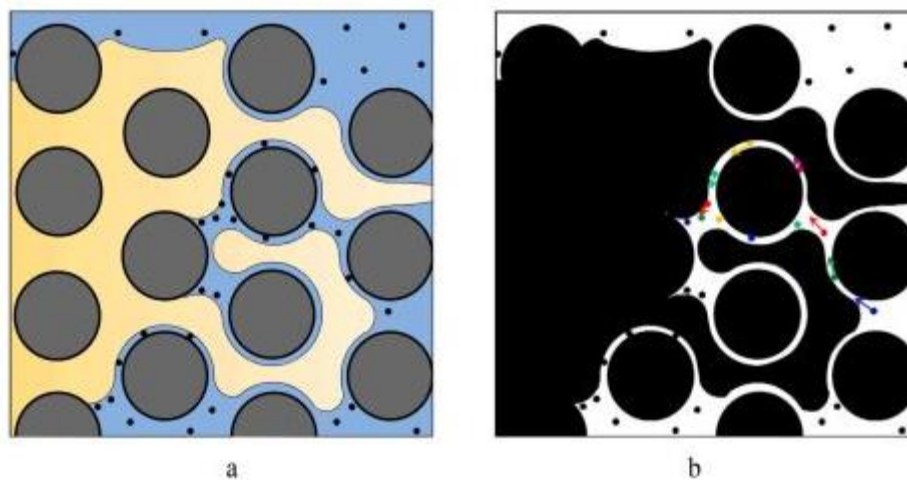
Figure 2.12: Captured water film and its hydraulic connectivity based on image processing. (a) Water distribution in the pore structure. (b) The captured water film and its hydraulic connectivity, and the particles of different colors are captured tracers to calculate the hydraulic connectivity.

2.13.2. Migration and retention of salt

Key problem description

Under certain conditions during CO_2 injection into saline aquifers, the precipitated salt may migrate with CO_2 and then accumulate in the pore throat, as shown in Figure 2.9. The second key scientific problem for revealing the mechanism of reservoir impairment caused by salt precipitation is how to analyse the migration and retention behaviour of precipitated salt and its influence on reservoir pore throat.

Method for remediating this critical issue

To eliminate the influence of the CO_2-water-rock geochemical reaction on the rock porosity and permeability during the analysis of the migration and retention process of precipitated salt,

water saturated with CO_2 should be injected into the rock first. Furthermore, the impact of cementation and particles shed from the rock grain can be eliminated during this period of water injection. Second, the core is dried and scanned to establish the 3Dpore structure of the entire core prior to CO_2 injection, allowing the following salt precipitation location to be identified. Finally, the CO_2 flooding experiment is carried out to allow the dissolved salts to precipitate out of the water. Fourth, after salt precipitation, the core is dried and scanned to establish the 3D pore structure of the entire core, and SEM is used to identify the detailed distribution of precipitated salt in the pore structure. Finally, the lattice Boltzmann method is used to simulate the migration and retention of precipitated salt in the pore throat. (LBM). Figure 2.13 depicts the particle migration and retention process in the pores using the LBM.
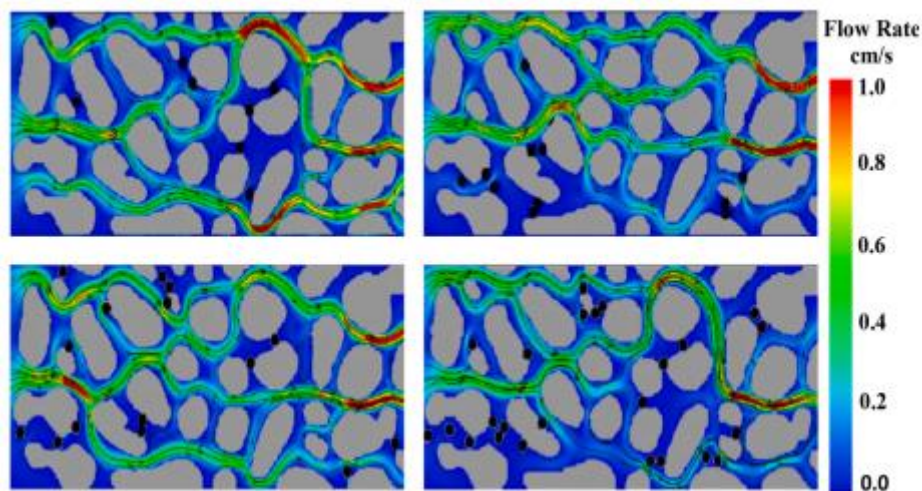
Figure 2.13: The calculated particle migration and retention in pores based on the lattice Boltzmann method [107]

The pore throat structures obtained in the CO_2 flooding experiment before and after salt precipitation are extracted and established first. The fluid flow is simulated using the LBM, and the precipitated salt migration and retention is simulated using the discrete element method. The immersed moving boundary method is used to simulate the interaction of water and precipitated salt [107].

During the simulation, the effect of precipitated salt on fluid flow is realized by modifying LBM with an additional collision operator based on the percentage of the site covered by solid, whereas the effect of fluid flow on solid is realized by modifying LBM with an additional collision operator based on the percentage of the site covered by solid. Calculating fluid force and torque acting on precipitated salt results in precipitated salt migration. The permeability

change caused by the precipitated salt can be obtained by inverting the flow rate field with the mass and momentum conservation equation in the LBM [108]. This method has the potential to provide a reliable guarantee for revealing the dynamic migration of precipitated salt and its impact on permeability.

2.13.3. Salt precipitation simulation model

Key problem description

Given that there is no simulation mode that takes into account the process of salt crystallization, migration, and accumulation, the simulation results would be inaccurate in terms of the distribution and amount of precipitated salt. As a result, it is critical to establish an integrated framework to integrate these dynamic processes into existing models. Based on the salt crystallization kinetics and precipitated salt dynamic migration obtained from lab-on-chip and CO_2 flooding experiments, a new comprehensive simulation model taking salt crystallization, migration, and retention into account can be developed to accurately predict salt precipitation distribution and its influence on CO_2 injectivity.

Method for resolving this critical issue

The convection-diffusion equation of vapor can be used in this simulation model (shown in Figure 2.14) to simulate the evaporation process by changing the vapor solubility in the CO_2 phase in each calculation period. The precipitation kinetic equation of salt and other minerals can be established using the Arrhenius equation, which we have completed. Combining the sand-arch-stability criterion approach and the solute transport and adsorption equation can be used to model precipitated salt migration and retention [41, 109]. The permeability change in the macroscopic continuum model can reflect reservoir impairment caused by salt precipitation, and the porosity change can be directly calculated by the volume change caused by the precipitated salt. As a result, the pore-permeability relationship is a useful tool for characterizing the effect of salt precipitation on reservoir impairment due to pore-scale blockage. Specifically, the equations of salt precipitation, migration, and retention can be coupled to establish a comprehensive simulation model of CO_2 injection into saline aquifers based on the existing CO_2-water two-phase seepage module and porosity-permeability relation. The kinetic parameters of water evaporation in the model can be changed based on the vapor production rate in the experiments, and the dynamic parameters of salt migration can be corrected based on the precipitated salt distribution in the experiments.
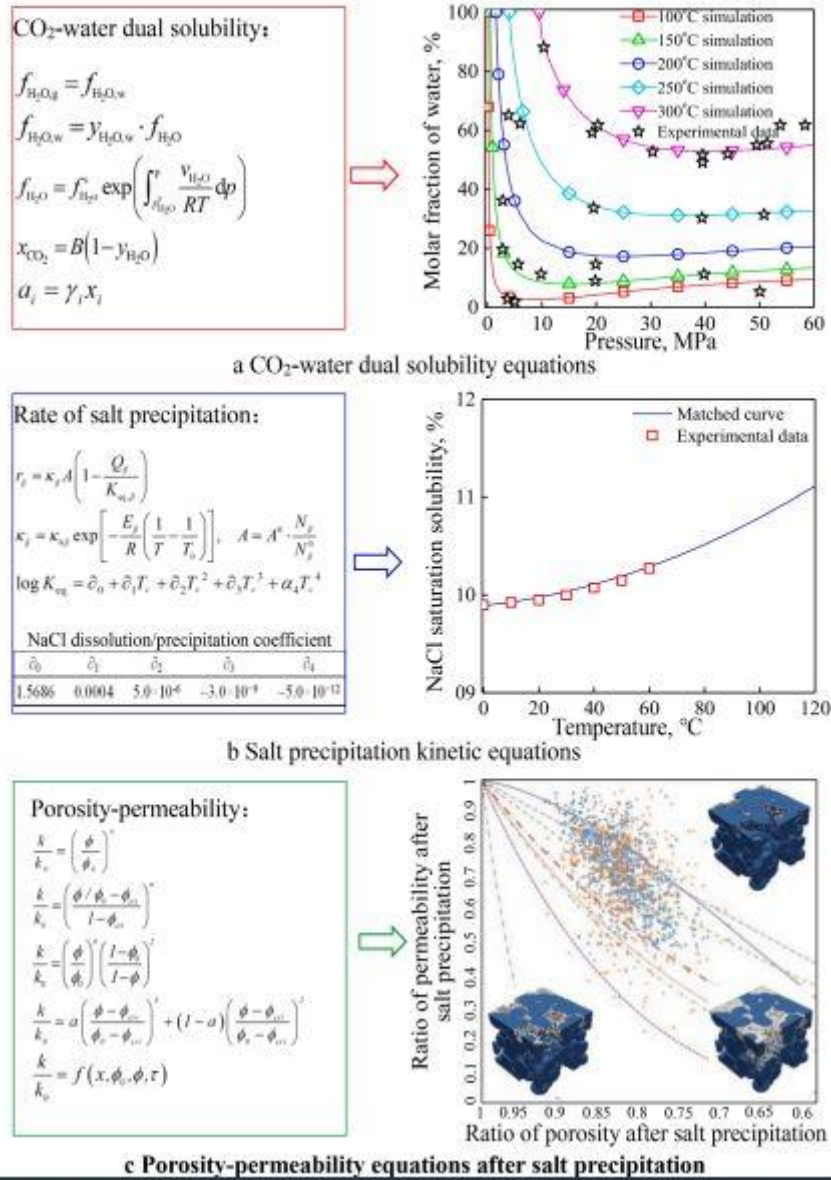
Figure 2.14: Preliminary equations describing water evaporation, salt precipitation rate, and relation of porosity and permeability. (a) CO2-water dual solubility equations; (b) Salt precipitation kinetic equations; (c) Porosity-permeability equations after salt precipitation.

Thus, this chapter on the review of literature will lead to the next chapter which is the experimental setup and methodology.

Chapter 3: Experimental Setup and Methodology

3.1. Overview

This chapter presents the experimental setup and the methodology used in this study to investigate the CO_2 storage in deep saline aquifers and the remediation technique in order to enhance the storage capacity. Detailed analysis of the experimental setup, the materials used in the experiments and their mode of preparation is discussed in detail within this Chapter.

Figure 3.1 shows the specific Phases and the sequence of the experimental procedure undertaken in this research.
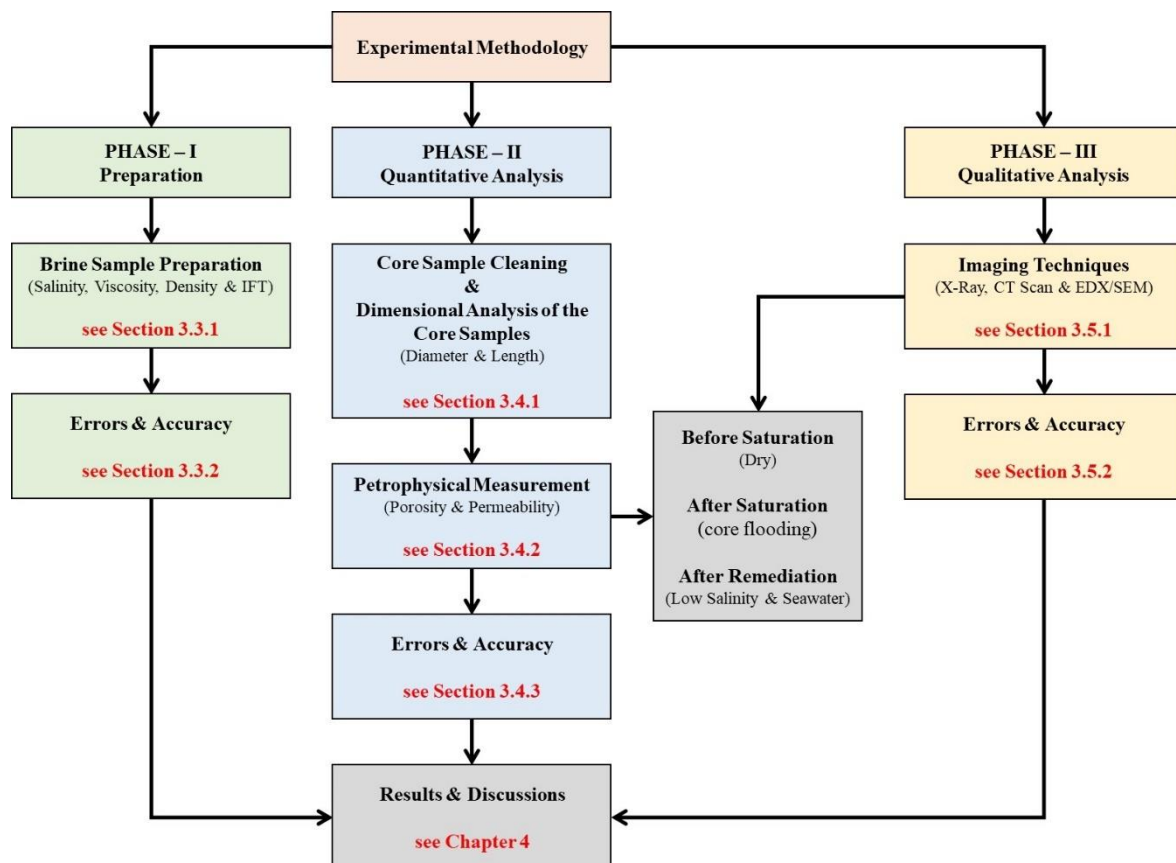
Figure 3.1: Experimental Methodology

As it is shown in Figure 3.1, the experimental procedure is divided into three Phases as follows:

- ***Phase-I (Preparation):*** The corresponding core samples, supplied by Kocurek Industries, Inc in USA, were analysed dimensionally (diameter and the length). In this

stage, four different salts were also mixed with water to obtain different brine salinities. Further details and explanations are provided in Section 3.2.

- *Phase-II (Quantitative Analysis):* In this Phase, the petrophysical properties of the core samples such as porosity and permeability were analysed in three different scenarios: (i) before saturation where the measurements conducted for each sample without any brine injection, (ii) after saturation where the measurement conducted after injecting the brine with different salinity at the reservoir conditions, and (iii) after remediation where the low salinity water or seawater injected into the saturated core samples to dissolve the salts into the water and open the blocked pores.

- *Phase-III (Qualitative Analysis):* This phase involves the use of high-class Scanning Electron Microscopy (SEM) and Energy Dispersive X-Ray mapping (EDX) techniques to qualitatively analyse the core samples. The comparative evaluation to the experimental data (obtained in Phase-II) carried out to know the level of precipitated salt in the matrix of the core samples, as well as the extent of the removal of the precipitated salt through the use of different remediation fluids.

3.2. Materials

3.2.1. Sandstone Core Samples

Three different sandstone core samples with different porosity and permeability were tested in this study. These core samples are categorized as homogenous and were selected based on their physical properties and suitability to accommodate different flow conditions. These samples, supplied by Kocurek Industries Inc. in USA, are:

- *Bentheimer:* Due to their lateral continuity and block scale homogeneity, Bentheimer sandstone outcrop samples are suited for laboratory experiments. They have been used to research reservoir themes such as passive and active features of oil/gas/water/rock interaction and processes, as well as flow and transport. Bentheimer sandstone is found in the southwestern section of the Lower Saxony Basin and outcrops along the Dutch-German border, primarily in the area defined by Meppen, Adorf, Nordhorn, Bentheim, and Ochtrup.

- *Salt Wash North* is found in the Sid's Mountain Wilderness Area of the San Rafael Swell in Emery County, Utah east of the town of Ferron.

- *Grey Berea* sandstone, also known as Berea Grit, is a type of sandstone found in Michigan, Ohio, Pennsylvania, West Virginia, and Kentucky. It was named after the town of Berea, Ohio. Sandstone has been utilised as a building stone and as an oil and gas source.

3.2.2. Different Salts

Salt samples, with a purity of 99.9%, used in this study to prepare the brine solution were supplied by Fisher Scientific, UK (see Figure 3.2). These salts are Sodium Chloride (NaCl), Potassium Chloride (KCl), Calcium Chloride ($CaCl_2$), and Magnesium Chloride ($MgCl_2$).

Figure 3.2: Salt Samples for Brine Preparation

Further information of the above salt used for the research work is shown below in table 3.1

Table 3.1: Salt samples for brine preparation

S/N	Salt type	Molecular formula	Molecular weight	CAS	Code	Lot
1	Sodium Chloride	NaCl	58.44	7647-14-5	S/3105/63	1416237
2	Potassium Chloride	KCl	74,54	7447-40-7	P/4240/62	1405777
3	Calcium Chloride	$CaCl_2$	110,99	10043-52-4	C/1400/60	1723449
4	Magnesium chloride	$Cl_2Mg.6H_2O$	203,31	7791-18-6	M/0600/53	1989660

Further details and the method of brine preparation is explained in Section 3.3.1.

3.2.3. Gases

The gases used for the experimental and quantitative analysis are:

- _Helium_ is the expanding gas of choice in this experiment because it is an inert gas and therefore will not have any rock-fluid interactions that may alter the morphology of the sample being analysed. Also, helium has a high diffusivity and therefore will measure porosity very accurately.

- _Nitrogen_ gas was used to set-up the back pressure of the core flooding equipment.

- High grade _CO_2_ was used to investigate salt precipitation during storage. The characterization of the fluid (CO_2) was also conducted using PVTsim Reservoir software to determine the density and viscosity of the fluid.

All of them have 99.9% purity, reported by the supplied company (BOC, UK).

3.3. Phase-I: Preparation

3.3.1. Brine Sample Preparation

Brine is a high concentration of solution of salt in water. The brine samples were prepared using four different salts (NaCl, KCl, $CaCl_2$, and $MgCl_2$) which are notably present in the water formation of deep saline aquifers. The main brine component present in saline aquifers is NaCl, typically in the range of 70 to 90%. The brine concentration in deep saline aquifers has been reported to be in the range of 2 to 25 wt.%. Brine concentration increases with respect to reservoir depth in the range of 800 to 2000 m. In this work, the selected brine concentrations were 5 wt.%, 10 wt.%, 15 wt.%, 20 wt.%, and 25 wt.%, which covered the salinity range of a typical deep saline aquifer. For example, during the preparation of 5 wt.% brine concentration, 5g of salt were dissolved in 95g of distilled water. Also, during the preparation of 10 wt.% brine concentration, 10g of water were also dissolved in 90g of distilled water. The brines of various concentrations were made by dissolving the necessary amount of salt in distilled water and stirring with a magnetic stirrer (shown in Figure 3.3) to gently swirl the brine and enable the appropriate salt dissolution before saturation of the different core samples.
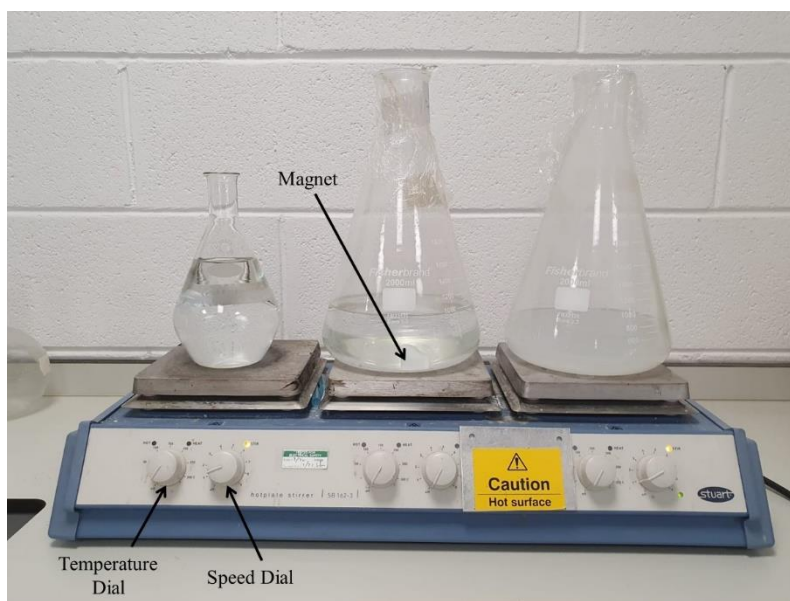
Figure 3.3: Hot plate with Magnetic Stirrer

It should be emphasised that the wt.% is used in preparation of the brine samples due to the macro effects of salt concentration on CO_2 storability. As crucial as mol percent is the variance in wt.% and salt type in understanding the dynamic extent to which these parameters affect rock characteristics and CO_2 injectivity. Testing these caveats can provide valuable information for effective sequestration methods. Furthermore, each reservoir has unique properties, and this work highlights and emphasises the distinction between salt kinds in terms of mass concentration.

3.3.1.1. Salinity Determination

Salinity is the measurement of dissolved salt in water which can be determined by a refractometer (shown in Figure 3.4) which produces an exact measurement of refraction caused by the density.
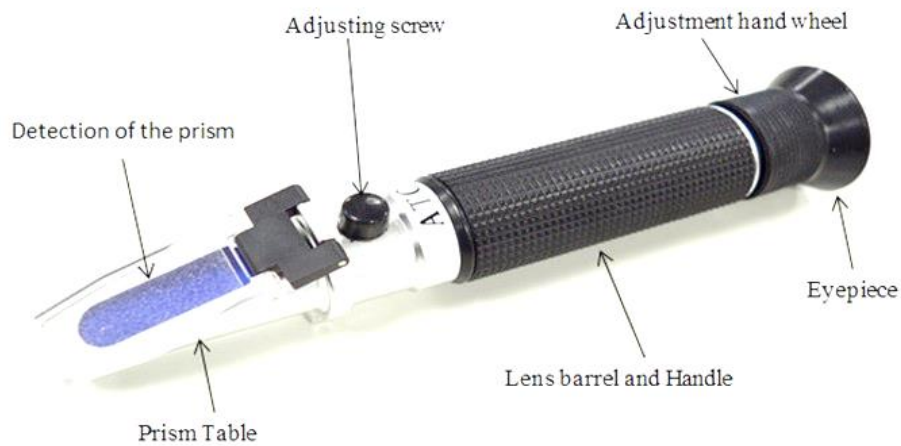
Figure 3.4: A refractometer for measuring Brine Salinity

Refractometers are cheap and simple to use and can be applied in multiple scenarios. It is a model tool to analyse water concentration mixes quickly. The refractometer allows simple and accurate dilution control. The prism screen has a greater refractive index than the sample solution. A small sample of the brine solution is placed on the prism table, and whilst holding it under a light, by looking through the eyepiece, salinity scale and observable line can be seen in which the salinity of the brine can be measured

3.3.1.2. Viscosity Measurement

Viscosity is a very important parameter to measure while dealing with liquids in oil and gas industry. Viscosity (μ) is a physical property of a fluid that describes its tendency or resistance of a fluid to flow. In order to measure the fluid's viscosity, the experiment must be run over a set of temperatures, since by increasing the temperature, the liquid viscosity decreases and vice versa. OFITE-1100 (shown in Figure 3.5) was used in this study to measure the viscosity.
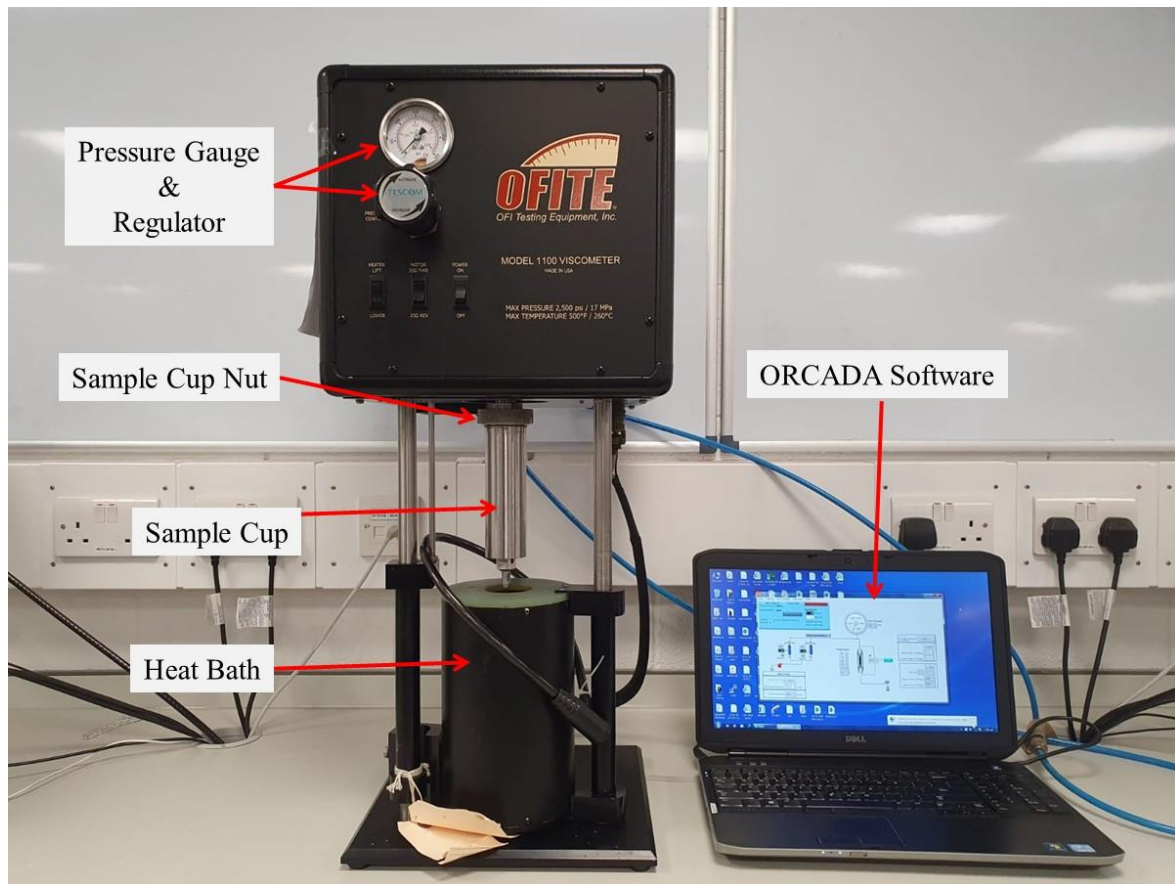
Figure 3.5: OFITE-1100 Viscometer

Procedure

To measure the fluid's viscosity with OFITE-1100, the experiment must be run over a set of temperatures. The apparatus includes a thermal bath in which the spinning fluid holder can be placed in to warm the fluid. The fluid's viscosity and shear stress were measured at the temperatures of 20 to 60 °C at 5 degrees intervals. Once the experiment for a certain salinity ended at 60 °C, the sample cup was placed in an icy water to cool down. Once the cup was cooled down and the new fluid was poured in, the experiment commenced again at 20 °C. To calculate the fluid's dynamic viscosity (absolute viscosity) in Pa.s or centipoise (cP), the shear stress is divided by the shear rate. The viscosity can be calculated by using Equation 3.1.

$$\mu = T \times F \times \frac{\theta}{\omega} \tag{3.1}$$

Where, "μ" is the brine viscosity (cP), "F" is the spring factor and it equals to 1 for the corresponding OFITE-1100, "T" is temperature which equals to 300 K, "θ" is the device dial reading for shear stress (N/m^2), and "ω" is the speed (rpm).

3.3.1.3. Density Measurement

Although the SI unit for reporting the fluid density (ρ) is kg per m3 (kg/m^3), however, this parameter in oil and gas industry is being identified as pound per gallon (lb/gallon) or ppg. Therefore, there is a need to measure the brine density with a specific device called a mud balance as shown in Figure 3.6.
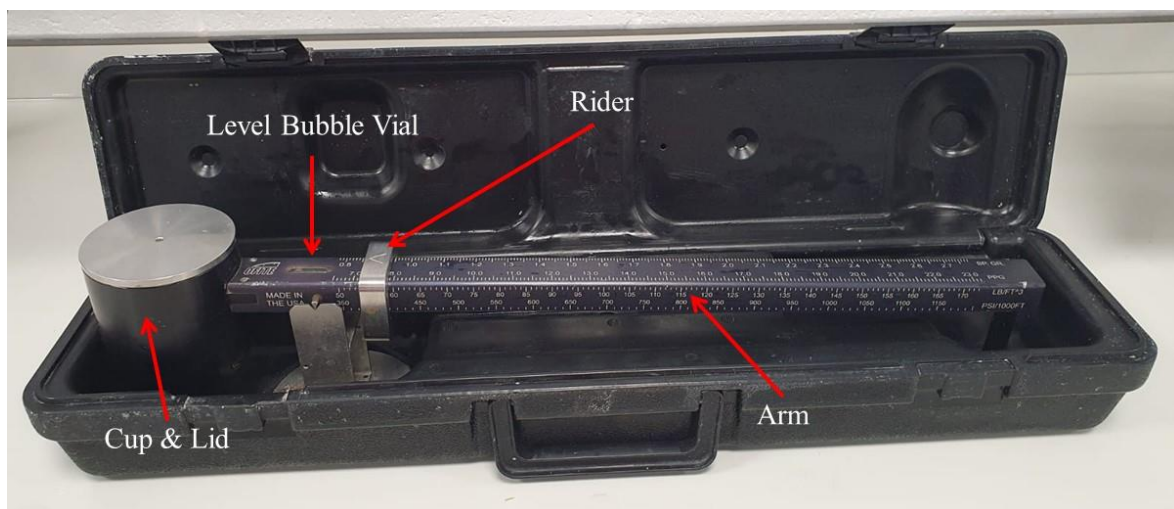
Figure 3.6: Mud Balance for Measuring the Brine Density

The mud balance features a fixed-volume cup that's located at the end of a graduated beam and a known counterweight on the opposite end. The graduated beam has a slider-weight attached to it which can be moved along the beam until the bubble indicator shows that its level, thus the density value can be measured. To calibrate the mud balance, a liquid of with a known density (usually water) is used. Similarly, to the refractometer, in order to improve the accuracy of the density readings, the brine solution must be free of minerals and contaminants. To calibrate the mud balance, the following steps needs to be considered:

1. Initially, a measurement of the laboratory temperature must be attained.
2. First, remove the lid from the cup and completely fill it with water.
3. Replace the lid and ensure there is no excess water on the lid.

4. Put the balance arm on the base with the knife-edge resting on the fulcrum.

5. The level vial should be centred when the rider is set on 8.33 ppg. If not, add to or remove shot from the well in the end of the beam.

Procedure

1. Remove the lid from the cup and completely fill the cup with the brine solution.

2. Replace the lid and rotate until firmly seated, making sure some of the solution has expelled through the hole in the cup.

3. Ensure that there is no excess solution on the outside of the cup.

4. Place the balance arm on the base, with the knife-edge resting on the fulcrum.

5. Move the rider until the graduated arm is level, as indicated by the level vial on the beam.

6. At the left-hand edge of the rider, read the density on either side of the lever in all desired units without disturbing the rider.

3.3.1.4. Interfacial Tension Measurement (IFT)

In this study, a Corelab high-pressure high-temperature surface interaction energy experimental setup (see Figure 3.7) was used to analyse the interfacial tension between the CO_2 and the brine samples.

(1&2) accumulators, (3) Rame hart digital camera, (4) IFT cell, (5) Monitor, (6) Vent Valve, (7) Vacuum Valve, (8) Vacuum pump, (9) Heating element, (10) Injection Needle, (11) data logger and temperature controller

Figure 3.7: Setup arrangement of IFT

The IFT setup consists of a high-pressure measurement cell with a pressure rating of up to 12,000 psig, a Rame-Hart optical video camera system for onscreen real time image display that is connected to a computer and interfaced with a digital image processing software (DropImage software developed by Rame-hart Instruments Co.) used for IFT determination by image analysis of the gas bubble captured by the camera, and a high pressure HiP 62-6-10 manual pump with a pressure rating of 10,000 psig for charging the external phase (brine), and a Temco temperature controller used to establish the system's temperature within $\pm$ 0.3 °C of the predetermined temperature. The IFT is calculated by using DropImage software, which employs a theoretical procedure to evaluate the parameter based on the created bubble profile and dimensions.

Procedure

To ensure proactive experimentation and trustworthy results, preventative procedures were done prior to each measurement to rid the system of any pollutant. The accumulators (1 and 2), the IFT cell (4), the injection needle (10), and the delivery tubing were all soaked in acetone for 2 hours before being tested for the first time. These components were reconnected and then evacuated using a vacuum pump (8). The accumulators were then filled with hot distilled water, which was then injected into the IFT cell to flush the entire system. The entire system was then dried with dry compressed air. The external phases (brine/distilled water) were then charged into the cell with a manual pump until the desired pressure was reached, and the temperature was controlled with a Corelab temperature controller. The gas (CO_2) was then fed into the drop phase accumulator once the pressures and temperatures had stabilised. Subsequently, the gas was pressurised to the desired test pressures using a manual pump. The bubble was created within the test cell by slowly opening the injection needle valve and observing its development. The formation and demise of the bubble were documented. For repeatability and acquired data dependability, this bubble measurement was repeated for three bubbles in each experiment using the DropImage software, and the IFT measurement was repeated on each bubble picture obtained.

3.3.2. Errors and Accuracy

- The errors considered in *salinity* measurement are:
    - Using the weight scale, with ± 0.1 g accuracy, to measure the mass of the salts diluted in water.
    - The error in reading the refractometer which is ± 0.2%
- Errors arose when measuring the *viscosity* at the desired temperature. The thermal bath's temperature readings were very high, between 119 and 140 °C. In addition, during the time which it takes to manually remove the cup from the thermal bath and the cup reaching to 1000 rpm speed, the sample cup's temperature kept on increasing. Therefore, it is hard to predict that at what time the cup would reach 1000 rpm and record the desired temperature. The speed accuracy (rpm) is 0.1, the minimum viscosity at 600 rpm has accuracy of 0.5 cP, and the maximum viscosity at 600 rpm has accuracy of 33,000 cP.
- The *density* of the fluid is measure by the mud balance. The arm is graduated and permits accurate measurements to within ± 0.1 ppg or ± 0.01 specific gravity (sg).

- The errors and accuracy of Interfacial Tension (IFT) depends on some factors such as human errors (i.e., measuring the bubble diameter from the image) and accuracy on setting the pressure by the pressure regulator ($\pm$ 0.1 bar) or the needle exit diameter which produces gas bubble ($\pm$ 0.1 mm).

3.4. Phase-II: Quantitative Analysis
3.4.1. Core Sample Preparation
3.4.1.1. Cleaning

Before conducting any experiment, the sandstone core samples were properly cleaned and dry to ensure that there is no contaminant residing in the core sample to acquiring concise and reliable results. Thus, upon receipt of the core samples, they were subjected to cleaning using Soxhlet Extraction in which both organic and inorganic residues in the core sample were removed. Soxhlet extraction equipment consists of a Pyrex flask (which is a long neck round-bottom flask), a thimble, a condenser in which cold water circulates and an electrical heater to provide the necessary heat to evaporate the methanol solvent around the system.

Procedure for core sample cleaning using Soxhlet Extraction

The setup for Soxhlet Extraction is shown in Figure 3.8. In this process, methanol is heated to about 70 °C so that it evaporates upwards into the condenser. The vapour thus condenses in the condenser, which has cold water circulating through it and then drips into the Thimble which houses the core sample and serves as a receiver of the fluid extracted from the sample. The core sample becomes saturated with the methanol vapour and the re-condensed methanol fills up the Thimble till it reaches the liquid level within the Soxhlet tube to the top of siphon tube arrangement, the liquid within the Soxhlet tube automatically drains itself by siphon effect and flow into the Pyrex flask containing the boiling toluene.

This process allows the methanol to clean any organic fluid within the core sample in a reflux state. The process could continue for 48 hours for a thorough cleaning. A moderate temperature was permitted so that the methanol will not boil off.
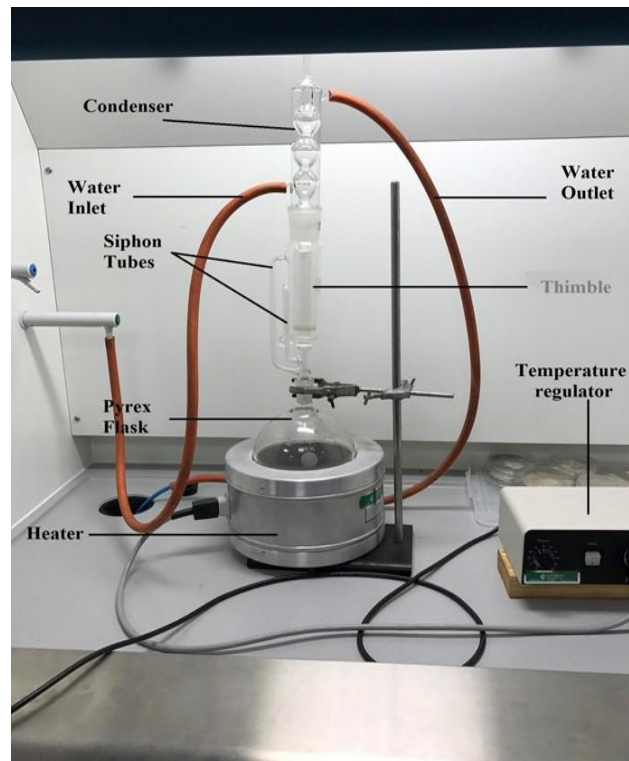
Figure 3.8: Soxhlet Extraction Apparatus

3.4.1.2. Dimensional Analysis of the Core Samples

Table 3.1 shows the dimensional analysis and petrophysical properties of the sandstone core samples, reported by the supplier (Kocurek Industries Inc. in USA), as well as their corresponding images.

Table 3.2: Dimensions and Petrophysical Properties of the Core samples

	Diameter [mm]	Length [mm]	Ref. Porosity [%]	Ref. Permeability [mD]	
Bentheimer (BEN)	25.49	76.23	23 – 26	1500 – 3500	
Salt Wash North (SWN)	25.26	75.62	20 – 22	440 – 800	
Grey Berea (GB)	25.22	76.27	19 – 20	200 – 315	

3.4.2. Petrophysical Measurement

3.4.2.1. Porosity Determination

Porosity is a measure of the capacity of reservoir rocks to contain or store fluids. The fluids stored in the pore spaces within the reservoir rocks could be gas, oil, and water. High porosity values indicate high capacities of the reservoir rocks to contain these fluids, while low porosity values indicate the opposite. The porosity determines the capacity or void of a core sample which translates to how much hydrocarbon is stored within the pore spaces of the core sample. It can simulate the original gas in place for efficiency determination during the core flooding experiments. Basically, two methods (helium porosimetry and saturation method) are employed to evaluate the porosity parameter for consistency.

3.4.2.1.1. Helium Porosimetry

This method enables the determination of the rock core porosity by using the grain volume of the core sample which is the volume of the rock grains or solids alone without the voids enclosed therein. The pore volume is determined from the difference between the grain volume obtained by this method and the bulk volume which is defined as the total physical volume the sample occupies in space. The "Bulk Volume" is determined empirically through measuring the dimension of the core samples and thus evaluating the total volume from analytical measurements, in this case using the volume of a cylinder.

$$\text{Pore Volume} = \text{Bulk Volume} - \text{Grain Volume}$$

(3.2)

$$\text{Porosity} (\%) = \frac{\text{Pore Volume}}{\text{Bulk Volume}} \times 100$$

Bulk Volume

With the dimensional analysis of the core samples and by knowing the core diameter (d) and the core total length (L), the bulk volume can be found as:

$$\text{Bulk Volume} = \frac{\pi d^2}{4} \times L \qquad (3.3)$$

Helium is the expanding gas used in this study because it is an inert gas and it will not have any rock-fluid interactions that may alter the morphology of the sample being analysed. Also, helium has a high diffusivity and therefore will measure porosity very accurately.

__Grain Volume:__

Grain volume of the corresponding core samples can be obtained by using the Helium Porosimeter (PORG-200TM) as shown in Figure 3.9. The apparatus consists of a 'Matrix cup' used to hold the core sample. There is a set of steel disks used to fill the cup for calibration purposes and a thermometer to measure the temperature.

(a)
(b)
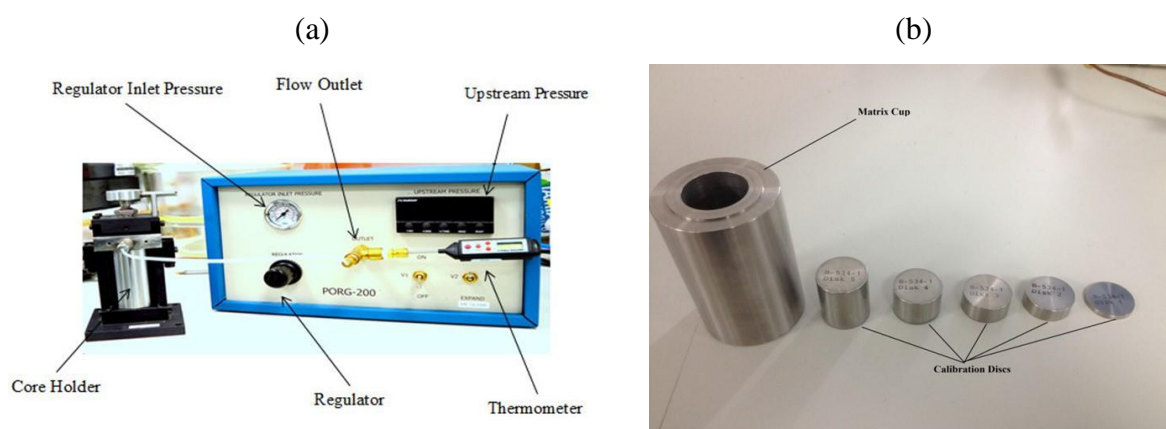
Figure 3.9: (a) Helium Porosimeter, (b) Calibration Disks and Matrix Cup

The apparatus provides measurements by utilising Boyle's Law which states that the volume of an ideal gas is inversely proportional to the pressure at a fixed temperature. The porosimeter uses helium that is supplied to the apparatus using a cylindrical gas canister. The equipment has two volume chambers or cells termed the reference cell and the sample chamber. The reference cell has a fixed volume V_1 at a regulated pressure between 90 to 95 psig and the sample chamber V_2 which is of an unknown volume at normal atmospheric pressure. The helium gas was first introduced into the reference cell then expanded into the sample cell of unknown volume, and it was allowed to stabilise all through the chambers. Then P_1 and P_2 were recorded, and the unknown volume V_2 which is the grain volume was determined with the application of Boyle's law. From ideal gas law.

$$\frac{P_1 V_1}{T_1} = \frac{P_2 V_2}{T_2}$$

(3.4)

Where, P_1 is the initial absolute pressure, V_1 is the initial volume, T_1 is the initial absolute temperature, P_2 is the expanded absolute pressure, V_2 is the expanded volume, and T_2 is the expanded absolute temperature.

The reference volume is always pressurised to about 90 psig and expanded into a Matrix Cup or sample holder containing the sample to be analysed. The second pressure is read and used to compute the unknown volume. The equation below shows how the grain volume is determined.

$$V_g = V_c - V_r \left(\frac{P_1 - P_2}{P_2 - P_a}\right) + V_y \left(\frac{P_2}{P_2 - P_a}\right)$$

(3.5)

Where, V_g is the Grain Volume, V_c is the Sample Chamber Volume, V_r is the Reference Chamber Volume, V_y is the Valve Displacement Volume, and P_a is the Absolute atmospheric Pressure Initially in Sample Chamber.

- *Procedure for Grain Volume Measurement*

  Before any tests, it is pertinent to conduct pressure testing to ensure that the system is leak tight. To achieve this, the system was powered on for about thirty minutes to stabilise and ensure that the pressure transducer reaches equilibrium. Then the helium gas supply was connected to the helium inlet port of the instrument and was set to 120 psig on the Helium gas bottle regulator. After the leak test, the system grain volume calibration was performed on the Porosimeter. The matrix cup with reference disks was connected to the instrument. Valve V_2 was switched to vent and valve V_1 was switched to ON. Then the regulator was set to 90 psig as the reference pressure P_1; the valve V_1 was switched to OFF and valve V_2 to EXPAND position to equilibrate the pressure in the chamber till a pressure drop was stabilised and a reading was taken as expanded pressure P_2. This was done for all the calibration disks. Subsequently, the sample grain volume measurement was performed with the same procedure used for the system grain volume calibration. The obtained results for both calibrations were recorded in the provided application written in an excel spreadsheet to calculate the grain volume of each sample (as shown in Figure 3.10). It is of immense importance to note that the

matrix cup used with the PORG-200TM should always be kept clean and the presence of dirt will adversely affect the accuracy of data.

Figure 3.10: Excel Spreadsheet for Porosity Determination using Helium Porosimeter

3.4.2.1.2. Saturation Method for Porosity Determination

The main apparatus needed in this method is a precision balance. Other apparatus that would be needed is a wetting fluid. The wetting fluid may be used to saturate the core in two different ways; it can either be used to simply soak the core sample by placing the core into a beaker of the fluid, or it can saturate the core using a vacuum pump (see Figure 3.11). Both methods are effective, yet the latter is quicker than the former.

First, the core sample needs to be cleaned and dried completely. Subsequently, the weight of the dry sample (W_{dry}) needs to be measured. It should be noted that by knowing the dimensions of the core sample, the bulk volume (V_{bulk}) can be easily calculated (as described in Section 3.4.2.1.1). Finally, the core sample should be completely saturated by putting the sample in the beaker (filled by the brine to simulate the reservoir condition) and using a vacuum pump. The weight of the saturated core sample (W_{sat}) also needs to be recorded. Since the density of the brine solution is known (described in Section 3.3.1), the volume of the liquids trapped in the core sample pores can be identified.

Figure 3.11: Vacuum Pump for Saturation Method

3.4.2.2. Permeability Measurement

Permeability is a property of a porous medium which is a measure of the ability of a porous medium to transmit fluid. The permeability determination for the core sample selected for this research was determined using a core flooding setup. The fluid properties obtained from the experimental setup as well as the operating variables such as differential pressure, flow rate, dimension of the samples were used to calculate absolute gas permeability of the core samples. The operating principle of the equipment setup was based on Darcy's law.

$$Q = \frac{KA(P_1 - P_2)}{\mu L} \tag{3.6}$$

Where, "K" is the permeability parameter (Darcies), "μ" is the fluid viscosity (cP), "Q" is the flow rate (cc/sec), "L" is the length of the core sample or the length that the liquid flows (cm), "A" is the cross-section area of the core sample or the area that liquid flows (cm^2), "P_1" is the upstream pressure (atm), "P_2" is the downstream pressure (atm). By rearranging the Darcy's Law, and changing the units of permeability (k) to millidarcies and pressure (P_1 and P_2) to psig, Equation 3.7 can be achieved as follow:

$$K = \frac{14500 \times V\mu L}{\Delta P \times A \times t} \tag{3.7}$$

Where, "K" is the permeability parameter (millidarcies, mD), "μ" is the fluid viscosity (cP), "V" is the flow volume (ml), "L" is the length of the core sample or the length that the liquid flows (cm), "A" is the cross-section area of the core sample or the area that liquid flows (cm^2), "ΔP" is the differential pressure between upstream and downstream of the flow (psig), "t" is the time of the flow (sec).

Darcy experimentally defined fluid flow in porous media as being proportional to the differential pressure per unit length [110]. Thus, Darcy's formula to obtained permeability can be expressed as:

$$K = 2000 \times \frac{L}{A} \times Q \times \frac{P_{atm}}{(P_2^2 - P_1^2)} = 2000 \times \frac{L}{A} \times \mu \times \frac{\Delta V}{\Delta t} \times \frac{P_{atm}}{(P_2^2 - P_1^2)} \qquad (3.8)$$

3.4.2.2.1. Core Flooding Experimentation

The PREL-300TM is a core flooding apparatus (shown in Figure 3.12) which is manually operated liquid or gas permeameter incorporating digital technology to yield accurate data for specific, effective, and relative permeability determinations by the unsteady-state method. The design incorporates safety, durability, and ease of operation into a compact, low-cost unit.
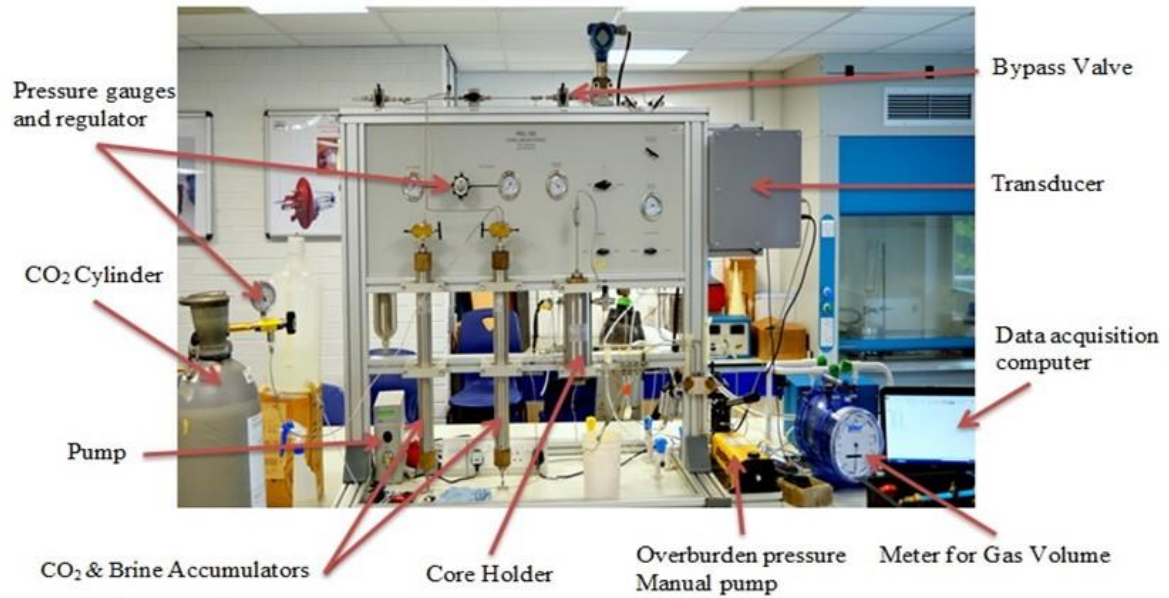
Figure 3.12: PREL-300TM Core Flooding Setup (Front and Back View)

The apparatus is made up of a core holder system with confining pressure, system pressure, and differential pressure controls. For fluid injection, a Lab Alliance pump is provided with

floating piston accumulators. It has a downstream flow system for applying back pressure and monitoring effluent volumes. The SmartFlood software forms an integral part of this system which interfaces PREL-300TM system and the computer data-acquisition-and-control system hardware. This provides on-screen display of all measure values such as temperature, pressure, volume, change in pressure, and automatic logging of test data to a computer data file. The schematic diagram of the experimental setup utilised in this study is shown in Figure 3.13.
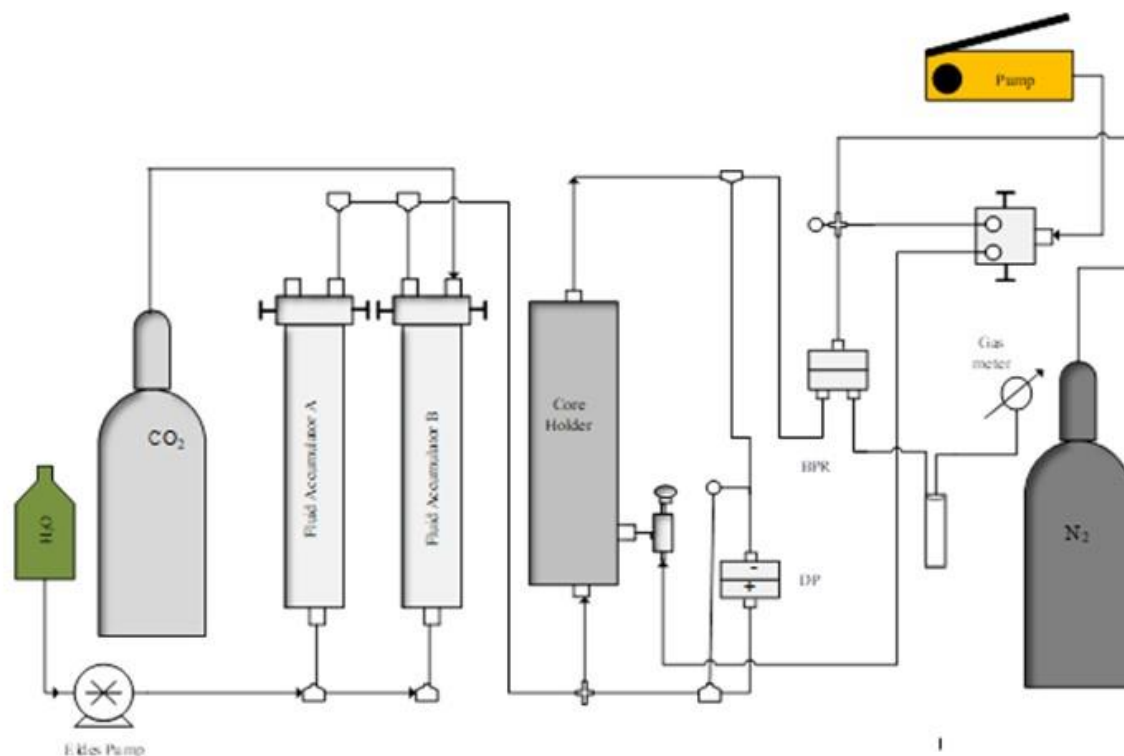
Figure 3.13: Schematics Diagram of the Experimental Setup for Core Flooding

The core flooding rig utilises several components and it will be described in an order of the experimental process (i.e., from upstream to downstream). The basic physical parameters of the core sample as shown in table 3.1 were measured after drying the core in an oven at 75 °C for 24 h to remove any trace of solvent and moisture present after cleaning with Soxhlet extraction. The sandstone core sample was then immersed in a vacuum chamber containing different brine concentrations (5, 10, 15, 20 and 25) for 24 hours. This was done to remove any entrapped air bubbles in the core sample. After undergoing external saturation with the desired brine, the core sample was then wrapped in heat shrink and aluminium (Figure 3.14) foil to prevent CO_2 permeation into the Viton sleeve before it was inserted into the Viton sleeve in

the core holder. When CO_2 permeates into the Viton sleeve, it causes damage that could lead to the bursting of the sleeve, thereby ruining the experiments.

  Figure 3.14: Core samples wrapping in cling film

Next, the same concentration of the brine used for the external saturation was injected into the core sample to ensure sufficient saturation. The dead volume excess brine was then evacuated to allow the test to be conducted using just the brine in the core sample.

To maintain the desired experimental temperature, the core holder was wrapped with a heat jacket and the temperature regulator was adjusted until a temperature of 45 °C was displayed on the SmartFlood software. Hydraulic oil (pressure medium) was pumped into the annulus of the core holder with the help of a hydraulic pump to provide the overburden pressure of 2500 psig. A pressurized liquid CO_2 cylinder was connected to "fluid accumulator B", with a capacity of 500 mL, and the back pressure (BPR) was set to 1500 psig to maintain the pressure at the operating condition of 1500 psig. The pressure decay test was carried out first, and this involves measuring the drop or decrease in pressure of CO_2 in an aqueous brine solution in the saturated core sample. To conduct the test, CO_2 was injected into the brine-saturated core sample by opening the Accumulator B delivery valve, and the pore pressure reduction (decay)

was recorded over a period until no more significant drop in pore pressure was observed. Equation 3.9 shows the calculation of the pressure decay rate.

$$\text{Pressure Decay Rate} \left(\frac{\text{psi}}{\text{min}}\right) = \frac{\text{initial injected pressure} - \text{final pressure}}{\text{time taken for the pressure change}} \quad (3.9)$$

After the equilibration of the system pressure, an Eldex pump was switched on to aid in applying pressure to the fluid (CO_2), thereby allowing it to flow into the core sample in the core holder. The injection rate for this work was adjusted to 3 mL/min and the recording, as well as the logging, of the pore pressure began. As CO_2 traverses the saturated core sample, the gas effluent was routed to the gas meter, which in turn accounted for the volume of effluent CO_2 collected. An air-tight measuring cylinder with a laboratory rubber stopper was placed at the downstream core holder and the upstream gas meter. The brine displaced by the CO_2 was collected by this measuring cylinder while maintaining an air-tight passageway for the CO_2 to enter the gas meter to accurately measure the gas effluent. Therefore, the brine saturation can be evaluated by using Equation 3.10.

$$\text{Brine Saturation (\%)} = \left(1 - \frac{\text{Volume of Water Collected}}{\text{Core Sample Pore Volume}}\right) \times 100 \quad (3.10)$$

In this experimental setup, the pressure measurement was achievable via pressure gauges and a transducer (with accuracy of 0.01%). The overburden pressure and the backpressure were measured using pressure gauges, while the upstream pressure and differential pressure were measured through a pressure transducer. After measuring the volume of the CO_2 effluent and water collected, the core flooding rig was depressurized, and the core sample was removed from the core holder. The sample was dried, and changes in porosity were assessed as well as the permeability reduction. The experiments were repeated for different brine types and concentrations while the other parameters were kept constant. The core sample was thoroughly cleansed by Soxhlet extraction for 48 hr using methanol heated to 70 °C. A moderate temperature was permitted so that the methanol did not boil off. Thereafter, the core was subjected to testing for porosity and permeability before using it for another core flooding experiment. Evaluation of the porosity was to ensure that there were no salt deposits in the respective core samples.

Precautionary Measures during Core Flooding

To proceed with the core flooding experiment, the following precautionary measures must be taken into consideration:

- 500ml of brine is poured into fluid accumulator A if the core sample is not saturated externally with the desired brine.

- A substantial amount of liquid CO_2 is supplied into fluid accumulator and noting that the CO_2 does not continuously supply the fluid accumulator.

- The backpressure regulator is supplied with Nitrogen gas at 1500 psig, and also noting that the Nitrogen does not continuously supply the backpressure regulator.

- The sample core is secured into the core holder.

- The overburden pressure is applied to the core holder within the acceptable UCS range.

- The data acquisition computer is fully connected to the transducer and has the software setup and open to use Figure 3.15.

- The Eldex pump is switched on and connected to the computer Once all preparations have been made, the experiment can commence.
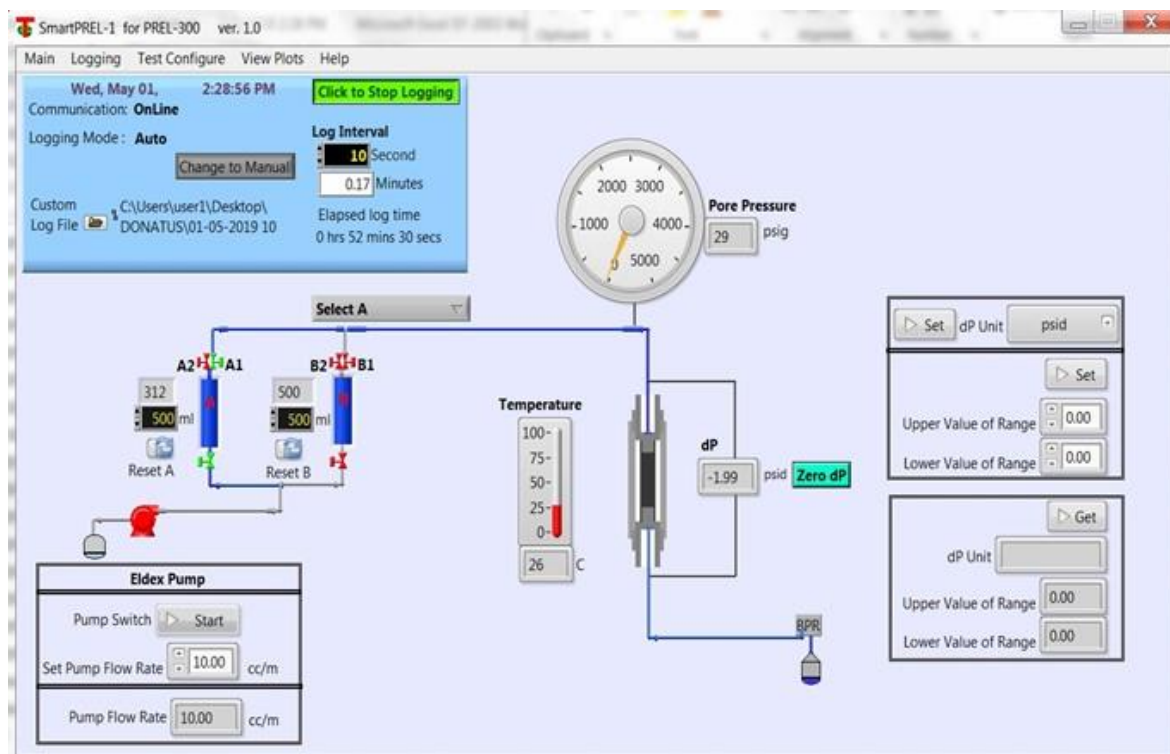
Figure 3.15: PREL-300 data acquisition software

The drum-type gas meter is observed for the first sign of CO_2 exiting the saturated core. Once the first sign of gas exiting arrives, a separate data log is produced to measure the volume of gas exiting at 5-minute intervals. The experiment then comes to an end when the amount of CO_2 in the fluid accumulator finishes, resulting to the gas meter no longer collecting any volume of gas. Thus, when the floating piston has reached its limit, the water pumped by the Eldex pump will overflow at the bypass valve. At this point, the logging of the data was stopped. Data was recorded to an excel spreadsheet in the computer. The data file is organized in two parts. These are file header and experiment data, which are the measurements and calculations in the experiment (Figure 3.16).

Figure 3.16: Data file structure

Remediation Experimental Procedure

The basic physical parameters of the core sample were measured after drying the core in an oven at 75 °C for 24 hours to remove any trace of solvent and moisture present after cleaning with Soxhlet extraction. The sandstone core samples, (Bentheimer, Salt Wash North, Idaho Gray) were then immersed in a vacuum chamber containing 20 wt.% brine prepared from four different salts for 24 hours under vacuum. This was done to remove any entrapped air bubbles in the core sample. The core sample after undergoing external saturation with the desired brine

was then wrapped in heat shrink and Aluminium foil to prevent CO_2 permeation into the viton sleeve before it was inserted into the Viton sleeve in the core holder. When CO_2 permeates into the viton sleeve, it causes damages that could lead to bursting of the sleeve and ruining the experiments. Then the same concentration of the brine used for external saturation was then injected into the core sample to ensure sufficient saturation. The dead volume excess brine was then evacuated to allow the test to be conducted using just the brine in the core sample.

To maintain the desired experimental temperature, the core holder was wrapped with a heat jacket and the temperature regulator was adjusted until a temperature of 45 °C was displayed on a SmartFlood software. Hydraulic oil (pressure medium) was pumped into the annulus of the core holder with the help of a hydraulic pump to provide the overburden of 2500 psig. This overburden pressure is necessary for the experiment to provide enough pressure differential between the pore pressure and the overburden pressure, thus avoiding a negative drawdown. A pressurized liquid CO_2 cylinder was connected to fluid accumulator B, with the 500 ml capacity, and the back pressure regulator (BPR) was set to 1500 psig.

To conduct remediation test, CO_2 was injected into the brine saturated core sample by opening Accumulator B delivery valve. Eldex pump was switched-on to aid in applying pressure to the fluid (CO_2), thereby flowing into the core holder. The injection rate for this work was adjusted to 3 ml/min and the recording as well as logging of the pore pressure began. As CO_2 traverses the saturated core sample, the gas effluent was routed to the gas meter which in turns accounted for the volume of effluent CO_2 collected. An air-tight measuring cylinder with laboratory rubber stopper was placed at the downstream core holder and the upstream gas meter. The brine displaced by CO_2 was collected by this measuring cylinder while maintaining and air-tight passageway for the CO_2 to enter the gas meter to accurately measure the gas effluent.

After precipitation of salt in the core sample, accumulator B valve was shut down in order to cut off the supply of CO_2 into the core sample. At this juncture, accumulator A valve was opened to inject remediation fluid into already precipitated core sample to improve CO_2 injectivity and permeability. Remediation fluids use in this work are low salinity brine: 0 wt.% (distilled water), 0.5 wt.%, and 3.5 wt.% (sea water) respectively. The slug size was maintained by injecting 20% of pore volume of each core sample with the remediation fluids. After injection of the so called the remediation fluids, accumulator valve A was closed, and accumulator valve B was opened thereby injecting more CO_2 gas into the core sample. This phenomenon can also be expressed as water (brine) alternating gas injection.

In this experimental setup, pressure measurement was achievable through pressure gauges and transducer. The overburden pressure and the back pressure were measured using pressure

gauges while upstream pressure and differential pressure were measured through pressure transducer. The volume of CO_2 effluent exiting after remediation fluid was measured and the experimental runs were ended when the value of differential pressure is constant. At this point, the core flooding rig was depressurized, and the core sample was removed from the core holder. The sample was dried and changes in porosity as well as permeability were assessed after core flooding and remediation tests. The experiments were repeated for different core samples and remediation fluids while other parameters were kept constant. The core sample was subjected to cleaning by Soxhlet extraction for 48 hours using methanol heated to 70 °C. A mild temperature was used in order to avoid methanol boils off. Thereafter, the core sample was subjected to Porosity and permeability tests before using it for another core flooding experiment. This was to be ensured that, there were no salt deposits in the core samples.

3.4.3. Errors and Accuracy

The system is rated to 3,500 psig pore pressure, and 5,000 psig confining pressure at ambient temperature. A pump system with a flow rate range adjustable from 0 to 200 ml/min and a maximum pressure rating of 3,750 psig. Floating-piston accumulators are provided as part of the system and are rated for 5,000 psig pressure and 350 °F (177 °C) temperature.

3.5. Phase-III: Qualitative Analysis

The core samples (Bentheimer-BEN, Salt Wash North-SWN, Idaho Gray-IDG) were examined using the FEI Quanta FEG 250 FEG high-resolution Scanning Electron Microscope (SEM) interfaced to EDAX Energy Dispersive X-ray Analysis (EDX) as shown in Figure 3.17

Figure 3.17: FEI Quanta FEG250 SEM

Sample preparation involved fixing the cut core samples onto standard SEM stubs using rapid setting Araldite. The small pieces approximately 1 cm x 1 cm x 0.5 cm were cut from the core plugs with a diamond-edged saw for imaging. A small area of the edge of the core sample was painted with a thin line of silver adhesive to help conduction from the surface to the sample stub. The samples were then coated with 10nm of platinum/palladium using the Cressington 208 sputter coating unit.

Analysis of the samples involved obtaining SEM micrographs from different regions of the cut face of the core sample using system magnifications of 100x and 200x respectively. In total, 3 separate areas were chosen from each sample. The chosen detection system for the analysis was Back Scattered Electron Detection (BSED), which is effective in showing differences in atomic number based on contrast variation.

More so, due to the extremely complex nature of finding the existence of the different salts within the pores of the core sample, it was decided to utilise EDX mapping. This technique allows the distribution of the different salts across the cut face to be observed. Without the use of EDX mapping, it would be extremely time consuming to examine every pore with the hope of identifying an area of precipitated salt.

Thus, this chapter which is based on experimental setup will lead to the next chapter which is the experimental results and discussion of the results.

Chapter 4: Results and Discussions

4.1. Overview

This research centred on the investigation of salt precipitation during CO_2 storage in deep saline aquifer as well as the possible remediation strategies. This research brings about the concept of the formation of precipitation during sequestration of CO_2 extracted from the atmosphere. In this work, the injection of CO_2 is carried out in the laboratory to investigate experimentally the various conditions that are responsible for salt precipitation as well as the possible remediation strategies. This study has generated data in which a convenient operating condition can be chosen for the storage of CO_2 and thereby limiting high rate of salt precipitation.

4.2. Phase-I: Brine Sample Preparation

4.2.1. Salinity, Viscosity, and Density

The brine was prepared by dissolving desired amount of salt ($NaCl$, KCl, $CaCl_2$, and $MgCl_2$) into distilled water at concentration of 5, 10, 15, 20, and 25 wt.% respectively. A magnetic stirrer was used to stir the brine vigorously to ensured proper mixing before saturation of the core samples. Table 4.1 shows the viscosity and density measurements for each brine concentration.

Table 4.1: Measurements of Brine Viscosity and Density at Different Concentrations

Brine Salinity (%)	Viscosity (cP)	Density (ppg)	Specific gravity
5	0.6	8.35	1.00
10	0.9	8.41	1.01
15	1.1	8.45	1.01
20	1.4	8.50	1.02
25	2.1	8.57	1.025

4.2.2. Interfacial Tension (IFT) between the CO_2 and the brine

Several investigations have been carried out to measure the interfacial tension in CO_2-brine systems under different conditions, as described before in Section 3.3.1.4, and the relationship between the interfacial tension and solubility is underlined. These investigations have revealed that the forces that occur at the interfaces of two interacting phases or fluids are a function of the fluids system's densities, temperatures, and pressures. There is also mass transfer between the phases in contact, which can be related to the solubility of one fluid species in another. This

bubble measurement was repeated for three bubbles in each experiment to ensure repeatability and the reliability of the recorded data, and the IFT measurement was performed on each bubble picture produced.

The rising bubble technique was used to measure the experimental fluid-fluid IFT. This approach takes advantage of the buoyancy of the gas bubble in relation to the brine employed, allowing it to rise through the denser fluid. The IFT measurement is analysed using the Young-Laplace Equations (see Equations 2.2 and 2.3) to determine the profile of the gas bubble in the brine generated in the IFT cell. To monitor the development and collapse of the bubble created, the IFT was first measured when the external phase (brine) was not saturated with the drop phase (CO_2). Table 4.2 shows the results for all the test fluids when IFT measurements were conducted continuously.

Table 4.2: IFT measurement (mN/m) of CO_2 at 45 °C with distilled water (0 % salinity)

Time (sec)	Run #1 (450 psig)	Run #2 (447 psig)	Run #3 (441 psig)
0	0.81	0.81	0.83
1	0.81	0.81	0.83
2	0.81	0.81	0.83
3	0.81	0.81	0.83
4	0.81	0.81	0.83
5	0.81	0.81	0.83
6	0.81	0.81	0.83
7	0.81	0.81	0.83
8	0.81	0.81	0.83
9	0.81	0.81	0.83
Average	**0.81**	**0.81**	**0.83**

Table 4.3: IFT measurement (mN/m) of CO_2 at 45 °C with 5% brine concentration (NaCl)

Time (sec)	Run #1 (513 psig)	Run #2 (509 psig)	Run #3 (505 psig)
0	1.28	1.33	1.36
1	1.28	1.33	1.35
2	1.28	1.33	1.35
3	1.28	1.33	1.36
4	1.28	1.33	1.36
5	1.28	1.33	1.36
6	1.28	1.33	1.36
7	1.29	1.33	1.36
8	1.29	1.34	1.35
9	1.29	1.33	1.36
Average	**1.28**	**1.33**	**1.36**

Table 4.4: IFT measurement (mN/m) of CO_2 at 45 °C with 10% brine concentration (NaCl)

Time (sec)	Run #1 (564 psig)	Run #2 (559 psig)	Run #3 (554 psig)
0	1.33	1.35	1.36
1	1.33	1.35	1.36
2	1.33	1.35	1.36
3	1.33	1.35	1.36
4	1.33	1.34	1.36
5	1.33	1.35	1.37
6	1.33	1.35	1.37
7	1.33	1.35	1.37
8	1.33	1.34	1.37
9	1.33	1.35	1.37
Average	**1.33**	**1.35**	**1.37**

Table 4.5: IFT measurement (mN/m) of CO_2 at 45 °C with 15% brine concentration (NaCl)

Time (sec)	Run #1 (522 psig)	Run #2 (516 psig)	Run #3 (505 psig)
0	2.08	2.06	2.20
1	2.08	2.06	2.21
2	2.08	2.06	2.20
3	2.08	2.06	2.20
4	2.08	2.06	2.20
5	2.08	2.06	2.20
6	2.08	2.05	2.21
7	2.08	2.05	2.20
8	2.07	2.06	2.20
9	2.07	2.06	2.20
Average	**2.08**	**2.06**	**2.20**

Table 4.6: IFT measurement (mN/m) of CO_2 at 45 °C with 20% brine concentration (NaCl)

Time (sec)	Run #1 (525 psig)	Run #2 (520 psig)	Run #3 (516 psig)
0	2.18	2.29	2.35
1	2.18	2.29	2.36
2	2.18	2.29	2.35
3	2.18	2.29	2.35
4	2.18	2.30	2.36
5	2.18	2.30	2.36
6	2.19	2.30	2.36
7	2.19	2.30	2.36
8	2.19	2.30	2.36
9	2.20	2.30	2.36
Average	**2.19**	**2.30**	**2.36**

Table 4.7: IFT measurement (mN/m) of CO_2 at 45 °C with 25% brine concentration (NaCl)

Time (sec)	Run #1 (450 psig)	Run #2 (442 psig)	Run #3 (441 psig)
0	2.42	2.48	2.44
1	2.43	2.49	2.45
2	2.43	2.47	2.44
3	2.44	2.47	2.44
4	2.42	2.49	2.45
5	2.43	2.49	2.45
6	2.44	2.50	2.45
7	2.44	2.50	2.45
8	2.44	2.50	2.46
9	2.45	2.51	2.46
Average	**2.19**	**2.49**	**2.45**

Figure 4.1 shows typically the CO_2 gas bubble in distilled water as well as the gas bubble in the different brine solutions. It was observed that the rate of reduction or shrinkage of the gas bubble is more pronounced in the distilled water as compared to brine when the system is left for a few seconds without any interruption. Thus, the rate of shrinkage of the CO_2 gas in brine decreased as the salinity of the brine increased. Also, it could be observed that, there is virtually no difference in the figures shown in Figure 4.1 but the shrinkage and dissolution of CO_2 in the brine solution was predominant in distilled water as compared to 5 wt.% brine. Thus, the rate of dissolution of CO_2 in brine decreases as the brine concentration increases.
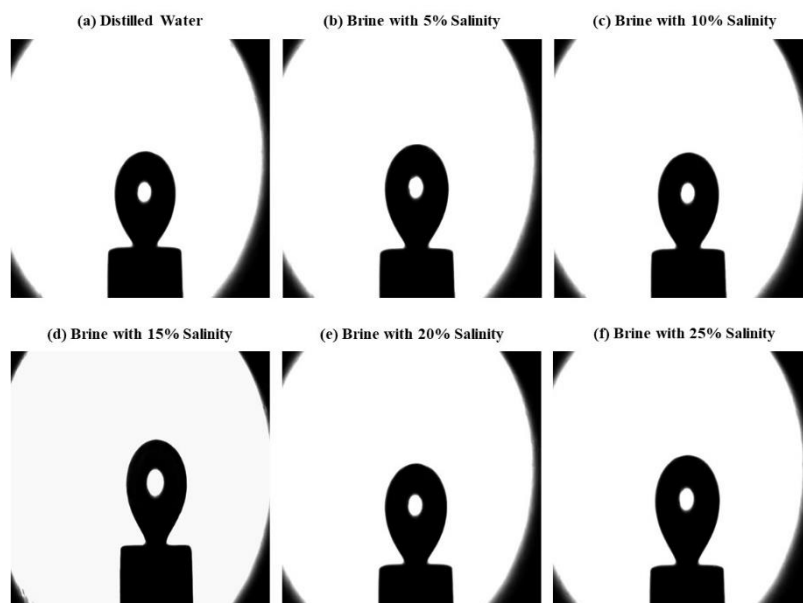
Figure 4.1: Typical images of CO_2 bubble in distilled water and different brine solution (5 to 25 Wt.%)

The rate of mass transfer at the interface between the gas bubbles and the brine phase in the cell was a clear indicator of bubble shrinkage. As a result, IFT fell significantly in the distilled water, explaining the observed shrinkage. However, when the salinity was increased to 5 wt.%, the IFT rate declined at a slower rate, and it was even slower at 25 wt.% brine. This reaffirms that the higher the salinity of the brine the lower the gas solubility.

Other authors have extensively addressed the variation of IFT with salinity, and they have all agreed that IFT increases with salinity or the molality of salt and always exceeds that of salt-free water under the same conditions [89, 99, 111, 112]. We also attempted to explore the association between IFT and NaCl brine at various concentrations, and the result is graphically shown in Figure 4.2.
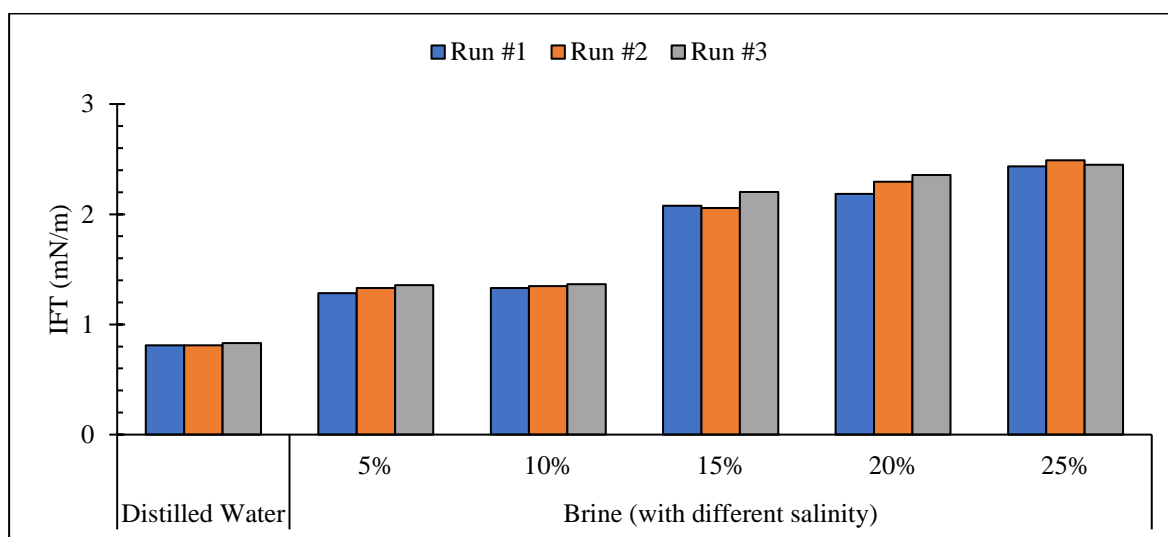
Figure 4.2: IFT measurement for CO_2 and brine at 45 °C and different concentrations of NaCl

Furthermore, assuming pressure was increased to a specific point at fixed temperature (45 °C), IFT will hit a plateau, but the plateau rose with temperature and NaCl molality. Solubility of CO_2 in brine, which was earlier discussed in this Chapter, on the other hand, can explain IFT variations with temperature and salinity indirectly. A rise in temperature or salinity can produce a decrease in aqueous phase solubility, resulting in an increase in IFT. Moreover, based on literature [100-103], it was found that IFT generally decreased with increasing pressure (or vice versa) and increased with increasing temperature and NaCl molality, as shown in Figure 4.2. As a result of the preceding discussion, gases had the highest interfacial tension in the brine with the highest salinity and the lowest interfacial tension value in distilled water. This explains

why more CO_2 appeared to collect during the test with distilled water versus the run with different salt concentration (5 wt.% or higher).

4.3. Phase-II: Quantitative Analysis

The experiments carried out in this research work will highlighted and discussed in conformity with the experimental procedure discussed earlier on in chapter 3. The sandstone core samples were subjected to thorough cleaning with methanol, dried in an oven at 100 °C temperature for 12 hours before determination of the petrophysical properties of the core samples. These sandstones are:

- Bentheimer (BEN)
- Salt Wash North (SWN)
- Grey Berea (GB)

The results obtained from the core samples characterisation include porosity and permeability measurements of the different core samples from the different techniques highlighted in Chapter 3. The results are presented in the next section.

4.3.1. Characterisation of the Core Samples – Before Saturation with Brine (DRY)
4.3.1.1. Porosity

This section deals with one of the most important reservoir parameters known as porosity. The methods used in determining this property include (i) Helium gas porosimetry and (ii) saturation methods. Each method has its own distinctiveness and the results obtained are compared in order to recognise the preciseness of each method used in this research.

Helium Gas Porosimetry

The grain volume (V_g) of the core samples were measured by using the helium gas porosimetry as shown in Table 4.8 and using Equation 3.5.

Table 4.8: Grain Volume Determination using Helium Gas Porosimetry

	Bentheirmer (BEN)	Salt Wash North (SWN)	Grey Berea (GB)
Upstream Pressure, P_1 [psig]	92.500	90.027	90.069
Downstream Pressure, P_2 [psig]	25.150	26.237	24.947
Grain Volume, V_g [ml]	29.790	31.313	30.181

By knowing the physical dimensions of the core samples (shown in Table 3.1) and using the Equation 3.3, the bulk volume (V_b) of each core samples can be calculated. Subsequently the pore volume (V_p) of each core sample and the porosity can be obtained by using Equation 3.2 as shown in Table 4.8.

Table 4.8: Porosity Determination Results from using Helium Porosimetry

	Bentheirmer (BEN)	Salt Wash North (SWN)	Grey Berea (GB)
Dimensions, Dia. [cm] x Length [cm]	2.549 x 7.623	2.526 x 7.562	2.522 x 7.627
Bulk Volume, V_b [cm^3]	38.893	37.9	38.106
Grain Volume, V_g [cm^3]	29.790	29.736	30.181
Pore Volume, V_p [cm^3]	9.103	8.165	7.925
Porosity (%)	23.41	21.54	20.78

__Saturation Method__

In this method of porosity determination, the weight of the dry core samples was measured before saturation. Subsequently, under the vacuum condition, distilled water passed through the core samples and the weight of the core sample was measured every 30 minutes until it gets stabilise. This implied that saturation limit of the core sample was reached, and it is technically wise to presumed that the core samples were 100% saturated with distilled water. The weight difference between the dry and saturated sample was then calculated, and by knowing the density of the distilled water (about 0.998 g/ml), the pore volume and the porosity can be calculated. These have been shown in Table 4.9.

Table 4.9: Porosity Determination Results by using Saturation Method

	Bentheirmer (BEN)	Salt Wash North (SWN)	Grey Berea (GB)
Dry Weight, W_{dry} [g]	80.09	81.52	80.10
Saturated Weight, W_{sat} [g]	85.40	88.08	85.44
Pore Volume, V_p [ml]	5.32	6.57	5.35
Bulk Volume, V_b [ml]	38.90	37.90	38.10
Porosity (%)	13.7	17.3	14.0

In summary, Table 4.10 shows the comparison of the porosity measurement by two different methods compared to the reference porosity reported by the supplier.

Table 4.10: Comparison of Porosity Measurements from Two Different Methods

	Bentheirmer (BEN)	Salt Wash North (SWN)	Grey Berea (GB)
Reference Porosity (reported by supplier)	23 – 26	20 – 22	19 – 20
Porosity measured by Helium Gas Porosimetry	23.41	21.54	20.78
Porosity measured by Saturation Method	13.70	17.30	14.0

The measured porosity using helium porosimetry showed a tendency of closeness to value from the supplier as compared to the value of porosity obtained from liquid saturation method. More so, there is disparity in values obtained for pore volume in the different method used. This is attributed to the compressibility of gas. Since water is an incompressible fluid, the effective pore volumes are usually lower than gas which is a compressible fluid.

4.3.1.2. Permeability

Permeability is a measure of the fluid conductivity of any material (Porous media). Darcy investigated the flow of water through sand filters for water purification and through his observation and interpretation he came up with an equation called Darcy's equation as presented in Chapter 3, Equation 3.6. This equation is also applied in this research to determine each sample permeability. The viscosity of the flowing fluid (carbon dioxide) was evaluated as 0.0221 cP at the operating conditions (45 $^{\circ}$C temperature and 1500 psig pressure). This data was generated with the use of PVTsim-20.0 software and is presented in Appendix section. The laboratory measurement of the gas permeability for each of the core sample is presented in Table 4.11.

Table 4.11: Permeability Measurement of the Sandstone Core Samples (DRY Condition)

	Bentheirmer (BEN)	Salt Wash North (SWN)	Grey Berea (GB)
Measured Permeability, K [mD]	1967	620	293.8

The values for permeability determination for all the core samples were found to be within the given range of the individual permeability (see Table 4.12). The overburden pressure applied during the experiments was within the required specification (UCS) for each core sample. It exerts the required pressure on the sleeve around the core sample within the core holder and thereby preventing the simulated pore pressure build up from overpowering the sleeve enclosure. It is pertinent to state categorically that overburden pressure lowers the permeability

of the formation by either compressing the pore opening or interconnected pore channels of the pore structure. It is also important to note that, overburden pressure should be kept at least 200 psi higher than the flow pressure.

Table 4.12: Permeability Comparison of Core Samples Between the Measurement and Values Reported by the Supplier

	Bentheirmer (BEN)	Salt Wash North (SWN)	Grey Berea (GB)
Reference Permeability (reported by supplier)	1500 – 3500	440 – 800	200 – 315
Measured Permeability	1967	620	293.8

4.3.2. Characterisation of the Core Samples – After Saturation with Brines (Core Flooding)

Core flooding experiment can be conducted in different ways depending on the requirements of specific conditions and the interpretation methods available. In this work, a continuous core flooding test was considered at the expenses of interrupted core floods. Prior to core flood experiment, it is pertinent to determine the petrophysical properties of the core samples (as explained in Section 4.3.1). This will aid the experimental investigation to analyse the flow behaviour, CO_2 solubility based on the pressure decay, CO_2 stored or produced (collected), reduction in porosity and permeability variation of the core samples after flooding, for all salts and their concentration in the context of CO_2 storage and sequestration.

4.3.2.1. Flow Behaviour

The magnitude of differential pressure fluctuations and the duration of the drainage process were used to investigate the flow behaviour of CO_2 to determine the extent of supercritical CO_2 behaviour in relation to the kind and concentration of brine saturating the core sample. This is based on Darcian's discovery that fluid permeability to a porous medium is a function of differential pressure (dp).

Figure 4.3 exhibits differential pressure (dp) against time charts depicting the flow behaviour of supercritical CO_2 in several brines at 5% salt concentration for three different sandstone core samples tested in this study.
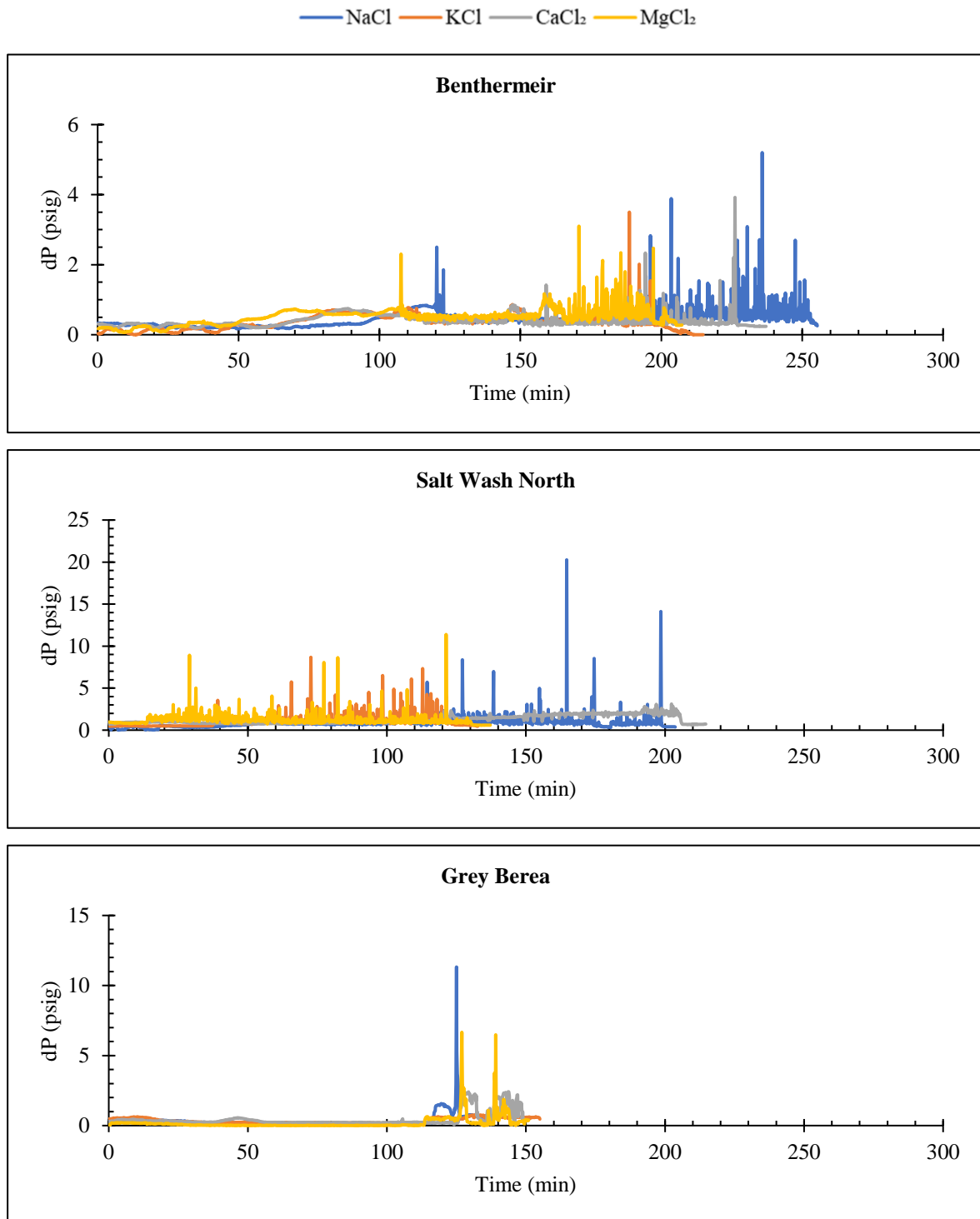
Figure 4.3: Flow Behaviour of different core samples at 5 wt.% salt concentration

For Bentheirmer, the first high fluctuation was noticed at 107 minutes, which corresponds to the CO_2 breakthrough for the $MgCl_2$. However, such a large variation in $CaCl_2$ and KCl was detected much later, when the CO_2 breakthrough occurred. When compared to other brines,

NaCl had the largest fluctuation of differential pressure. This implies that in the NaCl brine scenario, there was a continuous slug-type flow, which resulted in various variable pressure responses, and this sort of flow pattern is characterised by lighter, faster-moving, continuous fluid separated by relatively large gas pockets (gas bubbles). Due to the decreased density of the brine, which did not fully occupy the narrower pore spaces inside the pore matrix, the accessible mobile aqueous phase during the CO_2 injection provided the channel for this slug-like flow.

By looking at Salt Wash North, the early CO_2 breakthrough was observed in the core sample saturated with $MgCl_2$ brine followed by KCl, NaCl and $CaCl_2$ brine respectively. High fluctuation of CO_2 was observed immediately after the CO_2 breakthrough in $MgCl_2$, with NaCl having the highest fluctuation of differential pressure as compared to KCl and $CaCl_2$ systems respectively. This means that there was a continuous slug-type flow in the NaCl brine situation, which resulted in varied variable pressure responses, and this type of flow pattern is characterised by lighter, faster-moving, continuous fluid separated by relatively large gas pockets. Due to the decreased density of the brine, which did not fully occupy the narrower pore spaces inside the pore matrix, the accessible mobile aqueous phase during the CO_2 injection provided the channel for this slug-like flow.

Furthermore, the result obtained for the Grey Berea sample is quite different from the previous core samples. In this case, an early breakthrough of CO_2 was observed from the sample saturated with $CaCl_2$ then followed by NaCl while the late breakthrough was seen in KCl and $MgCl_2$ respectively. NaCl brine at this concentration (5 wt.%) was found to have the highest fluctuation of differential pressure as compared to other brines. As a result, the duration of CO_2 breakout in these core samples varies across all circumstances. This is due to the fact that each core sample has distinct linked pores, resulting in varying porosity and permeability.

Figure 4.4 shows differential pressure (dp) against time charts depicting the flow behaviour of supercritical CO_2 in several brines at 10% salt concentration for three different sandstone core samples.
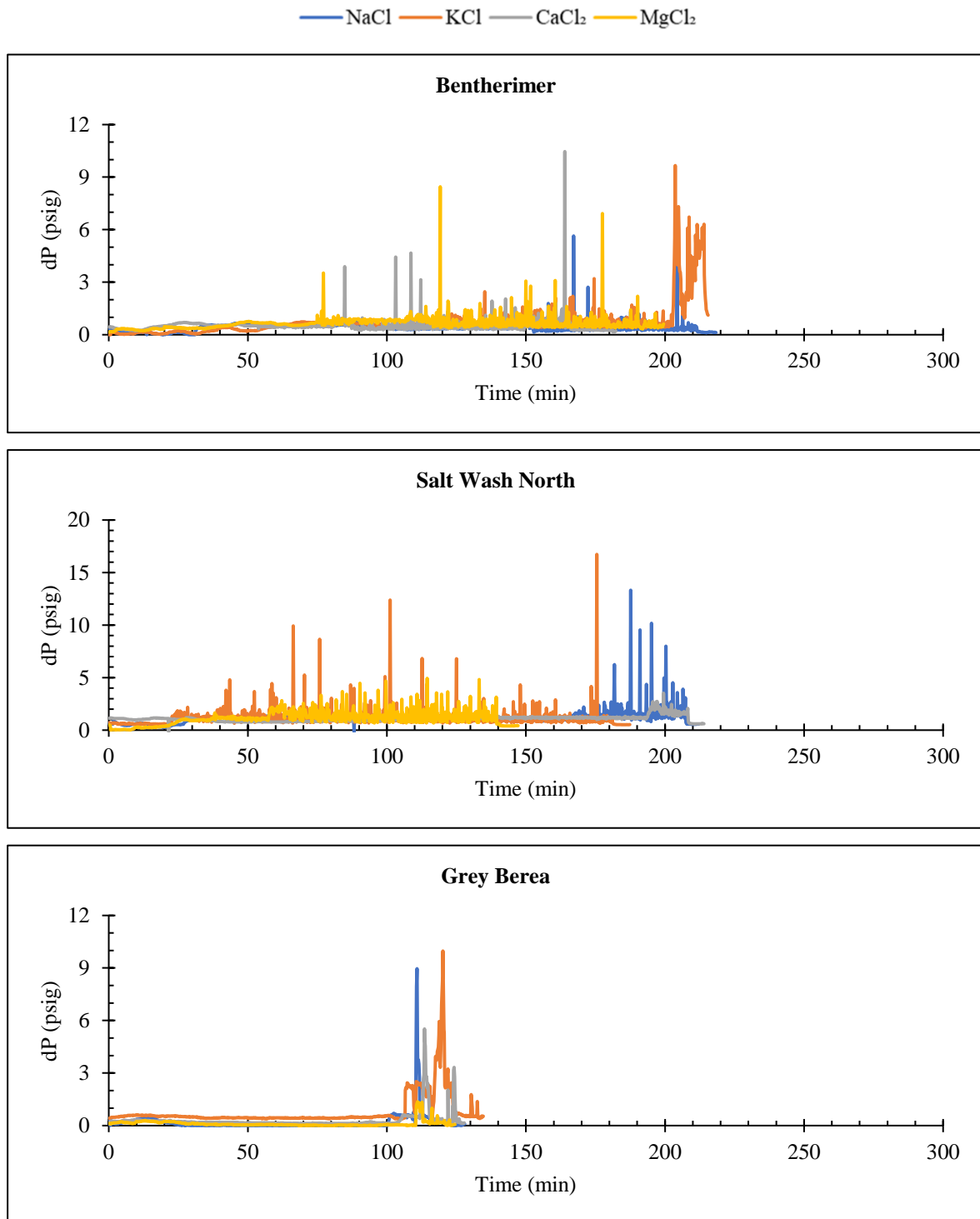
Figure 4.4: Flow Behaviour of different core samples at 10 wt.% salt concentration

As illustrated in Figure 4.4, for Bentheirmer core sample, there was an early CO_2 breakout in $CaCl_2$ and $MgCl_2$ divalent brines compared to NaCl and KCl brines. This was because of their proclivity for salting-out effects. At 10 wt.% concentration, both divalent salt solutions have

higher differential pressure fluctuations than the monovalent brine, even though the KCl brine had consistently higher fluctuations near the end of the run. At this concentration, the NaCl brine situation is quite stable, which could be due to CO_2 and brine streaming as a single unit. In the case of a significant differential pressure fluctuation observed in any brine scenario, the solubility can be assumed to be low due to greater capillary pressures inside the pore matrix, which is suggestive of relatively high interfacial tension between competing fluids. Due to the substantial oscillations in differential pressure that result in a slug fluid flow regime, the solubility of CO_2 in NaCl brine is significantly lower than in other brines with the same concentration (KCl, $MgCl_2$, and $CaCl_2$), as confirmed in the literature by Liu et al. [113]. Considerable solubility, on the other hand, is observed when the gas pocket is tiny, and the differential pressure is high. This is evident in the case of $MgCl_2$, where the dP increased continuously after 50 minutes, unlike in other brine conditions. This is due to the commencement of the drying-out action of the $MgCl_2$ brine, in which the CO_2 imbibes the moisture and so raises the viscosity of the now moisture-laden CO_2 plume. Similarly, before the 50-minute mark, the tendency was detected in the $CaCl_2$ brine. At this concentration, KCl displayed similar behaviour during the CO_2 injection, implying that CO_2 solubility is significant in the majority of the brines tested.

With regards to Salt Wash North, there was, also, an early breakthrough of CO_2 in KCl and $MgCl_2$ brine and subsequently followed by NaCl and $CaCl_2$ brines. In this case, slug flow regime was found to be predominant in the core sample initially saturated with KCl brine before flooding. Since it has highest differential pressure fluctuation, thus the solubility of CO_2 in this scenario can be stated to be low as a result of the higher capillary pressures within the pore matrix of the core sample. Conversely, the high solubility of CO_2 in any brine is observed when the gas pocket is relatively smaller and hence low fluctuation in differential pressure. NaCl and $CaCl_2$ exhibited low fluctuation of differential pressure until it gets towards the tail end of the experiment and thus creating room for high solubility of CO_2. The $MgCl_2$ scenario could not proceed more than 150 mins, and this could be attributed to the onset of the drying-out effect of the $MgCl_2$ brine, where the CO_2 imbibes the moisture and therefore increases the viscosity of the now moisture-laden CO_2 plume.

Regarding the Grey Berea, early breakthrough of CO_2 was obvious in monovalent brine as compared to divalent brine with a late breakthrough time. Monovalent brine also exhibited higher fluctuation of differential pressure when compared to divalent brine under the same experimental condition. The CO_2 flow behavioural pattern in Grey Berea is quite different from

other core samples with regard to the breakthrough time. This may be attributed to the low level of permeability of Grey Berea as compared to either Bentheimer or Salt wash north.

Figure 4.5 shows differential pressure (dp) against time charts depicting the flow behaviour of supercritical CO_2 in several brines at 15% salt concentration for three different sandstone core samples.

As it shows, $MgCl_2$ brine had the earliest CO_2 breakthrough, followed by NaCl, KCl, and $CaCl_2$ for Bentherimer core sample. This means that a significant amount of CO_2 was dissolved in the $CaCl_2$ brine, which had a late breakthrough time when compared to the other brines, with all experiments performed under the same conditions and with extremely good reproducibility. It is also worth noting that all brines with a concentration of 15% wt. showed different differential pressure fluctuation before and after breakthrough. This is due to a reduction in the pore volume of the core sample occupied by higher density brine within the core sample's pore matrix.

The earlier breakthrough of CO_2, for Salt Wash North, was observed in KCl brine, followed by $MgCl_2$, NaCl, and $CaCl_2$ respectively. This means that a significant amount of CO_2 was dissolved in the $CaCl_2$ brine, which had a late breakthrough time when compared to the other brines, with all experiments performed under the same conditions and with extremely good reproducibility. It is worth noting that KCl brine exhibited more differential pressure fluctuation after CO_2 breakthrough as compared to other brines. This is due to a reduction in the pore volume of the core sample occupied by higher density brine within the core sample's pore matrix.

For Grey Berea, there is a high level of differential pressure fluctuation in $MgCl_2$ when compared to other brines at this concentration (15 wt.%). The sandstone initially saturated with NaCl exhibited the longest breakthrough time and this indicated that a greater percentage of CO_2 had been dissolved in this concentration. Earlier breakthrough time of CO_2 was observed in $CaCl_2$ brine then followed by KCl brine respectively.
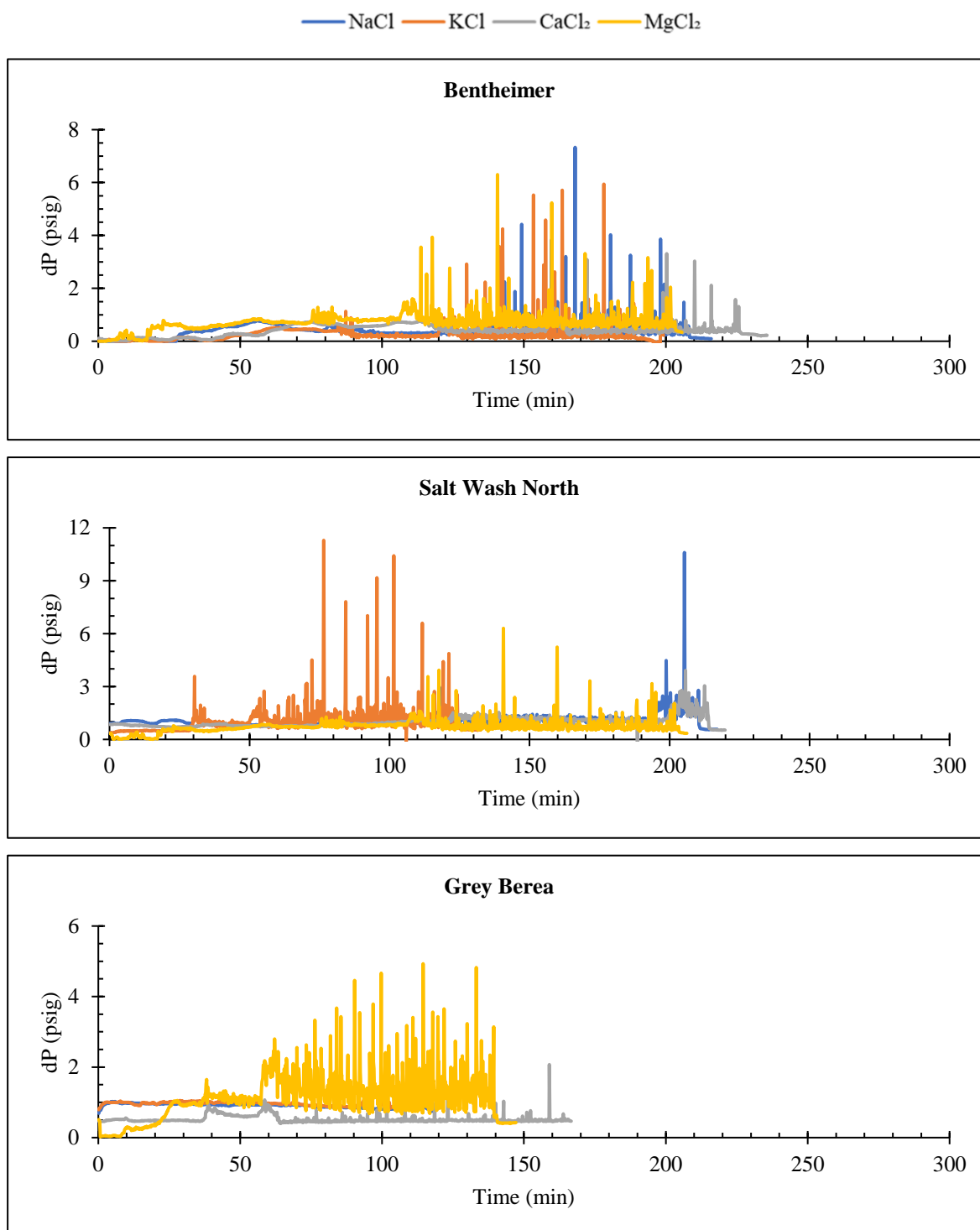
Figure 4.5: Flow Behaviour of different core samples at 15 wt.% salt concentration

Figure 4.6 shows differential pressure (dp) against time charts depicting the flow behaviour of supercritical CO_2 in several brines at 20% salt concentration for three different sandstone core samples.
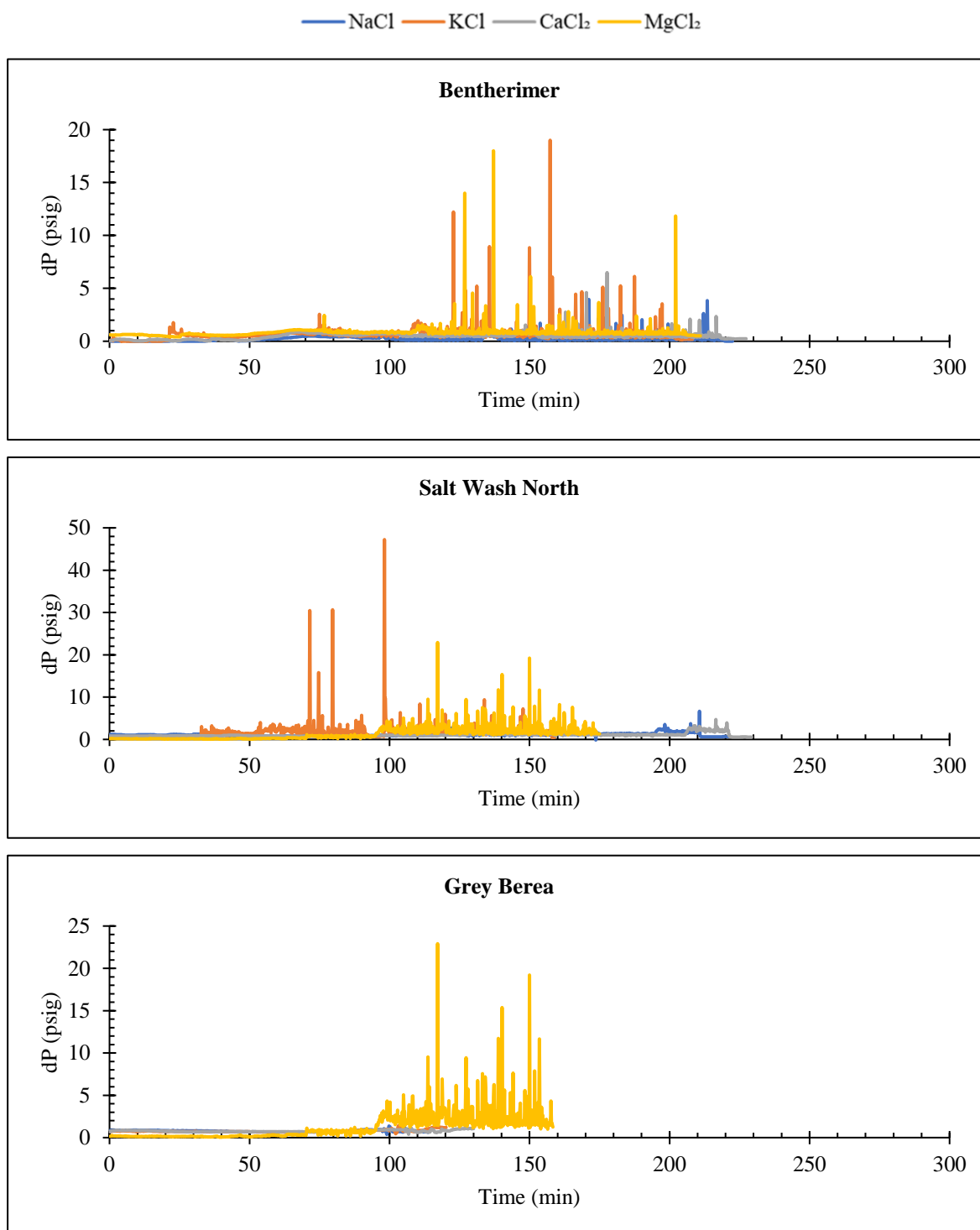
Figure 4.6: Flow Behaviour of different core samples at 20 wt.% salt concentration

As it shows, an early CO_2 breakthrough time for Bentherimer was seen in the KCl brine, followed by $MgCl_2$, NaCl, and $CaCl_2$ brines at a 20 wt.% concentration. Since KCl brine has the highest differential pressure fluctuation and early breakthrough, the storability of CO_2 in this brine is the lowest when compared to other brine concentrations, which is substantial due

to the amount of water displaced in comparison to other scenarios. This is consistent with the findings of Abba et al. [114] who discovered that KCl had the largest dp trend after the CO_2 breakthrough. CO_2 solubility in NaCl brine solution is slightly lower than in CaCl2 brine, and both are significantly lower than in KCl and $MgCl_2$ brines.

The early breakthrough time of CO_2 for Salt Wash North was observed in the KCl brine, followed by $MgCl_2$, NaCl and $CaCl_2$ brines respectively. Since KCl brine has the most differential pressure fluctuation and early breakthrough, the storability of CO_2 in this brine is the lowest when compared to other brine concentrations, which is mostly due to the amount of water displaced in comparison to other scenarios.

For Grey Berea at 20 wt.% concentration, the flow pattern exhibited the same characteristic before the CO_2 breakthrough and different behavioural patterns after the CO_2 breakthrough. The earliest breakthrough was observed in $CaCl_2$ then followed by KCl and NaCl brine under the same experimental conditions. Late breakthrough time however was observed in the Grey Berea sandstone saturated with $MgCl_2$.

Figure 4.7 shows differential pressure (dp) against time charts depicting the flow behaviour of supercritical CO_2 in several brines at 25% salt concentration for three different sandstone core samples.

$CaCl_2$ demonstrated the earliest breakthrough for Bentheimer, followed by NaCl, $MgCl_2$, and KCl brines, in that order. When compared to NaCl and $CaCl_2$ brines, $MgCl_2$ and KCl brines had the highest level of differential pressure variation. The salting-out effect is responsible for the high level of variation in differential pressure and the decrease in CO_2 solubility in the brine (salt-induced precipitation). This is explained further by the fact that as the ions are dissolved, some of the water becomes unavailable for solute interaction due to vaporisation and is thus salted out of the aqueous phase. Furthermore, although having the same anion, the size of K^+ is bigger than that of Na^+. According to Bostrom and Ninham [115], the hydration action of Na+ is greater than that of K^+, implying that in the aqueous NaCl brine, there are less free H_2O molecules acting on CO_2 molecules than in the KCl brine. As a result, at the identical temperature, pressure, concentration, and injection rate conditions, the salting-out impact of NaCl is greater than that of KCl. In terms of the salting-out effect, ion charge density is far more essential than ion size [113]. This was not the case with this effort. The amount of water in the core sample had a substantial impact on the observed trend, with more brine maintained in the NaCl situations than in the other brines.
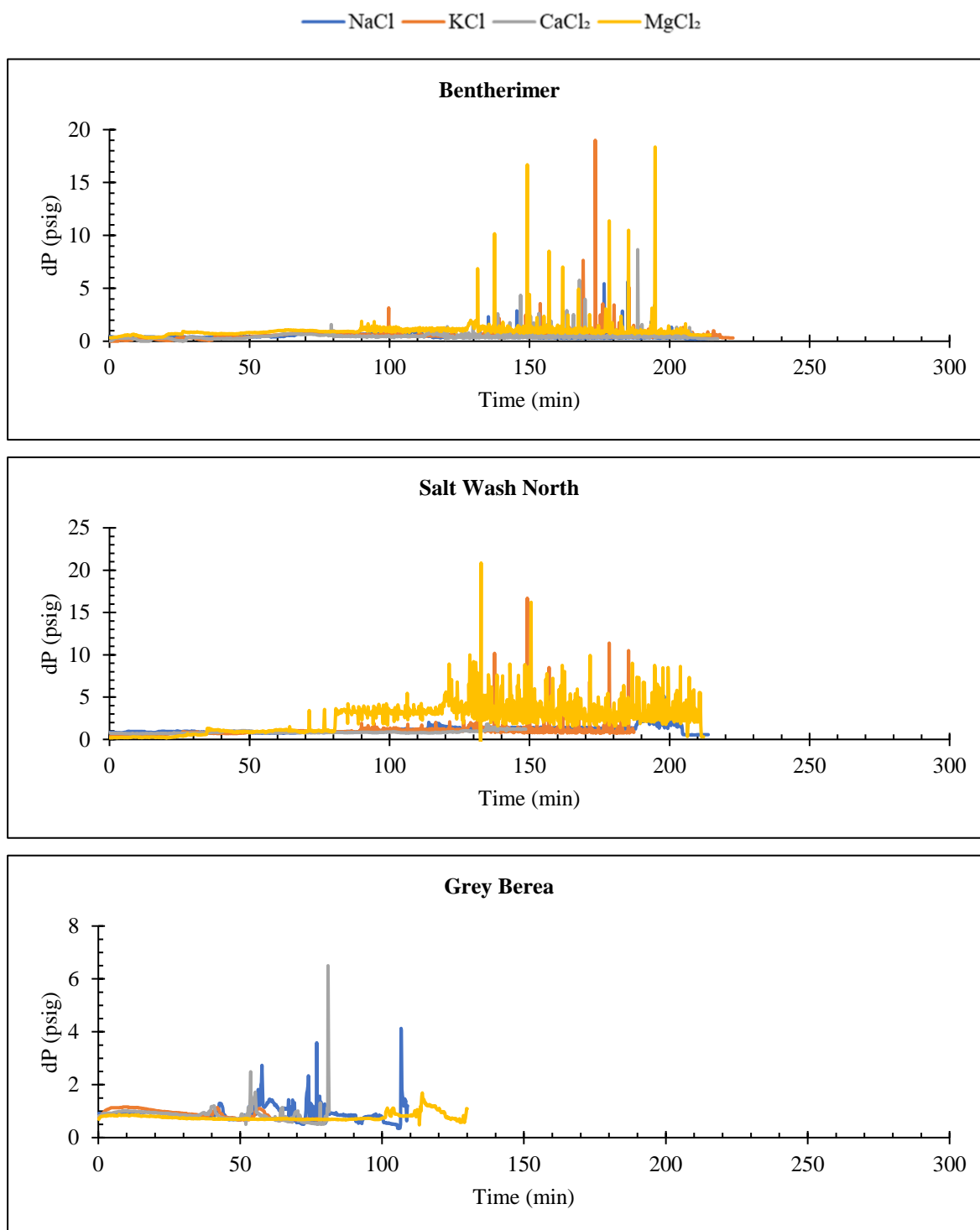
Figure 4.7: Flow Behaviour of different core samples at 25 wt.% salt concentration

The flow behaviour of CO_2 in Salt Wash North showed the same pattern until it reaches 66.33 mins, which depicts the early breakthrough of CO_2 in $MgCl_2$ brine, followed by KCl, NaCl, and $CaCl_2$ respectively. Predominant fluctuation of differential pressure was found in $MgCl_2$ and KCl as compared to NaCl and $CaCl_2$ brine. The salting-out effect is responsible for the

high level of variation in differential pressure and the decrease in CO_2 solubility in the brine (salt-induced precipitation). This is explained further by the fact that when the ions are dissolved, some of the water will not be available for solute interaction due to vaporisation and will thus be salted-out of the aqueous phase.

Table 4.13, 4.14, and 4.15 shows the summary of the core flooding results for Bentheimer, Salt Wash North, and Grey Berea respectively.

Table 4.13: Summary of core flooding results at reservoir pressure of 1500 psig and temperature of 45 ºC for Benthemier core sample

Salt	Salt Conc. (%)	Breakthrough Time [min]	Porosity Reduction [%]	Permeability Variation [%]
NaCl	5	120.34	1.15	37.0
	10	88.34	1.88	42.0
	15	81.01	3.42	49.1
	20	97.50	3.55	50.0
	25	79.17	6.15	51.7
KCl	5	107.17	3.50	19.4
	10	52.33	24.57	27.5
	15	115.67	25.34	31.0
	20	102.33	27.39	37.0
	25	77.17	35.26	43.1
CaCl_2	5	109.83	20.80	17.1
	10	90.51	21.74	23.7
	15	84.17	24.81	31.0
	20	73.17	33.58	40.8
	25	97.67	33.82	44.2
MgCl_2	5	107.33	22.82	44.2
	10	74.51	24.79	56.1
	15	75.68	34.19	61.3
	20	76.01	36.15	62.1
	25	89.50	40.94	63.3

Table 4.14: Summary of core flooding results at reservoir pressure of 1500 psig and temperature of 45 ºC for Salt Wash North sample

Salt	Salt Conc. (%)	Breakthrough Time [min]	Porosity Reduction [%]	Permeability Variation [%]
NaCl	5	72.51	0.21	30.8
	10	111.51	0.55	35.8
	15	116.71	2.97	42.9
	20	120.84	3.09	43.8
	25	113.17	5.25	45.5
KCl	5	119.34	1.81	13.2
	10	118.51	3.95	21.3
	15	119.67	6.08	24.8
	20	129.34	9.98	30.0
	25	118.00	13.56	36.9
CaCl$_2$	5	37.69	13.34	10.9
	10	22.17	1.81	17.5
	15	29.33	7.24	24.8
	20	32.67	14.72	34.6
	25	76.50	18.66	41.7
MgCl$_2$	5	16.34	5.35	33.8
	10	65.83	7.96	38.4
	15	61.17	9.23	41.5
	20	54.51	18.70	44.2
	25	66.33	20.22	56.3

Table 4.15: Summary of core flooding results at reservoir pressure of 1500 psig and temperature of 45 ºC for Grey Berea sample

Salt	Salt Conc. (%)	Breakthrough Time [min]	Porosity Reduction [%]	Permeability Variation [%]
NaCl	5	93.3	7.7	16.6
	10	97.17	9.5	26.2
	15	107.17	12.3	34.7
	20	85.50	14.9	40.5
	25	43.84	17.3	45.2
KCl	5	103.33	35.4	15.5
	10	99.5	38.2	22.1
	15	94.84	44.3	30.2
	20	70.50	50.1	40.4
	25	39.50	53.6	49.6
CaCl$_2$	5	90.83	30.5	18.7
	10	102.33	39.8	26.9
	15	93.51	40.1	37.5
	20	37.80	46.2	44.6
	25	40.34	48.9	50.6
MgCl$_2$	5	105.33	36.0	47.3
	10	105.0	40.4	58.2
	15	94.84	48.8	63.4
	20	99.0	53.3	65.6
	25	41.51	57.2	67.2

4.3.2.2. Pressure Decay

CO_2 solubility varies with brine type, and it is critical for CO_2 storage in deep saline aquifers. An in-line pressure decay test was used to evaluate a comprehensive research of CO_2 solubility in several brine solutions. The pressure decay rate for all brine concentrations with respect to salt type was calculated using the starting CO_2 injection pressure and the constant pressure acquired at the end of the pressure decay test. CO_2 was introduced into the brine-saturated core sample to the appropriate pressure. A reduction in pressure was expected over a period owing to the CO_2 dissolution in the simulated formation brine. This pressure drop can be used to calculate the solubility of CO_2 in brines at various concentrations, as well as to explore and infer the interplay of the in-situ fluids. As a result, a high-pressure decay rate in the pressure decay test (PDT) indicates increased solubility.

Pressure Decay Rate for Bentheimer Core Sample

Table 4.16 depicts the summary of pressure decay results for Bentheimer core sample. Figure 4.8 depicts the pressure decay trend for Bentheirmer core sample at various brine concentrations while Figure 4.9 shows the actual pressure decay rate for all salt types at various brine salinity

Table 4.16: Summary of pressure decay results for BEN core samples

Salt	Salt Conc. (%)	Pressure Change [psi]	Pressure Decay Rate [psi/min]	Brine Saturation [%]
NaCl	5	16	1.06	89
	10	8	0.53	87
	15	11	0.73	91
	20	10	0.60	85
	25	6	0.40	91
KCl	5	5	0.30	85
	10	8	0.53	90
	15	2	0.13	91
	20	6	0.40	92
	25	3	0.20	96
CaCl$_2$	5	2	0.13	87
	10	4	0.23	96
	15	4	0.26	85
	20	5	0.30	97
	25	2	0.13	89
MgCl$_2$	5	8	0.53	89
	10	4	0.25	89
	15	3	0.20	95
	20	7	0.46	95
	25	6	0.40	93
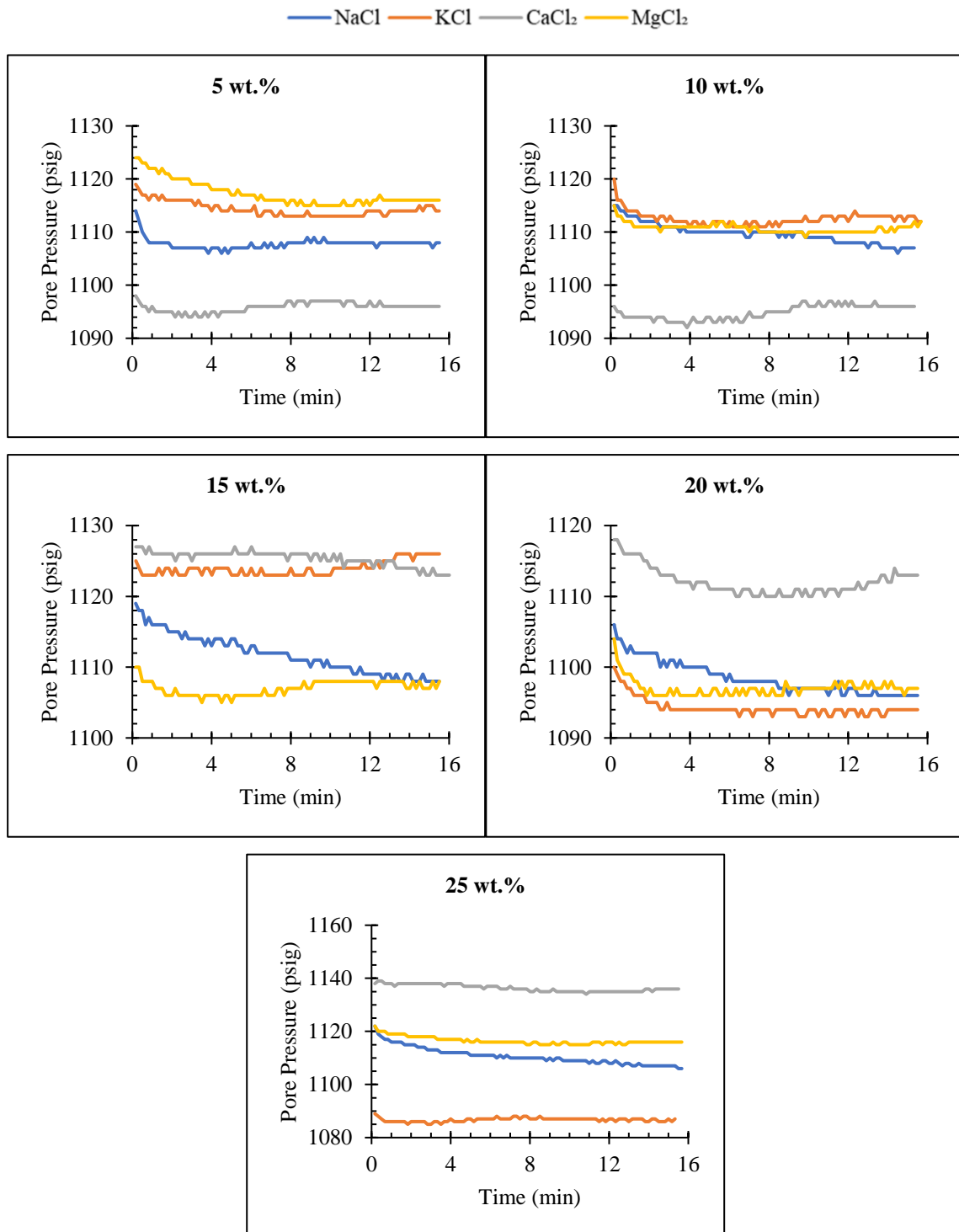
Figure 4.8: Pressure Decay Trend for Bentheirmer Core Sample at various brine concentrations
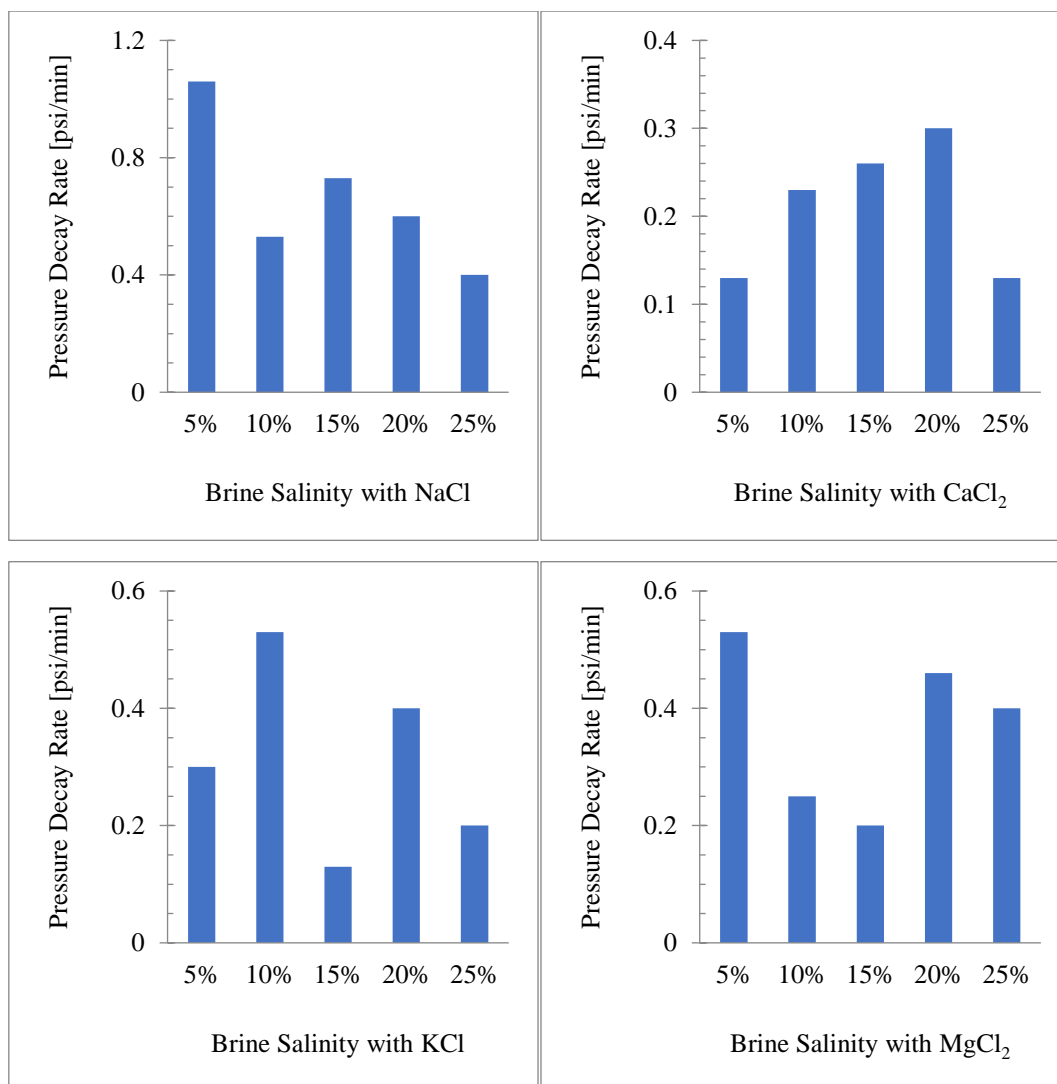
Figure 4.9: Pressure Decay Rate for Bentheirmer Core Sample at various brine types and concentrations

From Figure 4.9, at 5 wt.% concentration, the pressure decay rate for $CaCl_2$ brine solution is the lowest, while NaCl has the highest. Pressure decay rates for KCl and $MgCl_2$ are in the intermediate ranges, with KCl having a lower pressure decay rate than NaCl. As shows in Table 4.16, the late breakthrough time of CO_2 in NaCl confirms that more CO_2 was held and stored at this concentration compared to other salt scenarios.

The dissolution of CO_2 in monovalent salt solution followed the same pattern as the divalent salt, as illustrated in Figure 4.8. The pressure decay rate for NaCl is 1.06 psi/min while that of KCl is 0.30 psi/min. Conversely, the pressure decay rate for $CaCl_2$ and $MgCl_2$ are 0.13 psi/min and 0.053 psi/min respectively. This demonstrates that the solubility of CO_2 in monovalent salt brines (NaCl and KCl) is greater than in divalent brines ($CaCl_2$ and $MgCl_2$). The initial water of saturation was also higher in the monovalent brine-saturated core sample than in the

divalent brine-saturated core sample, which explains why more CO_2 dissolved in the former than in the latter.

Furthermore, the decay rate was also determined to be the higher with the sandstone saturated with 15 wt.% NaCl brine. This is due to the fact that the initial water of saturation was higher in this case, resulting in a higher-pressure decay rate of roughly 0.73 psi/min. KCl brine and NaCl brine, on the other hand, produced distinct pressure decay rates at this concentration while having the same amount of initial water saturation. When opposed to $CaCl_2$, $MgCl_2$ showed a considerable decrease in pressure with time. This is owing to the presence of pore spaces in the core sample saturated with $MgCl_2$. Furthermore, the level of brine saturation is lower than in $CaCl_2$ brine-saturated sandstone. As a result, NaCl brine had the highest level of solubility with respect to 15 wt.% brine.

In addition, all concentrations showed the same kind of pattern immediately after CO_2 injection although at different pressure decay rates. Furthermore, NaCl brine has the highest-pressure decay rate of 0.60 psi/min at 20 wt.% concentration, whereas $CaCl_2$ has the lowest pressure decay rate of 0.30 psi/min. This is also due to CO_2 dissolution in the core sample, which has higher initial water saturation from the NaCl brine. The pressure decay rates for KCl and $MgCl_2$ were 0.40 psi/min and 0.46 psi/min, respectively. As a result, when compared to the other brines, NaCl brine had the highest level of CO_2 solubility.

At the highest concentration of all salt types (25 wt.%), however, the sharp decline in pore pressure is not observed at this concentration. This was a result of the reduction in the tortuous flow paths of the porous medium with high saline brines [114]. NaCl and $MgCl_2$ brines had the highest values of pressure decay rate while $CaCl_2$ with the lowest value of 0.13 psi/min. This implies that the solubility of CO_2 was higher in NaCl concentration as compared to other types of salts. Thus, the Pressure Decay Rate (PDR) is a function of CO_2 solubility in different brine types and concentrations. This relationship can be used to evaluate critical CO_2 solubility at operational conditions in all brine types. The critical CO_2 solubility in NaCl and $MgCl_2$ brines was discovered to be at 5 wt.% concentrations, where the PDR is maximum within the studied ranges. The maximum PDR for KCl brine was realised at 10 wt.%, with $CaCl_2$ at 20 wt.%.

Pressure Decay Rate for Salt Wash North Core Sample

Table 4.17 depicts the summary of pressure decay results for Salt Wash North core sample. Figure 4.10 depicts the pressure decay trend for Salt Wash North core sample at various brine concentrations while Figure 4.11 shows the actual pressure decay rate for all salt types at various brine salinity

Chapter 4: Results and Discussions

Table 4.17:Summary of pressure decay results for Salt Wash North sample

Salt	Salt Conc. (%)	Pressure Change [psi]	Pressure Decay Rate [psi/min]	Brine Saturation [%]
NaCl	5	16	1.06	82
	10	8	0.53	85
	15	11	0.73	90
	20	10	0.67	82
	25	6	0.40	81
KCl	5	26	1.73	92
	10	12	0.80	91
	15	11	0.73	93
	20	7	0.47	83
	25	4	0.27	79
CaCl$_2$	5	25	1.67	97
	10	24	1.60	91
	15	24	1.60	90
	20	12	0.80	93
	25	11	0.73	89
MgCl$_2$	5	24	1.60	88
	10	22	1.47	91
	15	17	1.13	90
	20	15	1.00	92
	25	14	0.93	96
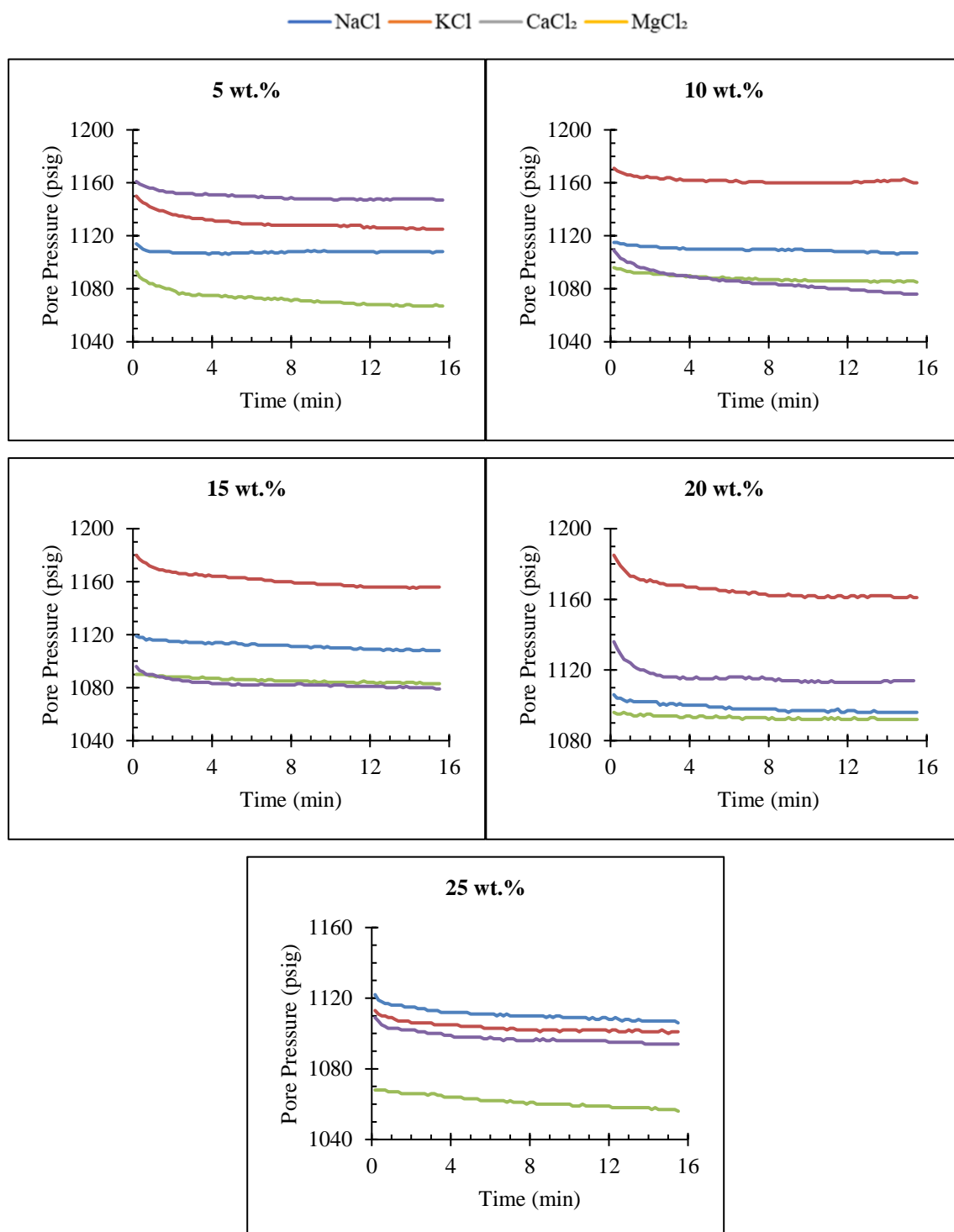
Figure 4.10: Pressure Decay Test for Salt Wash North Core Sample at various brine concentrations
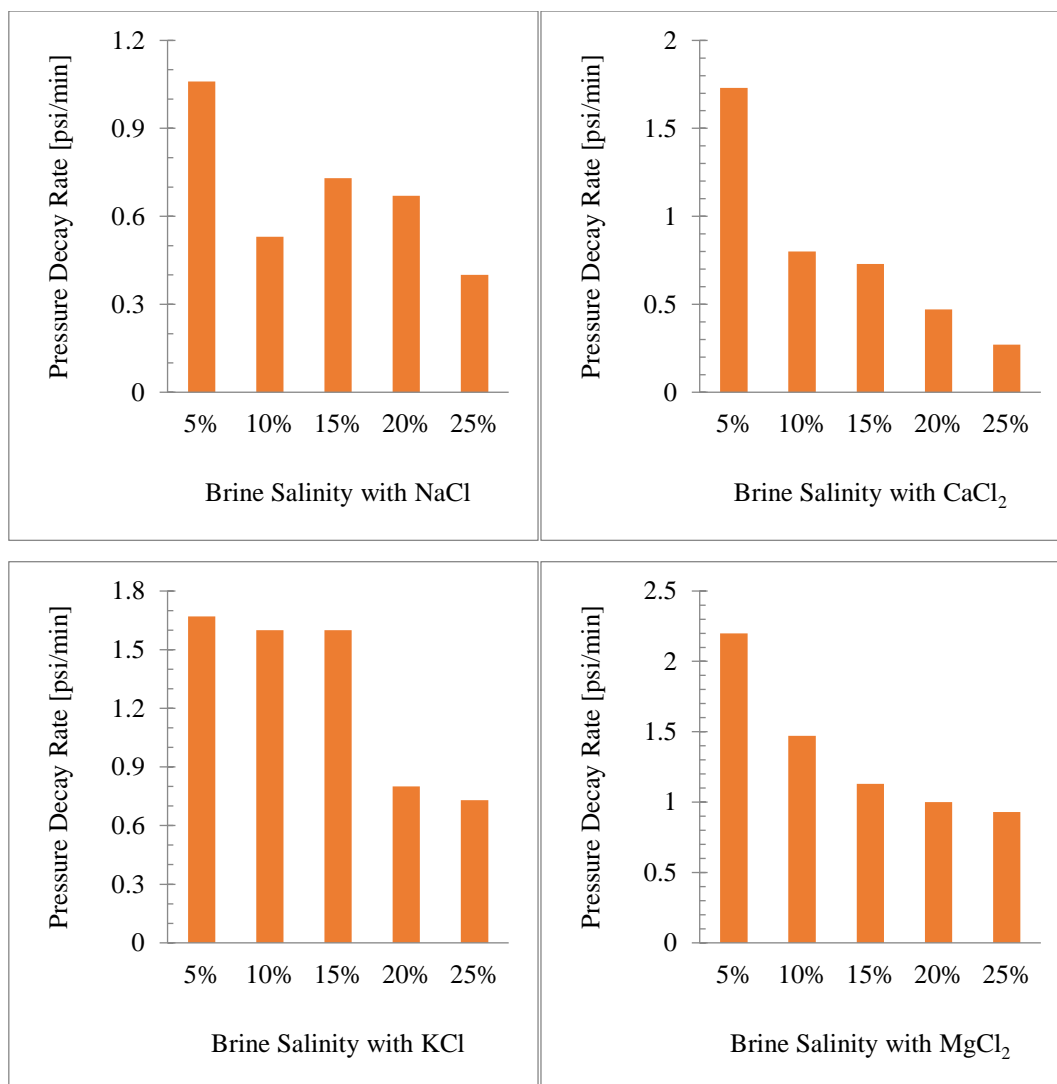
Figure 4.11: Pressure Decay Rate for Salt Wash North Core Sample at various brine types and concentrations

As shown in this Figure 4.11, NaCl has the highest decay rates in all core flooding scenarios (Pressure Decay Test (PDT)), indicating that CO_2 solubility was greatest in the NaCl solutions. However, the amount of water recovered from the core sample downstream of the backpressure regulator in the NaCl salts was smaller than in the other brine solutions following the experiments. As a result, the amount of stored water within the core sample was greater, resulting in more interactions with the injected CO_2. Thus, under varied conditions, the solubilities of the divalent salts ($CaCl_2$ and $MgCl_2$) were found to be identical, as supported in the literature [113].

At a 5 wt.% brine concentration for all brine types (NaCl, $CaCl_2$, KCl, $MgCl_2$), the pressure decay rate was noteworthy at greater than 1 psi/min. This is because the brine utilised for initial saturation of the core sample had a low concentration level. The permeability of the core

sample, as well as the interaction between the brine and the CO_2 passing through the core sample, also contributed to such a high decay rate.

The core sample saturated with monovalent brine (KCl) displayed the highest level of pressure decay rate, as shown in Figure 4.11, with a value of 1.73 psi/min. This is further evidenced by the steepness of the graph as well as the initial brine saturation. This indicates that the solubility of CO_2 is higher in this brine as compared to other brines with the same level of concentration. On the other hand, the pressure decay rate is at its lowest level with the sandstone saturated with divalent salt ($CaCl_2$). Thus, the solubility of CO_2 is higher with sandstone saturated with monovalent brine than in divalent brine.

Furthermore, as seen in Figure 4.10, at 15 wt.% KCl displayed a sharp decline in pressure over time as compared to $MgCl_2$ with the same level of brine saturation. This is however due to the availability of pore spaces in the core sample saturated with KCl brine. It is pertinent to note that, at this brine concentration, both NaCl and KCl brine-CO_2 systems exhibited the same value of rate decay rate while possessing different brine saturation levels.

More so, $CaCl_2$ and $MgCl_2$ showed the same trend with a pressure decay. The aforementioned CO_2-brines system exhibited the same kind of trend immediately after injection of CO_2 but then displayed approximately the same pressure decay rate. The above analogy was also found concerning the other brine (NaCl, KCl) at 20 wt.% but with nearly the same level of brine saturation. NaCl pressure decay rate was found to be 0.67 psi/min while KCl was 0.47 psi/min. By and large, the pressure decay rate of 25 wt.% concentration followed the same pattern. At this concentration, the reduction in the tortuous flow paths of the porous medium with high saline brine had been experienced. Thus, the value of pressure decay in all the brine types is lower as compared to lesser brine concentrations. The value of pressure decay in this CO_2-brines system ranges from 0.27 to 0.93 psi/min.

Pressure Decay Rate for Grey Berea Core Sample

The pressure decay data for the Grey Berea core sample are summarised in Table 4.18. Figure 4.12 represents the pressure decay trend for the Salt Wash North core sample at different brine concentrations, whereas Figure 4.13 depicts the actual pressure decay rate for all salt types at different brine salinity.

Table 4.18: Summary of pressure decay results for Grey Berea samples

Salt	Salt Conc. (%)	Pressure Change [psi]	Pressure Decay Rate [psi/min]	Brine Saturation [%]
NaCl	5	26	1.73	87
	10	14	0.93	91
	15	11	0.73	89
	20	9	0.60	88
	25	4	0.26	90
KCl	5	12	0.80	93
	10	11	0.73	92
	15	16	1.60	91
	20	8	0.53	90
	25	4	0.25	85
$CaCl_2$	5	16	1.06	93
	10	8	0.53	91
	15	10	0.60	87
	20	4	0.26	80
	25	3	0.20	85
$MgCl_2$	5	24	1.60	87
	10	4	0.26	91
	15	8	0.53	89
	20	6	0.40	90
	25	5	0.30	90

At 5 wt.% concentration, NaCl has the highest decay rates (1.73 psi/min) in all flooding scenarios, indicating that CO_2 solubility was highest in the NaCl solutions; however, after the tests, the amount of water displaced (recovered) from the core sample downstream of the backpressure regulator was lower in the NaCl salts than in the other brine solutions. When compared to other salts, the pressure decay rate for KCl brine solution is the lowest (0.80 psi/min). $CaCl_2$ and $MgCl_2$ pressure decay rates are in the intermediate ranges with the the same value of 1.06 psi/min.. The CO_2 breakthrough time in NaCl demonstrates that this concentration stores more CO_2 than other salt situations. Moreso, at 10 wt.% concentration, the range of pressure decay rates is between 0.26 psi/min to 0.93 psi/min with NaCl brine having the highest-pressure decay value. It is worth noting that the pressure decay rate varied for salt types of the same concentration and initial water saturation.
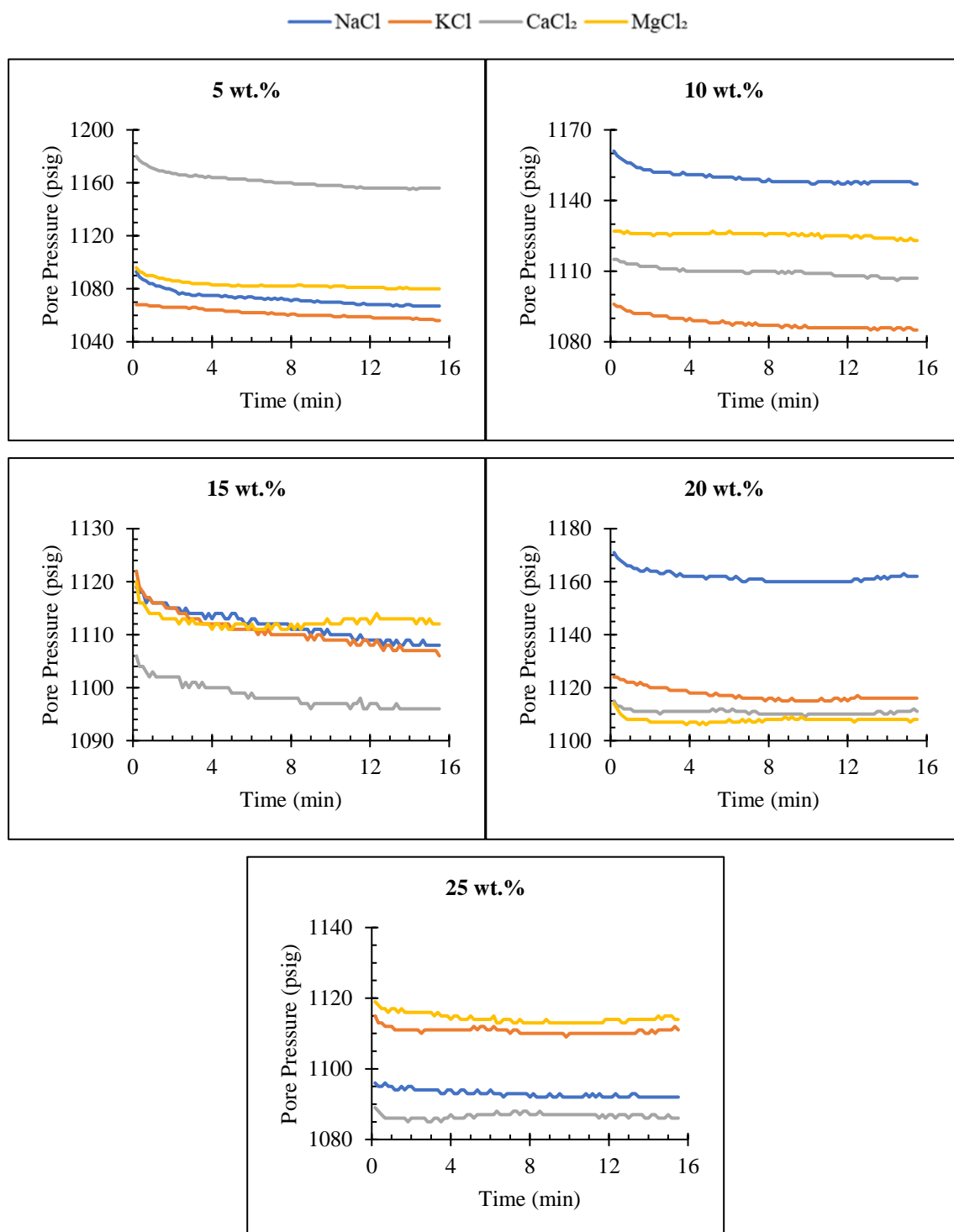
Figure 4.12: Pressure Decay Test for Grey Berea Core Sample at various brine concentrations

Also, at 15 wt.% brine concentration, the pressure decay rate was found to be the highest with the sandstone initially saturated with monovalent brine than that saturated with divalent brine. For the monovalent brine, the NaCl decay rate was 0.73 psi/min while that of KCl was found to be 1.60 psi/min, and thus 0.87 psi/min higher than NaCl. By and large, the trend in pressure

decay observed in 20 wt.% is almost similar to 15 wt.% concentration with the monovalent brines having the highest-pressure decay when compared to divalent brine. Thus, monovalent brine (NaCl) brine possessed the highest level of solubility with regard to 20 wt.% brine. For all salt varieties, the pressure decay rate is within the range of 0.20 to 0.30 psi/min at the highest level of brine concentration (25 wt. percent). This could be due to a reduction in the sinuous flow routes occupied by high-concentration brine in the porous media. Here, $MgCl_2$ has the highest decay rate of 0.30 psi/min, whereas $CaCl_2$ brine has the lowest value of 0.20 psi/min. On the other hand, NaCl pressure decay rate was 0.26 psi/min while KCl decay rate value was 0.25 psi/min.
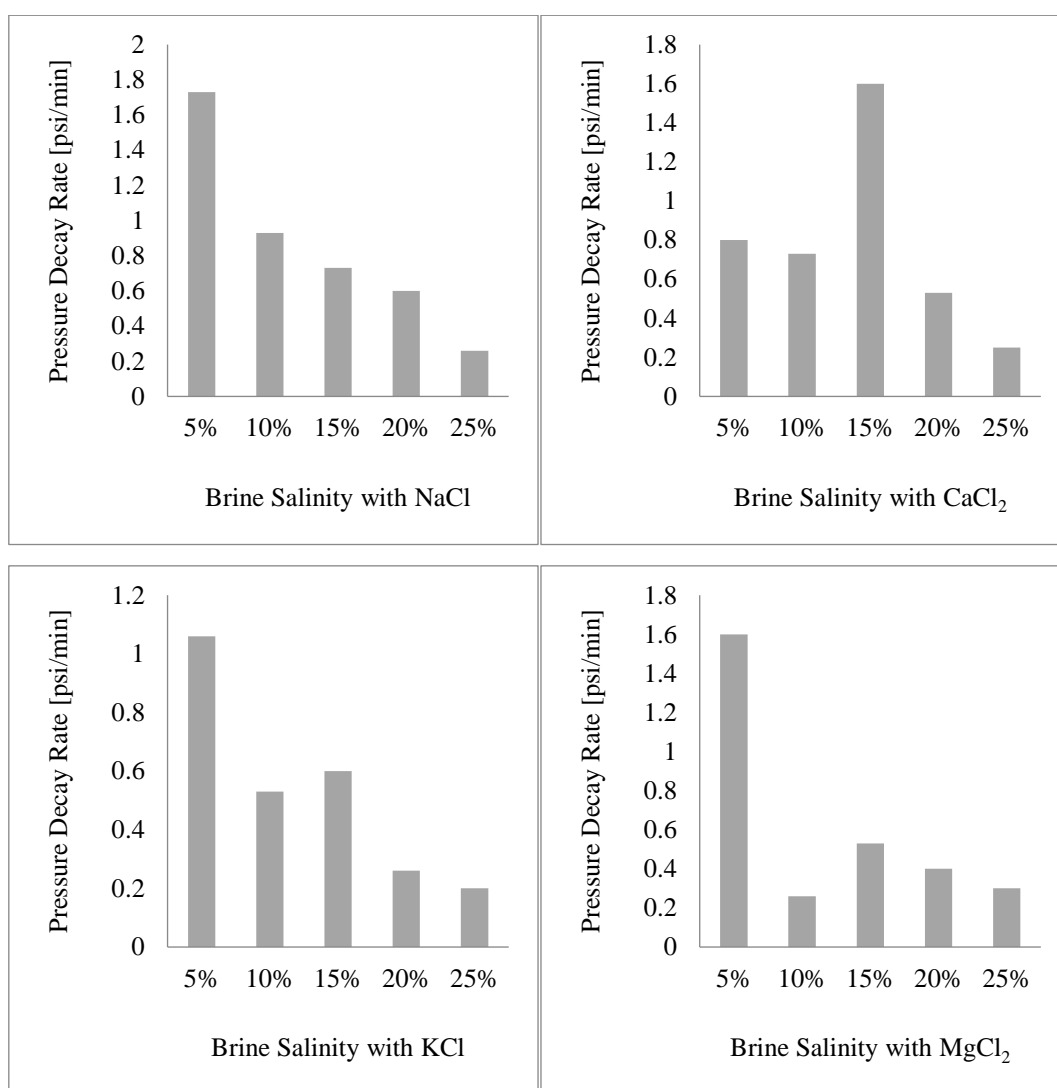
Figure 4.13: Pressure Decay Rate for Grey Berea Core Sample at various brine types and concentrations

4.3.2.3. Effect of Different Salts and Concentrations on CO_2 Storage

The brines used in the studies were made from four of the most prevalent salts found in deep saline aquifers. Breakthrough time of CO_2 from the core sample saturated with different brines and salinities varied. From Figure 4.14, the breakthrough time of CO_2 in Bentheimer core sample with NaCl brine took longer as compared to other brine salinities ($CaCl_2$, KCl, and $MgCl_2$). This indicates a greater interaction as a result of retention time between CO_2 and host brine at 5 wt.% salinity, thereby resulting in less CO_2 production. Thus, more CO_2 is stored at 5 wt.% NaCl brine, followed by $MgCl_2$ brine and KCl. The $CaCl_2$ brine exhibited the same characteristics for storage. Moreover, the salting-out effect or precipitation was not well pronounced initially for all types of brine at this salinity (5 wt.%). This can be seen around the 100 mins mark as shown in Figure 4.14 for Bentherimer core sample after a breakthrough for the various brine.

The CO_2 breakthrough time for Salt Wash North in $MgCl_2$ was faster than in other brine salinities (NaCl, $CaCl_2$, and KCl). This suggests that there is less interaction as a result of the retention duration between CO_2 and the host brine at 5 wt.% salinity, resulting in greater CO_2 production than storage. More CO_2 storage at this brine concentration was evidenced in $CaCl_2$ followed by NaCl and KCl brine respectively. This can be affirmed as a result of late breakthrough and thus, the salting-out effect or precipitation was not well pronounced initially for all the brine types at this concentration (5 wt.%). More so, as the brine grew more saturated with CO_2, CO_2 occupied more of the pore spaces within the core sample due to increased capillary pressure and, thus, interfacial tension [113]. As a result of the increased interfacial tension between the brine and the CO_2, there is less CO_2 trapping and hence less interaction in terms of dissolution.

For Grey Berea sandstone saturated with 5 wt.% brine prepared from different salt, the CO_2 breakthrough times in this sample are so close and is within the range of 90.83 to 105.33 mins. The breakthrough time of CO_2 in $CaCl_2$ took the shortest time while the breakthrough of CO_2 in KCl and $MgCl_2$ took the longest time. This suggests a stronger interaction as a result of CO_2 retention period in the host brine at 5% salinity. Thus, the 5 wt.% $MgCl_2$ brine stores the most CO_2, followed by KCl, NaCl brine, and $CaCl_2$ respectively. It is critical to notice in Figure 4.14(c) that the amount of CO_2 produced by all salinities is extremely similar to one another. This could be due to the petrophysical properties of the core sample under inquiry.
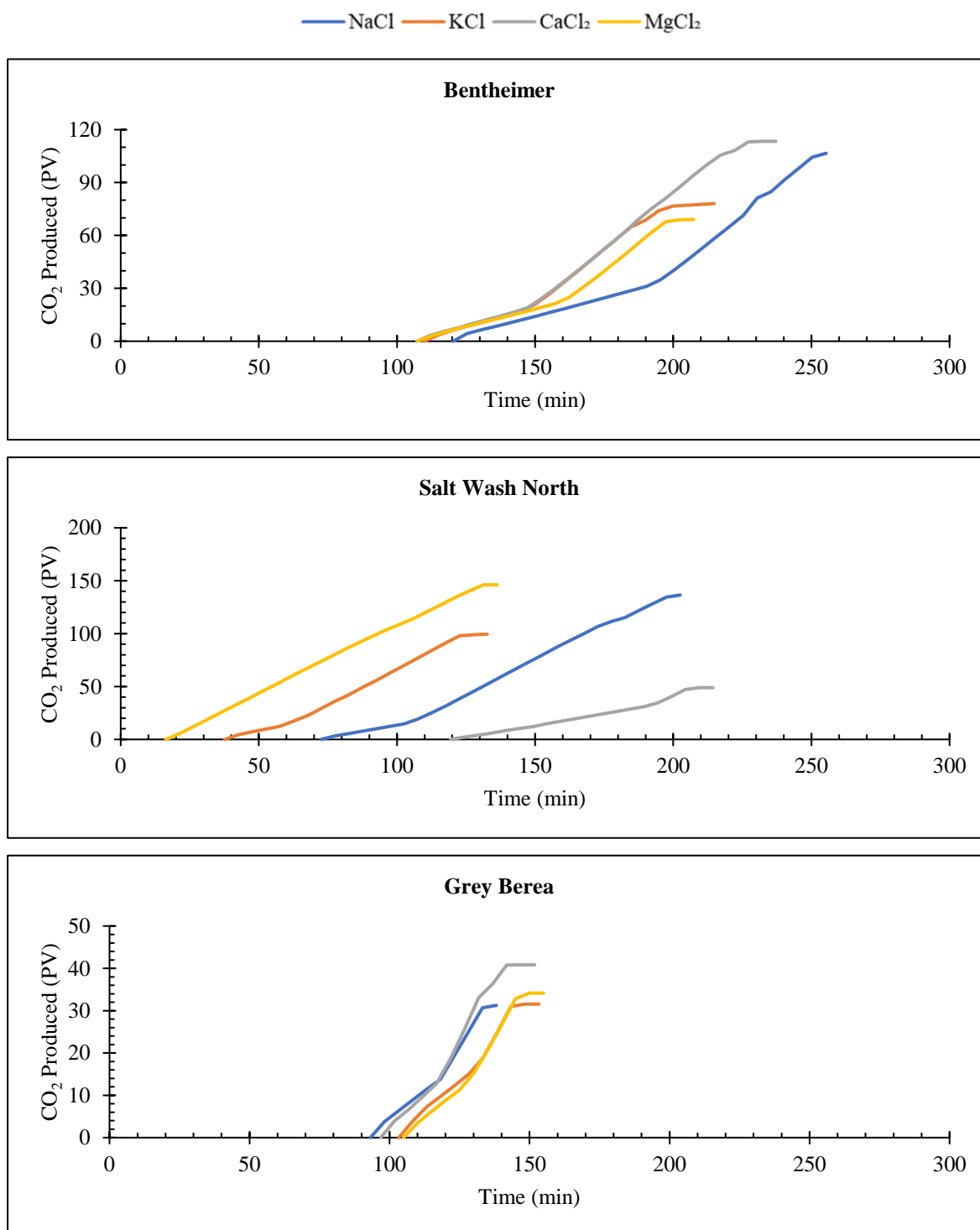
Figure 4.14: CO_2 collected after saturating the core sample with 5 wt.% brine

Figure 4.15 shows the CO_2 breakthrough at 10 wt.% salinity for all three sandstone samples. As it shows, the early CO_2 breakthrough for $CaCl_2$ brine for Bentheimer is due to the low solubility of CO_2 in brine. This is due to decreased CO_2 and brine retention or interaction within the core sample. In this regard, CO_2 breakthrough was observed sooner from the core sample,

and the initial water saturation was reduced at this salinity when compared to high solubility cases in KCl and NaCl brine. Furthermore, the late breakthrough time seen in NaCl and KCl (monovalent salts) is a clear indicator of CO_2 solubility in the core sample at this salinity. Less CO_2 was produced in this case because a significant amount of CO_2 was dissolved in the NaCl brine that saturated the core sample. The trend of CO_2 produced in the $MgCl_2$ brine scenario at this salinity falls between $CaCl_2$ and KCl brines. The foregoing findings are consistent with the experimental results obtained by Duan and Sun [116] which show that a NaCl brine with the same molality has greater solubility than a $CaCl_2$ brine.

More so, as shown in Figure 4.15 for Salt Wash North, early CO_2 breakthrough was detected in KCl brine, indicating poor CO_2 solubility in the brine. Furthermore, the late breakthrough time found in NaCl and $CaCl_2$ indicates CO_2 solubility in brine-rock systems. In this regard, compared to KCl and $MgCl_2$ brines, these brines produced less CO_2. Due to the increased CO_2 production, there was less CO_2 interaction and trapping inside the Salt wash north core sample at this brine salinity, resulting in reduced CO_2 sequestration in the core sample as compared to 5 wt.% salinity. Furthermore, for Grey Berea sandstone saturated with 10 wt.% brine concentration, CO_2 breakthrough took the longest time in $MgCl_2$ brine as compared to other brines. This was exactly the same scenario observed in the case of 5 wt.% brine and it is also worth again noting that the breakthrough time for all salt types for this concentration is between 97.17 to 105 min. From Figure 4.15, irrespective of the longer breakthrough time observed in $CaCl_2$ brine, more CO_2 was produced as compared to other brine types. NaCl and KCl brine with nearly the same CO_2 breakthrough time possesses the same characteristics in terms of storage and this can be depicted in Figure 4.15.
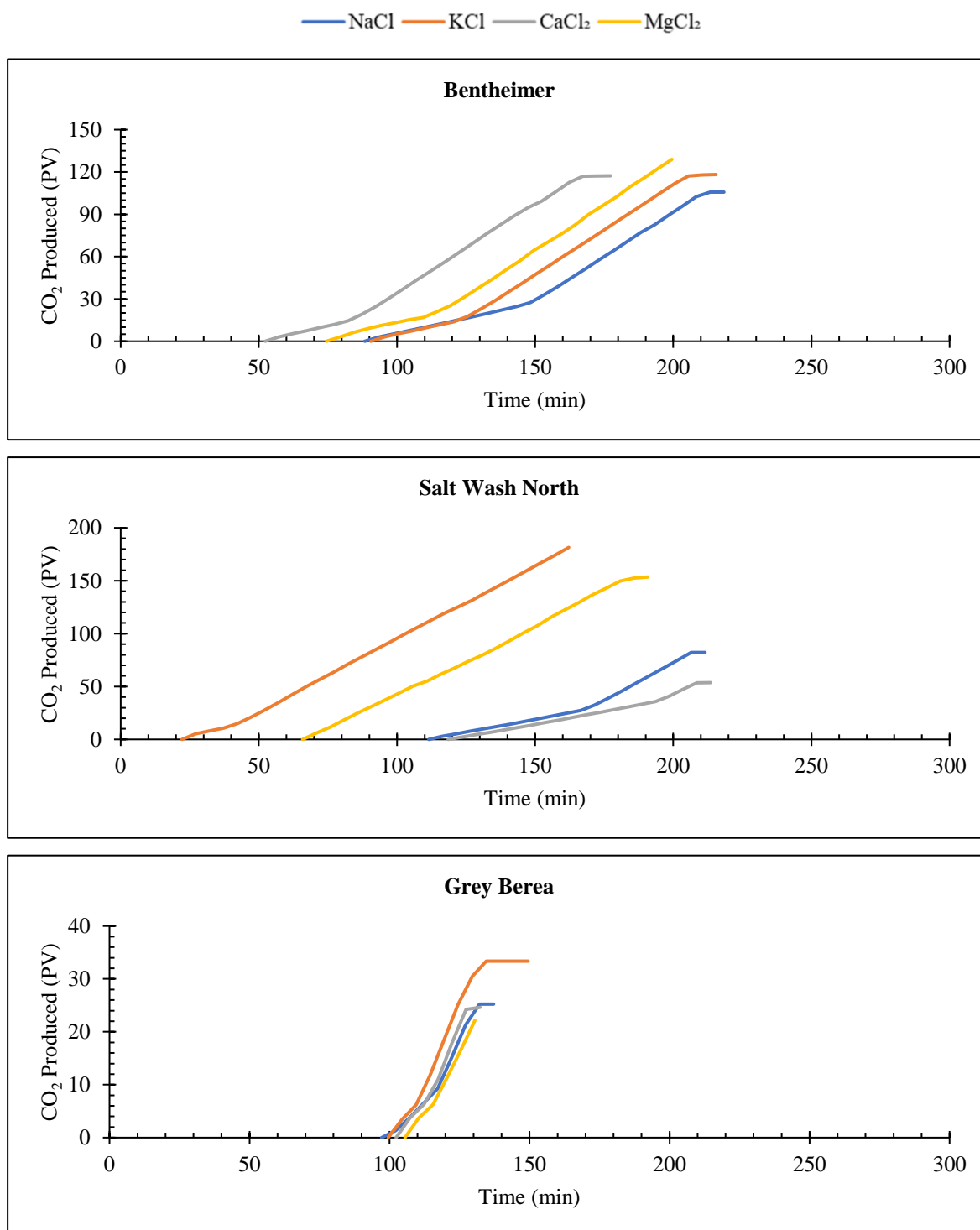
Figure 4.15: CO$_2$ collected after saturating the core sample with 10 wt.% brine

The CO$_2$ recovered after saturating the core sample with 15 wt.% brine for all three sandstone is shown in Figure 4.16. It is worth noting that CO$_2$ solubility in CaCl$_2$ brine for Bentheimer was second only to NaCl, but it had a later breakthrough time than the other brine scenarios. In this situation, it is assumed that in the case of CaCl$_2$, CO$_2$ has interacted significantly with the

brine and dissolved within the pore spaces of the core sample. It is also worth noting that at this salinity (15 wt.%), the solubility of the major salt in aquifers (NaCl) and breakthrough time have changed dramatically when compared to the prior salinity. At 15 wt.% salinity, CO_2 had the lowest solubility in KCl brine, but $MgCl_2$ had the earliest breakthrough. This observation is not unrelated to the drying out impact of the divalent brine ($MgCl_2$), which results in early breakthrough and CO_2 production as compared to KCl brines.

As shown in Figure 4.16, at 15 wt.% salinity for Salt Wash North, CO_2 had the lowest solubility in the KCl brine, followed by $MgCl_2$, which had the next earliest breakthrough. This observation is not unrelated to the drying-out effect of divalent brine ($MgCl_2$), which induces early breakthrough and CO_2 production as compared to KCl brines. It is worth noting that CO_2 solubility in NaCl brine was second only to $CaCl_2$, but it occurred at a later time than the other brine situations. In addition, significant CO_2 storage was seen in the core sample saturated with both NaCl and $CaCl_2$ brines. This could be due to brine saturation in the core sample, which would allow for further CO_2 sequestration. Due to the fact that, brine (15 wt.%) had a higher density than the brine (10 wt.%), CO_2 was trapped within the pore spaces due to the brine's greater density occupying the narrow pore space in the core sample.

Furthermore, for Grey Berea sandstone saturated with 15 wt.% brine concentration, NaCl brine had a longer CO_2 breakthrough time than other brine kinds. Under the identical testing conditions, both KCl and $MgCl_2$ had the same CO_2 breakthrough time. CO_2's earlier breakthrough, on the other hand, was noticed in the instance of $CaCl_2$ brine. Furthermore, as seen in Figure 4.16, the CO_2 produced decreased for the 15 wt.% NaCl and $CaCl_2$ brine situations. This required significant CO_2 storage when compared to the other brine salinities, with the NaCl brine having the maximum CO_2 storability. This could be due to brine saturation within the core sample, which allows for increased CO_2 sequestration.
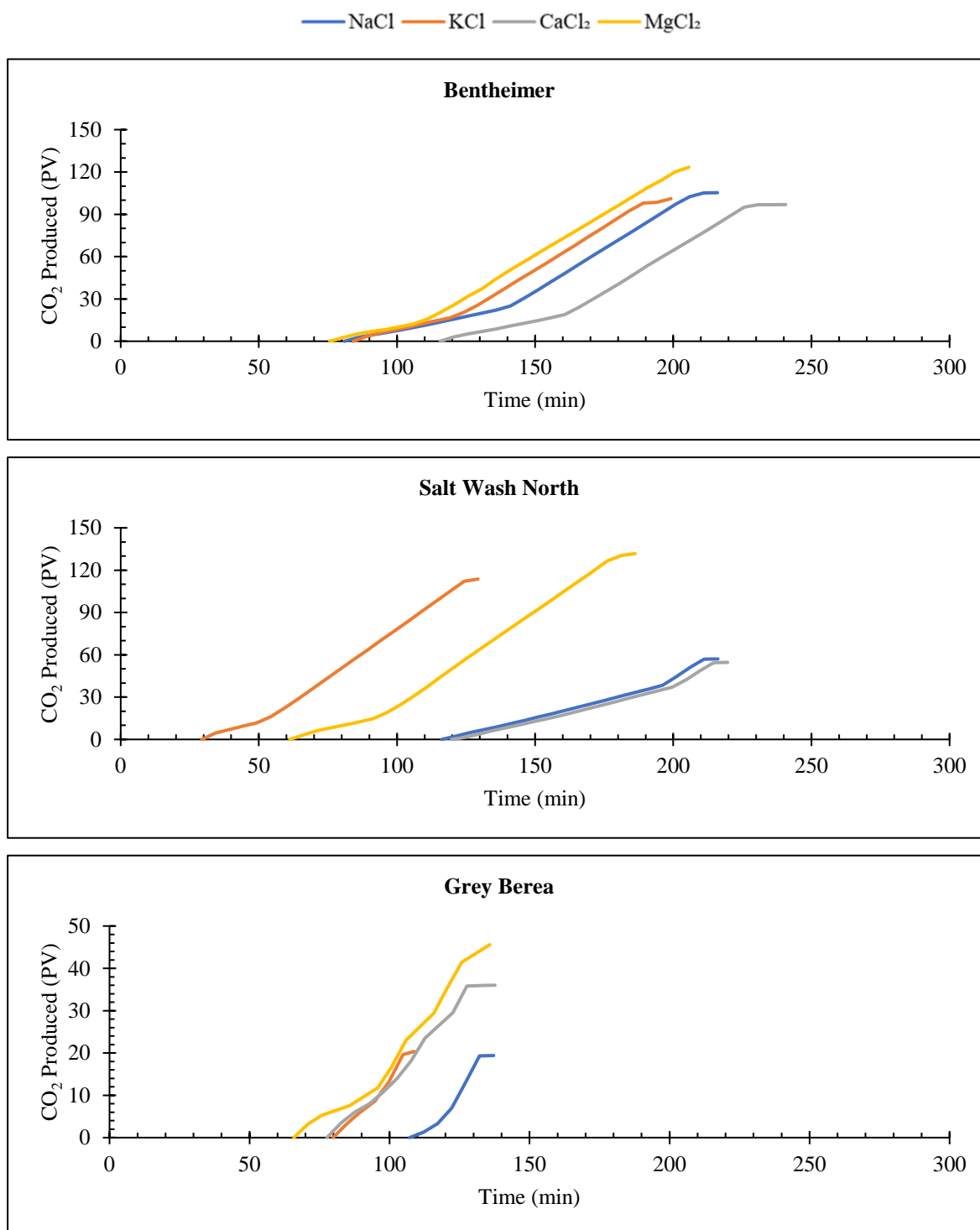
Figure 4.16: CO₂ collected after saturating the core sample with 15 wt.% brine

Figure 4.17 depicts the breakthrough results at a salinity of 20% by weight. The solubility of CO_2 in different brines for Bentheimer changes with regard to breakthrough time and CO_2 produced as brine concentration increases. KCl and $MgCl_2$ have comparable breakthrough

times, as does CO_2 produced at this salinity (20 wt.%). In addition, $CaCl_2$ appears to have the earliest breakthrough time when compared to other brines (KCl, $MgCl_2$), with NaCl brine trailing somewhat behind. The CO_2 produced in this scenario (20 wt.% salinity) is much more than that produced in the previous salinities. CO_2 had the lowest level of storability in $MgCl_2$ and KCl brine scenarios due to high CO_2 production and early breakthrough.

It is worth noting that, for Salt Wash North sample, when brine concentration increases, the solubility of CO_2 in different brines changes in relation to breakthrough time and CO_2 produced. There appeared to be a wide margin in terms of CO_2 produced between the two monovalent and the other two divalent salts. In this scenario (20 wt.% salinity), CO_2 produced is significantly more than that produced from the previous salinities. CO_2 exhibited the lowest level of storability in $MgCl_2$ and KCl brine scenarios as a result of excessive production of CO_2 and early breakthrough. On the other hand, an appreciable amount of CO_2 was stored in $CaCl_2$ and NaCl brines as a result of early breakthroughs and less production of CO_2.

Moreso, for Grey Berea sandstone saturated with 20 wt.% brine concentration, $CaCl_2$ brine exhibited earlier CO_2 breakthrough while $MgCl_2$ brine showed late CO_2 breakthrough. The CO_2 produced in this scenario irrespective of the salt type nearly have the same value. This may be due to the permeability of the core sample in which the CO_2 traversed.
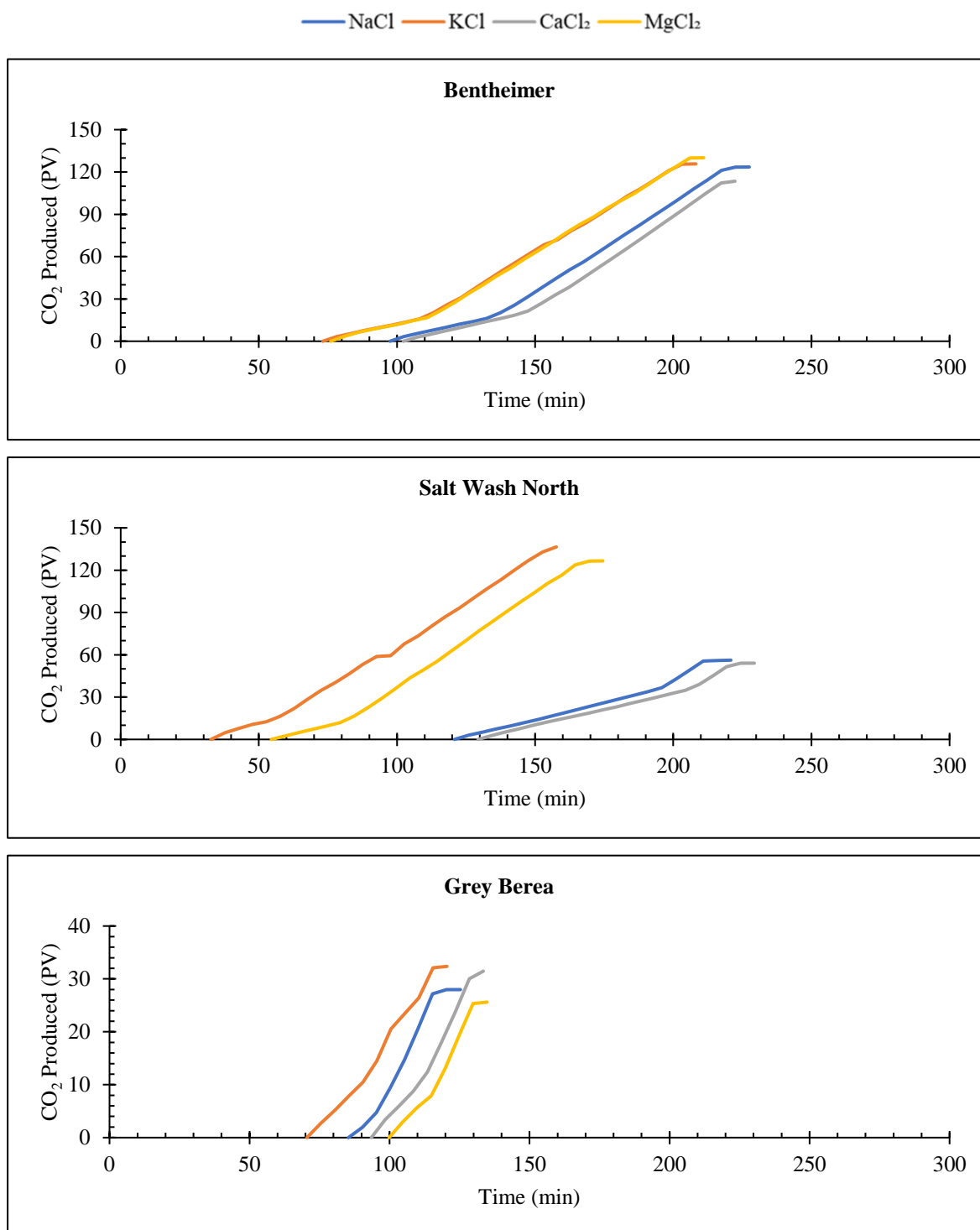
Figure 4.17: CO_2 collected after saturating the core sample with 20 wt.% brine

Due to high salinity level of all brines in Figure 4.18 with 25 wt.% salt, the breakthrough time for the various brine concentrations was invariably shorter. This meant that at this concentration, less CO_2 could be dissolved and stored. The concentration of the brine makes it difficult to dissolve more CO_2 as the density of the brine increases. Less CO_2 was stored in the

NaCl brine than in the $CaCl_2$, KCl, and $MgCl_2$ brines. The concentration of the brine makes it challenging to dissolve more CO_2 as a result of an increase in brine density. The density of the brine is critical for CO_2 sequestration at the pore scale, and CO_2 storability is also affected by the composition of the rock during injection.
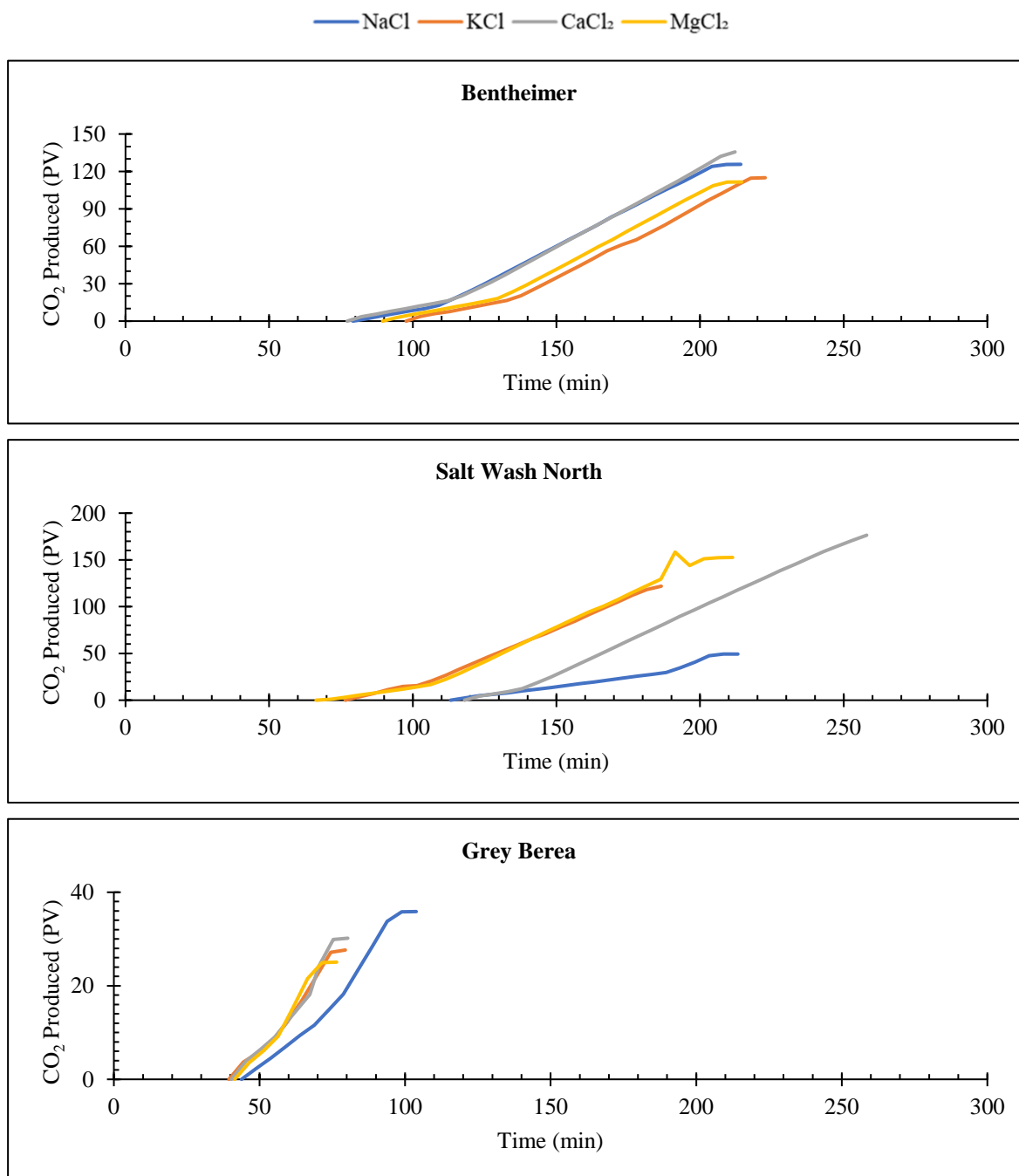
Figure 4.18: CO$_2$ collected after saturating the core sample with 25 wt.% brine

Moreso, for Grey Berea sandstone saturated with 25 wt.% brine concentration, the breakthrough time is very close to one another and are between the range of 39.50 to 43.54 minutes. This meant that less CO_2 could be kept at this concentration. As a result of the increased brine density, the concentration of the brine makes it difficult to dissolve more CO_2.

4.3.2.4. Effect of Different Salts and Concentrations on CO_2 Solubility

There is a consistency in the amount of CO_2 produced from 5 wt.% to 10 wt.% salinity experiments in all the flooding scenarios. At 5 wt.%, more CO_2 was produced in $CaCl_2$ brine as compared to other brines, with NaCl having the least CO_2 produced. This indicated that more CO_2 was dissolved in NaCl than $CaCl_2$ in Bentheimer core sample by solubility trapping as well as capillary and structural mechanisms. This incremental trend of CO_2 produced from 5 wt.% to 10 wt.% can be related to the salinity of the brine, in that, as salinity increases, the amount of CO_2 produced also increases. In addition, at this 5 wt.% concentration, a significant amount of CO_2 was dissolved in the brine, thereby resulting in a further increase in brine density. As the density increases, it reduces the free path of the gas and creates an avenue for trapping and storing CO_2 gas. In this regard, CO_2 occupied more of the pore spaces within the core sample because of higher capillary pressure and, thus, interfacial tension at the time where the brine gets more saturated with the CO_2. Therefore, a further increase in density leads to less CO_2 trapping due to an increase in the interfacial tension between the brine and the CO_2; hence, not much interaction in terms of dissolution. Furthermore, by considering the amount of CO_2 dissolved/stored and produced with respect to the 10 wt.% salinity, it is pertinent to point out that, comparatively, CO_2 storage was poor in lieu of the 5 wt.% concentration. This is because the brine had occupied more of the pore spaces and the solubility of CO_2 in this brine is lower than the preceding one and eventually resulted in the excessive production and lower storage of CO_2 in the core sample. The interaction between CO_2, the 10 wt.% brines (NaCl, $CaCl_2$, KCl, and $MgCl_2$), and the core sample was not very pronounced here as compared to the 5 wt.% brines.

Moreso, At the 10 wt.% salinity, there was no significant or drastic change in density of the brine as the CO_2 traversed the core sample. A lower interaction of CO_2 and trapping within the core sample was realized at this brine salinity because of the higher amount of CO_2 produced, and thus less sequestration of CO_2 in the core sample was observed. In addition, there was a decline in CO_2 produced for the 15 wt.% brines in all the brine scenarios, with exception of the NaCl brine. This entailed significant storage of CO_2 as compared to the other brine salinities and the $CaCl_2$ brine possessed the highest CO_2 storability. This may be due to brine saturation

within the core sample, thus creating more room for CO_2 sequestration. This brine concentration provided substantial pathways for a better sweep efficiency of CO_2 within the core sample through a better brine distribution and profile along the longitudinal and transverse axes. Higher permeability could be responsible for more CO_2 trapping since there is no restriction in the interaction between the in-situ fluid and CO_2. Conversely, low permeability could lead to the restriction of flow, which negates the interaction between the fluids. In the case of the 15 wt.% salinity, significant pore spaces were occupied by the brine, which eventually plugs the narrow paths reduces room for CO_2 storage when it is injected into the core sample. Most of the narrower pore spaces of the core sample were occupied as a result of an increase in brine density [117]. Furthermore, as salinity increases, the solubility of CO_2 in the brine drastically decreases [114]. The brine (15 wt.%) has a higher density than the 10 wt.% brine, and so CO_2 was trapped within the pore spaces by virtue of an increase in density of the brine occupying the narrow pore space in the core sample. As observed from Figure 4.17 or the 20 wt.% concentration, KCl and $MgCl_2$ exhibited the same trend with respect to CO_2 production. This indicated that both brines stored similar amounts of CO_2 in the core sample at the 20 wt.% salinity while the highest CO_2 storage was observed for the NaCl and $CaCl_2$ brines. There is not much tendency for CO_2 to be stored at 25 wt.% because of the high density of the brine. Although an appreciable amount of CO_2 can be stored in the KCl and $MgCl_2$ brines as compared to the NaCl and $CaCl_2$ brines. The density of the brine played an important role for CO_2 sequestration at the pore scale, and CO_2 storability also depends on the nature of the rock during injection as a result of the offset of the local equilibrium. This offset results in changes in the petrophysical nature of the formation.

4.3.2.5. Effect of Different Salts and Concentrations on Porosity and Permeability Reduction

After the core flooding experiments with different brine compositions and salt types, the porosity and permeability of the core sample were altered in comparison to reference measurements (as previously mentioned). Table 4.19 summarises reduction in porosity and permeability with varying salt and brine concentrations. Porosity decreases increases down the trend in all the core samples with Bentheimer core sample ranging from 1.15 % to 6.15 % for NaCl brine compositions ranging from 5 wt.% to 25 wt.%, whereas permeability reduction ranged from 37 % to 51.7 %. This suggests that increasing the brine concentration reduces both the porosity and permeability of the core samples, hence decreasing CO_2 injectivity.

Table 4.19: Summary of porosity and permeability reduction for different sandstone core samples

	Salt Conc. [%]	Porosity Reduction [%]			Permeability Variation [%]		
		BEN	SWN	GB	BEN	SWN	GB
NaCl	5	1.15	0.21	7.7	37.0	30.8	16.6
	10	1.88	0.55	9.5	42.0	35.8	26.2
	15	3.42	2.97	12.3	49.1	42.9	34.7
	20	3.55	3.09	14.9	50.0	43.8	40.5
	25	6.15	5.25	17.3	51.7	45.5	45.2
KCl	5	3.50	1.81	35.4	19.4	13.2	15.5
	10	24.57	3.95	38.2	27.5	21.3	22.1
	15	25.34	6.08	44.3	31.0	24.8	30.2
	20	27.39	9.98	50.1	37.0	30.0	40.4
	25	35.26	13.56	53.6	43.1	36.9	49.6
CaCl$_2$	5	20.80	1.34	30.5	17.1	10.9	18.7
	10	21.74	1.81	39.8	23.7	17.5	26.9
	15	24.81	7.24	40.1	31.0	24.8	37.5
	20	33.58	14.72	46.2	40.8	34.6	44.6
	25	33.82	18.66	48.9	44.2	41.7	50.6
MgCl$_2$	5	22.82	5.35	36.0	44.2	33.8	47.3
	10	24.79	7.96	40.4	56.1	38.4	58.2
	15	34.19	9.23	48.8	61.3	41.5	63.4
	20	36.15	18.70	53.3	62.1	44.2	65.6
	25	40.94	20.22	57.2	63.3	56.3	67.2

For clarity and easy understanding of the trend in the reduction of porosity and variation of permeability, Table 4.19 is represented graphically as shown below for all the core samples at different brine concentrations as well as salt types.
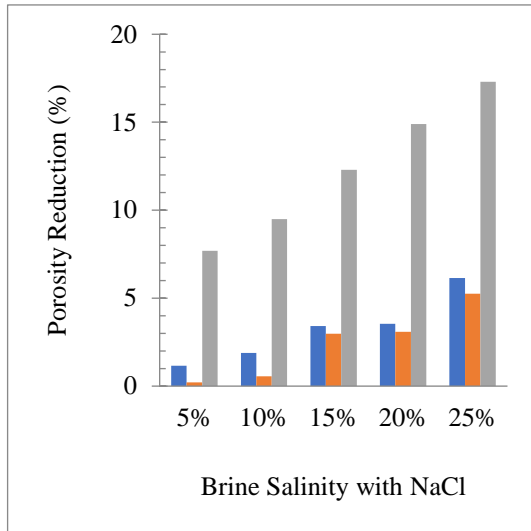
Figure 4.19: Porosity reduction vs Brine (NaCl) with different salinity
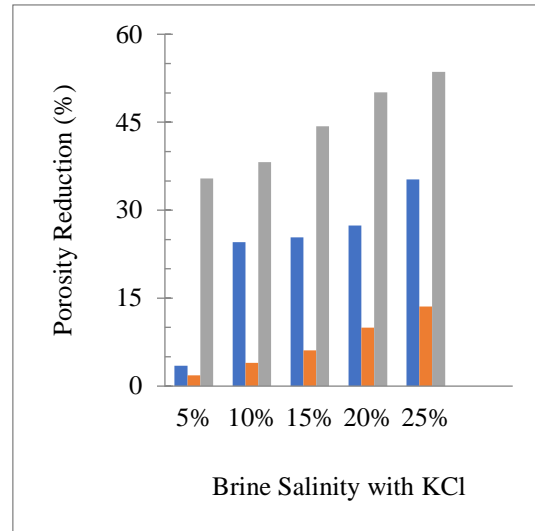
Figure 4.20: Porosity reduction vs Brine (KCl) with different salinity
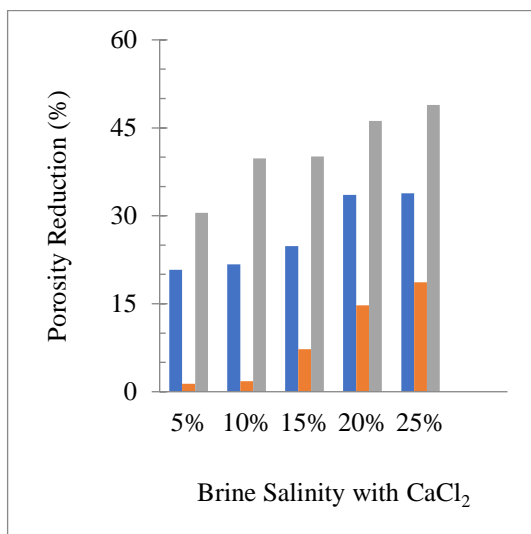
Figure 4.21: Porosity reduction vs Brine (CaCl₂) with different salinity
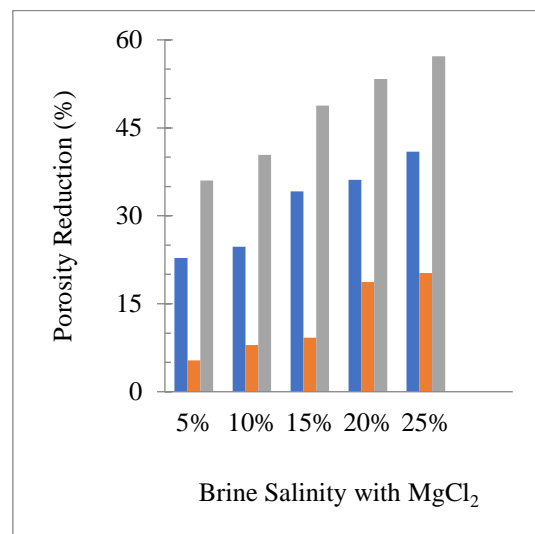
Figure 4.22: Porosity reduction vs Brine (MgCl₂) with different salinity
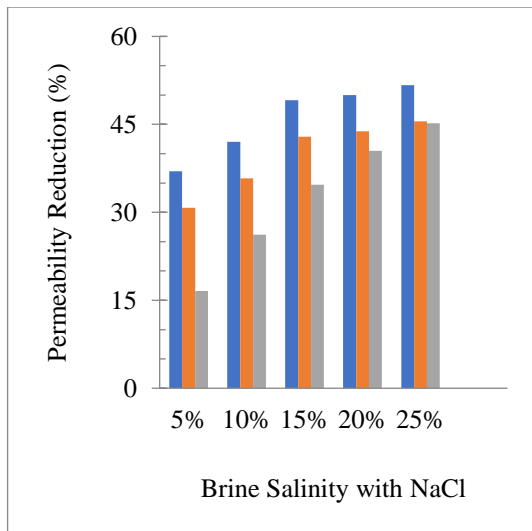
Figure 4.23: Permeability variation vs Brine (NaCl) with different salinity
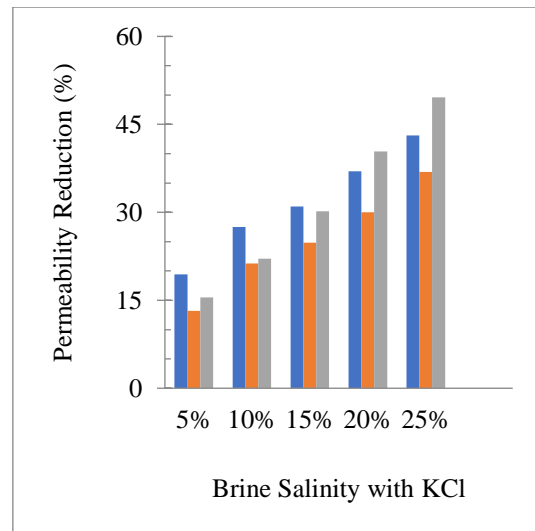
Figure 4.24: Permeability variation vs Brine (KCl) with different salinity
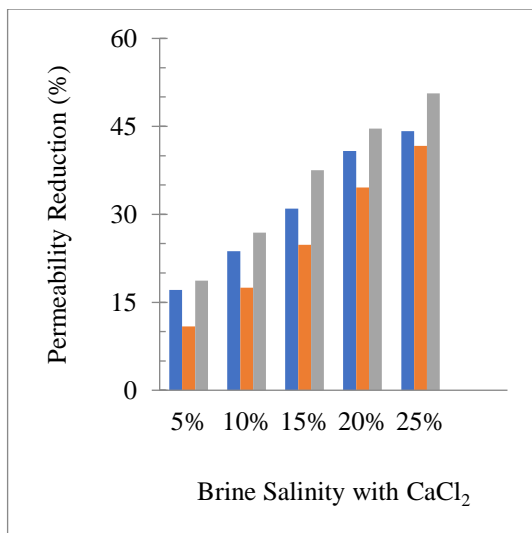
Figure 4.25: Permeability variation vs Brine (CaCl₂) with different salinity
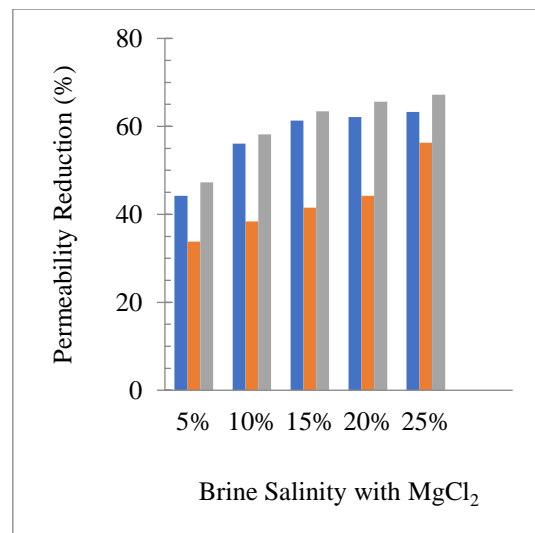
Figure 4.26: Permeability vs Brine (MgCl₂) with different salinity

Higher porosity decrease was seen in KCl brine, with a 3.5 percent reduction in 5 wt.% and 35.3% reduction in 25 wt.% KCl brine compositions. The degree of porosity reduction here is greater than that of the NaCl brine. This is due to the presence of precipitated salt after CO_2 injection, which has drying effects and gradually plugs the smaller, narrower pores, causing the core sample to have fewer convoluted flow routes. In this situation, however, there was a lower decline in permeability, with 19.4% and 43.1% reflecting the lowest and highest brine

compositions, respectively. These differences in porosity and permeability make comparing the salting-out effects of NaCl and $CaCl_2$ more difficult.

As a result, a greater degree of porosity reduction was seen in the varied amounts of brine prepared from $CaCl_2$ salt. The lowest $CaCl_2$ brine concentration was found to have a 20.8 % reduction in porosity, while the 25 wt.% brine had a 33.8 % reduction. When compared to NaCl brine, all concentrations of this brine have a higher degree of pore space blockage or plugging. Thus, the permeability of the core sample decreased as the brine content increased.

The brine prepared from $MgCl_2$ had the greatest drop in reservoir characteristics (porosity and permeability) of the core sample. The decrease in these parameters showed that there is more salt deposition inside the core sample. For the maximum brine concentration prepared from $MgCl_2$, porosity was reduced by 40.9 percent, while permeability was reduced by 63.3 percent. As a result, increasing the brine content reduced both the porosity and permeability of all the core samples.

Based on the results, it is obvious that the best salinity in terms of performance for CO_2 storage in the deep saline aquifer is between 10 and 20 wt.%, and this can be utilised as a screening criterion. Furthermore, reservoirs with large quantities of divalent ions are poor candidates for sequestration. KCl also has an effect on CO_2 storage in deep saline aquifers. Interestingly, the interaction between the salt and the brine has a significant impact in the drying-out effect and, hence, CO_2 storability. The pressure decay tests demonstrated CO_2 solubility in various brine concentrations and types, indicating that brines with higher CO_2 solubilities can effectively deliver superior sequestration. However, this was not the case, as later CO_2 storage studies revealed a different narrative. The ability of salt to precipitate out of solution is also linked to its solubility, and as a result, the drying-out effect and CO_2 storability will be influenced by this phenomenon.

The findings clearly demonstrated that aquifers containing a high fraction of divalent salts are likely to pose issues to injectivity during CO_2 aquifer storage. This comes in the form of reduced permeability and porosity, as well as increased CO_2 solubility in brine. The research focused solely on fluid interactions (CO_2 and brines), leaving out the reactive proponent—the rock. This is done to better understand how salt type and concentration affect overall sequestration processes. Individual testing was required to determine their distinct dispositions when it comes to injectivity studies in porous material under increased reservoir conditions. As a result, this information will be useful in screening storage sites for a successful injection approach.

These findings may have an impact on harnessing the potential of an aquifer to leverage all CO_2 trapping mechanisms. The dominating salt type in terms of mineralization, solubility, and ability to trap free CO_2 can be used to determine preference for the type of trapping mechanism. The shortcoming of this study is that it only relates to sandstone rocks, and this impact may not be applicable to more reactive formation types such as carbonates; yet it is indicative of probable underlying assumptions.

4.3.3. Characterisation of the Core Samples – After Remediation (Low Salinity and Seawater)

This section presents the findings for the effects of different brine types at 20 wt.% concentration on two different core samples (Bentheimer and Salt Wash North), flow behaviour during core flooding, the use of remediation fluids (low salinity brine with 0.5 wt.%, and Seawater with 3.5 wt.% salinity) to abate the precipitated salt during core flooding, and the effects of remediation fluids on the porosity and permeability of the core samples respectively. This concentration (20 wt.%) and core samples were chosen for the remediation experiments as a result of adequate evidence of salt precipitation. It has been established that CO_2 reaches its critical condition at a temperature of 31 °C (88 °F) and pressure of 7.38 MPa (1070 psia) [117]. According to Yang et al. [72], deep saline aquifers in a sandstone formation extend up to 2400 m (8000 ft) deep and 20 °C/km (1.4 °F/100 ft); as a result, the temperature chosen for this experiment was 45 °C. In addition, the injection pressure was kept constant between 1100 and 1200 psig to replicate reservoir pressure (1500 Psig). As a result, at these conditions, CO_2 will remain supercritical during the simulated CO_2 injection experiment. The temperature of the system was kept constant throughout the investigation to preserve homogeneity, and different remediation fluids were injected immediately after salt precipitation based on our prior investigations [39]. The results for the remediation test using low salinity brine after initial saturation of core samples with 20 wt.% of different brines are shown in Table 4.20. This Table also show the results of the remediation test utilising sea water after initial saturation of core samples with 20 wt.% of various brine.

Table 4.20: Core flooding after saturation of core samples with 20 wt.% of different brines and followed by injection of low salinity brine and seawater

	Bentheimer				Salt Wash North			
	NaCl	KCl	$CaCl_2$	$MgCl_2$	NaCl	KCl	$CaCl_2$	$MgCl_2$
With Injection of Low Salinity Brine (0.5 wt.%)								
Brine Breakthrough Time (min)	97.17	99.50	84.83	76.17	102.34	93.17	88.00	86.01
dP (psig)	0.99	0.62	0.78	0.85	1.07	0.81	1.03	0.83
CO_2 Breakthrough Time (min)	48.53	73.17	97.67	91.17	47.50	101	97.17	92.17
dP (psig)	1.00	0.66	0.92	2.22	1.44	1.03	1.59	1.75
Brine Saturation (%)	89	90	90	94	93	89	94	95
Volume of CO_2 collected before injection of low salinity (Litres)	1.25	3.09	4.19	5.83	2.34	3.86	3.35	4.12
Low Salinity Injection Time (min)	107.17	109.50	102.67	95.51	112.34	110.83	103.17	96.67
Volume of CO_2 collected after injection of low salinity (Litres)	5.34	5.89	6.01	6.38	4.95	5.08	5.32	6.03
With Injection of Seawater (3.5 wt.% salt concentration)								
Brine Breakthrough Time (min)	112.17	76.18	86.01	84.17	81.83	82.01	85.83	82.67
dP (psig)	0.69	0.68	0.71	0.69	0.70	0.73	0.68	0.71
CO_2 Breakthrough Time (min)	113.51	87.01	91.51	98.83	91.67	90.51	96.83	100.83
dP (psig)	0.70	0.73	0.66	0.70	0.91	0.89	0.70	0.79
Brine Saturation (%)	85	92	97	95	91	85	91	95
Volume of CO_2 collected before injection of low salinity (Litres)	1.55	2.99	3.99	5.72	2.30	3.88	3.37	4.15
Low Salinity Injection Time (min)	123.17	97.01	102.34	114.17	101.67	100.51	114.00	115.67
Volume of CO_2 collected after injection of low salinity (Litres)	5.23	5.01	4.70	5.83	4.27	4.35	4.58	4.29

For clarity and easy understanding of Table 4.20, it is represented graphically as shown below (Figure 4.27 to Figure 4.30) for all the core samples used for remediation test after saturating the core sample with 20 wt.% brine from different salt types.
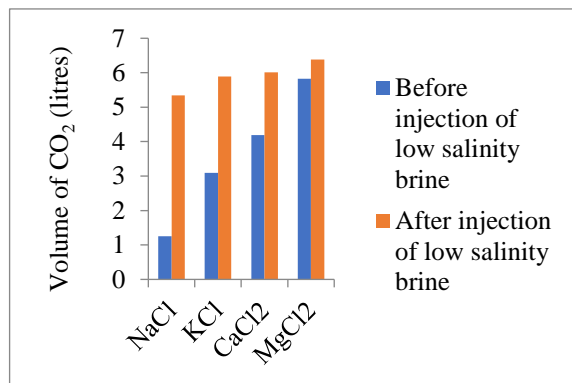
Figure 4.27: Remediation with injection of low salinity brine (0.5 wt.%) in Benthemier sample
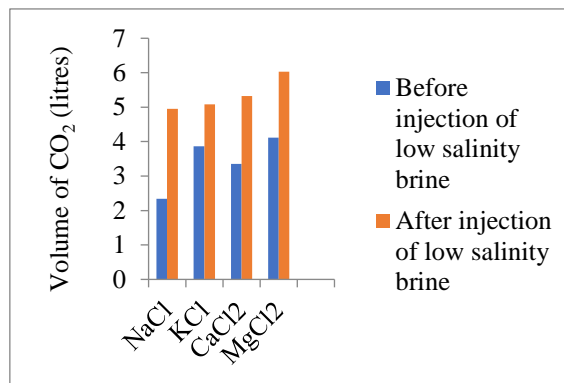
Figure 4.28: Remediation with injection of low salinity brine (0.5 wt.%) in Salt Wash North
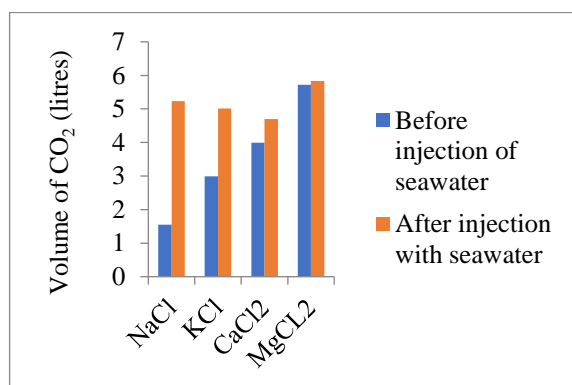
Figure 4.29: Remediation with injection of seawater in Bentheimer sample
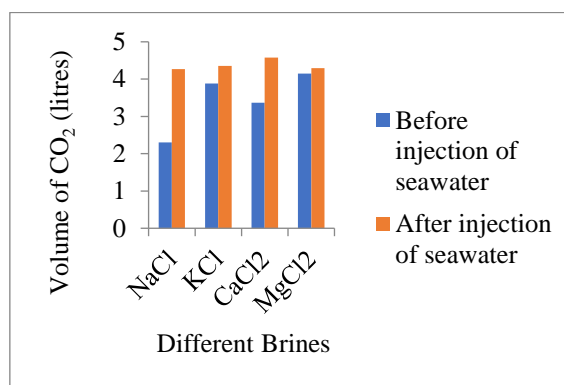
Figure 4.30: Remediation with injection of seawater in Salt Wash North samples

Precipitation of salts within the core sample was particularly noticeable at higher concentrations due to salting out and drying out effects. One of the mechanisms underlying these events was the evaporation of brine into the injected CO_2 stream [16, 42, 114]. In this investigation, 20 wt.% brine from the four major salt types found in deep saline aquifers was employed. This narrowed and eventually closed the smaller pore spaces of the sandstone core sample tested, as evidenced by an increase in differential pressures during flooding [39]. To fight the effect of precipitated salt, remediation fluids such as low salinity brine (0.5 wt.%) and seawater (3.5 wt.%) were utilised, with the projection of consequently enhancing CO_2 storage capacity.

Furthermore, based on our previous experimental work [38-40] the onset of the remediation procedure can be justified. This is the time when the precipitation effect or salt particle nucleation occurs. More so, depending on the pore volume (PV) of the core sample, a standard slug size of 10% was utilised. This refers to the injection of 10% remediation fluid, which was relative to the pore volume of the independent core sample. This slug size would present the ideal protocol as it has represented the most suitable scenarios based on the injection rates tested.

4.3.3.1. CO_2-Brine-Remediation Fluids Flow Behaviour

As the solubility of CO_2 in brine decrease with increasing concentration, salting-out effects become prominent, increasing the rate of interaction between the two fluids as the flow pathways of the injected CO_2 within the pore spaces become progressively constrained due to salt precipitation. The flow behaviour of the injected CO_2 as it contacts the brine and remediation fluid as it dissolves the precipitated salt can be used to identify a typical determinant of these flow constraints. The differential pressure (dP) variation throughout the core flooding process is the best approach to examine flow behaviour. The dP versus time graph in Figure 4.31 demonstrates the flow behaviour of supercritical CO_2 in a saturated Bentheimer core sample, followed by a flooding scenario with remediation fluid (low salinity brine). The flow behaviour and breakthrough times of each salt type flooding experiment can thus be compared. And, as shown, the flow behaviour adopted a regular displacement pattern with nearly constant dP prior to the CO_2 breakthrough. The peaks in the graphs represent CO_2 breakthrough. The first peak represents CO_2 breakthrough from a core sample saturated with various brines, while the second peak represents CO_2 breakthrough following injection of remediation fluid.
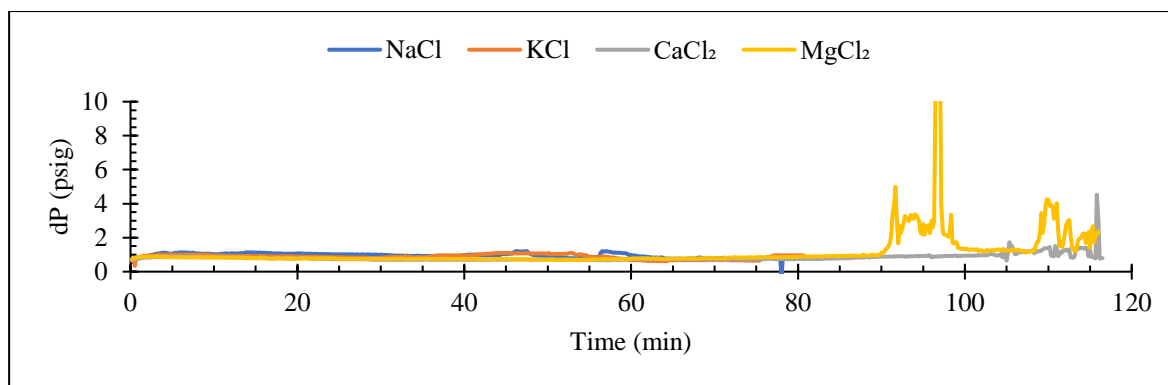
Figure 4.31: Differential pressure profile for low salinity brine (remediation fluid) in Bentheimer core sample

In divalent brine ($MgCl_2$, $CaCl_2$), CO_2 breakthrough occurred earlier than in monovalent brine (NaCl, KCl). This means that a significant amount of CO_2 was dissolved in KCl, NaCl brines, as opposed to $MgCl_2$, $CaCl_2$ brines, which demonstrated late breakthrough time, as with all experiments performed under the same conditions with extremely strong reproducibility. This is due to a reduction in the pore volume of the core sample occupied by higher density multivalent brines within the core sample's pore matrix. As CO_2 is constantly injected into the core sample, the concentration of dissolved salt in the brine increases, and when the concentration of salt surpasses its saturation limits, surplus salt precipitates. At this stage, injectivity is compromised, and it is necessary to introduce remediation fluid into the system to avoid injectivity issues during CO_2 injection. Injection of remediation fluid (low salinity brine) at this juncture leads to a drastic change in dP. This increase in dP is due to the higher density and viscosity of the remediation fluid. The magnitude of dP towards the end of the remediation process is lower than pre-flush in the case of monovalent salt (NaCl, KCl) than the divalent salt. This illustrates that more pore spaces are opened for traversing and storage of CO_2. This is further evidenced by the amount of CO_2 collected after flushing the core sample with the low salinity brine, as seen in Table 4.11.

For the Salt Wash North core sample, shown in Figure 4.32, the trend was like the previous sample before injection of the low salinity remediation brine, but a different trend was realised after injection, in that, the scale and magnitude of the dP were higher than the Bentheimer run. Interestingly, the divalent brine showed a peculiar behaviour of having early breakthroughs compared to monovalent brines. This suggested that a large amount of CO_2 was dissolved in KCl and NaCl brines compared to $MgCl_2$, and $CaCl_2$ brines, which displayed late breakthrough

time, as with all experiments performed under identical conditions and with exceptionally high reproducibility.
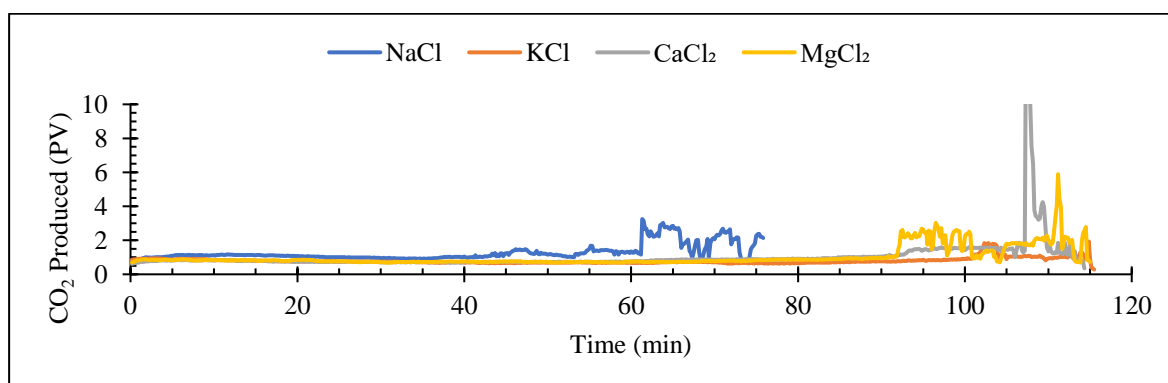
Figure 4.32: Differential pressure profile for low salinity brine (remediation fluid) in Salt Wash North core sample

The salting out effect, which is characterised by a continuous increase in dP after CO_2 breakthrough, was particularly prominent in the divalent salts. $CaCl_2$ exhibits a significant increase in dP following breakthrough when compared to $MgCl_2$, the other divalent brine. This is consistent with the findings of [114, 118] who discovered that $CaCl_2$ was more susceptible to salting out than $MgCl_2$ under various operating circumstances. After the remediation operation in the sample saturated with NaCl and KCl, dP becomes stable within a modest dP range, indicating that a significant amount of precipitated salt has been eliminated from the core sample. However, there was a constant rise in dP for the $MgCl_2$, and $CaCl_2$ brines systems, exhibiting a restricted flow with permeability impairment. Furthermore, because the same wt.% concentration of salts was employed in the saturation of the core sample prior to the remediation process, the pore channels were greatly reduced, allowing less uncontrolled movement through the pore matrix. This fact can be assessed using the volume of CO_2 collected before introducing remediation fluid.

4.3.3.2. CO_2-Seawater-Remediation Fluids Flow Behaviour

The flow behaviour with seawater as a remediation fluid, as illustrated in Figure 4.33, took a distinct turn in that the magnitude of dP following injection of saltwater differs significantly from that of the low salinity brine. For CO_2 passing through saturated brine, the average dP from 0 to 90 minutes was an average of 0.9 psig. There was no tailing of CO_2 after the remediation method, which could aid in a more accurate comparison before and after the test procedure.
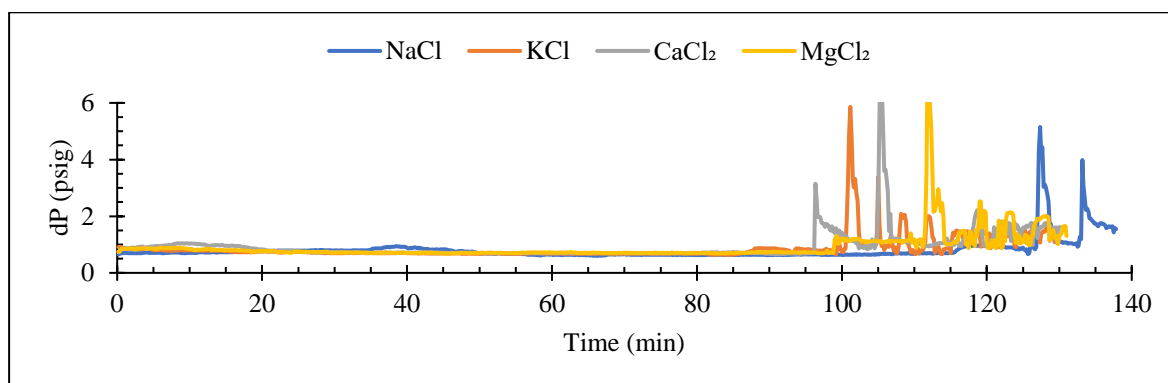
Figure 4.33: Differential pressure profile for sea water (remediation fluid) in Bentheimer core sample

Furthermore, the data indicated that permeability was constant prior to the injection of the remediation fluid (seawater). Fluctuations in DP were seen in the graph following the injection of remediation fluid, which might be attributable to variations in fluid characteristics and other matrix interactions within the core sample. KCl still had the highest dP, followed by $CaCl_2$, NaCl, and $MgCl_2$ in that order. This suggests that in the KCl brine saturated core, the resistance to the flow of CO_2 within the core sample was greater than in the other brine remediation test. These findings are consistent with the CO_2 breakthrough time indicated in the Tables 4.14, as KCl exhibits an earlier breakthrough than other brine systems. It was envisaged that once the injection of remediation fluid and CO_2 was stopped, the fluctuation patterns in dP would persist until dP became constant and CO_2 began to flow better. This was not exactly what was observed in the seawater remediation process, but it was demonstrated in the low salinity brine remediation test. As a result, it was projected that the average dP of the CO_2 injected after remediation would be lower than the average dP before seawater injection. As a result, the remediation procedure with low salinity fluid is more effective than with high salinity brine.
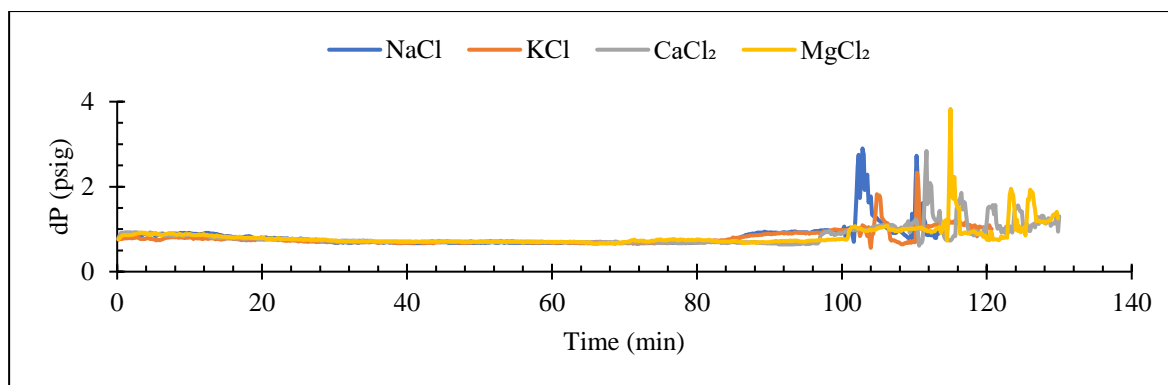
Figure 4.34: Differential pressure profile for seawater (remediation fluid) in Salt Wash North core sample

The Salt wash north core sample graph (Figure 4.34) depicts a very different fluid flow behavioural pattern than the Bentheimer, which depicts the identical remediation process with seawater. The CO_2 breakthrough time for the core sample saturated with monovalent salts is nearly the same, with a smaller magnitude of dP before to the remediation process as compared to a greater dP after the remediation process. One probable explanation for this disparity is the high concentration of seawater in comparison to low salinity brine. The breakthrough time for CO_2 in the core sample saturated with the divalent salt, on the other hand, differed, with $CaCl_2$ having an earlier breakthrough than $MgCl_2$. Thus, the magnitude of dP after the remediation method is greater than before the saltwater injection. Furthermore, once the injection of remediation fluid and CO_2 was discontinued, the fluctuation patterns in dP were expected to persist until dP became constant and CO_2 flow improved. This was not noticed during the seawater clean-up process in this core sample, but it was demonstrated during the low salinity brine remediation test in the same core sample. As a result, the remediation process using seawater in this core sample is less effective than the remediation test with low salinity brine.

4.3.3.3. Porosity and Permeability Variations

After core flooding runs with different brine compositions (Salt types), the porosity and permeability of the core sample altered in comparison to reference data. At the same operating circumstances, remediation fluids such as low salinity brine and high salinity brine were utilised to remove the precipitated salt from the pore spaces of the samples under investigation. Table 4.21 highlights the results of the sandstone samples' reduction in porosity and permeability prior to remediation treatments, as well as the rise in porosity and permeability after remediation.

Table 4.21: Porosity and Permeability Variations After Remediation

	Low Salinity Brine (0.5 wt.%)				Seawater (3.5 wt.%)			
	% Reduction in Porosity (After core flooding)	% Increase in Porosity (After remediation)	% Reduction in Permeability (After core flooding)	% Increase in Permeability (After remediation)	% Reduction in Porosity (After core flooding)	% Increase in Porosity (After remediation)	% Reduction in Permeability (After core flooding)	% Increase in Permeability (After remediation)
Benthiermer								
NaCl	13.6	22.7	50.0	64.5	16.9	11.7	40.1	15.1
KCl	24.8	20.7	40.8	65.3	22.7	12.9	39.3	17.2
$CaCl_2$	27.4	16.7	37.0	53.2	28.3	8.3	41.5	12.6
$MgCl_2$	36.2	15.6	36.2	50.1	34.1	6.5	52.8	10.2
Salt Wash North								
NaCl	10.2	24.8	49.1	68.4	18.3	6.7	50.3	12.1
KCl	22.8	18.5	34.5	45.3	25.2	10.5	31.8	13.7
$CaCl_2$	14.1	14.0	48.6	43.2	12.1	3.1	32.5	8.8
$MgCl_2$	18.7	28.5	52.2	40.6	15.8	2.2	35.0	7.4

4.3.3.3.1. Porosity Variations

The remediation fluids (low salinity brine and seawater) increased the Porosity and permeability of core samples by different orders of magnitude, as shown in Table 4.22. Throughout the cleaning procedure, it is reasonable to claim that salt removal from core samples was quite effective, with low brine salinity compared to seawater. The results obtained for the reductions in Porosity and permeability align with our previous work [38-40]. It's also in line with those published in the literature [15, 35, 119-121]. The Porosity of the Bentheimer core sample indicates various declinations irrespective of the salt type used for initial saturation for core flooding. For example, the saturated sample with $CaCl_2$ experienced the highest reduction in Porosity, while the sample saturated with NaCl showed the lowest drop in porosity. By removing the salt via low salinity remediation fluid, an increase in Porosity was mostly observed in the sample saturated with monovalent salts compared to the divalent salt. On the other hand, the rise in Porosity was not well pronounced when using high salinity brine as the remediation fluid. This is due to the high concentration of seawater compared to low salinity brine. Also, remediation with high salinity brine (Seawater) could not effectively open the pores and pore throats which could have been partially or fully blocked with salt. This could significantly lower the hydraulic connectivity of the fluid phases and reduce CO_2 storage in the formation.

More so, porosity reduction of Sea wash north core sample did not follow the same train as observed in Bentheimer core sample in terms of the brine used for core sample saturation before core flooding. This showed that the rate of salt deposition differs from one reservoir due to differences in the petrophysical properties of each reservoir. In this case, salt deposition was very high in the core sample initially saturated with KCl brine with a total reduction of 14.1% of the sample porosity. A lower reduction in porosity was also observed for samples initially saturated with NaCl, just like that found in the Bentheimer core sample. The remediation exercise was very effective with low salinity brine with an increase in porosity of 18.3% and 25.2% for salt north wash sample initially saturated with NaCl and KCl, respectively. However, remediation with seawater proves ineffective, noticeable in the two divalent brines with a bit of increase of 1.1% and 1.2% for sandstones saturated with $CaCl_2$ and $MgCl_2$ brines, respectively.

4.3.3.3.2. Permeability Variations

With the pore size distributions of sandstone core samples used in this study, it is apparent that the precipitated salt crystals could easily occlude the pore space and significantly reduce the

permeability of the rock. However, it is also worth noting that the precipitated salt may partially or fully block the flow paths in the rock, giving rise to unrealistic measurements of the various transport properties of the medium, especially permeability. Bentheimer core sample has the highest permeability value compared to salt wash north core sample. Thus, fluid flow is enormous in this core sample than others since it has the highest capacity to transmit fluid. From a previous study, divalent brine was found to exhibit a robust salting out effect in the presence of CO_2 compared to monovalent brines [73]. This phenomenon will most assuredly have substantial effects on the intricacies and channels of the pore matrix as observed in this porous medium. Thus, the core sample saturated with these so-called divalent brines has a higher permeability reduction than core rocks saturated with monovalent brines (Table 4.22). During the remediation process, the decrease in pressure drops across this sample, and subsequent increase in absolute permeability, indicated a successful cleaning process in opening the blocked flow path via low salinity remediation fluid. The result obtained using seawater is not as effective as compared to low salinity after saturation of the core samples with different brine. Thus, 64.5% and 15.1% increase in permeability were obtained for low salinity and seawater remediation fluids, respectively.

Permeability reduction/impairment is also eminent in the Salt wash north core sample without doubt of salt precipitation during core flooding. This restriction to flow eventually increases the interstitial velocity of the CO_2 as it traverses the core sample, thereby indicating that the deposition of salt crystal could block most of the pores. Thus, this leads to significantly lowering the fluid phase's hydraulic connectivity. This, in turn, may decrease the mobility of CO_2 in the porous medium and significantly impact the storage capacity of chosen aquifer. Thus, a more significant reduction in permeability is observed with the sample saturated with $CaCl_2$ and $MgCl_2$ than the sample saturated with NaCl and KCl, respectively. An increase in permeability was seen to increase with this core sample after successfully conducting a remediation test with low salinity and was found to be 68.4%. On the other hand, remediation with the seawater was found to be 13.7%, irrespective of the salt type used for core flooding.

4.4. Phase-III: Qualitative Analysis

This section provides a summary of the results for Scanning Electron Microscopy (SEM) and Energy Dispersive X-Ray (EDX) analysis to discover the physical phenomenon underlying the use of different fluids to remediate salt precipitation in distinct core samples. Then, using EDX and mapping from scanning electron microscopy, we examine precipitation and repair this effect in sandstone.

Several tiny rock pieces required for EDX-SEM imaging were cut from the core plugs to study the likelihood of salt precipitation and the presence of solid salt in the pore space because of variations in pressure and temperature conditions. The specimen was sliced from one of the core sample's two end faces after the core flooding, and remediation process and prepared for imaging using the process outlined in Section 3.5.

4.4.1. Mapping analysis from EDX using SEM on Bentheimer core sample

It is critical to investigate the impact of these salts in the context of salt precipitation and how to best minimise or eliminate them during CO_2 storage in a deep saline aquifer. The core samples' SEM examination revealed a large amount of salt precipitate. Salt crystals filled the pore walls and partially or completely occupied some pore elements and fissures, as shown in these pictures.

NaCl

KCl

(a)

(b)

(c)

(d)
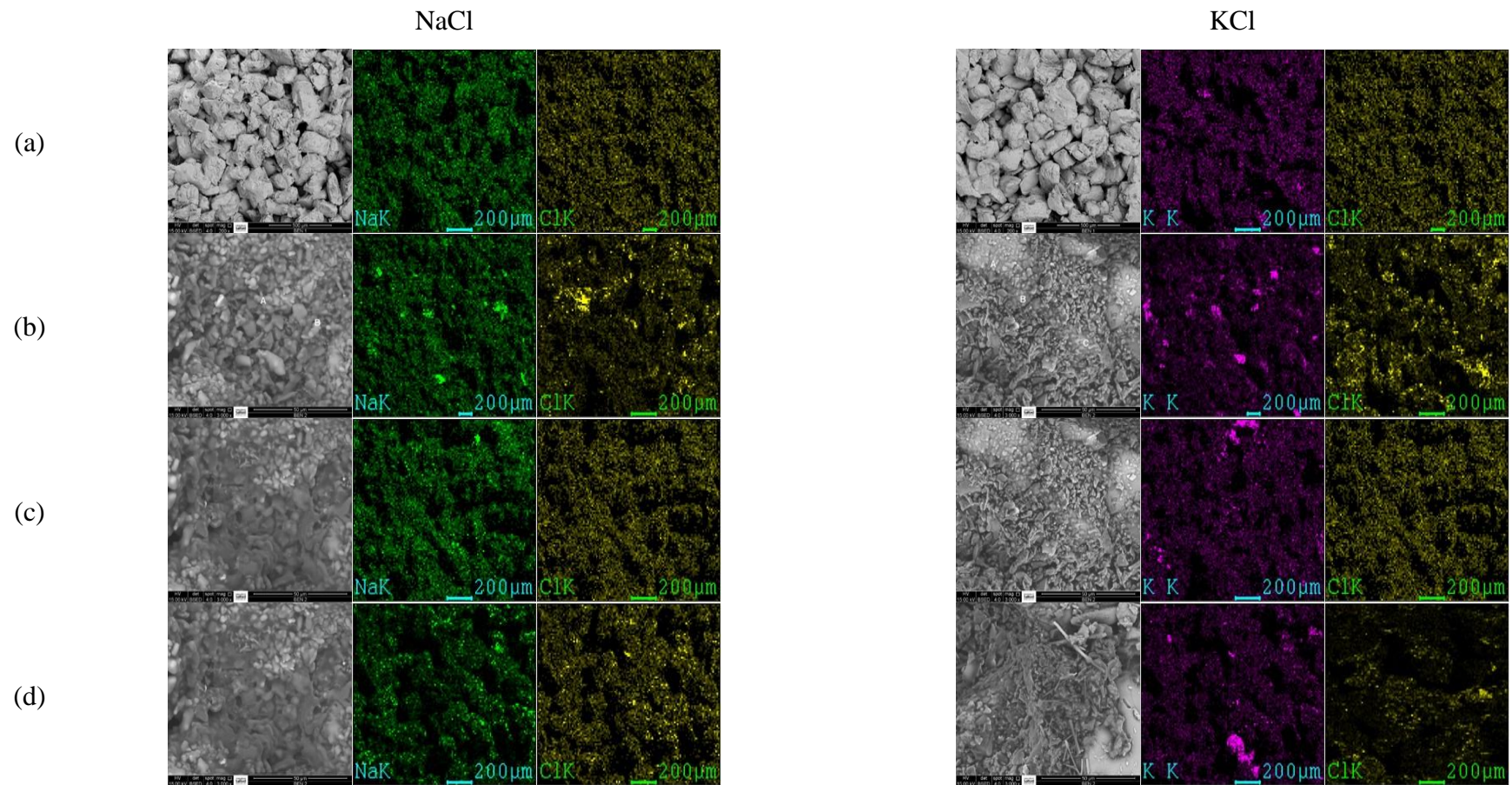
Figure 4.35: Mapping analysis from EDX using scanning electron microscopy for Benthemier core sample saturated with NaCl and KCl: (a) Before core flooding, (b) After core flooding, (c) After remediation with low salinity brine, (d) After remediation with sea water
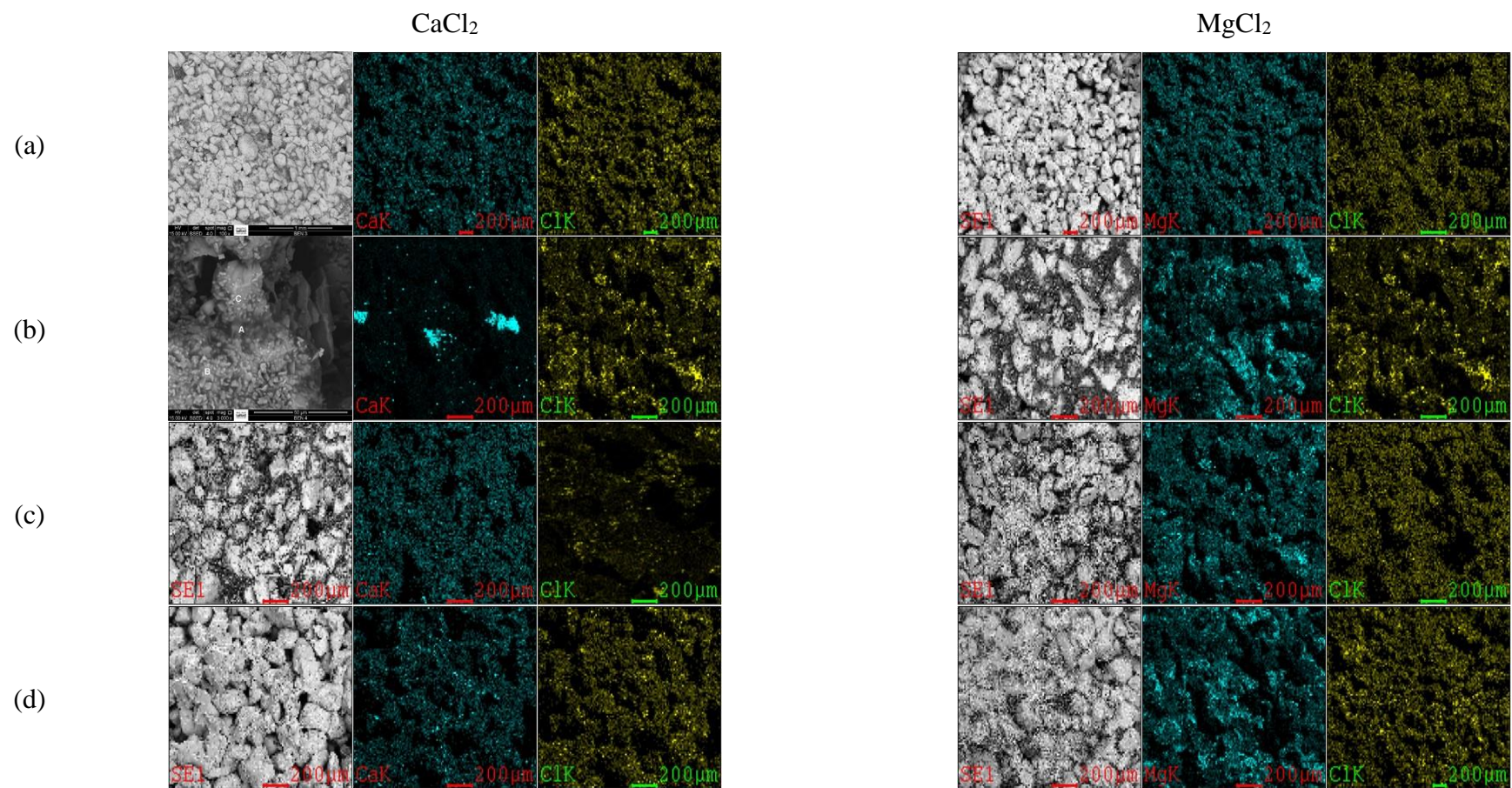
Figure 4.36: Mapping analysis from EDX using scanning electron microscopy for Benthemier core sample saturated with CaCl$_2$ and MgCl$_2$: (a) Before core flooding, (b) After core flooding, (c) After remediation with low salinity brine, (d) After remediation with sea water

Furthermore, Figure 4.35 shows the salt crystals of Calcium Chloride ($CaCl_2$) and Magnesium Chloride ($MgCl_2$). The SEM scans also revealed that the core sample (Benthermier) contained considerably more NaCl crystals than KCl crystals.

The abundance and scarcity of these two forms of salt might be linked to their concentration in the formation brine as well as the order in which they precipitated during changes in the core's temperature-pressure circumstances. It should be noted that the formation brine includes various types of salt (such as $CaCl_2$ and $MgCl_2$) that have a strong salt out effect when exposed to CO_2.

The presence of salt in the pore spaces of the core sample (Figures 4.35 and 4.36) suggested that salt precipitation could restrict flow routes, preventing additional CO_2 input into the formation (deep saline aquifers). This impact reduces porosity and degrades rock permeability. The findings in this study clearly revealed that salts deposited as a result of formation brine evaporation can cause noticeable changes in the pore matrix and a decrease in pore connectivity of the formation near the well bore, creating injectivity issues.

Furthermore, it is of utmost important at this point to introduce a substance that is capable of removing the precipitated salt from the pore matrix so as to increase CO_2 injectivity as well as storability. Fluid prepared from different brine concentrations such as low salinity brine (0.5 wt.%) and Sea water (3.5 wt.%) was injected to remediate the menace of the precipitated salt. Based on our previous study, remediation fluid was initiated after stopping the injection of CO_2. At this point the effect of salt precipitation is most realised as well as the onset of the nucleation of the salt particle. A slug size of 10% of the remediation fluids based on the pore volume of each of the core samples were injected before continuation of injection of CO_2.

During the low salinity brine injection process, the pressure drop (dP) across the core sample decreased and this was attributed to the removal of salt from the pore spaces. This can be seen in the images (remediation with low salinity column) of the SEM picture alongside with the mapping results from the SEM image. On the other hand, the remediation action was not as effective as the former when applying sea water as a remediation fluid. This is likely due to the high concentration of sea water as compared to low salinity brine used in the cleansing process. Also, this is further evidenced from the mapping result obtained from both remediation scenarios. It is worth to note from the mapping result that, there is a reduction of precipitated salt after remediation processes as compared to that prior the injection of remediation with the greater part of the reduction witness in the remediation runs with low salinity. This reduction in the ions is prevalent in mono divalent salt (NaCl, KCl) than high divalent salt ($CaCl_2$, $MgCl_2$) as depicted in Figure 4.35 and Figure 4.36 respectively.

Furthermore, it is worth to note that the cleaning process was initiated slowly with the help of accumulator valve because of the presence of the salt crystals in the pore space, and later the valve was fully open as more pore elements were opened due to remediation fluid injection. Also, the slow nature of injecting the remediation fluid into a precipitated core samples aid in cubbing the thermal shock associated with high injection rate.

Figures 4.37 and 4.38 showed mapping analysis from EDX using scanning electron microscopy (SEM) with Salt wash north core sample saturated with different brines at the same level of saturation. SEM and EDX were carried out on the sample before core flooding, after core flooding (before remediation), after remediation with low salinity brine (0.5 wt.%), and with sea water (3.5 wt.%). As seen in the images from Figure 4.37, the presence of halite (NaCl) precipitants in the core sample was as a result of flooding CO_2 through the core plug initially saturated with 20 wt.% NaCl brine. Thus, the precipitant in the SEM images of the rock pore matrix were identified has halite based on EDX analysis as shown in Figure 4.37. Other precipitants such as carnallite ($KMgCl_3.6H_2O$), Antarcicite ($CaCl_2.6H_2O$), and Bischofite ($MgCl_2.6H_2O$), based on EDS analysis were identify from Figures 4.37 and 4.38 respectively. This is further confirmed from our operating condition (Temperature) which is 45 °C. Halite and Carnallite are form at 25 °C while Bischofite deposits when the temperature is greater than 35 °C [122].
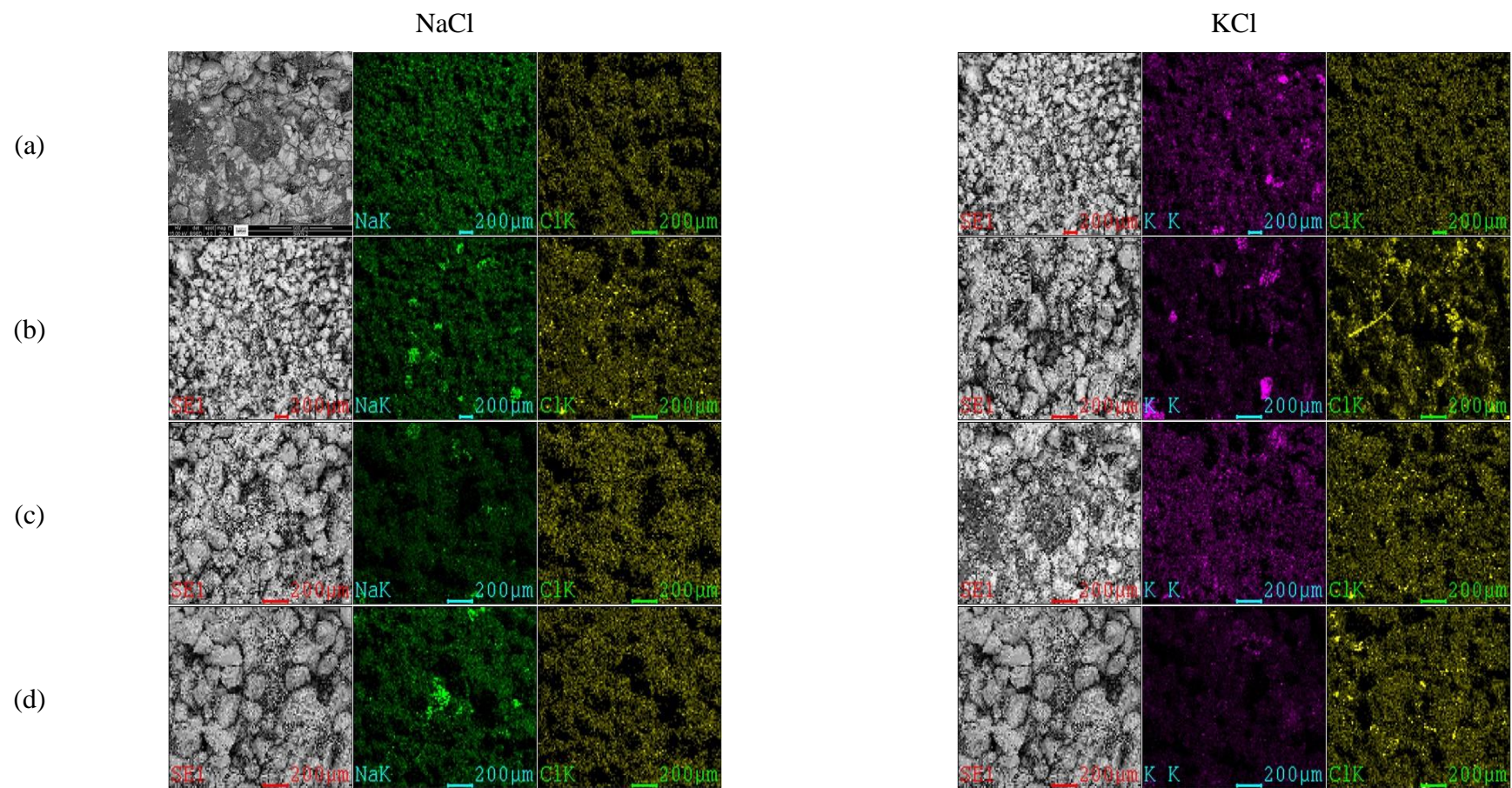
Figure 4.37: Mapping analysis from EDX using scanning electron microscopy for Salt Wash North core sample saturated with NaCl and KCl: (a) Before core flooding, (b) After core flooding, (c) After remediation with low salinity brine, (d) After remediation with sea water
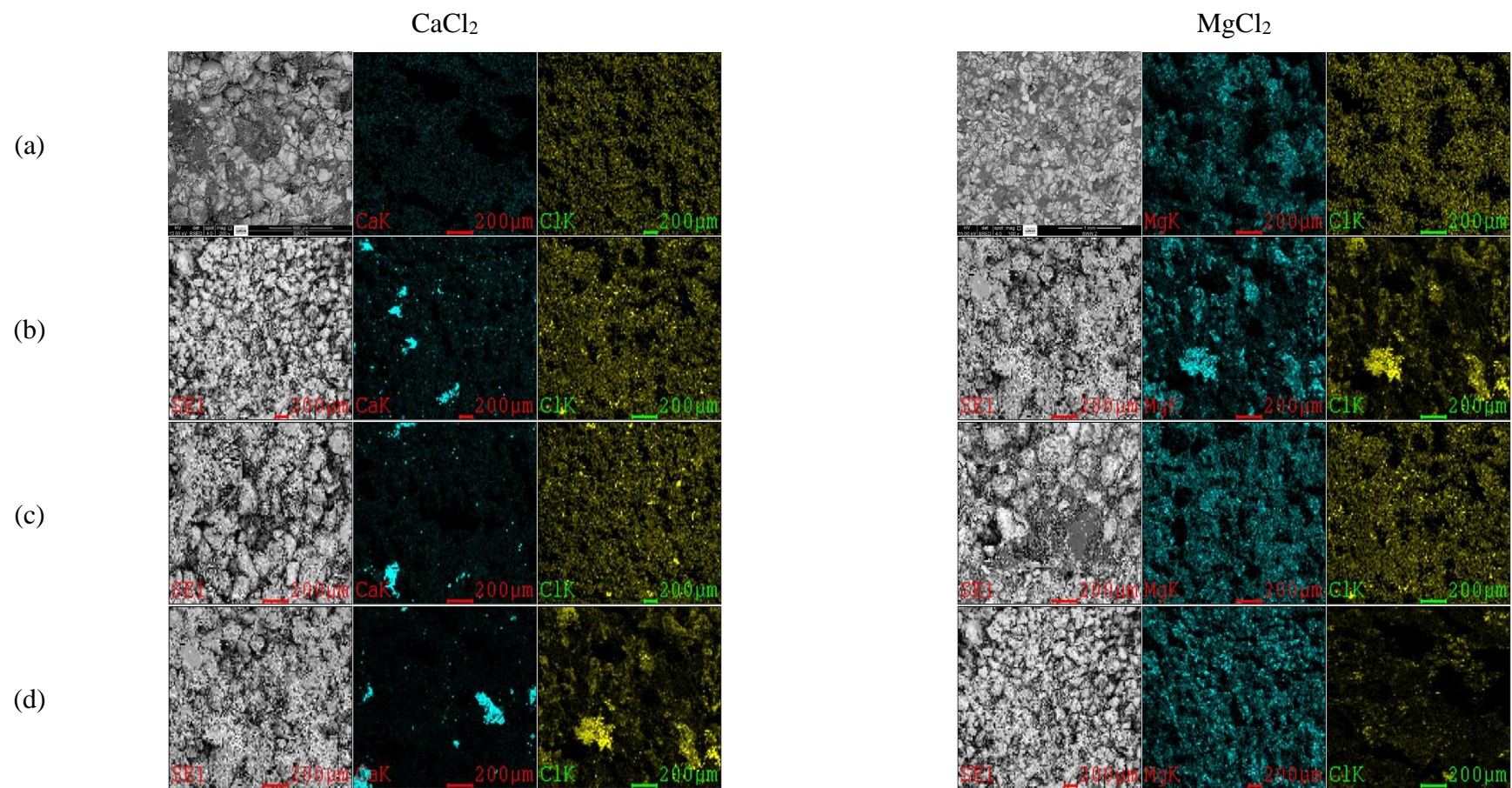
Figure 4.38: Mapping analysis from EDX using scanning electron microscopy for Salt Wash North core sample saturated with CaCl₂ and MgCl₂: (a) Before core flooding, (b) After core flooding, (c) After remediation with low salinity brine, (d) After remediation with sea water

The SEM analysis revealed a significant amount of salt precipitate and increased agglomeration of salts after core flooding as shown in the images. As observed in this figure, salt precipitate partially or wholly occupied the rock matrix and thereby blocking the pore space. The prevalence of salt within the pore spaces of the core sample indicated that salt precipitation might blocked flow paths, which could in turn prevent further injection of more CO_2 into the formation (deep saline aquifers). This effect impairs rock permeability as well as reduction in porosity. It is pertinent at this point to inject remediation fluid in order to open the pore spaces as well as CO_2 injectivity and the effect of these fluid on porosity and permeability will be discussed in our next session.

The observation in our previous study by Edem et al. [40] clearly demonstrated that salts deposited due to evaporation of the formation brine might result in noticeable changes in the pore matrix and decrease in pore connectivity of the formation near the well bore thereby causing injectivity problems. Thus, SEM analysis also revealed that greater portion of ions $(Na^+, K^+, Ca^{2+}, Mg^{2+})$ were removed during remediation procedure and thereby opening the pore spaces of the core sample. Greater portion of the ions were removed when low salinity brine was used as a mitigation fluid as compared to when sea water was used for the same purpose.

Thus, this chapter which is basically on the experimental results will lead to the next chapter which is on the conclusions and future work recommendations.

Chapter 5: Conclusions and Future Work Recommendations

5.1. Conclusions

The interaction between CO_2 and various salt concentrations in a core sample with respect to CO_2 storage and produced (collected), the solubility of carbon dioxide, pressure decay rate, CO_2-brine flow behaviour, and reduction of sandstone porosity and permeability as well as feasible remediation approaches to reduce the impacts of salt precipitation have been studied. This work has provided a framework to show interactions between CO_2-brine-sandstone and precipitation of salt during storage of CO_2 in deep saline aquifer. By carrying out different successful experiments to investigate these effects, several conclusions can be drawn with respect to salt types, brine salinity, and different experimental scenarios. These conclusions are stated as follows:

- The Porosity and permeability decreased drastically in all the core samples (Grey Berea, Bentheimer, Salt Wash North) as salinities increases. The most reduction in porosity and permeability was observed when the core sample was saturated with 25 wt.% brine. Thus, increase in salinity leads to decreased in dissolution of CO_2 in brine which promote the near well bore formation dry out and salt deposition problems.

- The optimum range for CO_2 sequestration in deep saline aquifers is within the range of 10 to 20 wt.% concentration (salinity). A substantial volume of CO_2 was found to be stored at this range of brine concentration.

- An increase in the brine density because of increase in salinity reduces the free flow path of gas, as well as reduction of CO_2 storage capacity. Breakthrough times of CO_2 from the core sample at lower brine concentrations are longer than those of the higher brine concentrations. This implies that CO_2-brine-rock interaction is predominant at lower brine concentration.

- A higher-pressure decay rate indicates high solubility of CO_2 in different brine solutions in a porous media. The solubility of CO_2 is clearly dependent on the salt type as well as the concentration of the brine.

- The CO_2 breakthrough occurred earlier in divalent brine ($MgCl_2$, $CaCl_2$) than in monovalent brine (NaCl, KCl). This suggests that a large amount of CO_2 was dissolved in KCl and NaCl brines, as compared to $MgCl_2$ and $CaCl_2$ brines, as with all

experiments performed under identical conditions and with exceptionally high reproducibility. The salting-out effect at the highest brine concentration is greater in $MgCl_2$ and $CaCl_2$ brine as compared to NaCl and KCl brine.

- Injection of low salinity brine revealed that as the flooding process advanced, the salt content of the core samples reduced, while porosity and permeability to low salinity increased. As a result, the remediation procedure with low salinity fluid is more effective than with sea water.

Moreover, other conclusion based on the study are as follows:

- The high fluctuation of differential pressure (dp) indicates that there is a slug-type flow in the core sample as the CO_2 is injected into the simulated deep saline aquifer.

- By varying the CO_2 injection rates, higher injection rates induce high salt precipitation which caused reduction in porosity and permeability. From the experimental runs with respect to reservoir condition, the breakthrough times of CO_2 for each result decreases with an increasing injection rate. There was an early breakthrough of CO_2 for 3 ml/min injection flow rate as compared to 1 ml/min. In deep saline aquifers, the higher the injection rate, the lower CO_2 efficiency is and the poorer the CO_2 storage capacity will be. This suggests that, selecting a remarkable injection rate to improve the injectivity is very essential for CO_2 storage.

- Salt solubility in water/aqueous phase also affects the storability of CO_2 in deep saline aquifers with highly insoluble salts precipitating out more easily than their higher solubility counterparts. The drying-out effect was observed to be more noticeable in the divalent brine scenarios compared to the monovalent scenarios. However, KCl showed a lower tolerance in terms of CO_2 storability compared to its monovalent counterpart, NaCl.

- The appropriate strategy for remediation approach is a standard slug size of 10%, which represents the most suited scenarios based on the injection rates assessed.

- The magnitude of dP towards the end of the remediation process is lower than pre-flush in the case of the core sample saturated with monovalent brine (NaCl, KCl) than the divalent brine. This demonstrates that more pore areas are opened for CO_2 traversal and storage.

- The decrease in pressure drops across the core sample and rise in absolute permeability throughout cleaning suggested that the remediation method successfully reopened the obstructed flow pathways.

5.2. Recommendation and future work

Sequel on the laboratory investigations and discussions presented in this study, the following recommendations are made:

- Future work should cover the relative CO_2-brine relative permeabilities at different concentrations and conditions and the effect of brine type on the injectivity of the CO_2 for aquifer storage.
- The use of more sophisticated imaging techniques like Nuclear Magnetic Resonance (NMR) could be used to see the pore distribution before and after the core flooding in order to locate the pore region susceptible for salt precipitation.
- Data obtained from this study should be used to design mitigation strategies by altering some of the parameters that are responsible for salt precipitation. This design will be useful to investigate the extent at which CO_2 could be stored without any eventualities in terms of leakage or fracture.
- In view of the above study on sandstone, similar investigations are recommended to be conducted on non-homogeneous carbonate rock counterparts and evaluation of similar salt types on injectivity.
- A pore network simulation could be used to determine the extent of CO_2 phase influence on the relative permeability and capillary pressure of CO_2 and brine in porous media.

References

1. Niemi, A., K. Edlmann, J. Carrera, C. Juhlin, A. Tatomir, I. Ghergut, M. Sauter, J. Bensabat, F. Fagerlund, and F.H. Cornet, *Site characterization*, in *Geological Storage of CO2 in Deep Saline Formations*. 2017, Springer. p. 309-380. DOI: https://doi.org/10.1007/978-94-024-0996-3_7.

2. Olivier, J.G., K. Schure, and J. Peters, *Trends in global CO2 and total greenhouse gas emissions.* PBL Netherlands Environmental Assessment Agency, 2017. **5**: p. 1-11.

3. Nicot, J.-P., S. Solano, J. Lu, P. Mickler, K. Romanak, C. Yang, and X. Zhang, *Potential Subsurface Impacts of CO2 Stream Impurities on Geologic Carbon Storage.* Energy Procedia, 2013. **37**: p. 4552-4559. DOI: https://doi.org/10.1016/j.egypro.2013.06.362.

4. Loa, M., *Trends in atmospheric carbon dioxide*. 2015. DOI: https://doi.org/10.15138/9N0H-ZH07.

5. Bachu, S., A. Melnik, and R. Bistran, *Approach to Evaluating the CO2 Storage Capacity in Devonian Deep Saline Aquifers for Emissions from Oil Sands Operations in the Athabasca Area, Canada.* Energy Procedia, 2014. **63**: p. 5093-5102. DOI: https://doi.org/10.1016/j.egypro.2014.11.539.

6. Leung, D.Y.C., G. Caramanna, and M.M. Maroto-Valer, *An overview of current status of carbon dioxide capture and storage technologies.* Renewable and Sustainable Energy Reviews, 2014. **39**: p. 426-443. DOI: https://doi.org/10.1016/j.rser.2014.07.093.

7. Miri, R., R. van Noort, P. Aagaard, and H. Hellevang, *New insights on the physics of salt precipitation during injection of CO2 into saline aquifers.* International Journal of Greenhouse Gas Control, 2015. **43**: p. 10-21. DOI: https://doi.org/10.1016/j.ijggc.2015.10.004.

8. Hansen, O., D. Gilding, B. Nazarian, B. Osdal, P. Ringrose, J.-B. Kristoffersen, O. Eiken, and H. Hansen, *Snøhvit: The History of Injecting and Storing 1 Mt CO2 in the Fluvial Tubåen Fm.* Energy Procedia, 2013. **37**: p. 3565-3573. DOI: https://doi.org/10.1016/j.egypro.2013.06.249.

9. Ott, H., S.M. Roels, and K. de Kloe, *Salt precipitation due to supercritical gas injection: I. Capillary-driven flow in unimodal sandstone.* International Journal of Greenhouse Gas Control, 2015. **43**: p. 247-255. DOI: https://doi.org/10.1016/j.ijggc.2015.01.005.

10. Peysson, Y., L. André, and M. Azaroual, *Well injectivity during CO2 storage operations in deep saline aquifers—Part 1: Experimental investigation of drying effects, salt precipitation and capillary forces.* International Journal of Greenhouse Gas Control, 2014. **22**: p. 291-300. DOI: https://doi.org/10.1016/j.ijggc.2013.10.031.

References

11.   Kim, K.-Y., W.S. Han, J. Oh, T. Kim, and J.-C. Kim, *Characteristics of Salt-Precipitation and the Associated Pressure Build-Up during CO2 Storage in Saline Aquifers.* Transport in Porous Media, 2012. **92**(2): p. 397-418. DOI: https://doi.org/10.1007/s11242-011-9909-4.

12.   Delprat-Jannaud, F., A. Korre, J. Shi, B. McConnell, A. Arvanitis, D. Boavida, M. Car, M. Gastine, I. Grunnaleite, K. Bateman, N. Poulsen, C. Sinayuc, T. Vähäkuopus, S. Vercelli, and A. Wójcicki, *State-of-the-art of review CO2 Storage Site Selection and Characterisation Methods.* 2013.

13.   Busch, A., A. Amann, P. Bertier, M. Waschbusch, and B.M. Krooss. *The Significance of Caprock Sealing Integrity for CO2 Storage.* in *SPE International Conference on CO2 Capture, Storage, and Utilization.* 2010. DOI: https://doi.org/10.2118/139588-MS.

14.   Muller, N., R. Qi, E. Mackie, K. Pruess, and M.J. Blunt, *CO2 injection impairment due to halite precipitation.* Energy Procedia, 2009. **1**(1): p. 3507-3514. DOI: https://doi.org/10.1016/j.egypro.2009.02.143.

15.   Md Yusof, M.A., M.A. Mohamed, N.A. Md Akhir, M.A. Ibrahim, and M.K. Mardhatillah, *Combined Impact of Salt Precipitation and Fines Migration on CO2 Injectivity Impairment.* International Journal of Greenhouse Gas Control, 2021. **110**: p. 103422. DOI: https://doi.org/10.1016/j.ijggc.2021.103422.

16.   Bacci, G., A. Korre, and S. Durucan, *Experimental investigation into salt precipitation during CO2 injection in saline aquifers.* Energy Procedia, 2011. **4**: p. 4450-4456. DOI: https://doi.org/10.1016/j.egypro.2011.02.399.

17.   Peysson, Y., B. Bazin, C. Magnier, E. Kohler, and S. Youssef, *Permeability alteration due to salt precipitation driven by drying in the context of CO2 injection.* Energy Procedia, 2011. **4**: p. 4387-4394. DOI: https://doi.org/10.1016/j.egypro.2011.02.391.

18.   Luo, A., Y. Li, X. Chen, Z. Zhu, and Y. Peng, *Review of CO2 sequestration mechanism in saline aquifers.* Natural Gas Industry B, 2022. **9**(4): p. 383-393. DOI: https://doi.org/10.1016/j.ngib.2022.07.002.

19.   Spellman, F.R., *Environmental impacts of renewable energy.* 2014: CRC press. DOI: https://doi.org/10.1201/b17744.

20.   Jafari, M., S.C. Cao, and J. Jung, *Geological CO2 sequestration in saline aquifers: Implication on potential solutions of China's power sector.* Resources, Conservation and Recycling, 2017. **121**: p. 137-155. DOI: https://doi.org/10.1016/j.resconrec.2016.05.014.

21.   Zeidouni, M., M. Pooladi-Darvish, and D. Keith, *Analytical solution to evaluate salt precipitation during CO2 injection in saline aquifers.* International Journal of Greenhouse Gas Control, 2009. **3**(5): p. 600-611. DOI: https://doi.org/10.1016/j.ijggc.2009.04.004.

22.   Miri, R. and H. Hellevang, *Salt precipitation during CO2 storage—A review.* International Journal of Greenhouse Gas Control, 2016. **51**: p. 136-147. DOI: https://doi.org/10.1016/j.ijggc.2016.05.015.

References

23.   Ott, H., K. de Kloe, C. Taberner, F. Marcelis, Y. Wang, and A. Makurat. *Rock/fluid interaction by injection of supercritical CO2/H2S: investigation of dry-zone formation near the injection well*.

24.   Oh, J., K.-Y. Kim, W.S. Han, T. Kim, J.-C. Kim, and E. Park, *Experimental and numerical study on supercritical CO2/brine transport in a fractured rock: Implications of mass transfer, capillary pressure and storage capacity.* Advances in Water Resources, 2013. **62**: p. 442-453. DOI: https://doi.org/10.1016/j.advwatres.2013.03.007.

25.   Kim, M., A. Sell, and D. Sinton, *Aquifer-on-a-Chip: understanding pore-scale salt precipitation dynamics during CO 2 sequestration.* Lab on a Chip, 2013. **13**(13): p. 2508-2518.

26.   Gür, T.M., *Carbon Dioxide Emissions, Capture, Storage and Utilization: Review of Materials, Processes and Technologies.* Progress in Energy and Combustion Science, 2022. **89**: p. 100965. DOI: https://doi.org/10.1016/j.pecs.2021.100965.

27.   Beinashor, R.M., *Effect of Halite (NaCl) on Sandstone Permeability and Well Injectivity During CO2 Storage in Saline Aquifers*. 2017, University of Salford (United Kingdom). p. 137

28.   Benashor, R., A. Nourian, G. Nasr, and G. Enyi, *The effects of dissolved sodium chloride (NaCl) on well injectivity during CO2 storage into saline aquifers.* 2016.

29.   Ghafoori, M., S.A. Tabatabaei-Nejad, and E. Khodapanah, *Modeling rock-fluid interactions due to CO2 injection into sandstone and carbonate aquifer considering salt precipitation and chemical reactions.* Journal of Natural Gas Science and Engineering, 2017. **37**: p. 523-538. DOI: https://doi.org/10.1016/j.jngse.2016.11.063.

30.   Shogenov, K., A. Shogenova, O. Vizika-Kavvadias, and J.-F. Nauroy, *Reservoir quality and petrophysical properties of Cambrian sandstones and their changes during the experimental modelling of CO^ sub 2^ storage in the Baltic Basin.* Estonian Journal of Earth Sciences, 2015. **64**(3): p. 199. DOI: https://doi.org/10.3176/earth.2015.27.

31.   Kleinitz, W., G. Dietzsch, and M. Köhler, *Halite Scale Formation in Gas-Producing Wells.* Chemical Engineering Research and Design, 2003. **81**(3): p. 352-358. DOI: https://doi.org/10.1205/02638760360596900.

32.   Baumann, G., J. Henninges, and M. De Lucia, *Monitoring of saturation changes and salt precipitation during CO2 injection using pulsed neutron-gamma logging at the Ketzin pilot site.* International Journal of Greenhouse Gas Control, 2014. **28**: p. 134-146. DOI: https://doi.org/10.1016/j.ijggc.2014.06.023.

33.   Grude, S., M. Landrø, and J. Dvorkin, *Pressure effects caused by CO2 injection in the Tubåen Fm., the Snøhvit field.* International Journal of Greenhouse Gas Control, 2014. **27**: p. 178-187. DOI: https://doi.org/10.1016/j.ijggc.2014.05.013.

34.   Ott, H., J. Snippe, K. de Kloe, H. Husain, and A. Abri, *Salt Precipitation Due to Sc-gas Injection: Single Versus Multi-porosity Rocks.* Energy Procedia, 2013. **37**: p. 3319-3330. DOI: https://doi.org/10.1016/j.egypro.2013.06.220.

References

35. Jeddizahed, J. and B. Rostami, *Experimental investigation of injectivity alteration due to salt precipitation during CO2 sequestration in saline aquifers.* Advances in Water Resources, 2016. **96**: p. 23-33. DOI: https://doi.org/10.1016/j.advwatres.2016.06.014.

36. Tang, Y., R. Yang, Z. Du, and F. Zeng, *Experimental Study of Formation Damage Caused by Complete Water Vaporization and Salt Precipitation in Sandstone Reservoirs.* Transport in Porous Media, 2015. **107**(1): p. 205-218. DOI: https://doi.org/10.1007/s11242-014-0433-1.

37. Shaibu, R., Y.A. Sokama-Neuyam, and J.R. Ursin. *A Theoretical Study of the Effect of Salt Precipitation on CO2 Injectivity*. in *SPE International Conference and Exhibition on Formation Damage Control*. 2018. DOI: https://doi.org/10.2118/189470-MS.

38. Edem, D., M. Abba, A. Nourian, M. Babaie, and N. Mohammed. *The Effects of Different Salt Types and Concentration on CO2 Injectivity During CO2 Sequestration in Deep Saline Aquifers*. in *SPE Nigeria Annual International Conference and Exhibition*. 2020. DOI: https://doi.org/10.2118/203744-MS.

39. Edem, D., M. Abba, A. Nourian, M. Babaie, and Z. Naeem. *Experimental Investigation of the Extent of the Impact of Halite Precipitation on CO2 Injection in Deep Saline Aquifers*. in *SPE Europec*. 2020. DOI: https://doi.org/10.2118/200632-MS.

40. Edem, D.E., M.K. Abba, A. Nourian, M. Babaie, and Z. Naeem *Experimental Study on the Interplay between Different Brine Types/Concentrations and CO2 Injectivity for Effective CO2 Storage in Deep Saline Aquifers*. Sustainability, 2022. **14**, DOI: https://doi.org/10.3390/su14020986.

41. Cui, G., F. Ning, B. Dou, T. Li, and Q. Zhou, *Particle migration and formation damage during geothermal exploitation from weakly consolidated sandstone reservoirs via water and CO2 recycling.* Energy, 2022. **240**: p. 122507. DOI: https://doi.org/10.1016/j.energy.2021.122507.

42. Pruess, K. and N. Müller, *Formation dry-out from CO2 injection into saline aquifers: 1. Effects of solids precipitation and their mitigation.* Water Resources Research, 2009. **45**(3). DOI: https://doi.org/10.1029/2008WR007101.

43. André, L., Y. Peysson, and M. Azaroual, *Well injectivity during CO2 storage operations in deep saline aquifers – Part 2: Numerical simulations of drying, salt deposit mechanisms and role of capillary forces.* International Journal of Greenhouse Gas Control, 2014. **22**: p. 301-312. DOI: https://doi.org/10.1016/j.ijggc.2013.10.030.

44. Liu, H.-H., G. Zhang, Z. Yi, and Y. Wang, *A permeability-change relationship in the dryout zone for CO2 injection into saline aquifers.* International Journal of Greenhouse Gas Control, 2013. **15**: p. 42-47. DOI: https://doi.org/10.1016/j.ijggc.2013.01.034.

45. Meng, Q., X. Jiang, D. Li, and X. Zhong. *The Pressure Buildup and Salt Precipitation during CO2Storage in Closed Saline Aquifers*. in *Parallel Computational Fluid Dynamics*. 2014. Berlin, Heidelberg: Springer Berlin Heidelberg. DOI: https://doi.org/10.1007/978-3-642-53962-6_6.

References

46.   Guyant, E., W.S. Han, K.-Y. Kim, M.-H. Park, and B.-Y. Kim, *Salt precipitation and CO2/brine flow distribution under different injection well completions.* International Journal of Greenhouse Gas Control, 2015. **37**: p. 299-310. DOI: https://doi.org/10.1016/j.ijggc.2015.03.020.

47.   Van Bakel, M., F. Vos, A. Van Pelt, P. Legerstee, A. Bauer, K. Eide, A. Van Der Linden, and S. Berg, *Core-flood experiment for transport of reactive fluids in rocks.* Review of Scientific Instruments, 2012. **83**(8): p. 084501.

48.   Yiotis, A.G., A.G. Boudouvis, A.K. Stubos, I.N. Tsimpanogiannis, and Y.C. Yortsos, *Effect of liquid films on the drying of porous media.* AIChE Journal, 2004. **50**(11): p. 2721-2737. DOI: https://doi.org/10.1002/aic.10265.

49.   Ji, X., S.P. Tan, H. Adidharma, and M. Radosz, *SAFT1-RPM Approximation Extended to Phase Equilibria and Densities of CO2−H2O and CO2−H2O−NaCl Systems.* Industrial & Engineering Chemistry Research, 2005. **44**(22): p. 8419-8427. DOI: https://doi.org/10.1021/ie050725h.

50.   Miri, R., P. Aagaard, and H. Hellevang, *Examination of CO2–SO2 Solubility in Water by SAFT1. Implications for CO2 Transport and Storage.* The Journal of Physical Chemistry B, 2014. **118**(34): p. 10214-10223. DOI: https://doi.org/10.1021/jp505562j.

51.   Zeidouni, M., M. Pooladi-Darvish, and D. Keith. *Sensitivity Analysis of Salt Precipitation and CO2-Brine Displacement in Saline Aquifers*. in *SPE International Conference on CO2 Capture, Storage, and Utilization*. 2009. DOI: https://doi.org/10.2118/126690-MS.

52.   Eiken, O., P. Ringrose, C. Hermanrud, B. Nazarian, and T. Torp. *Lessons Learned from 14 years of CCS Operations: Sleipner, In Salah and Snohvit*. in *Proceedings of the Greenhouse Gas Control Technologies Conference, Amsterdam, The Netherlands, 19th–23rd September*. 2010. DOI: https://doi/10.1016/j.egypro.2011.02.541.

53.   Cui, G., S. Ren, L. Zhang, Y. Wang, and P. Zhang, *Injection of supercritical CO2 for geothermal exploitation from single- and dual-continuum reservoirs: Heat mining performance and salt precipitation effect.* Geothermics, 2018. **73**: p. 48-59. DOI: https://doi.org/10.1016/j.geothermics.2018.01.010.

54.   Giorgis, T., M. Carpita, and A. Battistelli, *2D modeling of salt precipitation during the injection of dry CO2 in a depleted gas reservoir.* Energy Conversion and Management, 2007. **48**(6): p. 1816-1826. DOI: https://doi.org/10.1016/j.enconman.2007.01.012.

55.   Chiquet, P., D. Broseta, and S. Thibeau, *Wettability alteration of caprock minerals by carbon dioxide.* Geofluids, 2007. **7**(2): p. 112-122. DOI: https://doi.org/10.1111/j.1468-8123.2007.00168.x.

56.   Zhang, Z., X. Chen, Y. Qian, Q. Liu, W. Lv, M. Luo, and X. Fan, *Experimental study of CO2 storage in water-flooded oilfields.* Petroleum Research, 2017. **2**(4): p. 378-382. DOI: https://doi.org/10.1016/j.ptlrs.2017.08.001.

References

57.   Roels, S.M., H. Ott, and P.L.J. Zitha, *μ-CT analysis and numerical simulation of drying effects of CO2 injection into brine-saturated porous media.* International Journal of Greenhouse Gas Control, 2014. **27**: p. 146-154. DOI: https://doi.org/10.1016/j.ijggc.2014.05.010.

58.   Wang, Y., J. Ren, S. Hu, and D. Feng, *Global Sensitivity Analysis to Assess Salt Precipitation for CO_2 Geological Storage in Deep Saline Aquifers.* Geofluids, 2017. **2017**: p. 5603923. DOI: https://doi.org/10.1155/2017/5603923.

59.   Bacci, G., S. Durucan, and A. Korre, *Experimental and Numerical Study of the Effects of Halite Scaling on Injectivity and Seal Performance During CO2 Injection in Saline Aquifers.* Energy Procedia, 2013. **37**: p. 3275-3282. DOI: https://doi.org/10.1016/j.egypro.2013.06.215.

60.   Oldenburg, C.M., *Joule-Thomson cooling due to CO2 injection into natural gas reservoirs.* Energy Conversion and Management, 2007. **48**(6): p. 1808-1815. DOI: https://doi.org/10.1016/j.enconman.2007.01.010.

61.   Hurter, S., D. Labregere, and J. Berge. *Simulations for CO2 Injection Projects With Compositional Simulator.* in *SPE Offshore Europe Oil and Gas Conference and Exhibition.* 2007. DOI: https://doi.org/10.2118/108540-MS.

62.   Wang, Y. and Y. Liu, *Dry-out effect and site selection for CO2 storage in deep saline aquifers.* Rock and Soil Mechanics, 2014. **35**(6): p. 1711-1717.

63.   Norouzi, A.M., M. Babaei, W.S. Han, K.-Y. Kim, and V. Niasar, *CO2-plume geothermal processes: A parametric study of salt precipitation influenced by capillary-driven backflow.* Chemical Engineering Journal, 2021. **425**: p. 130031. DOI: https://doi.org/10.1016/j.cej.2021.130031.

64.   Norouzi, A.M., V. Niasar, J.G. Gluyas, and M. Babaei, *Analytical Solution for Predicting Salt Precipitation During CO2 Injection Into Saline Aquifers in Presence of Capillary Pressure.* Water Resources Research, 2022. **58**(6): p. e2022WR032612. DOI: https://doi.org/10.1029/2022WR032612.

65.   Dashtian, H., N. Shokri, and M. Sahimi, *Pore-network model of evaporation-induced salt precipitation in porous media: The effect of correlations and heterogeneity.* Advances in Water Resources, 2018. **112**: p. 59-71. DOI: https://doi.org/10.1016/j.advwatres.2017.12.004.

66.   Cui, G., Z. Ren, L. Zhang, Y. Zhuang, Y. Wang, Z. Gong, and S. Su, *Effects of rock-fluid interaction and water back flow on heat mining efficiency of geothermal development via carbon dioxide injection.* Journal of Chemical Engineering of Chinese Universities, 2016. **30**(5): p. 1043-1052.

67.   Spycher, N. and K. Pruess, *A Phase-Partitioning Model for CO2–Brine Mixtures at Elevated Temperatures and Pressures: Application to CO2-Enhanced Geothermal Systems.* Transport in Porous Media, 2010. **82**(1): p. 173-196. DOI: https://doi.org/10.1007/s11242-009-9425-y.

68.   Cui, G., S. Ren, Z. Rui, J. Ezekiel, L. Zhang, and H. Wang, *The influence of complicated fluid-rock interactions on the geothermal exploitation in the CO2 plume*

References

geothermal system. Applied Energy, 2018. **227**: p. 49-63. DOI: https://doi.org/10.1016/j.apenergy.2017.10.114.

69.   Li, Y. and Q. Yu, *The Effects of Brine Species on the Formation of Residual Water in a CO2–Brine System.* Transport in Porous Media, 2014. **104**(3): p. 553-564. DOI: https://doi.org/10.1007/s11242-014-0349-9.

70.   Izgec, O., B. Demiral, H. Bertin, and S. Akin. *Experimental and Numerical Investigation of Carbon Sequestration in Saline Aquifers*. in *SPE/EPA/DOE Exploration and Production Environmental Conference*. 2005. DOI: https://doi.org/10.2118/94697-STU.

71.   Ülker, B., H. Alkan, and G. Pusch. *Implications of the Phase-Solubility Behaviour on the Performance Predictions of the CO2 Trapping in Depleted Gas Reservoirs and Aquifers*. in *EUROPEC/EAGE Conference and Exhibition*. 2007. DOI: https://doi.org/10.2118/107189-MS.

72.   Yang, F., B. Bai, D. Tang, D. Shari, and W. David, *Characteristics of CO2 sequestration in saline aquifers, Pet*. 2010, Sci

73.   Tong, D., J.P.M. Trusler, and D. Vega-Maza, *Solubility of CO2 in Aqueous Solutions of CaCl2 or MgCl2 and in a Synthetic Formation Brine at Temperatures up to 423 K and Pressures up to 40 MPa.* Journal of Chemical & Engineering Data, 2013. **58**(7): p. 2116-2124. DOI: https://doi.org/10.1021/je400396s.

74.   Li, Z., M. Dong, S. Li, and L. Dai, *Densities and Solubilities for Binary Systems of Carbon Dioxide + Water and Carbon Dioxide + Brine at 59 °C and Pressures to 29 MPa.* Journal of Chemical & Engineering Data, 2004. **49**(4): p. 1026-1031. DOI: https://doi.org/10.1021/je049945c.

75.   Rumpf, B., H. Nicolaisen, C. Öcal, and G. Maurer, *Solubility of carbon dioxide in aqueous solutions of sodium chloride: Experimental results and correlation.* Journal of Solution Chemistry, 1994. **23**(3): p. 431-448. DOI: https://doi.org/10.1007/BF00973113.

76.   Dilmore, R., P. Lu, D. Allen, Y. Soong, S. Hedges, J.K. Fu, C.L. Dobbs, A. Degalbo, and C. Zhu, *Sequestration of CO2 in Mixtures of Bauxite Residue and Saline Wastewater.* Energy & Fuels, 2008. **22**(1): p. 343-353. DOI: https://doi.org/10.1021/ef7003943.

77.   Pruess, K. and J. García, *Multiphase flow dynamics during CO2 disposal into saline aquifers.* Environmental Geology, 2002. **42**(2): p. 282-295. DOI: https://doi.org/10.1007/s00254-001-0498-3.

78.   Rochelle, C.A., I. Czernichowski-Lauriol, and A.E. Milodowski, *The impact of chemical reactions on CO2 storage in geological formations: a brief review*, in *Geological Storage of Carbon Dioxide*, S.J. Baines and R.H. Worden, Editors. 2004, Geological Society of London. p. 0. DOI: https://doi.org/10.1144/GSL.SP.2004.233.01.07.

References

79.   Jacob, R. and B.Z. Saylor, *CO2 solubility in multi-component brines containing NaCl, KCl, CaCl2 and MgCl2 at 297K and 1–14MPa.* Chemical Geology, 2016. **424**: p. 86-95. DOI: https://doi.org/10.1016/j.chemgeo.2016.01.013.

80.   Chapoy, A., A.H. Mohammadi, A. Chareton, B. Tohidi, and D. Richon, *Measurement and Modeling of Gas Solubility and Literature Review of the Properties for the Carbon Dioxide−Water System.* Industrial & Engineering Chemistry Research, 2004. **43**(7): p. 1794-1802. DOI: https://doi.org/10.1021/ie034232t.

81.   Austegard, A., E. Solbraa, G. De Koeijer, and M.J. Mølnvik, *Thermodynamic Models for Calculating Mutual Solubilities in H2O–CO2–CH4 Mixtures.* Chemical Engineering Research and Design, 2006. **84**(9): p. 781-794. DOI: https://doi.org/10.1205/cherd05023.

82.   Diamond, L.W. and N.N. Akinfiev, *Solubility of CO2 in water from −1.5 to 100 °C and from 0.1 to 100 MPa: evaluation of literature data and thermodynamic modelling.* Fluid Phase Equilibria, 2003. **208**(1): p. 265-290. DOI: https://doi.org/10.1016/S0378-3812(03)00041-4.

83.   Veiga, B.A., J.T.F. dos Santos, L.F. de Lima Luz Junior, and M.L. Corazza, *Phase equilibrium measurements and thermodynamic modelling for the systems involving valeric acid, ethanol, ethyl valerate and water plus CO2.* The Journal of Chemical Thermodynamics, 2017. **112**: p. 240-248. DOI: https://doi.org/10.1016/j.jct.2017.05.011.

84.   Nighswander, J.A., N. Kalogerakis, and A.K. Mehrotra, *Solubilities of carbon dioxide in water and 1 wt. % sodium chloride solution at pressures up to 10 MPa and temperatures from 80 to 200.degree.C.* Journal of Chemical & Engineering Data, 1989. **34**(3): p. 355-360. DOI: https://doi.org/10.1021/je00057a027.

85.   Kiepe, J., S. Horstmann, K. Fischer, and J. Gmehling, *Experimental Determination and Prediction of Gas Solubility Data for CO2 + H2O Mixtures Containing NaCl or KCl at Temperatures between 313 and 393 K and Pressures up to 10 MPa.* Industrial & Engineering Chemistry Research, 2002. **41**(17): p. 4393-4398. DOI: https://doi.org/10.1021/ie020154i.

86.   Werth, S., S.V. Lishchuk, M. Horsch, and H. Hasse, *The influence of the liquid slab thickness on the planar vapor–liquid interfacial tension.* Physica A: Statistical Mechanics and its Applications, 2013. **392**(10): p. 2359-2367. DOI: https://doi.org/10.1016/j.physa.2013.01.048.

87.   Kashefi, K., L.M.C. Pereira, A. Chapoy, R. Burgass, and B. Tohidi, *Measurement and modelling of interfacial tension in methane/water and methane/brine systems at reservoir conditions.* Fluid Phase Equilibria, 2016. **409**: p. 301-311. DOI: https://doi.org/10.1016/j.fluid.2015.09.050.

88.   Ahmadi, P. and A. Chapoy, *CO2 solubility in formation water under sequestration conditions.* Fluid Phase Equilibria, 2018. **463**: p. 80-90. DOI: https://doi.org/10.1016/j.fluid.2018.02.002.

References

89. Ayirala, S.C. and D.N. Rao, *Solubility, miscibility and their relation to interfacial tension in ternary liquid systems.* Fluid Phase Equilibria, 2006. **249**(1): p. 82-91. DOI: https://doi.org/10.1016/j.fluid.2006.09.020.

90. Chen, L., M. Wang, Q. Kang, and W. Tao, *Pore scale study of multiphase multicomponent reactive transport during CO2 dissolution trapping.* Advances in Water Resources, 2018. **116**: p. 208-218. DOI: https://doi.org/10.1016/j.advwatres.2018.02.018.

91. Ding, S., Y. Xi, H. Jiang, and G. Liu, *CO2 storage capacity estimation in oil reservoirs by solubility and mineral trapping.* Applied Geochemistry, 2018. **89**: p. 121-128. DOI: https://doi.org/10.1016/j.apgeochem.2017.12.002.

92. Jia, W., F. Pan, Z. Dai, T. Xiao, and B. McPherson, *Probabilistic Risk Assessment of CO2 Trapping Mechanisms in a Sandstone CO2-EOR Field in Northern Texas, USA.* Energy Procedia, 2017. **114**: p. 4321-4329. DOI: https://doi.org/10.1016/j.egypro.2017.03.1581.

93. Li, B., H.A. Tchelepi, and S.M. Benson, *Influence of capillary-pressure models on CO2 solubility trapping.* Advances in Water Resources, 2013. **62**: p. 488-498. DOI: https://doi.org/10.1016/j.advwatres.2013.08.005.

94. Pooladi-Darvish, M. and A. Firoozabadi, *Cocurrent and Countercurrent Imbibition in a Water-Wet Matrix Block.* SPE Journal, 2000. **5**(01): p. 3-11. DOI: https://doi.org/10.2118/38443-PA.

95. Rashid, S., B. Harimi, and E. Hamidpour, *Prediction of CO2-Brine interfacial tension using a rigorous approach.* Journal of Natural Gas Science and Engineering, 2017. **45**: p. 108-117. DOI: https://doi.org/10.1016/j.jngse.2017.05.002.

96. Shabani, B. and J. Vilcáez, *Prediction of CO2-CH4-H2S-N2 gas mixtures solubility in brine using a non-iterative fugacity-activity model relevant to CO2-MEOR.* Journal of Petroleum Science and Engineering, 2017. **150**: p. 162-179. DOI: https://doi.org/10.1016/j.petrol.2016.12.012.

97. Yan, W., S. Huang, and E.H. Stenby, *Measurement and modeling of CO2 solubility in NaCl brine and CO2–saturated NaCl brine density.* International Journal of Greenhouse Gas Control, 2011. **5**(6): p. 1460-1477. DOI: https://doi.org/10.1016/j.ijggc.2011.08.004.

98. Yuan, Z., X. Liao, K. Zhang, and Z. Chen. *The Inorganic Precipitation By CO2 and High Salinity Formation Water*. in *Carbon Management Technology Conference*. 2017. DOI: https://doi.org/10.7122/486297-MS.

99. Bennion, D.B. and S. Bachu. *A Correlation of the Interfacial Tension between Supercritical Phase CO2 and Equilibrium Brines as a Function of Salinity, Temperature and Pressure*. in *SPE Annual Technical Conference and Exhibition*. 2008. DOI: https://doi.org/10.2118/114479-MS.

100. Chalbaud, C., M. Robin, J.M. Lombard, F. Martin, P. Egermann, and H. Bertin, *Interfacial tension measurements and wettability evaluation for geological CO2*

storage. Advances in Water Resources, 2009. **32**(1): p. 98-109. DOI: https://doi.org/10.1016/j.advwatres.2008.10.012.

101. Mutailipu, M., Y. Liu, L. Jiang, and Y. Zhang, *Measurement and estimation of CO2–brine interfacial tension and rock wettability under CO2 sub- and super-critical conditions.* Journal of Colloid and Interface Science, 2019. **534**: p. 605-617. DOI: https://doi.org/10.1016/j.jcis.2018.09.031.

102. Pereira, L.M.C., A. Chapoy, R. Burgass, and B. Tohidi, *Interfacial tension of CO2+brine systems: Experiments and predictive modelling.* Advances in Water Resources, 2017. **103**: p. 64-75. DOI: https://doi.org/10.1016/j.advwatres.2017.02.015.

103. Valle, L.M., R. Rodríguez, C. Grima, and C. Martínez, *Effects of supercritical CO2 injection on sandstone wettability and capillary trapping.* International Journal of Greenhouse Gas Control, 2018. **78**: p. 341-348. DOI: https://doi.org/10.1016/j.ijggc.2018.09.005.

104. Hosseini, S.A., M. Asemani, F. Esmaeilzadeh, and D. Mowla, *Experimental investigation of inhibitors injection to control salt precipitation using wetted wall column.* Journal of Petroleum Science and Engineering, 2014. **122**: p. 667-674. DOI: https://doi.org/10.1016/j.petrol.2014.09.009.

105. Sokama-Neuyam, Y.A., J.R. Ursin, and P. Boakye *Experimental Investigation of the Mechanisms of Salt Precipitation during CO2 Injection in Sandstone*. C, 2019. **5**, DOI: https://doi.org/10.3390/c5010004.

106. Wang Lu, Y.S.P.X.D.H.L.L.M.Z.Q.K.W.Q., *Visual experiments on the occurrence characteristics of multi-type reservoir water in fracture-cavity carbonate gas reservoir.* Acta Petrolei Sinica, 2018. **39**(6): p. 686-696.

107. Zhou, K., J. Hou, Q. Sun, L. Guo, S. Bing, Q. Du, and C. Yao, *A Study on Particle Suspension Flow and Permeability Impairment in Porous Media Using LBM–DEM–IMB Simulation Method.* Transport in Porous Media, 2018. **124**(3): p. 681-698. DOI: https://doi.org/10.1007/s11242-018-1089-z.

108. Gu, Y., Z. Bao, and G. Cui, *Permeability prediction using hybrid techniques of continuous restricted Boltzmann machine, particle swarm optimization and support vector regression.* Journal of Natural Gas Science and Engineering, 2018. **59**: p. 97-115. DOI: https://doi.org/10.1016/j.jngse.2018.08.020.

109. Yu, L., L. Zhang, R. Zhang, and S. Ren, *Assessment of natural gas production from hydrate-bearing sediments with unconsolidated argillaceous siltstones via a controlled sandout method.* Energy, 2018. **160**: p. 654-667. DOI: https://doi.org/10.1016/j.energy.2018.07.050.

110. Kececioglu, I. and Y. Jiang, *Flow Through Porous Media of Packed Spheres Saturated With Water.* Journal of Fluids Engineering, 1994. **116**(1): p. 164-170. DOI: https://doi.org/10.1115/1.2910229.

References

111. Yahaya, A., E. Akpan, G. Enyi, G. Nasr, and A. Abbas, *Experimental investigation of methane-water and methane-brine IFT measurements using pendant drop (rising bubble) method.* Journal of Engineering Technology, 2018. **6**(1): p. 394-407.

112. Yan, W., G.-Y. Zhao, G.-J. Chen, and T.-M. Guo, *Interfacial Tension of (Methane + Nitrogen) + Water and (Carbon Dioxide + Nitrogen) + Water Systems.* Journal of Chemical & Engineering Data, 2001. **46**(6): p. 1544-1548. DOI: https://doi.org/10.1021/je0101505.

113. Liu, Y., M. Hou, G. Yang, and B. Han, *Solubility of CO2 in aqueous solutions of NaCl, KCl, CaCl2 and their mixed salts at different temperatures and pressures.* The Journal of Supercritical Fluids, 2011. **56**(2): p. 125-129. DOI: https://doi.org/10.1016/j.supflu.2010.12.003.

114. Abba, M.K., *Enhanced gas recovery by CO2 injection: Influence of monovalent and divalent brines and their concentrations on CO2 dispersion in porous media.* Journal of Natural Gas Science and Engineering, 2020. **84**: p. 103643. DOI: https://doi.org/10.1016/j.jngse.2020.103643.

115. Boström, M. and B.W. Ninham, *Contributions from Dispersion and Born Self-Free Energies to the Solvation Energies of Salt Solutions.* The Journal of Physical Chemistry B, 2004. **108**(33): p. 12593-12595. DOI: https://doi.org/10.1021/jp048517a.

116. Duan, Z. and R. Sun, *An improved model calculating CO2 solubility in pure water and aqueous NaCl solutions from 273 to 533 K and from 0 to 2000 bar.* Chemical Geology, 2003. **193**(3): p. 257-271. DOI: https://doi.org/10.1016/S0009-2541(02)00263-2.

117. Abba, M.K., A.J. Abbas, G.G. Nasr, A. Al-Otaibi, M. Burby, B. Saidu, and S.M. Suleiman, *Solubility trapping as a potential secondary mechanism for CO2 sequestration during enhanced gas recovery by CO2 injection in conventional natural gas reservoirs: An experimental approach.* Journal of Natural Gas Science and Engineering, 2019. **71**: p. 103002. DOI: https://doi.org/10.1016/j.jngse.2019.103002.

118. Messabeb, H., F. Contamine, P. Cézac, J.P. Serin, C. Pouget, and E.C. Gaucher, *Experimental Measurement of CO2 Solubility in Aqueous CaCl2 Solution at Temperature from 323.15 to 423.15 K and Pressure up to 20 MPa Using the Conductometric Titration.* Journal of Chemical & Engineering Data, 2017. **62**(12): p. 4228-4234. DOI: https://doi.org/10.1021/acs.jced.7b00591.

119. Othman, F., M.A. Naufaliansyah, and F. Hussain, *Effect of water salinity on permeability alteration during CO_2 sequestration.* Advances in Water Resources, 2019. **127**: p. 237-251. DOI: https://doi.org/10.1016/j.advwatres.2019.03.018.

120. Sokama-Neuyam, Y.A., S.L. Forsetløkken, J.-e. Lien, and J.R. Ursin *The Coupled Effect of Fines Mobilization and Salt Precipitation on CO2 Injectivity.* Energies, 2017. **10**, DOI: https://doi.org/10.3390/en10081125.

121. Sokama-Neuyam, Y.A., P.U.R. Ginting, B. Timilsina, and J.R. Ursin, *The impact of fines mobilization on CO2 injectivity: An experimental study.* International Journal of

Greenhouse Gas Control, 2017. **65**: p. 195-202. DOI: https://doi.org/10.1016/j.ijggc.2017.08.019.

122.   Cheng, H., Q. Hai, J. Li, J. Song, and X. Ma, *The Sensitivity of Temperature to Tachyhydrite Formation: Evidence from Evaporation Experiments of Simulated Brines Based on Compositions of Fluid Inclusions in Halite.* Geofluids, 2019. **2019**: p. 7808036. DOI: https://doi.org/10.1155/2019/7808036.

Appendices

Appendix A: Flow Sheets of Porosity Determination

Appendix B: Flow Sheets of Permeability Determination

Appendix C: Pore Volume Calculations

Appendix D: Core Flooding

Appendix A: Flow Sheets of Porosity Determination

A1: Grain Volume Measurement for **Bentheimer** Core Sample

How To Use The Spreadsheet

1) Never edit the red cells. If you mistakenly edited the red cells, reinstall the software.
2) Enter the volumes data in the yellow cells at the beginning of calibration and save the spreadsheet.
3) During each calibration, re-enter the data in the green cells.

Disc Volumes Table

Disc No.	Length inches	Diameter inches	Volume cc
1	0.124	1.000	1.595926
2	0.373	0.999	4.791052
3	0.498	1.000	6.407524
4	0.747	1.000	9.615419
5	1.248	0.999	16.02369
		Total	38.43361

To Measure Porosity

1) Edit the yellow cells in Disc Volumes Table and save the spreadsheet
2) Perform a calibration and fill in the green cells in the Calibration Table
3) Copy the coefficients from the graph equation into the green cells in Coefficients Table.
4) Perform a test; enter P1 and P2 in Testing Table. Grain Volume is automatically calculated.

Calibration Table

Disc No.	Volume cc	Reference Pressure psig (P1)	Expanded Pressure psig (P2)	P1/P2
empty	0	92.81	11.18	8.301
1	1.596	92.69	11.53	8.039
2	4.791	92.7	12.29	7.543
3	6.408	92.67	12.7	7.297
4	9.615	92.62	13.64	6.790
5	16.024	92.57	15.95	5.804
5+1	17.620	92.53	16.65	5.557
5+3	22.431	92.5	19.26	4.803
5+4	25.639	92.49	21.51	4.300
5+4+3	32.047	92.42	27.94	3.308
5+4+3+2	36.838	92.42	36.04	2.564

$$y = 0.0013x^3 - 0.02x^2 - 6.3365x + 53.185$$
$$R^2 = 1$$

Coefficients Table

A	B	C	D
0.0127	-0.1981	-5.5031	52.078

Testing Table

P1	P2	P1/P2	Grain Vol
92.5	25.15	3.677932406	29.790

A2: Grain Volume Measurement for **Salt Wash North** Core Sample

Disc Volumes Table

Disc No.	Length inches	Diameter inches	Volume cc
1	0.124	1.000	1.5359
2	0.373	0.999	4.7911
3	0.498	1.000	6.4075
4	0.747	1.000	9.6154
5	1.248	0.999	16.024
		Total	38.434

To Measure Porosity

1) Edit the yellow cells in Disc Volumes Table and save the spreadsheet
2) Perform a calibration and fill in the green cells in the Calibration Table
3) Copy the coefficients from the graph equation into the green cells in Coefficients Table.
4) Perform a test; enter P1 and P2 in Testing Table. Grain Volume is automatically calculated.

	P1	P2
1	90.02	26.2
2	90.04	26.25
3	90.02	26.26
	270.08	78.71
	90.027	26.237

$$y = -0.0017x^3 + 0.019x^2 - 6.4823x + 53.401$$
$$R^2 = 1$$

Calibration Table

Disc No.	Volume cc	Reference Pressure psig (P1)	Expanded Pressure psig (P2)	P1/P2
empty	0	90.02	10.85	8.297
1	1.596	89.99	11.2	8.035
2	4.791	90.02	11.92	7.552
3	6.408	90.05	12.3	7.321
4	9.615	90.05	13.24	6.801
5	16.024	90.04	15.5	5.809
5+1	17.620	90.03	16.17	5.568
5+3	22.431	90.03	18.69	4.817
5+4	25.639	90.03	20.84	4.320
5+4+3	32.047	90.02	27.16	3.314
5+4+3+2	36.838	90.03	35.02	2.571

	d	L
1	25.79	76.34
2	25.81	76.32
3	25.93	76.35
	77.53	229.01
	25.843	76.337
	2.5843	7.6337
Area	5.2476	
Bulk Volum	40.059	
Pore Volun	8.745	
Porosity	0.2183	
	21.832	

Coefficients Table

A	B	C	D
-0.002	0.019	-6.482	53.401

Testing Table

P1	P2	P1/P2	Grain Vol
90.027	26.237	3.43133	31.313

A3: Grain Volume Measurement for **Grey Berea** Core Sample

Disc Volumes Table

Disc No.	Length inches	Diameter inches	Volume cc
1	0.124	1.000	1.595926
2	0.373	0.999	4.791052
3	0.498	1.000	6.407524
4	0.747	1.000	9.615419
5	1.248	0.999	16.02369
		Total	38.43361

Calibration Table

Disc No.	Volume cc	Reference Pressure psig (P1)	Expanded Pressure psig (P2)	P1/P2
empty	0	90.02	10.85	8.297
1	1.596	89.99	11.2	8.035
2	4.791	90.02	11.92	7.552
3	6.408	90.05	12.3	7.321
4	9.615	90.05	13.24	6.801
5	16.024	90.04	15.5	5.809
5+1	17.620	90.03	16.17	5.568
5+3	22.431	90.03	18.69	4.817
5+4	25.639	90.03	20.84	4.320
5+4+3	32.047	90.02	27.16	3.314
5+4+3+2	36.838	90.03	35.02	2.571

Gray Berea Sandstone Core Porosity

$$y = -0.0017x^3 + 0.019x^2 - 6.4823x + 53.401$$
$$R^2 = 1$$

Volume (CC) vs P1/P2 (psi)

Coefficients Table

A	B	C	D
-0.0017	0.019	-6.4823	53.401

Testing Table

P1	P2	P1/P2	Grain Vol
90.00667	24.94667	3.607983	**30.181**

	P1	P2
1	90	25
2	90	24.9
3	90.02	24.94
	270.02	74.84
	90.00666667	24.94666667

	d	L
1	25.12	76.09
2	25.12	76.08
3	25.11	76.12
	75.35	228.29
	25.11666667	76.09666667
	2.511666667	7.609666667
Area	4.956654563	
Bulk Volume	37.71848901	
Pore Volume	7.538	
	0.199846332	
Porosity (%)	19.98463321	

Appendix B: Flow Sheets of Permeability Determination

B1-1: Permeability Measurement for **Bentheimer** Core Sample – Saturated with **NaCl**

		Evaluation			Brines	K	% reduction	% increase
viscosity (cP)	0.022052							
Area (cm2)	4.2				5%	127.52	37.0	
L (cm)	7.6				10%	117.3166	42.0	
dp (psi)	0.29	0.019728			15%	102.9093	49.1	
Q(ml/min)	3	0.05			20%	101.135	50.0	
K		202.2701			25%	97.76387	51.7	

5wt%			10 wt%			15wt%			20wt%			25wt%		
		Evaluation			Evaluation			Evaluation			Evaluation			Evaluation
viscosity (cP)	0.022052		viscosity (	0.022052		viscosity (	0.022052		viscosity (	0.022052		viscosity (	0.022052	
Area (cm2)	4.2		Area (cm2	4.2		Area (cm2	4.2		Area (cm2	4.2		Area (cm2	4.2	
L (cm)	7.6		L (cm)	7.6		L (cm)	7.6		L (cm)	7.6		L (cm)	7.6	
dp (psi)	0.46	0.031293	dp (psi)	0.5	0.034014	dp (psi)	0.57	0.03877551	dp (psi)	0.58	0.039456	dp (psi)	0.6	0.040816
Q(ml/min)	3	0.05	Q(ml/min	3	0.05	Q(ml/min	3	0.05	Q(ml/min	3	0.05	Q(ml/min	3	0.05
K		127.5181	K		117.3166	K		102.909333	K		101.135	K		97.76387

B1-2: Permeability Measurement for **Bentheimer** Core Sample – Saturated with **KCl**

		Evaluation			Brines	K	% reduction
viscosity (cP)	0.022052						
Area (cm2)	4.2				5%	167.60	17.1
L (cm)	7.6				10%	154.364	23.7
dp (psi)	0.29	0.019728			15%	139.6627	31.0
Q(ml/min)	3	0.05			20%	119.7109	40.8
K		202.2701			25%	112.8045	44.2

5wt%			10 wt%			15. wt%			20wt%			25wt%		
		Evaluation			Evaluation			Evaluation			Evaluation			Evaluation
viscosity (cP)	0.022052		viscosity (	0.022052		viscosity (	0.022052		viscosity (	0.022052		viscosity (	0.022052	
Area (cm2)	4.2		Area (cm2	4.2		Area (cm2	4.2		Area (cm2	4.2		Area (cm2	4.2	
L (cm)	7.6		L (cm)	7.6		L (cm)	7.6		L (cm)	7.6		L (cm)	7.6	
dp (psi)	0.35	0.02381	dp (psi)	0.38	0.02585	dp (psi)	0.42	0.02857143	dp (psi)	0.49	0.033333	dp (psi)	0.52	0.035374
Q(ml/min)	3	0.05	Q(ml/min	3	0.05	Q(ml/min	3	0.05	Q(ml/min	3	0.05	Q(ml/min	3	0.05
K		167.5952	K		154.364	K		139.662667	K		119.7109	K		112.8045

B1-3: Permeability Measurement for **Bentheimer** Core Sample – Saturated with **CaCl₂**

		Evaluation			Brines	K	% reduction
viscosity (cP)	0.022052						
Area (cm2)	4.2				5%	162.94	19.4
L (cm)	7.6				10%	146.6458	27.5
dp (psi)	0.29	0.019728			15%	139.6627	31.0
Q(ml/min)	3	0.05			20%	127.5181	37.0
K		202.2701			25%	115.0163	43.1

5wt%			10 wt%			15wt%			20wt%			25wt%		
		Evaluation			Evaluation			Evaluation			Evaluation			Evaluation
viscosity (cP)	0.022052		viscosity (	0.022052		viscosity (	0.022052		viscosity (	0.022052		viscosity (	0.022052	
Area (cm2)	4.2		Area (cm2	4.2		Area (cm2	4.2		Area (cm2	4.2		Area (cm2	4.2	
L (cm)	7.6		L (cm)	7.6		L (cm)	7.6		L (cm)	7.6		L (cm)	7.6	
dp (psi)	0.36	0.02449	dp (psi)	0.4	0.027211	dp (psi)	0.42	0.02857143	dp (psi)	0.46	0.031293	dp (psi)	0.51	0.034694
Q(ml/min)	3	0.05	Q(ml/min	3	0.05	Q(ml/min	3	0.05	Q(ml/min	3	0.05	Q(ml/min	3	0.05
K		162.9398	K		146.6458	K		139.662667	K		127.5181	K		115.0163

B1-4: Permeability Measurement for **Bentheimer** Core Sample – Saturated with **MgCl₂**

	Evaluation			Brines	K	% reduction
viscosity (cP)	0.022052			5%	112.80	44.2
Area (cm2)	4.2			10%	88.87624	56.1
L (cm)	7.6			15%	78.21109	61.3
dp (psi)	0.29	0.019728		20%	76.67754	62.1
Q(ml/min)	3	0.05		25%	74.25104	63.3
K		202.2701				

5wt%			10 wt%			15wt%			20wt%			25wt%		
		Evaluation			Evaluation			Evaluation			Evaluation			Evaluation
viscosity (cP)	0.022052		viscosity (	0.022052		viscosity (	0.022052		viscosity (	0.022052		viscosity (	0.022052	
Area (cm2)	4.2		Area (cm2	4.2		Area (cm2	4.2		Area (cm2	4.2		Area (cm2	4.2	
L (cm)	7.6		L (cm)	7.6		L (cm)	7.6		L (cm)	7.6		L (cm)	7.6	
dp (psi)	0.52	0.035374	dp (psi)	0.66	0.044898	dp (psi)	0.75	0.05102041	dp (psi)	0.765	0.052041	dp (psi)	0.79	0.053741
Q(ml/min)	3	0.05	Q(ml/min	3	0.05	Q(ml/min	3	0.05	Q(ml/min	3	0.05	Q(ml/min	3	0.05
K		112.8045	K		88.87624	K		78.2110933	K		76.67754	K		74.25104

Appendix C: Pore Volume Calculations

$$P_1V_1 = P_2V_2$$

Where,

P_1 = operation pressure V_1 = equipment volume

P_2 = atmospheric pressure V_2 = equivalent of 9.103 cm^3 at 14.7 psi

	BEN	**SWN**	**GB**
P_1 (psig)	1500	1500	1500
V_1 (cm^3)	9.103	8.165	7.538
P_2 (psig)	14.7	14.7	14.7
V_2 (cm^3)	928.9	833.2	769.2
Pore Volume (cm^3)	9.28.9	833.2	769.2

Appendix D: Core Flooding

Bentheimer core sample saturated with 5 wt.% brine (NaCl) and flooded with CO_2 @ 3ml/min

Run	Cumulative Time (min)	dp (Psi)	Volume of CO_2 produced $V_g(l)$	Cumulative Volume of CO_2 Produced $V_g(l)$	Cumulative Volume of CO_2 Produced $V_g(cm^3)$	Cumulative Volume of CO_2 Produced (cm^3) over Pore volume (cm^3)
1	120.34	2.5	0	0	0	0
2	125.34	0.55	3.96	3.96	3960	4.26
3	130.34	0.45	1.96	5.92	5920	6.37
4	135.34	0.4	1.78	7.7	7700	8.29
5	140.34	0.42	1.8	9.5	9500	10.23
6	145.34	0.38	1.89	11.39	11390	12.26
7	150.34	0.41	1.81	13.2	13200	14.21
8	155.34	0.42	1.92	15.2	15200	16.37
9	160.34	0.43	1.96	17.08	17080	18.39
10	165.34	0.46	1.92	19	19000	20.46
11	170.34	0.45	1.96	20.96	2096	22.57
12	175.34	0.44	1.97	22.93	22930	24.69
13	180.34	0.44	1.96	24.89	24890	26.80
14	185.34	0.44	1.98	26.87	26870	28.93
15	190.34	0.43	2.01	28.88	28880	31.09
16	195.34	0.62	3.43	32.31	32310	34.79
17	200.34	0.92	5.18	37.49	37490	40.36
18	205.34	0.74	5.6	43.09	43090	46.39
19	210.34	1.28	5.82	48.91	48910	52.66
20	215.34	0.2	5.74	54.65	54650	58.84
21	220.34	0.53	5.79	60.44	60440	65.07
22	225.34	1.08	5.88	66.32	66320	71.40
23	230.34	0.42	6.19	72.51	72510	78.07
24	235.34	0.46	6.23	78.74	78740	84.78
25	240.34	0.47	6.32	85.06	85060	91.58
26	245.34	0.58	5.95	91.01	91010	97.99
27	250.34	0.76	5.95	96.96	96960	104.39
28	255.34	0.25	2.06	99.02	99020	106.61

Bentheimer core sample saturated with 10 wt.% brine (NaCl) and flooded with CO_2 @ 3ml/min

Run	Cumulative Time (min)	dp (Psi)	Volume of CO_2 produced V_g(l)	Cumulative Volume of CO_2 Produced V_g(l)	Cumulative Volume of CO_2 Produced V_g(cm^3)	Cumulative Volume of CO_2 Produced (cm^3) over Pore volume (cm^3)
1	88.34	0.88	0	0	0	0
2	93.34	0.44	2.64	2.64	2640	2.84
3	98.34	0.38	2.05	4.69	4690	5.05
4	103.34	0.35	1.86	6.55	6550	7.05
5	108.34	0.3	1.95	8.5	8500	9.15
6	113.34	0.35	2	10.5	10500	11.30
7	118.34	0.32	2	12.5	12500	13.46
8	123.34	0.37	1.99	14.49	14490	15.60
9	128.34	0.36	2.05	16.54	16540	17.81
10	133.34	0.39	2.09	18.63	18630	20.06
11	138.34	0.38	2.13	20.76	20760	22.35
12	143.34	0.35	2.1	22.86	22860	24.61
13	148.34	0.61	2.6	25.46	25460	27.41
14	153.34	0.28	5.23	30.69	30690	33.04
15	158.34	0.2	5.47	36.16	36160	38.93
16	163.34	0.23	5.78	41.94	41940	45.16
17	168.34	0.3	5.77	47.71	47710	51.37
18	173.34	0.3	6.02	53.73	53730	57.85
19	178.34	0.27	5.92	59.65	59650	64.22
20	183.34	0.29	5.91	65.56	65560	70.59
21	188.34	0.32	6.1	71.66	71660	77.15
22	193.34	0.57	5.17	76.83	76830	82.72
23	198.34	0.36	6.18	83.01	83010	89.37
24	203.34	0.28	6.02	89.03	89030	95.85
25	208.34	0.69	6.08	95.11	95110	102.40
26	213.34	0.15	3.04	98.15	98150	105.67
27	218.34	0.12	0.03	98.18	98180	105.71

Bentheimer core sample saturated with 15 wt.% brine (NaCl) and flooded with CO_2 @ 3ml/min

Run	Cumulative Time (min)	dp (Psi)	Volume of CO_2 produced V_g(l)	Cumulative Volume of CO_2 Produced V_g(l)	Cumulative Volume of CO_2 Produced V_g(cm^3)	Cumulative Volume of CO_2 Produced (cm^3) over Pore volume (cm^3)
1	81.01	0.57	0	0	0	0
2	86.01	0.42	2.56	2.56	2560	2.76
3	91.01	0.42	1.56	4.12	4120	4.44
4	96.01	0.39	1.55	5.67	5670	6.10
5	101.01	0.31	1.67	7.34	7340	7.90
6	106.01	0.29	1.77	9.11	9110	9.81
7	111.01	0.31	1.82	10.93	10930	11.77
8	116.01	0.31	1.86	12.79	12790	13.77
9	121.01	0.34	1.91	14.7	14700	15.83
10	126.01	0.31	1.94	16.64	16640	17.92
11	131.01	0.3	1.91	18.55	18550	19.97
12	136.01	0.31	1.94	20.49	20490	22.06
13	141.01	0.69	2.78	23.27	23270	25.05
14	146.01	0.25	5.06	28.33	28330	30.50
15	151.01	0.95	5.49	33.82	33820	36.41
16	156.01	0.25	5.68	39.5	39500	42.53
17	161.01	0.31	5.49	44.99	44990	48.44
18	166.01	0.25	5.77	50.76	50760	54.65
19	171.01	0.24	5.77	56.53	56530	60.86
20	176.01	0.33	5.59	62.12	62120	66.88
21	181.01	0.39	5.49	67.61	67610	72.79
22	186.01	0.3	5.69	73.3	73300	78.92
23	191.01	0.4	5.66	78.96	78960	85.01
24	196.01	0.32	5.64	84.6	84600	91.09
25	201.01	0.44	5.8	90.4	90400	97.33
26	206.01	0.37	4.84	95.24	95240	102.54
27	211.01	0.12	2.52	97.76	97760	105.25
28	216.01	0.09	0.04	97.8	97800	105.30

Bentheimer core sample saturated with 20 wt.% brine (NaCl) and flooded with CO_2 @ 3ml/min

Run	Cumulative Time (min)	dp (Psi)	Volume of CO_2 produced $V_g(l)$	Cumulative Volume of CO_2 Produced $V_g(l)$	Cumulative Volume of CO_2 Produced $V_g(cm^3)$	Cumulative Volume of CO_2 Produced (cm^3) over Pore volume (cm^3)
1	97.5	0.45	0	0	0	0
2	102.5	0.16	3.08	3.08	3080	3.32
3	107.5	0.22	2.15	5.23	5230	5.63
4	112.5	0.26	1.87	7.1	7100	7.64
5	117.5	0.2	1.98	9.08	9080	9.78
6	122.5	0.16	2.05	11.13	11130	11.98
7	127.5	0.21	1.91	13.04	13040	14.04
8	132.5	0.17	2.07	15.11	15110	16.27
9	137.5	0.53	3.63	18.74	18740	20.18
10	142.5	0.1	5.05	23.79	23790	25.61
11	147.5	0.2	5.68	29.47	29470	31.73
12	152.5	0.08	5.89	35.36	35360	38.07
13	157.5	0.11	5.81	29.47	29470	31.73
14	162.5	0.11	5.93	35.36	35360	38.07
15	167.5	0.12	5.13	41.17	41170	44.33
16	172.5	0.26	6.02	47.1	47100	50.71
17	177.5	0.13	6.01	52.23	52230	56.23
18	182.5	0.19	6.09	58.25	58250	62.72
19	187.5	0.09	5.77	64.26	64260	69.19
20	192.5	0.32	6	70.35	70350	75.74
21	197.5	0.19	5.94	76.12	76120	81.96
22	202.5	0.11	6.01	82.12	82120	88.42
23	207.5	0.22	6.34	88.06	88060	94.81
24	212.5	0.17	5.89	94.07	94070	101.28
25	217.5	0.35	6.14	100.41	100410	108.11
26	222.5	0.02	2.23	112.44	112440	121.06
27	227.5	0.03	0.06	114.73	114730	123.52

Bentheimer core sample saturated with 25 wt.% brine (NaCl) and flooded with CO_2 @ 3ml/min

Run	Cumulative Time (min)	dp (Psi)	Volume of CO_2 produced $V_g(l)$	Cumulative Volume of CO_2 Produced $V_g(l)$	Cumulative Volume of CO_2 Produced $V_g(cm^3)$	Cumulative Volume of CO_2 Produced (cm^3) over Pore volume (cm^3)
1	78.17	0.75	0	0	0	0
2	83.17	0.71	1.89	1.89	1890	2.03
3	88.17	0.66	1.96	3.85	3850	4.15
4	93.17	0.71	1.88	5.72	5720	6.16
5	98.17	0.73	1.83	7.56	7560	8.14
6	103.17	0.58	1.7	9.26	9260	9.97
7	108.17	0.55	2.58	11.84	11840	12.75
8	113.17	0.52	4.76	16.6	16600	17.87
9	118.17	0.42	5.02	21.62	21620	23.28
10	123.17	0.38	5.22	26.84	26840	28.90
11	128.17	0.39	5.55	32.39	32390	34.87
12	133.17	0.37	5.71	38.1	38100	41.02
13	138.17	0.4	5.49	43.59	43590	46.93
14	143.17	0.9	5.64	49.23	49230	53.00
15	148.17	0.35	5.74	54.97	54970	59.18
16	153.17	0.29	5.55	60.52	60520	65.16
17	158.17	0.32	5.45	65.97	65970	71.03
18	163.17	0.4	5.63	71.6	71600	77.09
19	168.17	0.32	5.97	77.57	77570	83.52
20	173.17	0.3	5.22	82.79	82790	89.14
21	178.17	0.54	5.39	88.18	88180	94.94
22	183.17	0.3	5.56	93.74	93740	100.93
23	188.17	0.32	5.13	98.87	98870	106.45
24	193.17	0.3	5	103.87	103870	111.83
25	198.17	0.36	5.73	109.6	109600	118.00
26	203.17	0.33	5.53	115.13	115130	123.96
27	208.17	0.21	1.55	116.68	116680	125.62
28	213.17	0.23	0.06	116.74	116740	125.69

Bentheimer core sample saturated with 5 wt.% brine (KCl) and flooded with CO_2 @ 3ml/min

Run	Cumulative Time (min)	dp (Psi)	Volume of CO_2 produced $V_g(l)$	Cumulative Volume of CO_2 Produced $V_g(l)$	Cumulative Volume of CO_2 Produced $V_g(cm^3)$	Cumulative Volume of CO_2 Produced (cm^3) over Pore volume (cm^3)
1	109.83	0.74	0	0	0	0
2	114.83	0.5	3.13	3.13	3130	3.37
3	119.83	0.34	2.6	5.73	5730	6.17
4	124.83	0.38	1.89	7.62	7620	8.20
5	129.83	0.37	1.89	9.51	9510	10.24
6	134.83	0.39	1.99	11.5	11500	12.38
7	139.83	0.44	2.01	13.51	13510	14.55
8	144.83	0.5	2.03	15.54	15540	16.73
9	149.83	0.69	2.81	19.35	19350	20.83
10	154.83	0.33	5.13	24.48	24480	26.36
11	159.83	0.47	5.77	30.25	30250	32.57
12	164.83	0.38	6.04	36.29	36290	39.07
13	169.83	0.37	5.91	42.2	42200	45.43
14	174.83	0.33	6.2	48.4	48400	52.11
15	179.83	0.56	5.95	54.35	54350	58.52
16	184.83	0.48	6.01	60.36	60360	64.99
17	189.83	0.27	3.29	63.65	63650	68.53
18	194.83	0.39	5.2	68.85	68850	74.13
19	199.83	0.3	2.29	71.14	71140	76.59
20	204.83	0.13	0.44	71.58	71580	77.07
21	209.83	0.04	0.41	71.99	71990	77.51
22	214.83	0.04	0.51	72.5	72500	78.06

Bentheimer core sample saturated with 10 wt.% brine (KCl) and flooded with CO_2 @ 3ml/min

Run	Cumulative Time (min)	dp (Psi)	Volume of CO_2 produced $V_g(l)$	Cumulative Volume of CO_2 Produced $V_g(l)$	Cumulative Volume of CO_2 Produced $V_g(cm^3)$	Cumulative Volume of CO_2 Produced (cm^3) over Pore volume (cm^3)
1	90.51	0.63	0	0	0	0
2	95.51	0.53	2.86	2.86	2860	3.08
3	100.51	0.54	2.06	4.92	4920	5.30
4	105.51	0.46	1.89	6.81	6810	7.33
5	110.51	0.59	2.03	8.84	8840	9.52
6	115.51	0.47	1.97	10.81	10810	11.64
7	120.51	0.58	1.96	12.77	12770	13.75
8	125.51	1.04	3.59	16.36	16360	17.61
9	130.51	1.07	5.02	21.38	21380	23.02
10	135.51	0.51	5.33	26.71	26710	28.76
11	140.51	0.66	5.82	32.53	32530	35.02
12	145.51	0.43	5.94	38.47	38470	41.42
13	150.51	0.47	5.9	44.37	44370	47.77
14	155.51	0.41	5.9	50.27	50270	54.12
15	160.51	0.43	6	56.27	56270	60.58
16	165.51	0.51	5.84	62.11	62110	66.87
17	170.51	0.86	5.87	67.98	67980	73.19
18	175.51	0.68	6	73.98	73980	79.65
19	180.51	0.5	6.02	80	80000	86.13
20	185.51	0.78	5.87	85.87	85870	92.45
21	190.51	0.53	6.01	91.88	91880	98.92
22	195.51	0.53	6.05	97.93	97930	105.44
23	200.51	0.53	6.02	103.95	103950	111.92
24	205.51	3.57	4.82	108.77	108770	117.11
25	210.51	4.16	0.71	109.48	109480	117.87
26	215.51	1.11	0.29	109.77	109770	118.18

Appendices

Bentheimer core sample saturated with 15 wt.% brine (KCl) and flooded with CO_2 @ 3ml/min

Run	Cumulative Time (min)	dp (Psi)	Volume of CO_2 produced $V_g(l)$	Cumulative Volume of CO_2 Produced $V_g(l)$	Cumulative Volume of CO_2 Produced $V_g(cm^3)$	Cumulative Volume of CO_2 Produced (cm^3) over Pore volume (cm^3)
1	84.17	0.39	0	0	0	0
2	89.17	0.18	3.26	3.26	3260	3.51
3	94.17	0.22	2.54	5.8	5800	6.24
4	99.17	0.22	1.73	7.53	7530	8.11
5	104.17	0.2	1.84	9.37	9370	10.09
6	109.17	0.18	2.25	11.62	11620	12.51
7	114.17	0.21	1.89	13.51	13510	14.55
8	119.17	0.2	2	15.51	15510	16.70
9	124.17	0.34	3.52	19.03	19030	20.49
10	129.17	0.52	4.8	23.83	23830	25.66
11	134.17	0.26	5.36	29.19	29190	31.43
12	139.17	0.12	5.68	34.87	34870	37.54
13	144.17	0.19	5.64	40.51	40510	43.62
14	149.17	0.37	5.55	46.06	46060	49.59
15	154.17	0.25	5.53	51.59	51590	55.54
16	159.17	0.11	5.62	57.21	57210	61.60
17	164.17	0.34	5.76	62.88	62880	67.70
18	169.17	0.37	5.76	68.64	68640	73.90
19	174.17	0.27	5.7	74.34	74340	80.04
20	179.17	0.16	5.88	80.22	80220	86.37
21	184.17	0.16	5.75	85.97	85970	92.56
22	189.17	0.15	4.93	90.9	90900	97.87
23	194.17	0.07	0.58	91.48	91480	98.49
24	199.17	0.23	2.4	93.88	93880	101.08

Bentheimer core sample saturated with 20 wt.% brine (KCl) and flooded with CO_2 @ 3ml/min

Run	Cumulative Time (min)	dp (Psi)	Volume of CO_2 produced $V_g(l)$	Cumulative Volume of CO_2 Produced $V_g(l)$	Cumulative Volume of CO_2 Produced $V_g(cm^3)$	Cumulative Volume of CO_2 Produced (cm^3) over Pore volume (cm^3)
1	73.17	0.65	0	0	0	0
2	78.17	0.63	3.09	3.09	3090	3.33
3	83.17	0.54	1.91	5	5000	5.38
4	88.17	0.66	2.05	7.05	7050	7.59
5	93.17	0.51	1.84	8.89	8890	9.57
6	98.17	0.71	1.85	10.74	10740	11.56
7	103.17	0.99	1.92	12.66	12660	13.63
8	108.17	1.09	2	14.66	14660	15.78
9	113.17	0.75	4.15	18.81	18810	20.25
10	118.17	0.85	5.32	24.13	24130	25.98
11	123.17	1.05	4.59	28.72	28720	30.92
12	128.17	0.56	6.09	34.81	34810	37.48
13	133.17	0.89	6	40.81	40810	43.94
14	138.17	0.83	5.82	46.63	46630	50.20
15	143.17	0.68	5.54	52.17	52170	56.17
16	148.17	0.51	5.67	57.84	57840	62.27
17	153.17	0.45	5.64	63.48	63480	68.35
18	158.17	6.07	3.4	66.88	66880	72.01
19	163.17	0.82	6.03	72.91	72910	78.50
20	168.17	0.34	4.76	77.67	77670	83.62
21	173.17	0.42	5.68	83.35	83350	89.74
22	178.17	3.1	5.96	89.31	89310	96.16
23	183.17	0.45	6.02	95.33	95330	102.64
24	188.17	0.4	5.21	100.54	100540	108.25
25	193.17	0.54	5.61	106.15	106150	114.29
26	198.17	0.98	6.04	112.19	112190	120.79
27	203.17	0.21	4.38	116.57	116570	125.51
28	208.17	0.19	0.21	116.78	116780	125.73

Appendices

Bentheimer core sample saturated with 25 wt.% brine (KCl) and flooded with CO_2 @ 3ml/min

Run	Cumulative Time (min)	dp (Psi)	Volume of CO_2 produced $V_g(l)$	Cumulative Volume of CO_2 Produced $V_g(l)$	Cumulative Volume of CO_2 Produced $V_g(cm^3)$	Cumulative Volume of CO_2 Produced (cm^3) over Pore volume (cm^3)
1	97.67	0.68	0	0	0	0
2	102.67	0.72	3.44	3.44	3440	3.70
3	107.67	0.46	2.17	5.61	5610	6.04
4	112.67	0.5	1.51	7.12	7120	7.67
5	117.67	0.49	2.05	9.17	9170	9.87
6	122.67	0.62	2.1	11.27	11270	12.13
7	127.67	0.53	1.97	13.24	13240	14.25
8	132.67	0.58	2.1	15.34	15340	16.52
9	137.67	0.47	3.55	18.89	18890	20.34
10	142.67	0.5	5.43	24.32	24320	26.18
11	147.67	0.49	5.45	29.77	29770	32.05
12	152.67	0.54	5.53	35.3	35300	38.01
13	157.67	0.45	5.53	40.63	40630	43.74
14	162.67	0.58	5.77	46.4	46400	49.96
15	167.67	0.73	5.95	52.35	52350	56.36
16	172.67	0.41	4.41	56.76	56760	61.11
17	177.67	0.36	3.7	60.46	60460	65.09
18	182.67	0.82	5.45	65.91	65910	70.96
19	187.67	0.41	5.64	71.55	71550	77.03
20	192.67	0.42	5.88	77.55	77550	83.49
21	197.67	0.45	5.92	83.55	83550	89.95
22	202.67	0.39	6.41	89.76	89760	96.64
23	207.67	0.42	5.38	95.14	95140	102.43
24	212.67	0.52	5.96	101.1	101100	108.85
25	217.67	0.37	5.28	106.38	106380	114.53
26	222.67	0.31	0.37	106.75	106750	114.93

Bentheimer core sample saturated with 5 wt.% brine (CaCl$_2$) and flooded with CO$_2$ @ 3ml/min

Run	Cumulative Time (min)	dp (Psi)	Volume of CO$_2$ produced V$_g$(l)	Cumulative Volume of CO$_2$ Produced V$_g$(l)	Cumulative Volume of CO$_2$ Produced V$_g$(cm^3)	Cumulative Volume of CO$_2$ Produced (cm^3) over Pore volume (cm^3)
1	107.17	0.54	0	0	0	0
2	112.17	0.45	3.22	3.22	3220	3.47
3	117.17	0.38	2	5.22	5220	5.62
4	122.17	0.49	1.96	7.18	7180	7.73
5	127.17	0.43	2	9.18	9180	9.88
6	132.17	0.46	1.99	11.17	11170	12.03
7	137.17	0.41	2.01	13.18	13180	14.19
8	142.17	0.34	2.07	15.25	15250	16.42
9	147.17	0.85	2.34	17.59	17590	18.94
10	152.17	0.37	4.84	22.43	22430	24.15
11	157.17	0.33	5.34	27.77	27770	29.90
12	162.17	0.37	5.69	33.46	33460	36.02
13	167.17	0.42	5.82	39.24	39240	42.25
14	172.17	0.32	5.86	45.1	45100	48.56
15	177.17	0.33	5.94	51.04	51040	54.95
16	182.17	0.37	6.09	57.13	57130	61.51
17	187.17	0.69	5.68	63.81	63810	68.70
18	192.17	0.41	6.08	69.86	69860	75.22
19	197.17	0.33	5.3	75.16	75160	80.92
20	202.17	0.36	5.99	81.15	81150	87.37
21	207.17	0.32	5.97	87.12	87120	93.80
22	212.17	0.31	5.93	93.05	93050	100.18
23	217.17	0.31	5.04	98.09	98090	105.61
24	222.17	0.35	2.46	100.55	100550	108.26
25	227.17	0.27	4.43	104.98	104980	113.03
26	232.17	0.25	0.27	105.25	105250	113.32
27	237.17	0.24	0.06	105.31	105310	113.38

Appendices

Bentheimer core sample saturated with 10 wt.% brine (CaCl$_2$) and flooded with CO$_2$ @ 3ml/min

Run	Cumulative Time (min)	dp (Psi)	Volume of CO$_2$ produced V$_g$(l)	Cumulative Volume of CO$_2$ Produced V$_g$(l)	Cumulative Volume of CO$_2$ Produced V$_g$(cm^3)	Cumulative Volume of CO$_2$ Produced (cm^3) over Pore volume (cm^3)
1	52.33	0.5	0	0	0	0
2	57.33	0.47	2.88	2.88	2880	3.10
3	62.33	0.5	2.09	4.97	4970	5.35
4	67.33	0.47	2.02	6.99	6990	7.53
5	72.33	0.46	2.08	9.07	9070	9.77
6	77.33	0.48	1.97	11.04	11040	11.89
7	82.33	0.63	2.38	13.42	13420	14.45
8	87.33	0.35	4.3	17.72	17720	19.08
9	92.33	0.35	5.16	22.88	22880	24.63
10	97.33	0.39	5.73	28.61	28610	30.80
11	102.33	0.3	5.91	34.52	34520	37.17
12	107.33	0.3	6.04	40.56	40560	43.67
13	112.33	0.63	5.87	46.43	46430	49.99
14	117.33	0.45	5.76	52.19	52190	56.19
15	122.33	0.41	6.07	58.26	58260	62.73
16	127.33	0.36	6.19	64.45	64450	69.39
17	132.33	0.6	6.13	70.58	70580	75.99
18	137.33	0.49	6.02	76.6	76600	82.47
19	142.33	0.36	5.9	82.5	82500	88.82
20	147.33	0.31	5.41	87.91	87910	94.65
21	152.33	0.4	4.26	92.17	92170	99.24
22	157.33	0.82	6.11	98.28	98280	105.81
23	162.33	0.75	6.21	104.49	104490	112.50
24	167.33	0.28	4.12	108.61	108610	116.94
25	172.33	0.28	0.12	108.73	108730	117.07
26	177.33	0.25	0.2	108.93	108930	117.28

Appendices

Bentheimer core sample saturated with 15 wt.% brine ($CaCl_2$) and flooded with CO_2 @ 3ml/min

Run	Cumulative Time (min)	dp (Psi)	Volume of CO_2 produced $V_g(l)$	Cumulative Volume of CO_2 Produced $V_g(l)$	Cumulative Volume of CO_2 Produced $V_g(cm^3)$	Cumulative Volume of CO_2 Produced (cm^3) over Pore volume (cm^3)
1	115.67	0.79	0	0	0	0
2	120.67	0.43	2.83	2.83	2830	3.05
3	125.67	0.44	2.02	4.85	4850	5.22
4	130.67	0.36	1.48	6.33	6330	6.82
5	135.67	0.36	1.72	8.05	8050	8.67
6	140.67	0.36	1.97	10.02	10020	10.79
7	145.67	0.34	1.74	11.76	11760	12.66
8	150.67	0.39	1.81	13.57	13570	14.61
9	155.67	0.44	1.84	15.41	15410	16.59
10	160.67	0.25	2.15	17.56	17560	18.91
11	165.67	0.35	4.65	22.21	22210	23.91
12	170.67	0.35	5.17	27.38	27380	29.48
13	175.67	0.59	5.39	32.77	32770	35.28
14	180.67	0.3	5.55	38.32	38320	41.26
15	185.67	0.59	5.61	43.93	43930	47.30
16	190.67	0.33	5.82	49.75	49750	53.56
17	195.67	0.36	5.44	55.19	55190	59.42
18	200.67	0.31	5.37	60.56	60560	65.20
19	205.67	0.36	5.46	66.02	66020	71.08
20	210.67	0.45	5.29	71.31	71310	76.78
21	215.67	0.41	5.74	77.05	77050	82.96
22	220.67	0.35	5.54	82.59	82590	88.92
23	225.67	1.31	5.74	88.33	88330	95.10
24	230.67	0.27	1.49	89.82	89820	96.71
25	235.67	0.23	0.11	89.93	89930	96.82
26	240.67	0.2	0.05	89.98	89980	96.88

Appendices

Bentheimer core sample saturated with 20 wt.% brine ($CaCl_2$) and flooded with CO_2 @ 3ml/min

Run	Cumulative Time (min)	dp (Psi)	Volume of CO_2 produced $V_g(l)$	Cumulative Volume of CO_2 Produced $V_g(l)$	Cumulative Volume of CO_2 Produced $V_g(cm^3)$	Cumulative Volume of CO_2 Produced (cm^3) over Pore volume (cm^3)
1	102.33	0.69	0	0	0	0
2	107.33	0.51	2.68	2.68	2680	2.89
3	112.33	0.48	2.02	4.7	4700	5.06
4	117.33	0.48	1.99	6.69	6690	7.20
5	122.33	0.62	2.05	8.74	8740	9.41
6	127.33	0.52	2.06	10.8	10800	11.63
7	132.33	0.48	2.11	12.91	12910	13.90
8	137.33	0.57	2.05	14.96	14960	16.11
9	142.33	0.48	2.14	17.1	17100	18.41
10	147.33	0.96	2.75	19.85	19850	21.37
11	152.33	0.93	5.16	25.01	25010	26.93
12	157.33	0.44	5.37	30.38	30380	32.71
13	162.33	0.45	5.17	35.55	35550	38.28
14	167.33	1.62	6.07	41.62	41620	44.81
15	172.33	0.36	6.12	47.74	47740	51.40
16	177.33	0.4	6.07	53.81	53810	57.93
17	182.33	0.59	6.2	60.01	60010	64.61
18	187.33	0.56	6.15	66.16	66160	71.23
19	192.33	0.49	6.31	72.47	72470	78.03
20	197.33	2.09	6.46	78.92	78920	84.97
21	202.33	0.51	6.22	85.15	85150	91.68
22	207.33	2.09	6.55	91.7	91700	98.73
23	212.33	0.51	6.24	97.94	97940	105.45
24	217.33	0.51	6.31	104.25	104250	112.24
25	222.33	0.24	1.1	105.34	105340	113.42

Appendices

Bentheimer core sample saturated with 25 wt.% brine ($CaCl_2$) and flooded with CO_2 @ 3ml/min

Run	Cumulative Time (min)	dp (Psi)	Volume of CO_2 produced $V_g(l)$	Cumulative Volume of CO_2 Produced $V_g(l)$	Cumulative Volume of CO_2 Produced $V_g(cm^3)$	Cumulative Volume of CO_2 Produced (cm^3) over Pore volume (cm^3)
1	77.17	0.61	0	0	0	0
2	82.17	0.45	3.19	3.19	3190	3.43
3	87.17	0.44	2.01	5.2	5200	5.60
4	92.17	0.5	1.96	7.16	7160	7.71
5	97.17	0.44	1.95	9.11	9110	9.81
6	102.17	0.49	2.05	11.16	11160	12.02
7	107.17	0.49	1.96	13.12	13120	14.13
8	112.17	0.45	2	15.12	15120	16.28
9	117.17	0.6	3.66	18.78	18780	20.22
10	122.17	0.38	5.09	23.87	23870	25.70
11	127.17	0.45	5.04	28.91	28910	31.13
12	132.17	0.74	5.66	34.57	34570	37.22
13	137.17	0.41	5.72	40.29	40290	43.38
14	142.17	0.32	5.86	46.15	46150	49.69
15	147.17	0.41	5.77	51.92	51920	55.90
16	152.17	0.45	5.95	57.87	57870	62.31
17	157.17	0.4	5.65	63.52	63520	68.39
18	162.17	0.51	5.75	69.27	69270	74.58
19	167.17	0.38	5.85	75.12	75120	80.88
20	172.17	0.36	5.79	80.91	80910	87.11
21	177.17	0.33	5.74	86.65	86650	93.29
22	182.17	0.36	5.84	92.49	92490	99.58
23	187.17	0.42	5.89	98.38	98380	105.92
24	192.17	0.46	5.88	104.26	104260	112.25
25	197.17	0.4	5.93	110.19	110190	118.64
26	202.17	0.51	6.18	116.37	116370	125.29
27	207.17	1.3	6.2	122.57	122570	131.97
28	212.17	0.25	3.41	125.98	125980	135.64

Bentheimer core sample saturated with 5 wt.% brine (MgCl$_2$) and flooded with CO$_2$ @ 3ml/min

Run	Cumulative Time (min)	dp (Psi)	Volume of CO$_2$ produced V$_g$(l)	Cumulative Volume of CO$_2$ Produced V$_g$(l)	Cumulative Volume of CO$_2$ Produced V$_g$(cm^3)	Cumulative Volume of CO$_2$ Produced (cm^3) over Pore volume (cm^3)
1	107.33	0.68	0	0	0	0
2	112.33	0.6	2.68	2.68	2680	2.89
3	117.33	0.54	2.11	4.79	4790	5.16
4	122.33	0.5	1.97	6.79	6790	7.31
5	127.33	0.54	1.93	8.69	8690	9.36
6	132.33	0.49	1.85	10.54	10540	11.35
7	137.33	0.48	1.64	12.18	12180	13.11
8	142.33	0.57	1.89	14.07	14070	15.15
9	147.33	0.54	1.88	15.95	15950	17.17
10	152.33	0.59	1.95	17.9	17900	19.27
11	157.33	0.74	2	19.9	19900	21.43
12	162.33	0.86	3.19	23.09	23090	24.86
13	167.33	1.03	5.18	28.27	28270	30.44
14	172.33	0.49	5.62	33.89	33890	36.49
15	177.33	0.61	5.78	39.67	39670	42.71
16	182.33	1.11	5.81	45.48	45480	48.97
17	187.33	0.54	6.08	51.56	51560	55.51
18	192.33	0.69	6.03	57.59	57590	62.00
19	197.33	0.33	5.42	63.01	63010	67.83
20	202.33	0.41	1	64.01	64010	68.92
21	207.33	0.28	0.13	64.143	64140	69.06

Appendices

Bentheimer core sample saturated with 10 wt.% brine ($MgCl_2$) and flooded with CO_2 @ 3ml/min

Run	Cumulative Time (min)	dp (Psi)	Volume of CO_2 produced $V_g(l)$	Cumulative Volume of CO_2 Produced $V_g(l)$	Cumulative Volume of CO_2 Produced $V_g(cm^3)$	Cumulative Volume of CO_2 Produced (cm^3) over Pore volume (cm^3)
1	74.5	0.7	0	0	0	0
2	79.5	0.74	2.87	2.87	2870	3.09
3	84.5	0.82	2.94	5.81	5810	6.26
4	89.5	0.87	2.59	8.4	8400	9.04
5	94.5	0.67	2.1	10.5	10500	11.30
6	99.5	0.79	1.8	12.3	12300	13.24
7	104.5	0.88	1.97	14.27	14270	15.36
8	109.5	0.87	1.39	15.66	15660	16.86
9	114.5	1.05	3.9	19.56	19560	21.06
10	119.5	0.73	4.06	23.62	23620	25.43
11	124.5	0.68	5.68	29.3	29300	31.55
12	129.5	1.03	5.73	35.03	35030	37.72
13	134.5	0.95	5.83	40.86	40860	43.99
14	139.5	0.5	6.05	46.91	46910	50.51
15	144.5	0.58	6.1	53.01	53010	57.07
16	149.5	0.67	6.83	59.84	59840	64.43
17	154.5	0.42	5.36	65.2	65200	70.20
18	159.5	0.62	5.44	70.64	70640	76.06
19	164.5	0.51	6.01	76.65	76650	82.53
20	169.5	1.06	7.06	83.71	83710	90.13
21	174.5	0.5	5.65	89.36	89360	96.21
22	179.5	0.44	5.83	95.19	95190	102.49
23	184.5	0.5	6.69	101.88	101880	109.69
24	189.5	0.43	5.71	107.59	107590	115.84
25	194.5	0.44	6.22	113.81	113810	122.53
26	199.5	0.62	5.93	119.74	119740	128.92

Appendices

Bentheimer core sample saturated with 15 wt.% brine ($MgCl_2$) and flooded with CO_2 @ 3ml/min

Run	Cumulative Time (min)	dp (Psi)	Volume of CO_2 produced V_g(l)	Cumulative Volume of CO_2 Produced V_g(l)	Cumulative Volume of CO_2 Produced V_g(cm^3)	Cumulative Volume of CO_2 Produced (cm^3) over Pore volume (cm^3)
1	75.68	1.15	0	0	0	0
2	80.68	0.68	2.47	2.47	2470	2.66
3	85.68	0.78	2.33	4.8	4800	5.17
4	90.68	0.83	1.6	6.4	6400	6.89
5	95.68	0.79	1.34	7.74	7740	8.33
6	100.68	0.8	1.65	9.39	9390	10.11
7	105.68	0.85	1.78	11.17	11170	12.03
8	110.68	1.61	3.18	14.35	14350	15.45
9	115.68	2.54	4.7	19.05	19050	20.51
10	120.68	0.65	4.95	24	24000	25.84
11	125.68	0.51	5.57	29.57	29570	31.84
12	130.68	1.01	5.84	34.41	34410	37.05
13	135.68	0.72	5.56	40.97	40970	44.11
14	140.68	6.3	5.65	46.62	46620	50.19
15	145.68	0.99	5.48	52.1	52100	56.09
16	150.68	0.84	5.47	57.57	57570	61.98
17	155.68	0.98	5.41	62.98	62980	67.81
18	160.68	0.55	5.41	68.39	68390	73.63
19	165.68	0.63	5.26	73.65	73650	79.30
20	170.68	0.77	5.46	79.11	79110	85.17
21	175.68	0.73	5.54	84.65	84650	91.14
22	180.68	0.65	5.44	90.09	90090	97.00
23	185.68	0.69	5.51	95.6	95600	102.93
24	190.68	0.76	5.56	101.16	101160	108.91
25	195.68	0.56	4.78	105.94	105940	114.06
26	200.68	0.51	5.49	111.43	111430	119.97
27	205.68	0.34	3.18	114.61	114610	123.40

Appendices

Bentheimer core sample saturated with 20 wt.% brine ($MgCl_2$) and flooded with CO_2 @ 3ml/min

Run	Cumulative Time (min)	dp (Psi)	Volume of CO_2 produced $V_g(l)$	Cumulative Volume of CO_2 Produced $V_g(l)$	Cumulative Volume of CO_2 Produced $V_g(cm^3)$	Cumulative Volume of CO_2 Produced (cm^3) over Pore volume (cm^3)
1	76.01	1.02	0	0	0	0
2	81.01	0.93	3.31	3.31	3310	3.56
3	86.01	0.78	2.52	5.83	5830	6.28
4	91.01	0.8	2.06	7.89	7890	8.49
5	96.01	0.87	1.71	9.6	9600	10.34
6	101.01	0.96	1.73	11.33	11330	12.20
7	106.01	0.84	2.3	13.63	13630	14.67
8	111.01	1.26	1.98	15.61	15610	16.81
9	116.01	0.74	4.8	20.41	20410	21.97
10	121.01	0.84	5.33	25.74	25740	27.71
11	126.01	0.85	5.86	31.6	31600	34.02
12	131.01	0.71	5.48	37.08	37080	39.92
13	136.01	1.04	5.68	42.76	42760	46.04
14	141.01	0.79	5.39	48.15	48150	51.84
15	146.01	0.73	5.9	54.05	54050	58.19
16	151.01	0.83	5.37	59.42	59420	63.98
17	156.01	0.83	5.77	65.19	65190	70.19
18	161.01	0.73	5.96	71.15	71150	76.60
19	166.01	0.81	5.61	76.76	76760	82.64
20	171.01	0.8	4.8	81.56	81560	87.81
21	176.01	0.74	6	87.56	87560	94.27
22	181.01	0.89	5.06	87.56	87560	94.27
23	186.01	1.04	4.9	92.62	92620	99.72
24	191.01	0.87	5.87	97.52	97520	105.00
25	196.01	0.69	5.89	103.39	103390	111.32
26	201.01	0.73	5.67	114.95	114950	123.76
27	206.01	0.62	5.64	120.59	120590	129.83
28	211.01	0.51	0.2	120.79	120790	130.05

Appendices

Bentheimer core sample saturated with 25 wt.% brine ($MgCl_2$) and flooded with CO_2 @ 3ml/min

Run	Cumulative Time (min)	dp (Psi)	Volume of CO_2 produced $V_g(l)$	Cumulative Volume of CO_2 Produced $V_g(l)$	Cumulative Volume of CO_2 Produced $V_g(cm^3)$	Cumulative Volume of CO_2 Produced (cm^3) over Pore volume (cm^3)
1	89.5	1.01	0	0	0	0
2	94.5	1.08	2.71	2.71	2710	2.92
3	99.5	0.96	2.03	4.74	4740	5.10
4	104.5	0.89	1.93	6.67	6670	7.18
5	109.5	1.15	1.88	8.55	8550	9.21
6	114.5	1.19	1.96	10.51	10510	11.32
7	119.5	1.27	1.97	12.48	12480	13.44
8	124.5	1.07	1.99	14.47	14470	15.58
9	129.5	1.76	2.41	16.88	16880	18.17
10	134.5	1.36	4.78	21.66	21660	23.32
11	139.5	1.23	5.22	26.88	26880	28.94
12	144.5	0.95	5.47	32.35	32350	34.83
13	149.5	0.82	5.69	38.04	38040	40.96
14	154.5	1.01	5.66	43.7	43700	47.05
15	159.5	1.23	5.7	49.4	49400	53.19
16	164.5	0.86	5.78	55.18	55180	59.41
17	169.5	0.77	5.59	60.77	60770	65.43
18	174.5	0.99	5.91	66.68	66680	71.79
19	179.5	1.76	5.77	72.45	72450	78.00
20	184.5	0.84	5.72	78.17	78170	84.16
21	189.5	0.85	5.78	83.95	83950	90.39
22	194.5	1.06	5.8	89.75	89750	96.63
23	199.5	0.79	5.37	95.12	95120	102.41
24	204.5	0.9	5.77	100.89	100890	108.62
25	209.5	0.59	2.62	103.51	103510	111.44
26	214.5	0.58	0.08	103.59	103590	111.53

Appendices

Salt Wash North core sample saturated with 5 wt.% brine (NaCl) and flooded with CO_2 @ 3ml/min

Run	Cumulative Time (min)	dp (Psi)	Volume of CO_2 produced V_g(l)	Cumulative Volume of CO_2 Produced V_g(l)	Cumulative Volume of CO_2 Produced V_g(cm^3)	Cumulative Volume of CO_2 Produced (cm^3) over Pore volume (cm^3)
1	72.51	0.93	0	0	0	0
2	77.51	0.74	2.78	2.78	2780	3.34
3	82.51	0.78	1.9	4.68	4680	5.62
4	87.51	0.66	1.88	6.56	6560	7.87
5	92.51	0.86	1.95	8.51	8510	10.21
6	97.51	0.84	1.86	10.37	10370	12.45
7	102.51	0.88	1.93	12.3	12300	14.76
8	107.51	1.13	3.68	15.98	15980	19.18
9	112.51	1.1	4.9	20.88	20880	25.06
10	117.51	0.98	5.38	26.26	26260	31.52
11	122.51	0.93	5.61	31.87	31870	38.25
12	127.51	2.28	5.7	37.57	37570	45.09
13	132.51	2.23	5.83	43.4	43400	52.09
14	137.51	1.36	5.81	49.21	49210	59.06
15	142.51	2.2	5.78	54.99	54990	66.00
16	147.51	0.68	5.73	60.72	60720	72.88
17	152.51	1.04	5.72	66.44	66440	79.74
18	157.51	1.19	5.86	72.3	72300	86.77
19	162.51	1.27	5.47	77.77	77770	93.34
20	167.51	1.05	5.39	83.16	83160	99.81
21	172.51	0.88	5.71	88.87	88870	106.66
22	177.51	0.4	3.91	92.78	92780	111.35
23	182.51	0.8	3.17	95.95	95950	115.16
24	187.51	0.69	5.49	101.44	101440	121.75
25	192.51	1.84	5.42	106.86	106860	128.25
26	197.51	1.26	5.22	112.08	112080	134.52
27	202.51	0.4	1.63	113.71	113710	136.47

Appendices

Salt Wash North core sample saturated with 10 wt.% brine (NaCl) and flooded with CO_2 @ 3ml/min

Run	Cumulative Time (min)	dp (Psi)	Volume of CO_2 produced V_g(l)	Cumulative Volume of CO_2 Produced V_g(l)	Cumulative Volume of CO_2 Produced V_g(cm^3)	Cumulative Volume of CO_2 Produced (cm^3) over Pore volume (cm^3)
1	111.51	1.03	0	0	0	0
2	116.5	1.07	2.52	2.52	2520	3.02
3	121.5	1.06	1.98	4.5	4500	5.40
4	126.5	1.04	1.91	6.41	6410	7.69
5	131.5	1.06	1.93	8.34	8340	10.01
6	136.5	1.05	1.93	10.27	10270	12.33
7	141.5	0.92	2.03	12.3	12300	14.76
8	146.5	1.13	2.07	14.37	14370	17.25
9	151.5	0.94	2.1	16.47	16470	19.77
10	156.5	0.95	2.08	18.55	18550	22.26
11	161.5	1.12	2.07	20.62	20620	24.75
12	166.5	1.16	2.1	22.72	22720	27.27
13	171.5	1.53	4.4	27.12	27120	32.55
14	176.5	1.48	5.44	32.56	32560	39.08
15	181.5	1.32	5.73	38.29	38290	45.96
16	186.5	2.05	6.05	44.34	44340	53.22
17	191.5	1.59	5.89	50.23	50230	60.29
18	196.5	2.04	5.91	56.14	56140	67.38
19	201.5	1.31	6.12	62.26	62260	74.72
20	206.5	3.9	6.18	68.44	68440	82.14
21	211.5	0.57	0.07	68.51	68510	82.23

Salt Wash North core sample saturated with 15 wt.% brine (NaCl) and flooded with CO_2 @ 3ml/min

Run	Cumulative Time (min)	dp (Psi)	Volume of CO_2 produced V_g(l)	Cumulative Volume of CO_2 Produced V_g(l)	Cumulative Volume of CO_2 Produced V_g(cm^3)	Cumulative Volume of CO_2 Produced (cm^3) over Pore volume (cm^3)
1	116.17	1.01	0	0	0	0
2	121.17	0.89	1.86	1.86	1860	2.23
3	126.17	1.18	2	3.86	3860	4.63
4	131.17	1.16	1.84	5.7	5700	6.84
5	136.17	0.86	1.75	7.45	7450	8.94
6	141.17	0.84	1.92	9.37	9370	11.25
7	146.17	1.33	1.9	11.27	11270	13.53
8	151.17	1.3	2.06	13.33	13330	16.00
9	156.17	0.96	1.93	15.26	15260	18.31
10	161.17	1.11	2.04	17.3	17300	20.76
11	166.17	1.29	2.08	19.38	19380	23.26
12	171.17	1.11	2.07	21.45	21450	25.74
13	176.17	1.16	2.06	23.51	23510	28.22
14	181.17	1.03	2.08	25.59	25590	30.71
15	186.17	1.04	2.07	27.66	27660	33.20
16	191.17	1.19	2.07	29.73	29730	35.68
17	196.17	1.87	2.3	32.03	32030	38.44
18	201.17	1.95	5.06	37.09	37090	44.52
19	206.17	1.69	5.55	42.64	42640	51.18
20	211.17	0.61	4.79	47.43	47430	56.93
21	216.17	0.58	0.11	47.54	47540	57.06

Salt Wash North core sample saturated with 20 wt.% brine (NaCl) and flooded with CO_2 @ 3ml/min

Run	Cumulative Time (min)	dp (Psi)	Volume of CO_2 produced $V_g(l)$	Cumulative Volume of CO_2 Produced $V_g(l)$	Cumulative Volume of CO_2 Produced $V_g(cm^3)$	Cumulative Volume of CO_2 Produced (cm^3) over Pore volume (cm^3)
1	120.84	1.15	0	0	0	0
2	125.84	1.84	2.43	2.43	2430	2.92
3	130.84	1.14	1.84	4.27	4270	5.12
4	135.84	1.18	1.87	6.14	6140	7.37
5	140.84	1.18	1.73	7.87	7870	9.45
6	145.84	1.25	1.96	9.83	9830	11.80
7	150.84	0.87	1.93	11.76	11760	14.11
8	155.84	0.95	1.97	13.73	13730	16.48
9	160.84	1.23	2.05	15.78	15780	18.94
10	165.84	1.32	2.05	17.83	17830	21.40
11	170.84	1.15	2.05	19.88	19880	23.86
12	175.84	1.25	2.06	21.94	21940	26.33
13	180.84	1.41	2.09	24.03	24030	28.84
14	185.84	1.27	2.09	26.12	26120	31.35
15	190.84	1.38	2.11	28.23	28230	33.88
16	195.84	2.24	2.29	30.52	30520	36.63
17	200.84	1.88	4.96	35.48	35480	42.58
18	205.84	1.84	5.45	40.93	40930	49.12
19	210.84	0.85	5.34	46.27	46270	55.53
20	215.84	0.62	0.34	46.61	46610	55.94
21	220.84	0.67	0.21	46.82	46820	56.19

Appendices

Salt Wash North core sample saturated with 25 wt.% brine (NaCl) and flooded with CO_2 @ 3ml/min

Run	Cumulative Time (min)	dp (Psi)	Volume of CO_2 produced $V_g(l)$	Cumulative Volume of CO_2 Produced $V_g(l)$	Cumulative Volume of CO_2 Produced $V_g(cm^3)$	Cumulative Volume of CO_2 Produced (cm^3) over Pore volume (cm^3)
1	113.17	1.16	0	0	0	0.00
2	118.17	1.74	2.05	2.05	2050	2.46
3	123.17	1.44	2.08	4.13	4130	4.96
4	128.17	1.27	1.17	5.3	5300	6.36
5	133.17	1.39	1.32	6.62	6620	7.95
6	138.17	1.47	1.55	8.17	8170	9.81
7	143.17	1.37	1.59	9.76	9760	11.71
8	148.17	1.36	1.56	11.32	11320	13.59
9	153.17	1.31	1.66	12.98	12980	15.58
10	158.17	1.34	1.65	14.63	14630	17.56
11	163.17	1.42	1.65	16.28	16280	19.54
12	168.17	1.39	1.66	17.94	17940	21.53
13	173.17	1.28	1.71	19.65	19650	23.58
14	178.17	1.3	1.7	21.35	21350	25.62
15	183.17	1.33	1.68	23.03	23030	27.64
16	188.17	1.77	1.73	24.76	24760	29.72
17	193.17	1.99	4.12	28.88	28880	34.66
18	198.17	1.36	5.02	33.9	33900	40.69
19	203.17	1.91	5.64	39.54	39540	47.46
20	208.17	0.55	1.47	41.01	41010	49.22
21	213.17	0.58	0.09	41.1	41100	49.33

Salt Wash North core sample saturated with 5 wt.% brine (KCl) and flooded with CO_2 @ 3ml/min

Run	Cumulative Time (min)	dp (Psi)	Volume of CO_2 produced $V_g(l)$	Cumulative Volume of CO_2 Produced $V_g(l)$	Cumulative Volume of CO_2 Produced $V_g(cm^3)$	Cumulative Volume of CO_2 Produced (cm^3) over Pore volume (cm^3)
1	37.69	0.79	0	0	0	0.00
2	42.69	0.86	3.87	3.87	3870	4.64
3	47.69	0.84	2.26	6.13	6130	7.36
4	52.69	0.88	2.03	8.16	8160	9.79
5	57.69	1.77	2.21	10.37	10370	12.45
6	62.69	1.12	4.23	14.6	14600	17.52
7	67.69	1.1	4.18	18.78	18780	22.54
8	72.69	0.84	5.68	24.46	24460	29.36
9	77.69	1.45	5.84	30.3	30300	36.37
10	82.69	1.13	5.01	35.31	35310	42.38
11	87.69	0.92	5.85	41.16	41160	49.40
12	92.69	1.7	5.87	47.03	47030	56.45
13	97.69	2.53	5.53	52.56	52560	63.08
14	102.69	0.93	5.82	58.38	58380	70.07
15	107.69	2.63	5.83	64.21	64210	77.06
16	112.69	0.9	5.88	70.09	70090	84.12
17	117.69	1.71	5.94	76.03	76030	91.25
18	122.69	1.04	5.54	81.57	81570	97.90
19	127.69	0.66	0.97	82.54	82540	99.06
20	132.69	0.48	0.34	82.88	82880	99.47

Salt Wash North core sample saturated with 10 wt.% brine (KCl) and flooded with CO_2 @ 3ml/min

Run	Cumulative Time (min)	dp (Psi)	Volume of CO_2 produced $V_g(l)$	Cumulative Volume of CO_2 Produced $V_g(l)$	Cumulative Volume of CO_2 Produced $V_g(cm^3)$	Cumulative Volume of CO_2 Produced (cm^3) over Pore volume (cm^3)
1	22.17	0.76	0	0	0	0.00
2	27.17	1.69	4.43	4.43	4430	5.32
3	32.17	1.51	2.35	6.78	6780	8.14
4	37.17	1.3	2.09	8.87	8870	10.65
5	42.17	3.79	3.58	12.45	12450	14.94
6	47.17	1.26	5.1	17.55	17550	21.06
7	52.17	0.85	5.74	23.29	23290	27.95
8	57.17	1.02	5.92	29.21	29210	35.06
9	62.17	1.47	6.38	35.59	35590	42.71
10	67.17	0.96	6.03	41.62	41620	49.95
11	72.17	0.85	5.81	47.43	47430	56.93
12	77.17	1.2	5.72	53.15	53150	63.79
13	82.17	0.76	6.02	59.17	59170	71.02
14	87.17	0.98	5.74	64.91	64910	77.90
15	92.17	0.78	5.66	70.57	70570	84.70
16	97.17	1.69	5.84	76.41	76410	91.71
17	102.17	1.73	5.88	82.29	82290	98.76
18	107.17	0.79	5.61	87.9	87900	105.50
19	112.17	0.86	5.8	93.7	93700	112.46
20	117.17	1.66	5.57	99.27	99270	119.14
21	122.17	1	5.13	104.4	104400	125.30
22	127.17	1.14	5.22	109.62	109620	131.57
23	132.17	1.47	5.98	115.6	115600	138.74
24	137.17	0.73	5.85	121.45	121450	145.76
25	142.17	2.02	5.81	127.26	127260	152.74
26	147.17	1.23	6.01	133.27	133270	159.95
27	152.17	0.74	5.79	139.06	139060	166.90
28	157.17	0.91	6.03	145.09	145090	174.14
29	162.17	1.4	6.1	151.19	151190	181.46

Appendices

Salt Wash North core sample saturated with 15 wt.% brine (KCl) and flooded with CO_2 @ 3ml/min

Run	Cumulative Time (min)	dp (Psi)	Volume of CO_2 produced V_g(l)	Cumulative Volume of CO_2 Produced V_g(l)	Cumulative Volume of CO_2 Produced V_g(cm^3)	Cumulative Volume of CO_2 Produced (cm^3) over Pore volume (cm^3)
1	29.33	0.75	0	0	0	0.00
2	34.33	1	3.75	3.75	3750	4.50
3	39.33	0.85	2.13	5.88	5880	7.06
4	44.33	0.98	2.01	7.89	7890	9.47
5	49.33	0.95	1.97	9.86	9860	11.83
6	54.33	1.02	3.63	13.49	13490	16.19
7	59.33	0.93	5.01	18.5	18500	22.20
8	64.33	1.18	5.59	24.09	24090	28.91
9	69.33	0.79	5.69	29.78	29780	35.74
10	74.33	2.2	5.82	35.6	35600	42.73
11	79.33	1.44	5.7	41.3	41300	49.57
12	84.33	7.81	5.88	47.18	47180	56.63
13	89.33	0.69	5.69	52.87	52870	63.45
14	94.33	1.84	5.75	58.62	58620	70.36
15	99.33	0.77	5.83	64.45	64450	77.35
16	104.33	1.24	5.65	70.1	70100	84.13
17	109.33	1.35	5.98	76.08	76080	91.31
18	114.33	0.85	5.74	81.82	81820	98.20
19	119.33	0.86	5.81	87.63	87630	105.17
20	124.33	0.91	5.81	93.44	93440	112.15
21	129.33	0.6	1.28	94.72	94720	113.68

Salt Wash North core sample saturated with 20 wt.% brine (KCl) and flooded with CO_2 @ 3ml/min

Run	Cumulative Time (min)	dp (Psi)	Volume of CO_2 produced $V_g(l)$	Cumulative Volume of CO_2 Produced $V_g(l)$	Cumulative Volume of CO_2 Produced $V_g(cm^3)$	Cumulative Volume of CO_2 Produced (cm^3) over Pore volume (cm^3)
1	32.67	0.87	0	0	0	0.00
2	37.67	2.09	3.86	3.86	3860	4.63
3	42.67	2.27	2.62	6.48	6480	7.78
4	47.67	1.37	2.33	8.81	8810	10.57
5	52.67	1.79	1.59	10.4	10400	12.48
6	57.67	1.5	3.22	13.62	13620	16.35
7	62.67	1.68	4.62	18.24	18240	21.89
8	67.67	1.32	5.55	23.79	23790	28.55
9	72.67	2.01	5.33	29.12	29120	34.95
10	77.67	0.91	4.4	33.52	33520	40.23
11	82.67	1.45	5.2	38.72	38720	46.47
12	87.67	1.74	5.62	44.34	44340	53.22
13	92.67	0.91	4.59	48.93	48930	58.73
14	97.67	0.81	0.58	49.51	49510	59.42
15	102.67	1.12	6.99	56.5	56500	67.81
16	107.67	1.82	4.63	61.13	61130	73.37
17	112.67	1.47	5.87	67	67000	80.41
18	117.67	1.44	5.64	72.64	72640	87.18
19	122.67	1.73	5	77.64	77640	93.18
20	127.67	1.34	5.72	83.36	83360	100.05
21	132.67	1.57	5.75	89.11	89110	106.95
22	137.67	1.87	5.19	94.3	94300	113.18
23	142.67	1.76	5.86	100.16	100160	120.21
24	147.67	1.23	5.62	105.78	105780	126.96
25	152.67	1.38	4.96	110.74	110740	132.91
26	157.67	1.68	2.99	113.73	113730	136.50

Salt Wash North core sample saturated with 25 wt.% brine (KCl) and flooded with CO_2 @ 3ml/min

Run	Cumulative Time (min)	dp (Psi)	Volume of CO_2 produced $V_g(l)$	Cumulative Volume of CO_2 Produced $V_g(l)$	Cumulative Volume of CO_2 Produced $V_g(cm^3)$	Cumulative Volume of CO_2 Produced (cm^3) over Pore volume (cm^3)
1	76.5	1.16	0	0	0	0.00
2	81.5	0.84	3.08	3.08	3080	3.70
3	86.5	0.82	2.9	5.98	5980	7.18
4	91.5	1.03	3.58	9.56	9560	11.47
5	96.5	1.06	2.62	12.18	12180	14.62
6	101.5	1.38	0.72	12.9	12900	15.48
7	106.5	1.8	4.41	17.31	17310	20.78
8	111.5	1.72	4.93	22.24	22240	26.69
9	116.5	2.01	5.6	27.84	27840	33.41
10	121.5	2.09	5.63	33.47	33470	40.17
11	126.5	2.28	5.53	39	39000	46.81
12	131.5	1.91	5.03	44.03	44030	52.84
13	136.5	1.45	5.42	49.45	49450	59.35
14	141.5	1.74	5.44	54.89	54890	65.88
15	146.5	0.9	4.65	59.54	59540	71.46
16	151.5	0.8	5.62	65.16	65160	78.20
17	156.5	1.23	5.4	70.56	70560	84.69
18	161.5	1.93	5.8	76.36	76360	91.65
19	166.5	3.25	5.7	82.06	82060	98.49
20	171.5	6.82	5.65	87.71	87710	105.27
21	176.5	1.72	5.82	93.53	93530	112.25
22	181.5	1.58	5.08	98.61	98610	118.35
23	186.5	0.98	2.95	101.56	101560	121.89

Salt Wash North core sample saturated with 5 wt.% brine ($CaCl_2$) and flooded with CO_2 @ 3ml/min

Run	Cumulative Time (min)	dp (Psi)	Volume of CO_2 produced $V_g(l)$	Cumulative Volume of CO_2 Produced $V_g(l)$	Cumulative Volume of CO_2 Produced $V_g(cm^3)$	Cumulative Volume of CO_2 Produced (cm^3) over Pore volume (cm^3)
1	119.34	1	0	0	0	0.00
2	124.34	1.51	1.82	1.82	1820	2.18
3	129.34	1.35	1.55	3.37	3370	4.04
4	134.34	1.46	1.71	5.08	5080	6.10
5	139.34	1.5	1.79	6.87	6870	8.25
6	144.34	1.5	1.75	8.62	8620	10.35
7	149.34	1.12	1.46	10.08	10080	12.10
8	154.34	1.76	2.28	12.36	12360	14.83
9	159.34	1.32	1.93	14.29	14290	17.15
10	164.34	1.98	1.86	16.15	16150	19.38
11	169.34	1.54	1.92	18.07	18070	21.69
12	174.34	2.01	1.96	20.03	20030	24.04
13	179.34	1.97	1.89	21.92	21920	26.31
14	184.34	2.09	1.99	23.91	23910	28.70
15	189.34	1.74	1.91	25.82	25820	30.99
16	194.34	2.36	2.99	28.81	28810	34.58
17	199.34	2.41	5.05	33.86	33860	40.64
18	204.34	2.31	5.52	39.38	39380	47.26
19	209.34	0.66	1.31	40.69	40690	48.84
20	214.34	0.72	0.06	40.75	40750	48.91

Salt Wash North core sample saturated with 10 wt.% brine ($CaCl_2$) and flooded with CO_2 @ 3ml/min

Run	Cumulative Time (min)	dp (Psi)	Volume of CO_2 produced $V_g(l)$	Cumulative Volume of CO_2 Produced $V_g(l)$	Cumulative Volume of CO_2 Produced $V_g(cm^3)$	Cumulative Volume of CO_2 Produced (cm^3) over Pore volume (cm^3)
1	118.51	1.1	0	0	0	0.00
2	123.51	1.16	1.82	1.82	1820	2.18
3	128.51	1.23	1.92	3.74	3740	4.49
4	133.51	1.18	1.8	5.54	5540	6.65
5	138.51	1.2	1.87	7.41	7410	8.89
6	143.51	1.21	1.85	9.26	9260	11.11
7	148.51	1.25	1.99	11.25	11250	13.50
8	153.51	1.25	1.98	13.23	13230	15.88
9	158.51	1.18	1.99	15.22	15220	18.27
10	163.51	1.18	2.06	17.28	17280	20.74
11	168.51	1.27	2.05	19.33	19330	23.20
12	173.51	1.23	2.05	21.38	21380	25.66
13	178.51	1.2	2.15	23.53	23530	28.24
14	183.51	1.12	2.08	25.61	25610	30.74
15	188.51	1.23	2.04	27.65	27650	33.19
16	193.51	1.2	2.12	29.77	29770	35.73
17	198.51	1.66	4.26	34.03	34030	40.84
18	203.51	1.29	5.38	39.41	39410	47.30
19	208.51	0.72	5.21	44.62	44620	53.55
20	213.51	0.62	0.12	44.74	44740	53.70

Appendices

Salt Wash North core sample saturated with 15 wt.% brine ($CaCl_2$) and flooded with CO_2 @ 3ml/min

Run	Cumulative Time (min)	dp (Psi)	Volume of CO_2 produced $V_g(l)$	Cumulative Volume of CO_2 Produced $V_g(l)$	Cumulative Volume of CO_2 Produced $V_g(cm^3)$	Cumulative Volume of CO_2 Produced (cm^3) over Pore volume (cm^3)
1	119.67	0.98	0	0	0	0.00
2	124.67	1.42	1.2	1.2	1200	1.44
3	129.67	1.29	1.98	3.18	3180	3.82
4	134.67	1.33	1.98	5.16	5160	6.19
5	139.67	1.26	1.83	6.99	6990	8.39
6	144.67	1.38	1.77	8.76	8760	10.51
7	149.67	1.16	1.78	10.54	10540	12.65
8	154.67	1.18	1.86	12.4	12400	14.88
9	159.67	1.13	1.88	14.28	14280	17.14
10	164.67	1.1	2.05	16.33	16330	19.60
11	169.67	1.13	2.05	18.38	18380	22.06
12	174.67	1.14	2.1	20.48	20480	24.58
13	179.67	1.02	2.06	22.54	22540	27.05
14	184.67	1.02	2.15	24.69	24690	29.63
15	189.67	1.05	2.12	26.81	26810	32.18
16	194.67	1.1	2.09	28.9	28900	34.69
17	199.67	1.33	2.05	30.95	30950	37.15
18	204.67	1.82	4.2	35.15	35150	42.19
19	209.67	1.76	5.41	40.56	40560	48.68
20	214.67	0.57	4.85	45.41	45410	54.50
21	219.67	0.53	0.1	45.51	45510	54.62

Salt Wash North core sample saturated with 20 wt.% brine ($CaCl_2$) and flooded with CO_2 @ 3ml/min

Run	Cumulative Time (min)	dp (Psi)	Volume of CO_2 produced $V_g(l)$	Cumulative Volume of CO_2 Produced $V_g(l)$	Cumulative Volume of CO_2 Produced $V_g(cm^3)$	Cumulative Volume of CO_2 Produced (cm^3) over Pore volume (cm^3)
1	129.34	1.57	0	0	0	0.00
2	134.34	1.38	2.35	2.35	2350	2.82
3	139.34	1.26	2	4.35	4350	5.22
4	144.34	1.15	2.01	6.36	6360	7.63
5	149.34	1.12	2.01	8.37	8370	10.05
6	154.34	1.26	1.94	10.31	10310	12.37
7	159.34	0.93	1.73	12.04	12040	14.45
8	164.34	1.14	1.79	13.83	13830	16.60
9	169.34	1.14	1.74	15.57	15570	18.69
10	174.34	1.15	1.79	17.36	17360	20.84
11	179.34	1.05	1.87	19.23	19230	23.08
12	184.34	1.15	1.92	21.15	21150	25.38
13	189.34	1.02	1.96	23.11	23110	27.74
14	194.34	1.17	1.96	25.07	25070	30.09
15	199.34	1	2	27.07	27070	32.49
16	204.34	0.92	1.98	29.05	29050	34.87
17	209.34	2.79	3.37	32.42	32420	38.91
18	214.34	1.89	5.12	37.54	37540	45.06
19	219.34	2.02	5.49	43.03	43030	51.64
20	224.34	0.56	1.92	44.95	44950	53.95
21	229.34	0.56	0.11	45.06	45060	54.08

Salt Wash North core sample saturated with 25 wt.% brine ($CaCl_2$) and flooded with CO_2 @ 3ml/min

Run	Cumulative Time (min)	dp (Psi)	Volume of CO_2 produced $V_g(l)$	Cumulative Volume of CO_2 Produced $V_g(l)$	Cumulative Volume of CO_2 Produced $V_g(cm^3)$	Cumulative Volume of CO_2 Produced (cm^3) over Pore volume (cm^3)
1	118	2.58	0	0	0	0.00
2	123	1.2	3.45	3.45	3450	4.14
3	128	1.13	1.98	5.43	5430	6.52
4	133	1.14	1.99	7.42	7420	8.91
5	138	1.81	2.86	10.28	10280	12.34
6	143	1.55	4.87	15.15	15150	18.18
7	148	1.72	5.37	20.52	20520	24.63
8	153	1.78	5.85	26.37	26370	31.65
9	158	4.95	6.04	32.41	32410	38.90
10	163	1.37	6.03	38.44	38440	46.14
11	168	1.29	6.02	44.46	44460	53.36
12	173	1.59	6.13	50.59	50590	60.72
13	178	1.78	6.01	56.6	56600	67.93
14	183	1.5	6	62.6	62600	75.13
15	188	0.97	5.99	68.59	68590	82.32
16	193	1.16	6	74.59	74590	89.52
17	198	1.27	5.84	80.43	80430	96.53
18	203	1.29	5.93	86.36	86360	103.65
19	208	1.97	5.83	92.19	92190	110.65
20	213	1.06	5.8	97.99	97990	117.61
21	218	1.4	5.86	103.85	103850	124.64
22	223	0.87	5.77	109.62	109620	131.57
23	228	1.3	5.8	115.42	115420	138.53
24	233	1.25	5.57	120.99	120990	145.21
25	238	1.2	5.72	126.71	126710	152.08
26	243	1.54	5.62	132.33	132330	158.82
27	248	1.05	5.1	137.43	137430	164.94
28	253	1.07	4.84	142.27	142270	170.75
29	258	1.12	4.71	146.98	146980	176.40

Salt Wash North core sample saturated with 5 wt.% brine ($MgCl_2$) and flooded with CO_2 @ 3ml/min

Run	Cumulative Time (min)	dp (Psi)	Volume of CO_2 produced $V_g(l)$	Cumulative Volume of CO_2 Produced $V_g(l)$	Cumulative Volume of CO_2 Produced $V_g(cm^3)$	Cumulative Volume of CO_2 Produced (cm^3) over Pore volume (cm^3)
1	16.34	1.36	0	0	0	0.00
2	21.34	1.18	4.59	4.59	4590	5.51
3	26.34	1.09	5.5	10.09	10090	12.11
4	31.34	5.02	5.5	15.59	15590	18.71
5	36.34	1.45	5.76	21.35	21350	25.62
6	41.34	1.12	5.53	26.88	26880	32.26
7	46.34	1.42	5.42	32.3	32300	38.77
8	51.34	1.26	5.77	38.07	38070	45.69
9	56.34	1.08	5.39	43.46	43460	52.16
10	61.34	2.61	5.8	49.26	49260	59.12
11	66.34	1.46	5.47	54.73	54730	65.69
12	71.34	2.44	5.46	60.19	60190	72.24
13	76.34	0.8	5.38	65.57	65570	78.70
14	81.34	1.22	5.63	71.2	71200	85.45
15	86.34	0.92	5.22	76.42	76420	91.72
16	91.34	0.9	5.18	81.6	81600	97.94
17	96.34	0.95	4.82	86.42	86420	103.72
18	101.34	0.92	4.57	90.99	90990	109.21
19	106.34	1.08	4.59	95.58	95580	114.71
20	111.34	0.97	5.57	101.15	101150	121.40
21	116.34	1.27	5.39	106.54	106540	127.87
22	121.34	1.38	5.46	112	112000	134.42
23	126.34	0.89	5.18	117.18	117180	140.64
24	131.34	0.61	4.51	121.69	121690	146.05
25	136.34	0.59	0.06	121.75	121750	146.12

Appendices

Salt Wash North core sample saturated with 10 wt.% brine ($MgCl_2$) and flooded with CO_2 @ 3ml/min

Run	Cumulative Time (min)	dp (Psi)	Volume of CO_2 produced $V_g(l)$	Cumulative Volume of CO_2 Produced $V_g(l)$	Cumulative Volume of CO_2 Produced $V_g(cm^3)$	Cumulative Volume of CO_2 Produced (cm^3) over Pore volume (cm^3)
1	65.83	1.14	0	0	0	0.00
2	70.83	1.67	5	5	5000	6.00
3	75.83	0.91	4.67	9.67	9670	11.61
4	80.83	1.48	5.73	15.4	15400	18.48
5	85.83	1.78	5.5	20.9	20900	25.08
6	90.83	1.57	5.1	26	26000	31.20
7	95.83	1.55	5.33	31.33	31330	37.60
8	100.83	0.87	5.26	36.59	36590	43.92
9	105.83	1.58	5.35	41.94	41940	50.34
10	110.83	3.41	3.96	45.9	45900	55.09
11	115.83	1.31	5.56	51.46	51460	61.76
12	120.83	1.13	4.7	56.16	56160	67.40
13	125.83	2.74	5.38	61.54	61540	73.86
14	130.83	1.53	4.86	66.4	66400	79.69
15	135.83	2.75	5.44	71.84	71840	86.22
16	140.83	0.57	5.93	77.77	77770	93.34
17	145.83	0.42	6.22	83.99	83990	100.80
18	150.83	0.6	5.71	89.7	89700	107.66
19	155.83	0.49	6.68	96.38	96380	115.67
20	160.83	0.95	5.83	102.21	102210	122.67
21	165.83	1.55	5.65	107.86	107860	129.45
22	170.83	0.48	6.01	113.87	113870	136.67
23	175.83	0.52	5.44	119.31	119310	143.19
24	180.83	0.49	5.36	124.67	124670	149.63
25	185.83	0.61	2.32	126.99	126990	152.41
26	190.83	0.4	0.91	127.9	127900	153.50

Salt Wash North core sample saturated with 15 wt.% brine ($MgCl_2$) and flooded with CO_2 @ 3ml/min

Run	Cumulative Time (min)	dp (Psi)	Volume of CO_2 produced V_g(l)	Cumulative Volume of CO_2 Produced V_g(l)	Cumulative Volume of CO_2 Produced V_g(cm^3)	Cumulative Volume of CO_2 Produced (cm^3) over Pore volume (cm^3)
1	61.17	1.61	0	0	0	0.00
2	66.17	1.42	2.65	2.65	2650	3.18
3	71.17	0.76	2.51	5.16	5160	6.19
4	76.17	0.69	1.78	6.94	6940	8.33
5	81.17	0.65	1.52	8.46	8460	10.15
6	86.17	0.73	1.83	10.29	10290	12.35
7	91.17	0.78	1.96	12.25	12250	14.70
8	96.17	0.63	3.36	15.61	15610	18.73
9	101.17	0.55	4.88	20.49	20490	24.59
10	106.17	0.98	5.13	25.62	25620	30.75
11	111.17	0.84	5.75	31.37	31370	37.65
12	116.17	0.99	6.02	37.39	37390	44.88
13	121.17	6.25	5.74	43.13	43130	51.76
14	126.17	0.72	5.83	48.96	48960	58.76
15	131.17	1.01	5.66	54.62	54620	65.55
16	136.17	0.51	5.65	60.27	60270	72.34
17	141.17	0.65	5.59	65.86	65860	79.04
18	146.17	2.54	5.62	71.48	71480	85.79
19	151.17	1.61	5.44	76.92	76920	92.32
20	156.17	0.85	5.65	82.57	82570	99.10
21	161.17	0.8	5.72	88.29	88290	105.96
22	166.17	0.79	5.63	93.92	93920	112.72
23	171.17	0.83	5.69	99.61	99610	119.55
24	176.17	0.78	5.78	105.39	105390	126.49
25	181.17	0.62	3.28	108.67	108670	130.42
26	186.17	0.55	1.07	109.74	109740	131.71

Salt Wash North core sample saturated with 20 wt.% brine ($MgCl_2$) and flooded with CO_2 @ 3ml/min

Run	Cumulative Time (min)	dp (Psi)	Volume of CO_2 produced $V_g(l)$	Cumulative Volume of CO_2 Produced $V_g(l)$	Cumulative Volume of CO_2 Produced $V_g(cm^3)$	Cumulative Volume of CO_2 Produced (cm^3) over Pore volume (cm^3)
1	54.51	0.27	0	0	0	0.00
2	59.51	0.86	1.96	1.96	1960	2.35
3	64.51	0.79	2.07	4.03	4030	4.84
4	69.51	0.72	1.96	5.99	5990	7.19
5	74.51	0.59	1.92	7.91	7910	9.49
6	79.51	1.36	2	9.91	9910	11.89
7	84.51	4.19	3.83	13.74	13740	16.49
8	89.51	3.1	5.08	18.82	18820	22.59
9	94.51	2.24	5.48	24.3	24300	29.16
10	99.51	2.5	5.79	30.09	30090	36.11
11	104.51	1.81	6.05	36.14	36140	43.37
12	109.51	2.01	4.98	41.12	41120	49.35
13	114.51	1.99	4.96	46.08	46080	55.30
14	119.51	1.86	5.86	51.94	51940	62.34
15	124.51	5.37	5.92	57.86	57860	69.44
16	129.51	1.68	5.99	63.85	63850	76.63
17	134.51	1.17	5.76	69.61	69610	83.55
18	139.51	1.56	5.7	75.31	75310	90.39
19	144.51	2.67	5.75	81.06	81060	97.29
20	149.51	1.71	5.33	86.39	86390	103.68
21	154.51	2.13	5.79	92.18	92180	110.63
22	159.51	1.16	4.79	96.97	96970	116.38
23	164.51	2.23	6.16	103.13	103130	123.78
24	169.51	0.08	2.24	105.37	105370	126.46
25	174.51	0.11	0.09	105.46	105460	126.57

Appendices

Salt Wash North core sample saturated with 25 wt.% brine ($MgCl_2$) and flooded with CO_2 @ 3ml/min

Run	Cumulative Time (min)	dp (Psi)	Volume of CO_2 produced $V_g(l)$	Cumulative Volume of CO_2 Produced $V_g(l)$	Cumulative Volume of CO_2 Produced $V_g(cm^3)$	Cumulative Volume of CO_2 Produced (cm^3) over Pore volume (cm^3)
1	66.33	1.53	0	0	0	0.00
2	71.33	3.41	0.76	0.76	760	0.91
3	76.33	3.56	1.83	2.59	2590	3.11
4	81.33	3.44	1.85	4.44	4440	5.33
5	86.33	3.13	1.8	6.24	6240	7.49
6	91.33	2.56	1.8	8.04	8040	9.65
7	96.33	3.94	1.84	9.88	9880	11.86
8	101.33	2.98	1.9	11.78	11780	14.14
9	106.33	5.44	2.1	13.88	13880	16.66
10	111.33	4.27	4.68	18.56	18560	22.28
11	116.33	3.24	5.49	24.05	24050	28.86
12	121.33	8.92	5.94	29.99	29990	35.99
13	126.33	1.92	6	35.99	35990	43.19
14	131.33	2.29	6.19	42.18	42180	50.62
15	136.33	6.2	6.16	48.34	48340	58.02
16	141.33	2.92	6.29	54.63	54630	65.57
17	146.33	5.89	6.14	60.77	60770	72.94
18	151.33	2.06	5.92	66.69	66690	80.04
19	156.33	2.25	5.92	72.61	72610	87.15
20	161.33	3.25	60.4	133.01	133010	159.64
21	166.33	1.55	5.8	138.81	138810	166.60
22	171.33	2.96	5.92	144.73	144730	173.70
23	176.33	2.83	6.25	150.98	150980	181.20
24	181.33	2.46	5.94	156.92	156920	188.33
25	186.33	2.89	6.03	162.95	162950	195.57
26	191.33	3.05	6.06	169.01	169010	202.84
27	196.33	3.16	6.07	175.08	175080	210.13
28	201.33	2.49	6.06	181.14	181140	217.40
29	206.33	0.33	0.99	182.13	182130	218.59
30	211.33	0.3	0.02	182.15	182150	218.61